Corrosion and Electrochemistry Studies for Molten Salt Reactor Alloy Development

By

William H. Doniger

A dissertation submitted in partial fulfillment of

the requirements for the degree of

Doctor of Philosophy

(Material Science & Engineering)

at the

University of Wisconsin-Madison

2022

Date of final oral examination: 05/10/2022

The dissertation is approved by the following members of the Final Oral Committee:

Kumar Sridharan, Distinguished Research Professor, Material Science & Engineering
Adrien Couet, Associate Professor, Material Science & Engineering
Xudong Wang, Professor, Material Science & Engineering
Yongfeng Zhang, Assistant Professor, Engineering Physics
Nathaniel Hoyt, Scientist, Argonne National Laboratory

Acknowledgements

I would like to express my sincere gratitude to my advisor, Distinguished Research Professor Kumar Sridharan, and co-advisor Professor Adrien Couet, for their inspiring guidance and consistent support throughout the pursuit of my PhD degree, and for their effort on reviewing papers and this dissertation. I also thank Professor Xudong Wang, Professor Yongfeng Zhang, and Dr. Nathaniel Hoyt for serving as my committee members and providing invaluable suggestions on my dissertation. Thank you to Associate Professor Mark Anderson and Instrument Specialist Paul Brooks for their design guidance in the fabrication of early molten FLiBe salt facilities. Thank you to Dr. Murali Govindarajan for your materials expertise and enabling research of exciting new materials. I would like to thank Dr. Glenn Kuswa for the valuable mentorship and the inspiration to pursue graduate school and a career in research.

I would like to thank several colleagues and friends for your knowledge, support, and companionship. Thank you Dr. Hwasung Yeom, Dr. Mohamed Elbakhshwan, and Dr. Yafei Wang for your mentorship and guidance. I am especially grateful to Dr. Karl Britsch, Dr. Cody Falconer, Matthew Weinstein, Noah Anderson, and Thomas Chrobak for your assistance with molten salt handling and corrosion experiments. Thank you to Kyle Quillin, John Patrik Lacy, and Nathan Curtis for your assistance with materials characterization. Thank you to Kasey DePoy and Matthew Roberts for preparing specimens and assisting with materials characterization.

I am grateful to my loving family for their support. Thank you to my mother and father who made it possible for me to pursue my undergraduate degree at the University of Wisconsin-Madison and for your encouragement and support through graduate school.

Of course, I am grateful to Leah Gruen for her support. Her enthusiasm for our studies provided much inspiration.

I gratefully acknowledge that this research was supported by a grant from the U.S. Department of Energy Nuclear Energy University Program (NEUP) Project 18-15280/DE-NE0008803. I would also like to acknowledge the UW-Madison Wisconsin Centers for Nanoscale Technology (wcnt.wisc.edu) partially supported by the NSF through the University of Wisconsin Materials Research Science and Engineering Center (DMR-1720415) for enabling the materials characterization presented.

Abstract

The Molten Salt Reactor (MSR) concept is attracting considerable interest as the next generation nuclear reactor because it provides key benefits, including, (i) high degree of passive safety, (ii) atmospheric pressure operation, (iii) high thermal efficiency, (iv) fuel design flexibility and (v) lower spent fuel per unit energy. Fluoride salt-cooled reactors are being actively developed for deployment because of the desirable thermophysical properties of fluoride salts, such as low melting and high boiling points, and high specific heat capacities and thermal conductivities, as well as their low cross sections for thermal neutron absorption. However, molten fluoride salts can be quite corrosive to structural materials at the intended high operating temperatures of MSRs due to the inherent instability of protective oxide layers induced by the inevitable presence of even trace levels of impurities in the salt. Of particular concern is the corrosion of the alloying element Cr which is present in notable concentrations in most high temperature alloys primarily for air-side oxidation resistance. For the successful implementation of MSRs, there is need for: (a) a greater understanding of the corrosion mechanisms in structural alloys, (b) development of electrochemical methods to evaluate materials based on electrochemical parameters that govern the thermodynamics and kinetics of corrosion, and (c) development of electrochemical methods to test and monitor the evolving chemistry of the molten salt to assess and control corrosion. In this research, a holistic approach to studying molten salt corrosion is undertaken through both static corrosion and electrochemistry experiments to address these scientific and engineering challenges. Two types of fluoride salts have been used for this research: (i) LiF-BeF_2 (66-34 mol %) (FLiBe), which is being considered either as the coolant in conjunction with solid TRISO fuel particles or as solvent salt for dissolving the fuel, and (ii) LiF-NaF-KF (46.5-11.5-42 mol %) (FLiNaK), which is a candidate for secondary coolant loop systems and also serves as a surrogate for understanding the mechanisms of corrosion in a wide range of fluoride salts.

Molten fluoride salt experiments are inherently challenging due to the hygroscopicity and toxicity of the fluoride salts, the high temperatures of these experiments, and the extreme sensitivity of materials to corrosive impurities in the molten salt. The study involved significant engineering for designing and

constructing experimental systems for safely preparing and handling fluoride salts both with and without beryllium. These systems offered a versatile environment to conduct corrosion and electrochemistry experiments accurately and reproducibly.

Corrosion studies were aimed at understanding the mechanisms and extent of corrosion in candidate ASME Boiler and Pressure Vessel Code, Section III Division 5 qualified alloys and advanced alloy concepts with potential for ASME code qualification. The iron-based 316H stainless steel (18 Cr, 10 Ni, 2 Mo, 2 Mn, 0.04-0.1 C, bal. Fe, wt. %) is currently one of the only code-qualified alloys suitable for construction of MSR, however, its compatibility with molten fluoride salts has not been adequately studied. In addition to studying 316H, 316L (<0.03 wt. % C) was also studied to understand the role of carbon in these stainless steels on molten salt corrosion. Hastelloy-N is a nickel-based alloy (7 Cr, 16 Mo, 4 Fe wt. %) originally developed for resistance to molten fluoride salt corrosion. Two new computationally designed high creep strength variants of Hastelloy-N (Alloy N) containing additions of Ta, W, Hf, Nb, and Ti, referred to in this study as Alloy 141 and Alloy 3, were also investigated as potential candidates for salt facing structural materials in MSRs.

Corrosion testing of 316L and 316H stainless steel in molten FLiNaK were conducted in capsules of pyrolytic boron nitride (PBN), 316L stainless steel, and glassy carbon to investigate the effects of dissimilar materials on corrosion. The slightly higher carbon content in 316H stainless steel had a notable effect on the mechanisms of corrosion. Sensitization of the stainless steel prior to and during the corrosion tests influenced the corrosion mechanisms and was more pronounced in 316H stainless steel on account of its higher carbon content. Sensitization leads to the formation of Cr-rich carbide precipitates at the grain boundaries which beneficially affects molten fluoride salt corrosion. Three dominant modes of corrosion, namely, surface recession (uniform corrosion), and preferential elemental dissolution within the bulk grains and grain boundaries were quantified. Although there were mechanistic differences in corrosion between the two stainless steels, their overall corrosion performance was comparable, a result that is of considerable significance to the MSR application, given that 316H is the only ASME BPVC qualified material that can currently be utilized for the manufacture of structural components of MSRs. The weld filler material 16-

8-2 (also a type of stainless steel) used commonly for joining stainless steel was also investigated for molten salt corrosion given the importance of welds in the construction of MSR.

The corrosion of three nickel-based alloys was investigated in molten FLiNaK in the aforementioned materials capsules. Hastelloy-N (Alloy N) was tested and used to bench-mark the corrosion performance of advanced higher creep strength Alloy 141, and Alloy 3 provided by ORNL. Corrosion stability of strengthening second-phase precipitate particles was a particular focus in these advanced alloys. In Alloy 3 for example, molybdenum-carbide was stable, but carbides containing Hf, Nb, Ta, Ti were not stable. XPS analysis revealed the formation of a carbon film on the alloy surface as a result of the reaction of certain carbide phases with the fluoride salt. The alloys showed preferential dissolution of alloying elements both along the grain boundaries and grain matrix. Selective corrosion of certain strengthening precipitate phases was also observed, but there was minimal surface recession. Here again, the capsule material influenced the mechanism and modes of corrosion.

Potentiodynamic polarization was applied to Cr, Fe, Ni, the binary alloy Ni-20Cr, and 316L stainless steel in FLiNaK at 700 ˚C to investigate corrosion mechanisms and to measure fundamental electrochemical parameters that govern corrosion. A notable achievement here was the innovative use of the K/K^+ dynamic reference electrode (DRE) that allows for more reliable and reproducible evaluation of the electrochemical parameters, such as apparent redox potential and kinetic parameters indicative of corrosion rate. Post-polarization examination of the electrodes showed that the microstructural mechanisms of corrosion were similar to those observed in samples exposed to prototypical salt environment. The pure metals experienced uniform corrosion and the relative hierarchy of the Ni, Fe, and Cr redox potentials was consistent with experimental observations and thermodynamic predictions based on the standard Gibbs free energy of formation of metal-fluorides. The corrosion behavior of Ni-20Cr was dependent on the applied potential relative to the redox potential of Ni and Cr. Preferential dissolution of Cr was observed at potentials below the Ni^{2+}/Ni redox potential. More uniform corrosion of the alloy surface was observed when the potential exceeded the Ni^{2+}/Ni redox potential due to dissolution of both elements. 316L, on the other hand, had the same redox potential as the Fe^{2+}/Fe reaction due to near-surface dissolution of Cr prior

to application of the overpotential. Both Cr and Fe in 316L experienced comparable corrosion rates, which led to an overall surface recession at all anodic overpotentials. The redox potentials provided a means of delineating the criteria for uniform corrosion vs. selective intergranular corrosion based on the magnitude of the applied overpotential. The experiments form the basis for the establishment of hierarchical activity of elements in molten fluoride salts analogous to the EMF or galvanic series in aqueous environments. They also provide a basis for cathodic protection methods in molten salt systems. The polarization plots exhibited Tafel behavior, and the thickness loss results calculated from electrochemical data and Faraday's law were consistent with the thickness loss observations. Pure metals experience more rapid thickness loss (surface recession) in increasingly anodic environments. Alloys experience more delayed thickness loss because the selective dissolution of alloying elements. At sufficiently high anodic potentials, dissolution of the alloy's matrix becomes energetically favorable, and the rate of thickness loss increases dramatically.

Electrochemical cyclic voltammetry method for quantitative concentration measurements of corrosion products, such as Cr^{2+}, was investigated for the study of structural materials corrosion in molten FLiBe salt at temperatures between 500 ˚C and 700 ˚C. These methods were benchmarked using the ICP-OES technique to independently verify the concentrations of Cr and Fe in the FLiBe salt. The redox potential of the Cr/Cr^{2+} couple was reported with respect to the Be/Be^{2+} DRE also developed in this study analogous to the K/K^{+} DRE. The relationship between Cr^{2+} concentration and salt temperature on the apparent reduction potential of Cr^{2+} was observed to obey the Nernst equation. Linear relationships between cathodic peak current density and Cr^{2+} concentration were obtained over a range of temperatures which allowed for the determination of Cr^{2+} concentration in situ after calibration with known quantities of trace impurities. The technique was used effectively for studying corrosion of 316H stainless steel, supported by SEM-EDS compositional analysis of the corrosion layers and ICP-OES for salt composition after the cyclic voltammetry test. The study validated the feasibility of the cyclic voltametry technique to monitor the salt chemistry during MSR operation to control and monitor the corrosion health of structural materials.

Table of Contents

Acknowledgements i

Abstract ii

List of Figures x

List of Tables xxiv

Variable Definitions xxvii

1 Introduction 1

1.1 Molten salts for advanced reactor coolants 3

1.2 Selection of molten salt for materials research 5

1.3 Alloy development for molten salt reactors 7

1.4 Molten salt corrosion and the molten salt redox condition 12

1.4.1 Thermodynamics of Corrosion 13

1.4.2 Acid-Base Chemistry 17

1.4.3 Mechanisms of Corrosion 18

1.4.4 Rate of Corrosion 22

1.5 Electrochemistry Theory 23

1.5.1 Cell Potential 24

1.5.2 Half-Cell Reduction Potential (Redox Potential) 25

1.5.3 Formal Half-Cell Reduction Potential 26

1.5.4 Overpotential & Charge Transfer Relationships 27

1.5.5 Potentiodynamic Polarization 29

1.5.6 Cyclic Voltammetry 30

1.5.7 Reference Electrodes for Fluoride Salts 32

2 Experimental Procedures 37

2.1 Design and construction of molten salt corrosion facilities 37

2.1.1 Gloveboxes 37

2.1.2 Beryllium Laboratory Safety 39
2.1.3 Electronics & Labview control systems 40
2.2 FLiBe and FLiNaK salt procurement & purification 41
2.2.1 Fluoride salt purification systems 42
2.2.2 FLiBe salt purification 44
2.2.3 FLiNaK salt procurement and purification 45
2.3 Static corrosion experimental design 47
2.3.1 Procurement & heat treatment of 316L & 316H stainless steel 47
2.3.2 Procurement of Alloy-N, Alloy 141, and Alloy 3 50
2.3.3 Procurement of 16-8-2 weld 51
2.3.4 Procurement of pyrolytic boron nitride 52
2.3.5 Pre-exposure processing of test specimens 53
2.3.6 Capsule design & corrosion experiment procedure 53
2.3.7 Post-exposure treatment of test specimens 55
2.4 Salt Chemistry Analysis & Metal Fluoride Impurity Additions 57
2.4.1 Inductively Coupled Plasma-Optical Emission Spectroscopy 58
2.4.2 Inductively Coupled Plasma-Mass Spectroscopy 59
2.4.3 Metal Fluoride Impurity Additions 60
2.5 Electrochemistry Experimental Procedures 61
2.5.1 Dynamic Reference Electrodes 62
2.5.2 Potentiodynamic Polarization Experimental Procedure 65
2.5.3 Cyclic Voltammetry Experimental Procedure 67
3 Results & Discussion 69
3.1 Corrosion Studies of 316L & 316H Stainless Steel 69
3.1.1 Overview 69
3.1.2 Comparison of as-received 316L and 316H corrosion resistance in FLiNaK 71

3.1.3 Microstructural effects on corrosion of 316L & 316H in FLiNaK 89
3.1.4 Corrosion resistance of 16-8-2 weld material in FLiNaK 103
3.2 Corrosion Studies of Alloy N, 141 & 3 113
3.2.1 Overview 113
3.2.2 Initial microstructure and composition characterization of alloys 114
3.2.3 Weight Change after exposure to molten FLiNaK 117
3.2.4 Exposed alloy surface morphology 118
3.2.5 Elemental analysis of the corrosion surface exposed in PBN capsules 122
3.2.6 Elemental analysis of the corrosion surface exposed in nickel capsules 126
3.2.7 Elemental analysis of the corrosion surface exposed in glassy carbon capsules 129
3.2.8 Compositional and phase stability calculations 133
3.2.9 XRD analysis on corrosion surface 138
3.2.10 Salt analysis 140
3.2.11 Pyrolytic boron nitride (PBN) capsules 141
3.2.12 Nickel capsules 143
3.2.13 XPS analysis of Alloy 3 145
3.2.14 Discussion 149
3.3 Potentiodynamic Polarization for Understanding Metals and Alloys Corrosion Performance in Molten FLiNaK Salt 155
3.3.1 Measuring the K/K^+ Reference Potential 156
3.3.2 Specimen Open Circuit Potential 157
3.3.3 FLiNaK Solution Resistance 157
3.3.4 Potentiodynamic Polarization of Pure Metals 158
3.3.5 Potentiodynamic Polarization of Ni-20Cr 164
3.3.6 Potentiodynamic Polarization of 316L 168
3.3.7 Thickness loss calculations 171

3.3.8 Driving forces for galvanic corrosion 172
3.3.9 Thermodynamic analysis 173
3.3.10 Polarization research in the context of static corrosion experiments and alloys development 174
3.4 Electrochemical Methods for Relating Salt Chemistry & Corrosion 176
3.4.1 Cyclic Voltammetry for measuring metal fluoride impurities 176
3.4.2 Electrochemical investigation of 316H Stainless Steel exposure to FLiBe containing CrF_2 and FeF_2 190
4 Conclusions 205
References 210

List of Figures

Figure 1. Temperature and irradiation dose ranges for the proposed generation IV nuclear reactor concepts the Gas-cooled Fast Reactor (GFR), Lead-cooled Fast Reactor (LFR), Sodium-cooled Fast Reactor (SFR), Supercritical Water-cooled Reactor (SCWR), very High-temperature Gas Reactor (VHTR), and the Molten Salt Reactor (MSR) [14]. 5

Figure 2. Time-temperature-sensitization (TTS) diagram of Type 316L stainless steel determined by boiling nitric acid test [19]. 10

Figure 3. Cross-sectional (a) SEM image and (b) EDS elemental Cr distribution in 316 stainless steel exposed to FLiBe salt in a 316 stainless steel capsules for 2000 hours at 700 ˚C [38]. 12

Figure 4. The Gibbs free energy of formation of fluoride per mole of fluorine gas. Unless otherwise stated the product is a solid fluoride. Data is from HSC 7.0 [40]. 16

Figure 5. Effect of fluoride batch purity shown in an Inconel thermal convection loops-500 hours at 815˚C [52]. 20

Figure 6. Micrographs of tubing and specimens exposed to molten LiF-BeF_2-ZrF_4-ThF_4-UF_4 (70-23-5-1-1) between 560-700˚C for 30,000 hours (9.2 years). As polished. 500x [53]. 21

Figure 7. (a) Schematic Diagram of an electrochemical cell for potentiodynamic polarization and cyclic voltammetry experiments. (b) Analysis of an idealized Tafel plot of potentiodynamic data [69]. 30

Figure 8. Environment-controlled argon atmosphere gloveboxes for research with (a) FLiBe and (b) FLiNaK. 37

Figure 9. Static corrosion furnace incorporated in environment-controlled glovebox (a) schematic, (b) heaters and well, and (c) corrosion cell assembly. 38

Figure 10. The FLiBe salt laboratory used for this research. 39

Figure 11. Electronics and LabVIEW software designed and constructed for operation of the glovebox furnaces and sensors. 41

Figure 12. Fluoride salt purification system including (a) gas distribution cabinets for H_2 (left) and HF (right), (b) purification reactor vessel, (c) effluent scrubber baths, and (d) purification reactor vessel attached to the glovebox. 44

Figure 13. FLiBe salt solidified in a nickel tray after being poured from a nickel transfer vessel [105], [116]. The large dendritic structures are a manifestation of the high purity of the salt. 45

Figure 14. Photograph of FLiNaK produced in collaboration Materion Corporation. 45

Figure 15. FLiNaK salt before (left) and after (right) purification. The white color generally indicates a higher purity salt. 46

Figure 16. 316L batches before and after heat treatment in ambient environment. Table 8 summarizes the heat treatment parameters. Surface oxide layer was removed prior to testing in molten salt by grinding with SiC grinding media. 49

Figure 17. Photographs of (a) Hastelloy-N sheet and the as-received and machined (b) Alloy 141 and (c) Alloy 3 obtained from Oak Ridge National Laboratory. 51

Figure 18. 16-8-2 weld material and 316H substrates (a) a schematic of the GTAW welding process, (b) image of the as-welded plate, c) image of the 316H substrate coupons, and (d) image of the 16-8-2 coupons [119]. 52

Figure 19. A pyrolytic boron nitride (PBN) specimen used to evaluate PBN as a potential capsule material for static corrosion studies. 52

Figure 20. Photograph of static corrosion specimens before exposure to molten FLiNaK salt in (a) PBN capsules and (b) glassy carbon capsules. Specimens are polished and then suspended from capsule lids by 316 stainless steel or nickel wires depending on the test material. 53

Figure 21. Schematic diagram of (a) 316 stainless steel or nickel capsules, (b) glassy carbon capsules, and (c) pyrolytic boron nitride (PBN) capsules for static corrosion experiments. Dimensions are in inches. 54

Figure 22. Preparation of FLiBe with varying concentrations of chromium fluoride prepared by dilution. a) 100 g of purified FLiBe with 85 mg of CrF_2 powder in a glassy carbon crucible, b) FLiBe with the

added CrF_2, before and after breaking in to small pieces, c) preparation of purified FLiBe and FLiBe with CrF_2 for dilution, d) FLiBe with 352 ppm Cr, e) FLiBe with 286 ppm, f) FLiBe with 185 ppm CrF_2, and g) FLiBe with 100 ppm CrF_2. 61

Figure 23. Schematic diagram of the electrochemical cell used in this study. 62

Figure 24. Electrochemical probe for molten salt chemistry and corrosion kinetics studies. 62

Figure 25. (a) Linear sweep voltammogram (LSV) of FLiBe salt with 286 ppm Cr at various temperatures. Scan rate is 100 mV/sec. (b) Open circuit potential between the beryllium dynamic reference electrode (DRE) and the Mo QRE as a function of time following the LSV [102] (from the author's research). 64

Figure 26. Cyclic voltammogram of FLiNaK salt at 700 ˚C acquired using Mo working electrode, Pt reference electrode, and graphite counter electrode. A scan rate 80 mV/sec was used, and the potential was normalized to the K/K^+ redox couple. 65

Figure 27. Weight change for 316L and 316H stainless steels after exposure to FLiNaK for 500 hours at 700 ˚C in pyrolytic boron nitride (PBN), 316 stainless steel (316L), and glassy carbon (GC) capsules. 71

Figure 28. Photographs of (a)(b)(d)(f)(g) 316L and (c)(e)(h) 316H specimens (a) before exposure in PBN or 316L capsules, (b-c) after exposure in PBN capsules, (c-d) after exposure in 316L capsules, (f) before exposure in glassy carbon capsules, and (g-h) after exposure in glassy carbon capsules... 73

Figure 29. SEM images of the surface of (a-d) 316L and (e-h) 316H (a)(e) before exposure, and after exposure to FLiNaK for 500 h at 700 ˚C in (b), (f) PBN capsules, (c), (g) 316L capsules, and (d), (h) in a glassy carbon capsules. 74

Figure 30. Profilometry of the surface of (a-c) 316L and (d-f) 316H after exposure to FLiNaK for 500 hours at 700 ˚C in (a),(d) PBN capsules, (b),(e) 316L capsules, and (c),(f) in a glassy carbon capsules (units are μm). 75

Figure 31. Profilometry topographical maps and linear slice plots of the salt-vapor interface of (a) 316L in pyrolytic boron nitride (PBN), (b) 316H in pyrolytic boron nitride (PBN), (c) 316L in glassy

carbon, and (d) 316H in glassy carbon. The bottom region of the topographical map was submerged in molten salt and the top region was exposed to the vapor phase (units are μm). 77

Figure 32. EDS large area average compositional analysis of the as-received 316L and 316H specimens and the net change in composition after exposure to FLiNaK salt in different capsules for 500 hours at 700 ˚C. Fe makes up the balance of the composition..... 79

Figure 33. Cross-sectional EDS compositional analysis of (a) 316L and (b) 316H surfaces exposed to FLiNaK in pyrolytic boron nitride (PBN) capsules for 500 hours at 700 ˚C. A Cu coating was electroplated on the sample surface prior to mounting and polishing. Yellow arrow in the SEM image denotes the path of the EDS line scan. 81

Figure 34. Cross-sectional EDS compositional analysis of (a) 316L and (b) 316H surfaces exposed to FLiNaK in 316L capsules for 500 hours at 700 ˚C. A Cu coating was electroplated on the sample surface prior to mounting and polishing. Yellow arrow in the SEM image denotes the path of the EDS line scan. 82

Figure 35. High magnification SEM images of the surface of (a) 316L and (b) 316H exposed to FLiNaK in 316L capsules for 500 hours at 700 ˚C. 82

Figure 36. Cross-sectional EDS compositional analysis of (a) 316L and (b) 316H surfaces exposed to FLiNaK in glassy carbon capsules for 500 hours at 700 ˚C. A Cu coating was electroplated on the sample surface prior to mounting and polishing. Yellow arrow in the SEM image denotes the path of the EDS line scan. 83

Figure 37. XRD patterns for (a) 316L and (b) 316H reference specimens and specimens exposed to FLiNaK in pyrolytic boron nitride (PBN), 316L, and glassy carbon capsules for 500 hours at 700 ˚C. 85

Figure 38. Calculated lattice parameter as a function of the Neslon-Riley extrapolation function ($\cos^2(\theta)/\sin(\theta) + \cos^2(\theta)/\theta$) for (a) 316L and (b) 316H specimens exposed in different capsule materials. 85

Figure 39. Concentration of trace impurities in FLiNaK salt before and after exposure to 316L and 316H stainless steel in pyrolytic boron nitride (PBN), 316 stainless steel (316L), and glassy carbon (GC) capsules for 500 hours at 700 ˚C.....86

Figure 40. Optical cross section images of etched (a) 316L, (b) 316L annealed 20 minutes at 1,100 ˚C, (c) 316L sensitized 24 hours at 700 ˚C, (d) 316L annealed 20 min at 1,100 ˚C & sensitized 24 h at 700 ˚C, (e) 316H, and (f) 316H sensitized 24 h at 700 ˚C. Specimens are etched by swabbing with 3:1 (by volume) $HCl:HNO_3$ for 1 minute. 90

Figure 41. Optical images of etched (a) as-received 316H, (b) 316H sensitized for 24 h at 700 ˚C, and (c) as-received 316H after 500 h at 700 ˚C in FLiNaK. Etchant is aqua regia solution.....90

Figure 42. Weight change of as-received and heat treated 316L and 316H after exposure to FLiNaK for 500 hours at 700 ˚C in pyrolytic boron nitride (PBN). 91

Figure 43. Photographs of (a) as-polished 316L and (b) 316L, (c) 316L batch I, (d) 316L batch II, (e) 316L batch III, (f) 316H, and (g) Sensitized 316H after exposure to molten FLiNaK for 500 hours at 700 ˚C in pyrolytic boron nitride (PBN) capsules. 92

Figure 44. SEM images of the surface of (a) as-received 316L, (b) 316L batch I, (c) 316L batch II, and (d) 316L batch III after exposure to FLiNaK in pyrolytic boron nitride (PBN) capsules for 500 hours at 700 ˚C.....93

Figure 45. SEM images of the surface of (a) as-received 316H and (b) pre-sensitized 316H after exposure to FLiNaK in pyrolytic boron nitride (PBN) capsules for 500 hours at 700 ˚C.....93

Figure 46. Profilometry of the surface of (a) as-received 316L, (b) 316L annealed for 20 minutes at 1,100 ˚C (batch I), (c) 316L sensitized for 24 hours at 700 ˚C (batch II), and (d) 316L annealed for 20 minutes at 1,100 ˚C (batch III), and sensitized for 24 hours at 700 ˚C after exposure to FLiNaK for 500 hours at 700 ˚C in PBN capsules (units are μm).....94

Figure 47. Profilometry of the surface of (a) as-received 316H, and (b) 316H sensitized for 24 hours at 700 ˚C after exposure to FLiNaK for 500 hours at 700 ˚C in PBN capsules (units are μm). 94

Figure 48. Profilometry topographical maps and linear slice plots of the salt-vapor interface of (a) as-received 316L, (b) 316L annealed for 20 minutes at 1,100 ˚C (batch I), (c) 316L sensitized for 24 hours at 700 ˚C (batch II), and (d) 316L annealed for 20 minutes at 1,100 ˚C and sensitized for 24 hours at 700 ˚C (batch III) after exposure to FLiNaK for 500 hours at 700 ˚C in PBN capsules (units are μm). 96

Figure 49. Profilometry topographical maps and linear slice plots of the salt-vapor interface of (a) as-received 316H, and (b) 316H sensitized for 24 hours at 700 ˚C after exposure to FLiNaK for 500 hours at 700 ˚C in PBN capsules (units are μm). 97

Figure 50. EDS large area average compositional analysis showing the net change in composition of as-received and heat treated 316L and 316H specimens after exposure to FLiNaK salt in pyrolytic boron nitride (PBN) capsules for 500 hours at 700 ˚C. Iron makes up the balance of the composition. 98

Figure 51. Cross-sectional EDS compositional analysis of (a) as-received 316L, (b) 316L annealed for 20 minutes at 1,100 ˚C (batch I), (c) 316L sensitized for 24 hours at 700 ˚C (batch II), and (d) 316L annealed for 20 minutes at 1,100 ˚C and sensitized for 24 hours at 700 ˚C (batch III) exposed to FLiNaK in pyrolytic boron nitride (PBN) capsules for 500 hours at 700 ˚C. A Cu coating was electroplated on the sample surface prior to mounting and polishing. Yellow arrow in the SEM image denotes the path of the EDS line scan. 99

Figure 52. Cross-sectional EDS compositional analysis of (a) as-received 316H, and (b) sensitized 316H exposed to FLiNaK in pyrolytic boron nitride (PBN) capsules for 500 hours at 700 ˚C. A Cu coating was electroplated on the sample surface prior to mounting and polishing. Yellow arrow in the SEM image denotes the path of the EDS line scan. 100

Figure 53. Concentration of trace impurities in FLiNaK salt before and after exposure to as-received and heat treated 316L and 316H for 500 hours at 700 ˚C in pyrolytic boron nitride (PBN). 100

Figure 54. SEM and EDS compositional maps of as-polished (a) 316H substrate and (b) 16-8-2 weld specimen surfaces. 104

Figure 55. Weight change for 316H substrate and 16-8-2 weld specimens after exposure to FLiNaK for 500 hours at 700 ˚C in pyrolytic boron nitride (PBN) capsules. 104

Figure 56. SEM images for (a)(c) 316H substrate and (b)(d) 16-8-2 weld specimens (a)(b) before and (c)(d) after exposure to FLiNaK for 500 hours at 700 ˚C in pyrolytic boron nitride (PBN) capsules. .. 105

Figure 57. SEM images for (a) 316H substrate and (b) 16-8-2 weld specimens after exposure to FLiNaK for 500 hours at 700 ˚C in pyrolytic boron nitride (PBN) capsules. 106

Figure 58. Profilometry of the surface of (a) 316H substrate and (b) 16-8-2 weld specimens after exposure to FLiNaK for 500 hours at 700 ˚C in pyrolytic boron nitride (PBN) capsules. 106

Figure 59. Profilometry topographical maps and linear slice plots of the salt-vapor interface of (a) 316H substrate and (b) 16-8-2 weld specimens after exposure to FLiNaK for 500 hours at 700 ˚C in pyrolytic boron nitride (PBN) capsules. 107

Figure 60. EDS large area average compositional analysis of the 316H substrate and 16-8-2 weld specimens and the net change in composition after exposure to FLiNaK salt in PBN capsules for 500 hours at 700 ˚C. Iron makes up the balance of the composition. 108

Figure 61. Cross-sectional EDS compositional analysis of (a) 316H substrate and (b) 16-8-2 weld specimens exposed to FLiNaK in pyrolytic boron nitride (PBN) capsules for 500 hours at 700 ˚C. A Cu coating was electroplated on the sample surface prior to mounting and polishing. The yellow arrow in the SEM image denotes the path of the EDS line scan. 109

Figure 62. Cross-sectional EDS compositional analysis of a 16-8-2 weld specimen exposed to FLiNaK in pyrolytic boron nitride (PBN) capsules for 500 hours at 700 ˚C. A Cu coating was electroplated on the sample surface prior to mounting and polishing. The yellow arrow in the SEM image denotes the path of the EDS line scan. 109

Figure 63. 16-8-2 surface (a) topographical map and linear slice and (b) compositional line scan after exposure to FLiNaK for 500 hours at 700 ˚C in a PBN capsule. The black arrow indicates the path of the slice and the line scan. The inset image in the topographical map is an optical image of the analyzed area. 110

Figure 64. XRD patterns for (a) 316H substrate and (b) 16-8-2 weld before (reference) and after exposure to FLiNaK in pyrolytic boron nitride (PBN) for 500 hours at 700 ˚C. 111

Figure 65. Concentration of trace impurities in FLiNaK salt before and after exposure to 316H substrate and 16-8-2 weld specimens for 500 hours at 700 ˚C in pyrolytic boron nitride (PBN). 111

Figure 66. SEM images of Alloy N, Alloy 141, and Alloy 3. Specimens are prepared by 3 hours of vibratory polishing with 0.02 μm colloidal silica. An accelerating voltage of 5 kV and an aperture of 120 μm was used. 114

Figure 67. EDS (a-c) large area average composition and (d-e) point scans of the matrix material and precipitates for as-received (a)(d) Alloy N, (b)(e) Alloy 141, and (c)(f) Alloy 3. 115

Figure 68. EDS compositional analysis of the Ni-based alloy specimens before exposure to molten salt (balance Ni). 116

Figure 69. Weight change of Ni-based alloys after exposure to FLiNaK for 500 hours at 700 ˚C in nickel (Ni), pyrolytic boron nitride (PBN), and glassy carbon capsules. 117

Figure 70. Photographs of nickel alloy specimens before and after exposure to molten FLiNaK salt for 500 hours at 700 ˚C. Alloy N (left), Alloy 141, and Alloy 3 (right) are shown (a) before exposure, and after exposure in (b) pyrolytic boron nitride (PBN) capsules, and (c) nickel capsules. Alloy N is shown (d) before and (e) after exposure in a glassy carbon capsule. Alloys 141 (left) and Alloy 3 (right) are shown (f) after exposure in glassy carbon capsules. 119

Figure 71. SEM images of the surface of (a-d) Alloy N, (e-h) Alloy 141, and (i-l) Alloy 3 (a),(e),(i) before exposure, and after 500 h exposure at 700 ˚C in (b),(f),(j) pyrolytic boron nitride (PBN) capsules, (c),(g),(k) nickel capsules, and (d),(h),(i) in a glassy carbon capsules. 120

Figure 72. Profilometry of the surface of (a-c) Alloy N, (d-f) Alloy 141, and (g-i) Alloy 3 after 500 h exposure at 700 ˚C in (a),(d),(g) pyrolytic boron nitride (PBN) capsules, (b),(e),(h) nickel capsules, and (c),(f),(i) in a glassy carbon capsules. 121

Figure 73. Profilometry topographical maps and linear slice plots of the salt-vapor interface of (a) Alloy N, (b) Alloy 141, and (c) Alloy 3 in pyrolytic boron nitride (PBN) and (d) Alloy N, (e) Alloy 141, and

(f) Alloy 3 in glassy carbon. The bottom region of the topographical map was submerged in molten salt and the top region was exposed to the vapor phase (units are μm). 122

Figure 74.EDS (a-c) area average composition and (d-e) point scans of the matrix and precipitates for (a)(d) Alloy N, (b)(e) Alloy 141, and (c)(f) Alloy 3, exposed to FLiNaK in PBN capsules for 500 hours at 700 ˚C..... 123

Figure 75. EDS compositional analysis of the net change in composition of the area average, matrix point scans, and precipitates point scans after exposure to FLiNaK salt in a PBN capsule for 500 hours at 700 ˚C..... 124

Figure 76. SEM image, EDS compositional maps, and EDS line scans of cross sections of (a) Alloy N, (b) Alloy 141, and (c) Alloy N in FLiNaK in pyrolytic boron nitride (PBN) capsules for 500 hours at 700 ˚C. A Cu coating was electroplated on the sample surface prior to mounting and polishing. Yellow arrow in the SEM image denotes the path of the EDS line scan. Cross sections were etched during 0.2 μm colloidal silica polishing..... 125

Figure 77. EDS point scan analysis of Alloy 3 exposed to FLiNaK in a PBN capsule for 500 hours at 700 ˚C. Point scans 1-3 are located on the matrix. Point scans 4-6 are located on Mo-rich surface precipitate particles. 125

Figure 78. EDS (a-c) area average composition and (d-e) point scans of the matrix and precipitates for (a)(d) Alloy N, (b)(e) Alloy 141, and (c)(f) Alloy 3, exposed to FLiNaK in nickel capsules for 500 hours at 700 ˚C..... 126

Figure 79. EDS compositional analysis of the net change in composition of the area average, matrix point scans, and precipitates point scans after exposure to FLiNaK salt in a nickel capsule for 500 hours at 700 ˚C..... 127

Figure 80. SEM image, EDS compositional maps, and EDS line scans of cross sections of (a) Alloy N, (b) Alloy 141, and (c) Alloy N in FLiNaK in nickel capsules for 500 hours at 700 ˚C. A Cu coating was electroplated on the sample surface prior to mounting and polishing. Yellow arrow in the SEM

image denotes the path of the EDS line scan. Cross sections were etched during 0.2 μm colloidal silica polishing. 129

Figure 81. EDS (a-c) area average composition and (d-e) point scans of the matrix and precipitates for (a)(d) Alloy N, (b)(e) Alloy 141, and (c)(f) Alloy 3, exposed to FLiNaK in PBN capsules for 500 hours at 700 ˚C..... 130

Figure 82. EDS compositional analysis of the net change in composition of the area average, matrix point scans, and precipitates point scans after exposure to FLiNaK salt in a glassy carbon capsule for 500 hours at 700 ˚C..... 131

Figure 83. SEM image, EDS compositional maps, and EDS line scans of cross sections of (a) Alloy N, (b) Alloy 141, and (c) Alloy N in FLiNaK in glassy carbon capsules for 500 hours at 700 ˚C. A Cu coating was electroplated on the sample surface prior to mounting and polishing. Yellow arrow in the SEM image denotes the path of the EDS line scan. Cross sections were etched during 0.2 μm colloidal silica polishing. 132

Figure 84 EDS point scan analysis of Alloy 3 exposed to FLiNaK in a glassy carbon capsule for 500 hours at 700 ˚C. Point scans 1-3 are located on the matrix. Point scans 4-6 are located on Mo rich surface particulate..... 133

Figure 85. The calculated Hastelloy-N microstructure (a) phase mass fraction and (b) concentration of Cr in each phase as a function of temperature. 134

Figure 86. The calculated Alloy A microstructure (a) phase mass fraction and (b) concentration of Cr in each phase as a function of temperature. 135

Figure 87. The calculated Alloy B microstructure (a) phase mass fraction and (b) concentration of Cr in each phase as a function of temperature. 135

Figure 88. Gibbs free energy of carbide formation at 700 ˚C calculated using HSC 7.0 [40]..... 137

Figure 89. XRD patterns of (a) Alloy N, (b) Alloy 141, and (c) Alloy 3 before and after exposure to FLiNaK in nickel, PBN, and glassy carbon capsules for 500 hours at 700 ˚C. 138

Figure 90. Calculated lattice parameter as a function of the Neslon-Riley extrapolation function ($\cos^2(\theta)/\sin(\theta) + \cos^2(\theta)/\theta$) for Alloy N, 141, and 3 reference specimens. 139

Figure 91. ICP-MS measurements of the S, Fe, and Cr concentration in FLiNaK salt before and after exposure to Alloys N, 141, and 3 in nickel, pyrolytic boron nitride (PBN), and glassy carbon (GC) for 500 hours at 700˚C. 141

Figure 92. ICP-MS measurements of the Nb, Ta, Ti, and Hf concentration in FLiNaK salt before and after exposure to Alloys N, 141, and 3 in nickel, pyrolytic boron nitride (PBN), and glassy carbon (GC) for 500 hours at 700˚C. 141

Figure 93. Images of (a) the inside of the bottom of the PBN capsule that contained Alloy N and (b) the PBN capsules specimens after sputter coating with 10 nm of Au to impart conductivity. Capsules were exposed to FLiNaK for 500 hours at 700 ˚C. 142

Figure 94. Compositional analysis of (a) the PBN reference coupon, (b) the inside diameter of the PBN capsule which contained Alloy N, (c) the EDS spectra for the capsule which contained Alloy N, and (d) the concentration of various alloying elements detected on the PBN capsules before and after exposure. The PBN is sputter coated with 10 nm of Au to improve conductivity. Au makes up the balance of the area average composition. 143

Figure 95. Nickel capsule SEM and EDS analysis of (a) the inside diameter of the nickel capsules that contained Alloy N, (b) photograph of a mounted capsule cross section. EDS line scan of cross sections of the nickel capsules which contained (c) Alloy N, (d) Alloy 141, and (e) Alloy 3 in FLiNaK for 500 hours at 700 ˚C. Cross sections were etched during 0.2 μm colloidal silica polishing..... 144

Figure 96. XPS spectra of Alloy 3 surface (a) before exposure, and after exposure to FLiNaK in (b) a PBN capsules, and (c) a glassy carbon capsules for 500 hours at 700 ˚C. 149

Figure 97. Open circuit potential of Ni, Fe, Cr, the binary alloy Ni-20Cr, and 316L vs. Pt QRE in FLiNaK at 700 ˚C..... 157

Figure 98. Polarization curves for (a) Ni, (b) Fe, and (c) Cr polarized to various anodic overpotentials, η, in FLiNaK at 700 ˚C. 160

Figure 99. Experimental and fitted polarization curves for Ni polarized to a final anodic overpotential of 300 mV in FLiNaK at 700 ˚C. The regions highlighted in red indicate the portion of the experimental data that is fitted. The blue lines indicate the fitted Tafel extrapolation. 162

Figure 100. SEM images of (a) as-received Ni, (b) Ni exposed to FLiNaK for 3 hours, (c) Ni polarized to η = 300 mV at 0.166 mV s^{-1} after exposure for 1 hour, (d) as-received Fe, (e) Fe exposed to FLiNaK for 3 hours, (f) Fe polarized to η = 300 at 0.166 mV s^{-1} after exposure for 1 hour, (g) as-received Cr, (h) Cr exposed to FLiNaK for 2.3 hours, (i) Cr polarized to η = 300 mV at 1 mV s^{-1} after exposure for 5 minutes. 164

Figure 101. Polarization curves for Ni-20Cr polarized to various anodic overpotentials in FLiNaK at 700 ˚C. 166

Figure 102. Surface SEM images of a) as-received Ni-20Cr, b) Ni-20Cr exposed to FLiNaK for 3 h, c) Ni-20Cr polarized to η = 300 mV, and d) Ni-20Cr polarized to η = 500 mV. Cross-sectional EDS composition maps of e) Ni-20Cr exposed to FLiNaK for 3 h, f) Ni-20Cr polarized to η = 300 mV, and g) Ni-20Cr polarized to η = 500 mV. Polarization was conducted at 0.166 mV s^{-1} after exposure for 1 hour. 168

Figure 103. Polarization curves for 316L polarized to various anodic overpotentials in FLiNaK at 700 ˚C. 169

Figure 104. Surface SEM images of a) as-received 316L, b) 316L exposed to FLiNaK for 3 h, and c) 316L polarized to η = 300 mV at 0.166 mV s^{-1} after exposure for 1 hour. Cross-sectional EDS compositional maps of d) 316L exposed to FLiNaK for 3 hours and e) 316L polarized to η = 300 mV at 0.166 mV s^{-1} after exposure for 1 hour. 170

Figure 105. Thickness loss of Ni, Fe, 316L, and Ni-20Cr specimens after polarization to various anodic overpotentials at a scan rate of 0.166 mV sec^{-1} in FLiNaK salt at 700 ˚C. 172

Figure 106. Redox potential of the Ni^{2+}/Ni, Fe^{2+}/Fe, and the Cr^{2+}/Cr redox couples. For Ni^{2+}/Ni and Fe^{2+}/Fe, the activity of the dissolved fluoride is 10^{-6} and the activity of the metal is unity. The redox potential of the Cr^{2+}/Cr redox couple is plotted as a function of the alloy's Cr activity for three hypothetical molten salt compositions containing different activities of dissolved Cr^{2+} 174

Figure 107. Cyclic voltammograms of molten FLiBe salt samples with various impurity additions at 650˚C. Scan rate was 80 mV/sec. 178

Figure 108. Cyclic voltammogram showing the first and second scan cycles of FLiBe containing 286 ppm Cr at 650˚C. Scan rate is 80 mV/sec. 178

Figure 109. CVs of a) FLiBe containing 286 ppm Cr at various temperatures and b) FLiBe containing various Cr concentrations at 700˚C. Scan rate is 80 mV/sec. 182

Figure 110. CV anodic and cathodic peak potentials of the Cr/Cr^{2+} couple with respect to the log of concentration at 500˚C and 700˚C. CVs are shown for salt samples 2, 4 and 6. Scan rate 80 mV/sec. 183

Figure 111. CV of FLiBe with 286 ppm Cr at 650°C. Analysis of current peaks is performed on the first scan cycle. 186

Figure 112. Cyclic voltammograms of FLiBe with 207 ppm Cr at 650°C at various potential scan rates. 187

Figure 113. CV faradaic cathodic peak current density at various temperatures as a function of the square root of potential scan rate. 187

Figure 114. CV faradaic cathodic peak current density at various temperatures as a function Cr concentration. 188

Figure 115. Cyclic voltammograms of corrosion FLiBe salts before and after 1000 hours exposure in a) capsule 1, b) capsule 2, c) capsule 3 and d) capsule 4. Scan Rate 80 mV/sec, Mo WE, Be/Be^{2+} dynamic reference electrode, Glassy Carbon CE 192

Figure 116. Weight change of 316H following exposure to salts in capsules 1 through 4 for 1000 hours at 700 °C. 196

Figure 117. XRD patterns of 316H exposed to (a) as-received 316H, (b) as-purified FLiBe, FLiBe with (c) 245 ppm CrF_2, (d) 99 ppm FeF_2 and (e) 392 ppm FeF_2 after 1000 hours at 700 °C. 198

Figure 118. SEM image of corroded 316H surface exposed to (a) as-purified FLiBe, FLiBe with (b) 245 ppm CrF_2, (c) 99 ppm FeF_2 and (d) 392 ppm FeF_2 after 1000 hours at 700 °C. 199

Figure 119. EDS line scan of near-surface region of 316H exposed to (a) as-purified FLiBe, FLiBe with (b) 245 ppm CrF_2, (c) 99 ppm FeF_2 and (d) 392 ppm FeF_2 after 1000 hours at 700 °C. 200

Figure 120. SEM & EDS line scan of near-surface region of 316H exposed to (a)-(c) as-purified FLiBe, FLiBe with (d)-(f) 245 ppm CrF_2, (g)-(i) 99 ppm FeF_2 and (j)-(l) 392 ppm FeF_2 after 1000 hours at 700 °C. (a), (d), (g), (j) SEM image, (b), (e), (h), (k) EDS chromium map, (c), (f), (i), (l) EDS iron map..... 202

List of Tables

Table 1. Comparison of advanced nuclear reactor heat transfer fluid properties. 4

Table 2. Abbreviated list of elements or isotopes which may be tolerable in high-temperature reactor fuels [15]. 6

Table 3. Summary of candidate fluoride salt coolants for MSRs [18]. 6

Table 4. Measured composition of the alloys investigated in static corrosion experiments. 8

Table 5. Comparison of nickel alloy mechanical properties at 850 ˚C [31]. 11

Table 6. Concentration of trace elements in FLiNaK salt before and after purification. 46

Table 7. Composition (in wt.%) of 316L and 316H stainless steels used in this study as measured independently by Anderson Laboratory. 47

Table 8. 316L & 316H heat treatment times and temperatures investigated for molten FLiNaK salt corrosion experiments. 48

Table 9. Composition (in wt.%) of Alloy-N, Alloy 141, and Alloy 3 as measured by Luvak Inc. 50

Table 10. Composition (in wt.%) of the 316H substrate, and 16-8-2 weld material used to produce the 16-8-2 weld pad. The compositions listed are certified by the manufacturer. 51

Table 11. Concentration of trace metals in purified FLiBe determined by ICP-OES. 58

Table 12. Composition of FLiNaK salt. The concentrations of the main salt constituents were measured with ICP-OES. The concentrations of trace elements were measured with ICP-MS. All values are in μg/g. 59

Table 13. Net change in lattice parameter of 316L and 316H specimens exposed in pyrolytic boron nitride (PBN), 316L, and glassy carbon capsules measured by Nelson-Riley function extrapolation. Units are in pm. 86

Table 14. Analysis of as-received 316L and 316H corrosion after exposure to FLiNaK for 500 hours at 700 ˚C in various capsule materials. 87

Table 15. Analysis of heat treated 316L and 316H corrosion after exposure to FLiNaK for 500 hours at 700 ˚C in PBN capsules. 102

Table 16. Analysis of the 316H substrate an 16-8-2 weld corrosion after exposure to FLiNaK for 500 hours at 700 ˚C in PBN capsules. 112

Table 17. Composition of nickel-based alloys used in phase stability calculations. 134

Table 18. Phase concentration (wt. %) in new advanced nickel-based alloys at 700 ˚C. 136

Table 19. Gibbs free energy of reaction between carbides and F_2 gas at 700 ˚C calculated using HSC 7.0 [40]. 137

Table 20. Net change in lattice parameter measured by Nelson-Riley function extrapolation. Units are in pm. 139

Table 21. Solubility of alloying elements in the nickel matrix obtained from phase diagrams. 145

Table 22. Summary of Alloy N, Alloy 141, and Alloy 3 corrosion rate and corrosion mechanisms in various capsule materials after exposure to FLiNaK for 500 hours at 700 ˚C. 150

Table 23. Summary of types of corrosion attack, phase stability predictions and observations, and effects of dissimilar capsule materials on the nickel alloys exposed to molten FLiNaK for 500 hours.. 153

Table 24. Electrochemical parameters for nickel obtained by linear fitting of iR_s-corrected polarization curves in FLiNaK at 700 ˚C. 162

Table 25. Electrochemical parameters for iron obtained by linear fitting of iR_s-corrected polarization curves in FLiNaK at 700 ˚C. 163

Table 26. Electrochemical parameters for chromium obtained by linear fitting of iR_s-corrected polarization curves in FLiNaK at 700 ˚C. 163

Table 27. Electrochemical parameters for Ni-20Cr obtained by linear fitting of iR_s-corrected polarization curves in FLiNaK at 700 ˚C. 166

Table 28. Electrochemical parameters for 316L stainless steel obtained by linear fitting of iR_s-corrected polarization curves in FLiNaK at 700 ˚C. 169

Table 29. Electrochemical Cell potentials generated by combination of an anode and cathode material in FLiNaK at 700 ˚C. Positive cell potential indicates reaction spontaneity. 172

Table 30. ICP-OES metals analysis before and after corrosion tests. The limit of quantification (LOQ) for Fe is approximately 65 ppm. Values below the LOQ are not reported..... 191

Variable Definitions

A = Surface area

a = Activity

a = atomic weight

α = charge transfer coefficient

β = Tafel slope

E = Cell potential

$E° =$ Standard cell potential

E_{app} = Applied potential

$E_{Ox/Red}$ = Half-cell reduction potential

$E°_{Ox/Red}$ = Standard half-cell reduction potential

$E°'_{Ox/Red}$ = Formal half-cell reduction potential

F = Faraday's constant

I = Current

j = Current density

j_f = Faradaic current

j_o = Exchange current density

$j_{p,c}$ = Cathodic current density

$j_{p,soluble-soluble}$ = Peak current density for a soluble-soluble reaction

$j_{p,soluble-insoluble}$ = Peak current density for a soluble-insoluble reaction

K = Equilibrium constant

m = Mass reacted

n = Number of equivalents exchanged

p = Partial pressure

r = Corrosion rate

t = Time

T = Temperature

μ = Chemical potential

η = overpotential

ΔG = Gibbs free energy of reaction

1 Introduction

The Molten Salt Reactor (MSR), a proposed Generation IV nuclear reactor concept, is attracting considerable attention from the U.S. Department of Energy and private sector to meet the needs of the increased global energy demand and to reduce the country's emission of green-house gasses. The molten salt coolant could enable higher operating temperatures and associated higher efficiency, in a safe and reliable manner [1]. The current knowledge base on MSR design and operation was largely created during the 1960s and 70s during the successful Molten Salt Reactor Experiment (MSRE) program at Oak Ridge National Laboratory (ORNL) [2]. During this program a 7.4 MW_{th} molten salt test reactor was designed, built, operated successfully. In the past decade, MSR research has been invigorated due to economic and environmental drivers to revitalize an aging nuclear power sector. Today, several private companies in the U.S. and overseas are engaged in design and licensing of pivotal MSR designs [3]. Selection of appropriate structural materials and control of molten salt chemistry continue to be challenges that are presently being addressed by researchers world-wide.

There is a strong motivation for innovation in the nuclear energy sector and for the development of molten salt reactors. The U.S. nuclear fleet, composed mainly of light water reactors (LWRs), presently supplies 20% of the country's electricity, but it struggles to keep cost competitive in today's energy market [1][2]. As of 2020, two thirds of the world's nuclear power reactors were over 30 years old. Many are scheduled to be retired in the coming years [6]. While the U.S. Energy Information Administration (EIA) projects in their reference case that new nuclear electricity generation capacity will be added in 2022, nuclear electricity generation is projected to decline by 2050 [7]. The closure of these baseload energy sources without sufficient replacements is likely to destabilize electricity grids and increase environmental pollution as utilities are forced to rely more heavily on fossil-fuel based technologies [4]. Supplementing the growing heat and electricity production needs with fossil fuels is not a sustainable solution to the world's energy needs.

A new generation of improved nuclear power plant technologies are needed to replace the retiring fleet. These new advanced reactor designs must meet present standards for safety. They must operate at higher temperatures to increase efficiency and to tap into energy intensive industrial applications. They must also be highly resistant to nuclear proliferation and deal responsibly with the byproducts of the nuclear fuel cycle [2][5]. Lastly, new advanced reactors must have flexible designs which enable fast and low-cost construction and operation – small modular reactors (SMRs) provide this flexibility and MSRs are conducive to SMR designs.

Chemically, in many ways, molten salts are more versatile fluid than water. The temperature range of stability and decomposition potential of most molten salt solvents is greater than water. This makes them very useful for carrying out industrial chemical processes not possible with water. As solvents, they can dissolve many substances including organic materials, metals, oxides, other salts, and nonmetallic elements. Molten salts can also be very stable and unreactive at high-temperatures. They can store very large amounts of thermal energy, making them useful for heat transfer applications [9]. Though the chemistry of molten salts offers an opportunity for discovery of many new technologies, understanding their chemistry remains a challenge complicated by high temperatures and often inhospitable melt environments.

The implementation of a molten salt test reactor under the MSRE program at ORNL demonstrated that nuclear reactor coolants composed of molten fluoride salts, such as LiF-BeF_2 (FLiBe), offer efficiency and safety benefits. Properties, such as high-temperature stability, excellent neutronics, high boiling point (>1,000˚C), and atmospheric pressure operation, make them ideal candidates for nuclear reactor coolants. However, the MSRE program revealed that molten fluoride salts can be highly corrosive to structural alloys particularly if the salt chemistry is not carefully controlled. To make the construction of cost-effective and durable reactors possible, corrosion-resistant materials and methods for controlling the corrosivity of molten fluoride salts must be developed [10].

The experimental methods used in this research were developed based on an extensive review of the current state-of-the art in the areas of salt chemistry, thermodynamics, experimental corrosion research, electrochemical and analytical chemistry methods, and then identifying critical research gaps. A survey of

much of the relevant corrosion data in molten halide salts reveals unresolved inconsistencies stemming from factors such as variations in salt purity, experimental design, salt type (fluoride vs. chloride), test materials, and characterization approaches [10]. The probability that a specific alloying element is vulnerable to corrosion is governed by the chemistry and thermodynamics of the salt mixture as well as its chemical state in the microstructure. The microstructure of structural materials may affect corrosion rate by providing barriers or by facilitating pathways for the migration of alloying elements. To make the construction of cost-effective and durable reactors possible, corrosion-resistant materials and electrochemical methods for controlling corrosion in molten fluoride salts must be developed to a high degree of reliability and perfection.

1.1 Molten salts for advanced reactor coolants

In 2001, the U.S. Department of Energy chartered the Generation IV International Forum (GIF), an international collective representing the governments of 14 countries, to organize the research and development of the next generation of nuclear power technology. GIF selected six reactor concepts for deployment between 2010 and 2030 for clean, safe, and cost-effective means of meeting increased energy demands on a sustainable basis. These designs were also chosen for their proliferation resistance. The concepts selected include, Gas-cooled Fast Reactor (GFR), Lead-cooled Fast Reactor (LFR), Sodium-cooled Fast Reactor (SFR), Supercritical Water-cooled Reactor (SCWR), very High-temperature Gas Reactor (VHTR), and the Molten Salt Reactor (MSR) [1].

Table 1. Comparison of advanced nuclear reactor heat transfer fluid properties.

Salt	Composition (mol. %)	Operating Temperature (˚C)	Melting Point (˚C)	Vapor pressure at 900˚C (mm Hg)	Density (g cm^{-3})	Specific Heat Capacity (kJ kg^{-1} K^{-1})	Viscosity (mPa•s)	Thermal Conductivity (W m^{-1} K^{-1})	Ref
He (P=7.5 MPa)		800			0.0030	5.505	0.04	0.29	[11]
LiF-BeF2	(67-33)	650	460	1.2	1.94	1.414	5.60	1	[11]
LiF-NaF-KF	(46.5-11.5-42)	650	454	~ 0.7	2.02	1.882	2.90	0.92	[11]
KCl-MgCl2	(68-32)	650	430	<2.0	1.66	1.116	1.40	0.4	[11]
Pb		600	327		10.32	0.15	1.55	18.8	[12]
Na @ 550°C		550	370.8		0.82		0.23	62	[11]
NaNO3-KNO3 @ 400°C	(48-52)	400	415		1.84	2.660	1.70	0.55	[11]
H2O @ 20°C		400	273		1.00	4.184	1.00	0.6	[11]

At present, the molten salt reactor (MSR) is a the leading candidate of the six Gen IV nuclear reactor concepts under research and development [1]. The high operating temperature is a distinct design feature that separates MSRs from their competitors in terms of reactor efficiency. As shown in Table 1, liquid fluoride salt coolants, such as FLiBe and FLiNaK, have relatively high operating temperatures. These molten salt coolants also have comparable specific heat capacities, densities, viscosities and thermal conductivities compared to other reactor heat transfer fluids, the important properties that dictate safety and efficiency of the reactor [11], [13]. One challenge for MSRs is that their design parameters require the salt facing materials for experience some of the highest temperatures and rates of irradiation damage. As shown in Figure 1, MSRs operate in the highest range of temperature and irradiation dose. Consequently, materials must meet strict microstructural, compositional, and mechanical requirements [14].

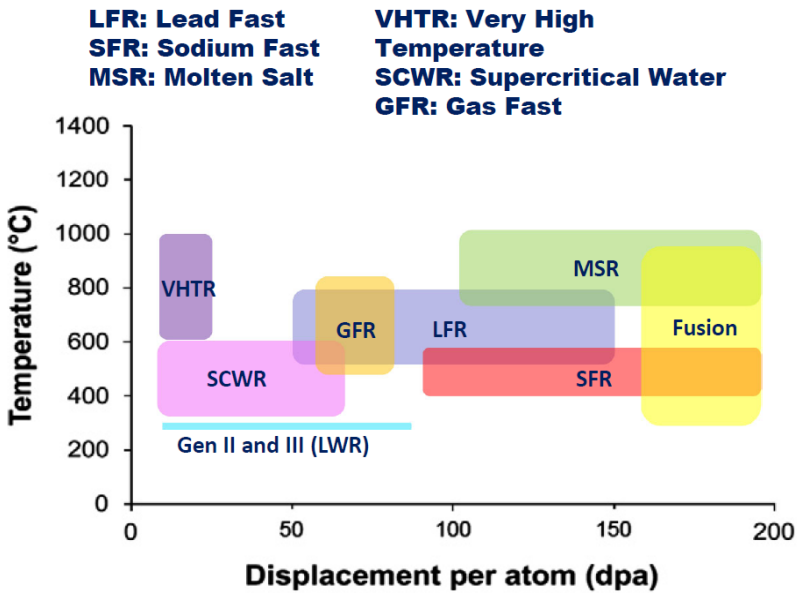

Figure 1. Temperature and irradiation dose ranges for the proposed generation IV nuclear reactor concepts the Gas-cooled Fast Reactor (GFR), Lead-cooled Fast Reactor (LFR), Sodium-cooled Fast Reactor (SFR), Supercritical Water-cooled Reactor (SCWR), very High-temperature Gas Reactor (VHTR), and the Molten Salt Reactor (MSR) [14].

1.2 Selection of molten salt for materials research

The composition of the salt coolants is dictated by several reactor design criteria. The salt chemistries must be compatible with liquid (dissolved) or solid fuel designs [16]. Under irradiation, the coolant must be stable and survive fission of the uranium or other fissionable material, and must tolerate fission product accumulation without any significant deterioration of thermophysical and thermochemical properties [15]. All coolant elements must have a low neutron capture cross-section for the energy spectrum of the reactor. Table 2 is an abbreviated list by Grimes [15] of acceptable elements in a thermal neutron flux (conventional nuclear power). Fluorine is the anion of choice for this energy spectrum. Be, Zr and the specific isotope ^{7}Li also have ideally low cross sections. It is important to note that ^{6}Li found in natural lithium has an unacceptably high cross section for neutron absorption at this energy and thus must be removed to prevent formation of dangerous levels of tritium, a fission byproduct [17].

Regardless of reactor fuel design, the coolant must be able to dissolve more than the critical concentration of fissionable material at temperatures safely below the coolest operating temperature [15]. In the unlikely event of rupture of a solid fuel system, the solvent must be able to dissolve the encapsulated

fuel. This would allow for the coolant and fuel to be extracted and replaced, preventing the dangerous accumulation of fissionable material that could affect criticality or accumulate in unanticipated locations of the reactor system.

Table 2. Abbreviated list of elements or isotopes which may be tolerable in high-temperature reactor [15].

Element or Isotope	Absorption Cross Section (barns at 2200 m/sec)
Fluorine	0.009
Beryllium	0.010
Lithium-7	0.033
Boron-11	0.050
Zirconium	0.180
Sodium	0.530
Choline-37	0.560

Table 3. Summary of candidate fluoride salt coolants for MSRs [18].

Salt	Composition (mol. %)	Melting Point (˚C)	Vapor pressure at 900˚C (mm Hg)
LiF-BeF2	(67-33)	460	1.2
LiF-NaF-BeF2	(31-31-38)	315	1.7
LiF-ZrF4	(51-49)	509	77
NaF-ZrF4	(59.5-40.5)	500	5
KF-ZrF4	(58-42)	390	
LiF-NaF-ZrF4	(26-37-37)	436	~ 5
LiF-NaF-KF	(46.5-11.5-42)	454	~ 0.7
LiF-NaF-RbF	(42-6-52)	435	~ 0.8

Finally, the coolant must have good stability at high temperature and exhibit a large gap between melting and boiling points providing for a large temperature window for safe and efficient operation. The composition, melting temperature and vapor pressure of several fluoride salt mixtures are shown in Table

3. Of the mixtures, FLiBe arguably has the best combination of properties for thermal neutron spectrum applications. Due to its toxicity, beryllium requires special engineering considerations to limit exposure to laboratory and plant personnel. FLiNaK, while less stable under irradiation, is an excellent secondary reactor loop coolant and good non-beryllium surrogate for FLiBe.

1.3 Alloy development for molten salt reactors

Selection of the alloys under investigation is guided by the needs of today's nuclear power industry and the two decades of materials research conducted during the Aircraft Reactor Experiment (ARE) and MSRE at Oak Ridge National Laboratory (ORNL). These materials need to be chemically compatible with the molten fluoride salt, resistant to air-side oxidation, have good high temperature strength, and capability of being fabricated into complicated shapes. Today, all austenitic stainless steels or nickel alloys for construction of a high-temperature reactor exceeding 425 ˚C must meet the construction rules and mechanical properties specified by the ASME Boiler and Pressure Vessel Code (BPVC) Section III Division 5. The composition of the selected alloys 316L stainless steel (<0.04 wt. % C), 316H stainless steel (0.04-0.1 wt. % C), Hastelloy-N (Alloy-N), Alloy-3, and Alloy-141 are listed in Table 4. In general, the composition of the chosen alloys is intended to minimize the alloy's susceptibility to selective dealloying of elements like Cr, while also good creep strength.

Table 4. Measured composition of the alloys investigated in static corrosion experiments.

Element	316L[a]	316H[a]	Hastelloy-N[b]	Alloy 3[b]	Alloy 141[b]
C	0.018	0.04	0.06	0.25	0.046
Cu			0.35	0.0064	0.0045
Mo	2.16	1.97	16	12.8	11.9
W			0.5	0.51	8.03
Ni	9.98	10.00	71	73.7	67.9
Co			0.2	0.018	0.016
Fe	Balance	Balance	4	0.03	0.015
Nb				1.16	0.015
P	0.032	0.031		0.003	0.003
Ta				1.22	4.03
Cr	16.77	16.77	7	6.96	7
Mn	1.66	1.5	0.8	0.82	0.78
Ti			0.5	1.12	0.0094
Hf				1.16	0.0005
Al			0.5	0.11	0.11
V			0.5	0.0029	0.0035
Si	0.35	0.3	1	0.037	0.038

[a]Composition determined by Anderson Laboratories Inc.

[b]Composition determined by Luvak Inc.

Type 316 stainless steel is a widely available and low-cost structural material that is a front runner for construction of high-temperature reactors due to its relatively well understood mechanical properties. 316 stainless steels with the nominal composition 18 Cr, 10 Ni, 2 Mo, and 2 Mn (wt. %) have excellent high-temperature creep and air side oxidation resistance, but they have higher concentrations of Cr than other alloys. In principle, the high Cr concentration makes it more prone to corrosion in molten fluoride salts.

An important distinction among commercially available 316 stainless steels that could be relevant to corrosion in MSRs is the concentration of carbon in type 316 stainless steel. 316H stainless steel (316H) has a higher carbon concentration (0.04–0.10 wt.% C), compared to the more common 316L stainless steel

(316L) (<0.03 wt.% C). 316H is currently ASME BPVC Section 5 Division III qualified at 700 ˚C and is therefore the preferred candidate for MSRs. While the increased carbon is beneficial for mechanical properties at higher temperatures, it could lead to a different corrosion behavior due to the behavior of carbon in the austenite matrix. At temperatures between 500 and 800 ˚C, the inherent thermodynamic instability of carbon in the austenite matrix leads to precipitation of carbon at the grain boundaries and the reaction between carbon and Cr in the alloy to form a carbide. In aqueous environments, the removal of Cr from solid solution around the grain boundaries reduces the local corrosion resistance. This can lead to intergranular corrosion attack. Additionally, the carbide phase can be brittle. The compounding effect in aqueous environments is an acceleration of intergranular stress corrosion cracking (IGSCC) in 300 series steels. This microstructural change which occurs in the temperature range of 500 ˚C to 800 ˚C in 300 series steels is called sensitization [19]–[22]. Sensitization affects the chemistry of steels at the nanometer scale and there for its influence on material properties must be measured indirectly through aggressive aqueous corrosion testing. Most tests for sensitization do not try to simulate testing conditions. Since resistance to intergranular corrosion attack is entirely influenced by the alloy's heat treatment parameters, the tests are designed to induce aggressive intergranular attack to reveal if a material's heat-treating procedure is incorrect. By following a standard nitric acid test (ASTM Method A262), Figure 2 shows the relationship between time, temperature and sensitization in terms of the inches of penetration per year (ipy) of intergranular corrosion [19]. Since the designation of 316H as the alloy of choice for MSRs, there has been little study of the impact of carbon content and sensitization on the rate of corrosion of 316 stainless steels in molten fluoride salts.

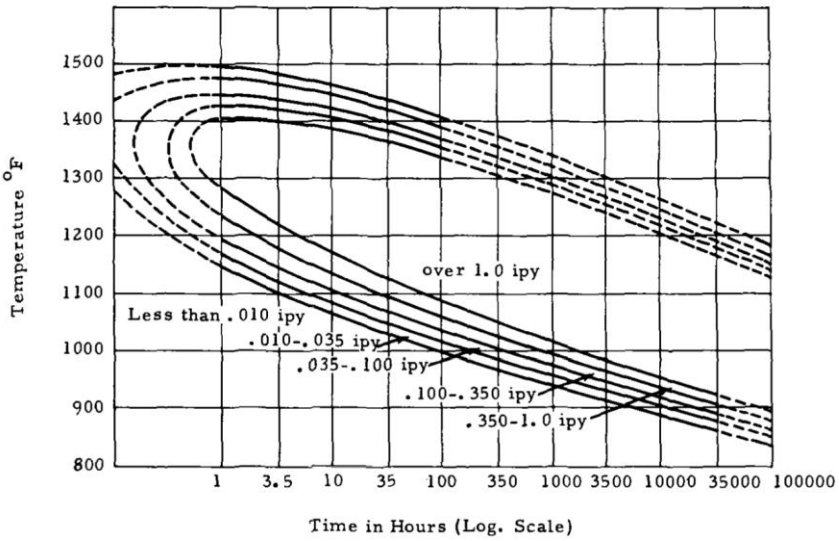

Figure 2. Time-temperature-sensitization (TTS) diagram of Type 316L stainless steel determined by boiling nitric acid test [19].

Ni-based alloys derive their high temperature strength from solid solution or precipitation strengthening nanometric γ' carbide phase precipitates. γ' formers come from group III, IV, and V elements (Al, Ti, Nb, Ta, Hf). Cr, Mo, W, Nb, Ta, Ti promote fine-scale carbide phase formation such as TiC, TaC, or HfC which upon heat-treatment decompose into $M_{23}C_6$ and M_6C type carbides and tend to form at the grain boundaries. The grain boundary pinning effect of these carbide phases is one mechanism that leads to high creep rupture strength of the alloys [23], [24].

During the MSRE, a new alloy, Hastelloy-N with a nominal composition of 16% Mo, 7% Cr, 5% Fe, 0.05% C (in wt.%) was developed for enhanced corrosion resistance in molten fluoride salts. While Hastelloy-N is a solid-solution strengthened alloy and does not exhibit classical age hardening, its mechanical properties can be altered by themo-mechanical treatments and radiation damage effects [23], [25]. During testing in the MSRE (1965-1969), which ran for over 20,000 hours, Hastelloy-N showed good corrosion resistance, but the alloy exhibited embrittlement during these long-term exposures. The embrittlement was attributed to the formation of tellurium fission products at the alloy's grain boundaries and the formation of helium due to transmutation of Ni under thermal neutron flux [26]–[28]. To address this challenge, addition of carbide forming elements such as Nb, Ti, Zr, and Hf was investigated to sequester helium. Nb additions were found to be effective at reducing Te embrittlement, but Ti had a deleterious

effect in this regard [29]. Today advanced alloy design is focused on compositional optimization to mitigate the effects of He and Te embrittlement of Ni-based materials while maintaining corrosion resistance.

Presently the new Ni-based alloys designated, Alloy 3 and Alloy 141 have been developed to address the limitations of Hastelloy-N. The composition of Alloy 141 is tailored towards improvement of overall high temperature mechanical strength of the material. The alloy is solid solution strengthened with 12wt%Mo and 8wt.%W which are γ phase forming refractory metals. A large portion of the mechanical strength is derived from the addition of 4wt.% Ta which increases the volume fraction of coherent γ' precipitates [30]. Due to the presence of carbon some carbides form providing moderate additional creep strength. The composition of Alloy 3 is primarily aimed at improving embrittlement resistance. The alloy contains addition of Hf, Nb, Ti, and Ta (all 1 wt.%) which promote γ' phase for increased strength. The addition of 0.25 wt.% C promotes the formation of carbides that are beneficial for preventing embrittlement while increasing strength. Alloy 3 is also strengthened by the prevalence molybdenum carbide precipitates.

New research at ORNL that has inspired these variants of Alloy N have led to the patenting of several alloy compositions including, Alloy 3 and Alloy 141 [32]. Table 5 compares the mechanical properties of Alloy N and Alloy 3 at 850 ˚C. Alloy 3 has a significantly higher creep rupture life based on limited short-term experiments [31], [33]. While not required for ASME code certification, the corrosion resistance of these alloys is important to their commercial viability and must be thoroughly investigated for the molten fluoride salt environments.

Table 5. Comparison of nickel alloy mechanical properties at 850 ˚C [31].

Material	Yield Strength (Ksi)	Tensile Strength (Ksi)	% Improvement in Yield Strength	Creep Rupture Life (at 12 Ksi)	% Improvement in Creep Rupture Life
Alloy N	35.29	45.7	0	3.77	0
Alloy 3	41.67	49.94	18.1	183.7	4773

1.4 Molten salt corrosion and the molten salt redox condition

In molten fluoride salts the passivating oxide layer that is usually relied upon for corrosion resistance in other environments is unstable and fluxed away by the salt leaving the material exposed to molten fluoride salt corrosion [34]. This phenomenon is instigated by the inevitable presence of trace impurities such as moisture, oxygen, and metallic impurities. The most common corrosion product of structural iron-based and nickel-based alloys in molten fluoride salt is dissolved chromium fluoride [3], [6]. Most of these alloys require chromium for air side oxidation resistance and typically contain 10 to 25 weight percent of Cr. Recent experimentation with alloys which contain significant manganese also indicate it to be highly susceptible to corrosion [35], [36]. The removal of chromium or manganese from the alloy establishes a concentration gradient that extends into the alloy and drives further transport of the alloying elements to the surface. Extensive depletion can lead to intragranular depletion of select alloying elements and or void formation in the bulk material due to coalescence of vacancies generated by the Kirkendall effect [37]. Figure 3 shows an example of SEM and EDS elemental chromium distribution in a 316 stainless steel specimen after 2000 hours at 700 ˚C in a steel capsule. At this temperature, Cr diffuses along the grain boundaries more quickly than through the bulk grains. The result is intergranular depletion of Cr in the near surface region of the alloy.

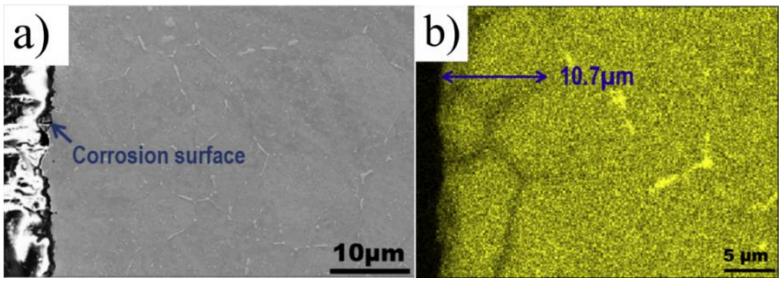

Figure 3. Cross-sectional (a) SEM image and (b) EDS elemental Cr distribution in 316 stainless steel exposed to FLiBe salt in a 316 stainless steel capsules for 2000 hours at 700 ˚C [38].

The process of corrosion is characterized by a reduction-oxidation (*redox*) reaction, an electrochemical reaction in which the oxidation states of atoms are changed by a charge transfer process.

An example is the oxidation (fluoridation) of a metal M to become a fluoride that is dissolved in the molten salt. The fluorine gas gains electrons and is reduced to two fluorides,

$$F_2(g) + 2e^- \rightarrow 2F^-(d) \quad (1)$$

In this case, the metal gives up two electron and is oxidized.

$$M(s) \rightarrow M^{2+}(d) + 2e^- \quad (2)$$

The sum of these two reactions makes up the total reaction.

$$M(s) + F_2(g) \rightarrow MF_2(d) \quad (3)$$

where (d), and (s) denote a dissolved, and solid species, respectively. Generally, the oxidation state of metal cation, *M*, is most relevant to corrosion scientists. However, the term 'redox' is specific to the anion *X* that is exchanged between two oxidation states of cation *M*. The *redox condition* of an electrolyte is related to the anion's chemical potential. This chemical potential energy governs the equilibrium quotient between high and low oxidation states of the cation present. To reproducibly measure and predict corrosion, the redox condition of the salt must be known. The redox condition can be expressed by a variety of metrics including a chemical equilibrium, a chemical potential or an electrical potential [39]. A theoretical understanding of how corrosion and other chemical processes in fluoride salts occur can be gained through a discussion of two factors which influence the salt's redox condition: the fluorine potential and the acid-base chemistry, also known as fluoroacidity.

1.4.1 Thermodynamics of Corrosion

The objective of this thermodynamics discussion is to describe the change in energy of a system in terms of heat and temperature and how it translates to useful work with respect to its surroundings. For most corrosion processes, work occurs through chemical reactions. Understanding the reactions and the energetics can guide the implementation of corrosion control methodologies as will be discussed later in this section.

In isothermal molten fluoride salts, the driving force for corrosion depends on two key aspects of the system: the standard Gibbs free energy of formation of the metal fluoride and the chemical potential

energy of the fluoride ions in the system. In molten salts, Reaction 3 likely requires at least two steps each with an associated change in Gibbs free energy. The first is an electrochemical step (exchange of electrons) where the oxidation state of the metal, *M*, is changed by *x*.

$$\frac{2}{x}M_{(s)} + F_{2(g)} \rightarrow \frac{2}{x}MF_{x(s)} \tag{4}$$

The second step is physical process (phase change and or solvation) in which the fluoride is dissolved by the liquid.

$$MF_{x(s)} \rightarrow MF_{x(d)} \tag{5}$$

The distinction between solid and dissolved metal fluoride is important because very little is known about the energetics of the physical process. This description of the corrosion reaction enables precise discussion of possible thermodynamic quantities involved and uncertainty in the thermodynamic prediction.

The electrochemical reaction step can be described by a hypothetical exchange of electrons between a fluorine gas molecule and a metal to form a solid fluoride.[1] The equilibrium constant, *K*, for the reaction is given by,

$$K_4 = \frac{{a_{MF_{x(s)}}}^{2/x}}{p_{F_{2(g)}}} \tag{6}$$

Where $p_{F_{2(g)}}$ is the partial pressure of F_2 gas, and a_i is the activity of species, *i*. Activity is the product of the species concentration or partial pressure times an activity coefficient, γ, and is the product of the ideal and non-ideal behavior of the species in an environnment. The activity of a pure metal is considered unity.

It is important to understand the role of the fluorine molecule in determining the equilibrium of Reaction 4. When the system is defined as a pure metal in contact with pure fluorine gas the Gibbs free energy of formation of the fluoride is given by,

$$\Delta G_4 = \frac{2}{x}\mu^{\circ}_{MF_{x(s)}} + RTln\left(\frac{{a_{MF_{x(s)}}}^{2/x}}{p_{F_{2(g)}}}\right) \tag{7}$$

[1] The gaseous fluorine molecule is used instead a dissolved fluoride anion in Reaction 4 because thermodynamic data is more readily available for pure F_2 gas. Practical demonstration of concepts is also more feasible by controlling the partial pressure of F_2 in the system rather than the activity F^- which is currently is difficult to measure.

where $\mathring{\mu}_{MF_{x(s)}}$ is the standard chemical potential of the fluoride species, R is the gas constant, and T is temperature. At equilibrium, the change in Gibbs energy is minimized when the sum of the chemical potentials of all chemical species in the system equals zero. When Reaction 4 is at equilibrium, the activity of the metal fluoride is given by,

$$a_{MF_{x(s)}} = p_{F_{2(g)}}^{x/2} - exp\left(\frac{\mathring{\mu}_{MF_{x(s)}}}{RT}\right) \quad (8)$$

Since $\mu_{F_{2(g)}} \equiv RTlnp_{F_2}$

$$a_{MF_{x(s)}} = exp\left(\frac{x\mu_{F_{2(g)}}}{2RT}\right) - exp\left(\frac{\mathring{\mu}_{MF_{x(s)}}}{RT}\right) \quad (9)$$

From equation 9, the activity of solid MF_x is dependent on the standard Gibbs free energy of formation of the fluoride and the chemical potential of F_2 gas in the system. Assuming Reaction 4 dominates the free energy change of the complete dissolution reaction, the alloying elements can be ranked in order of their tendency to be converted to a fluoride. In Figure 4, the hypothetical Gibbs free energy of formation of solid fluoride per mole of F_2 gas is plotted as a function of temperature for elements relevant to the alloys under investigation using data acquired from HSC 7 software [40].[2] Elements which undergo the most spontaneous reactions with fluorine have more negative free energies of formation. The salt components (LiF, NaF, KF, and BeF_2) have more negative Gibbs free energies of formation and are thus unlikely to interact with container or structural materials. Approximate calculations show that Cr, Hf, Ti, Mn, Ta, Nb, and Fe may be more susceptible to corrosion attack than more inert elements, such as Ni, W, Mo and C.

[2] Values are for the hypothetical case of unit activity solid fluoride. The reference state of pure F_2 gas is the standard pressure of 1.013 bar and temperature of 298 K.

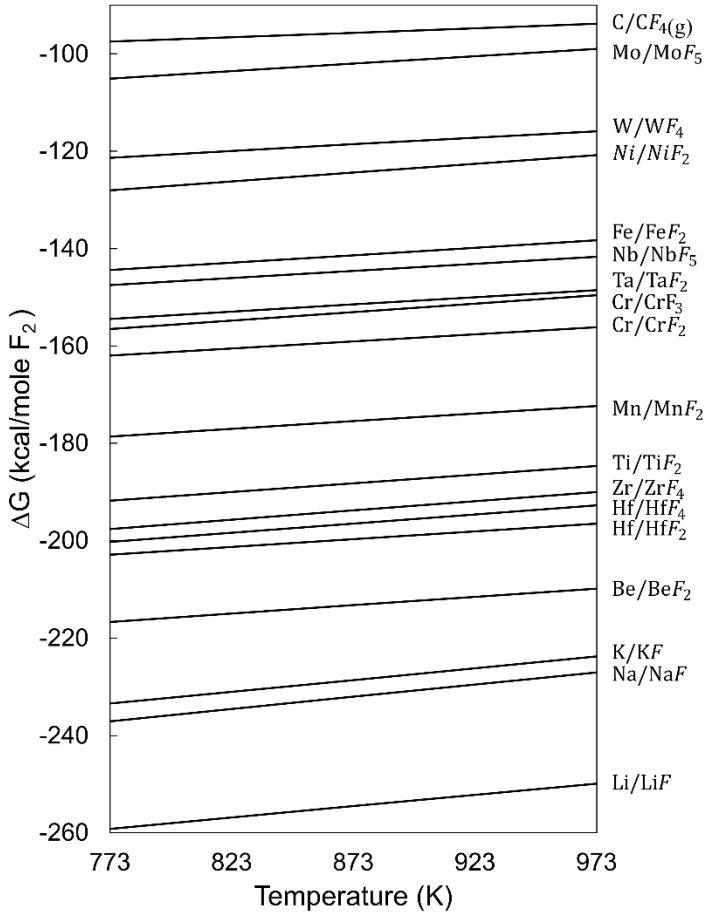

Figure 4. The Gibbs free energy of formation of fluoride per mole of fluorine gas. Unless otherwise stated the product is a solid fluoride. Data is from HSC 7.0 [40].

The second step is the dissolution reaction (Reaction 5) in which the solid metal fluoride becomes soluble in a specific fluoride salt. Often the dissolved metal fluoride is conceptualized as a supercooled liquid [41], [42], meaning the product is a fluoride that is liquid below its melting temperature when it is considered in isolation. Some thermodynamic data is available for conversion of solid fluorides to a supercooled fluorides enabling an approximation of liquid fluoride formation free energies [40]. The free energy change of Reaction 5 is assumed to be the sum of the energy of the phase change reaction and the energy change associated with dissolution of the solute into the solvent.

With the combination of these electrochemical and physical reaction steps, the free energy of Reaction 3 would then be the sum of Reactions 4 and 5,

$$\Delta G_3 = \Delta G_4 + \Delta G_5 \quad (10)$$

For many metals, the standard Gibbs free energy of formation of Reaction 4 are readily available. On the other hand, the Gibbs free energies of Reaction 5 are not yet known. If the temperature of the system is below the melting temperature of the fluoride, then the phase change component of Reaction 5 is energy intensive. In this case, the Gibbs free energy of the electrochemical reaction and or the solvation reaction must be significantly negative to make Reaction 3 spontaneous.

Construction a of a comprehensive thermodynamic database for many molten salt mixtures is underway [43], [44]. Accurate modelling of these systems will require a multitude of data for Reaction 5 for species of interest.

From a thermodynamics perspective there are two ways to actively reduce corrosion in molten fluoride salts. The first is to select structural materials composed of metals with relatively positive free energies of fluoride formation. The second is to mitigate the partial pressure of fluorine gas in the system. Hypothetical estimates of the probability of corrosion in a system containing one metal may be made by imposing a partial pressure of fluorine gas on the system in Equation 8. Corrosion is often initiated by the introduction of impurities such as moisture, oxygen, and metals into the salt. Theoretically, these impurities contribute to a change in the fluorine potential and the equilibrium of the corrosion reaction [42]. Maintaining salt chemistry control is therefore paramount to mitigating corrosion. Practical methods have been proposed to influence the fluorine potential. These methods include gas phase, major metal addition, and dissolved salt control [39], [41].

1.4.2 Acid-Base Chemistry

Another aspect of salt chemistry that influences the redox condition of molten fluoride salts is the acid-base chemistry. Certain salts, such as FLiBe, have an uneven distribution of anions among the various cations. Thus molten salts (e.g., LiF) are often classified as ionic liquids. Ionic liquids are a class of compounds possessing relatively weak ionic bonds at high temperature. At high temperature, the ions dissociate and give up electrons in the form of F^- relatively easily. Beryllium fluoride, on the other hand,

like SiO_2, has the tendency to form complexes such as polymeric anion chains in the molten state. The cation usually has a coordination number of 4. The anion can be shared between two cations or be coordinated to only one cation [45]. Increasing the fluorine potential (i.e. the activity of F^-) in the system may lead to breakage of some of the bridging anion bonds and lead to the formation of BeF_4^{-2} ion complexes with unshared anions [46]. The decomposition of this polymer can be written as,

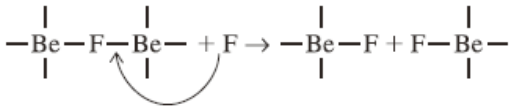

To account for the distribution of fluoride ions, the concept of fluoroacidity has been adapted analogous to oxoacidity in conventional aqueous environments by Tremillon [47].

Fluoroacidity refers to the predominance of various fluorocomplexes. It generally describes the coordination of the solvent and is influenced by the free fluoride content of the melt. Molten alkali fluorides (LiF, KF, NaF etc.) are Lewis bases. The metal cation easily dissociates from their fluoride ion, donating an electron. The alkaline fluorides (BeF_2 and $BeCl_2$) and some transition metal fluorides (ZrF_4) are Lewis acids, since they can accept electrons from fluoride ions and form complexes without shared anions, such as BeF_4^{-2}. Formation of the monomeric fluorocomplex helps minimize the fluorine potential of the melt.

Alloying elements in structural alloys are prone to corrosion in the presence of high activity fluoride ions as previously discussed. In basic solvents a significant amount of free fluoride anions exist which can interact with the environment. Increasing the acidity of the salt by adding an alkaline metal, such as Be, inhibits corrosion by increasing complexation with fluoride ions and decreasing the fluorine potential [48]. The fluoroacidity has major effects on the solvent activity, oxidation state of dissolved metals, conductivity, hydrodynamic properties, and vapor pressure of FLiBe [48], [49]. The effect of fluoroacidity on these properties is discussed in Appendix A.

1.4.3 Mechanisms of Corrosion

In molten salts, the three corrosion mechanisms of primary concern are impurity driven corrosion, thermal gradient driven corrosion, and dissimilar materials corrosion.

1.4.3.1 Impurity Driven Corrosion

Impurity driven corrosion is an important corrosion mechanism induced by metallic impurities and moisture in the salt. In general, a fluoride with a high free energy of formation is an oxidizing agent that will react with any available metal that can form a fluoride with a more negative Gibbs energy. There are several pathways for corrosive impurities to make their way into fluoride salts. Moisture may get into the salt through leaks in the system or simply from environmental humidity due to improper storage. Theoretically, moisture initiates impurity driven corrosion by forming hydrogen fluoride in the melt.

$$xH_2O + MF_x \rightarrow M(OH)_x + xHF \quad (11)$$

Common alloying elements *M* that are susceptible to attack include chromium, iron, and nickel [10], [50], [51]. According to Table 4, chromium is the predominant corrosion product because it forms one of the more stable fluorides and is more readily oxidized than nickel or iron. The selective attack of chromium occurs by the following reactions,

$$Cr + 2HF \rightarrow CrF_2 + H_2 \quad (12)$$

$$Cr + MF_2 \rightarrow CrF_2 + M \quad (13)$$

where *M* represents a cation with a fluoride formation free energy more positive than CrF_2. The main salt constituents (Li, Na, K and Be) form fluorides that are more stable than fluorides formed from constituents of common structural alloys. Therefore, no corrosion is expected from the pure salt constituents. Figure 5 shows the effect of these impurities on corrosion of Inconel, a high chromium nickel-based alloy. HF is one of the most corrosive fluorides and leads to extensive void formation due to the Kirkendall effect and coalescence of vacancies. Ni and Fe impurities in the salt also lead to extensive corrosion. Corrosion and void formation is minimized when impurity levels are kept low [52].

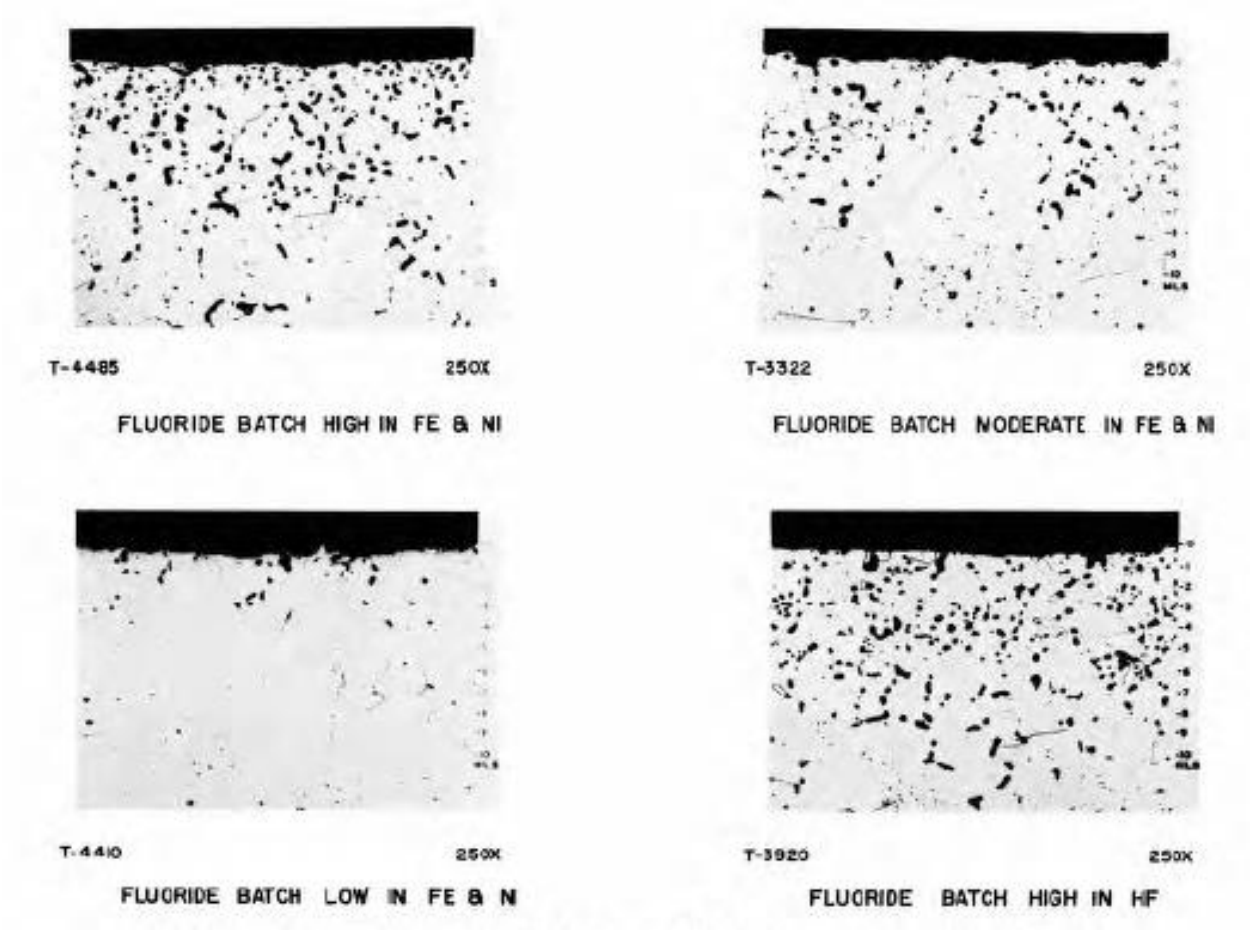

Figure 5. Effect of fluoride batch purity shown in an Inconel thermal convection loops-500 hours at 815˚C [52].

1.4.3.2 Thermal Gradient Driven Corrosion

Thermal gradient driven corrosion is a type of mass transport that occurs throughout the life of the reactor. It is common in primary and secondary loops of a reactor were significant temperature gradients exist. These temperature gradients have a subtle influence on the equilibrium constant, K, of all species exposed to the molten salt. Important equilibria are any reaction between alloying elements, like chromium, and metal fluorides in the salt melt,

$$Cr + MF_2 \leftrightarrow CrF_2 + M \quad (14)$$

Even salt constituents like Be, which have very small K values at most temperatures, are susceptible to small variation in K with temperature. The equilibrium of Reaction 14 shifts to the right with increasing

temperature, causing the oxidation of Cr. The equilibrium shifts to the left with the decreasing temperature resulting in deposition of Cr. This steady mass transport results in primarily corrosion of the hot side of the reactor. This mechanism was first observed in post exposure materials analysis of flowing molten salt loop constructed with Hastelloy-N during the MSRE shown in Figure 6. Cross-sectional imaging of the loop showed void formation in the hot sections because of corrosion and buildup of corrosion products in the cold sections [53]. More recently, it has been shown that in FLiNaK, it is possible for multiple alloying elements in 316H, such as Cr and Fe, to migrate from the hot section to the cold section [54].

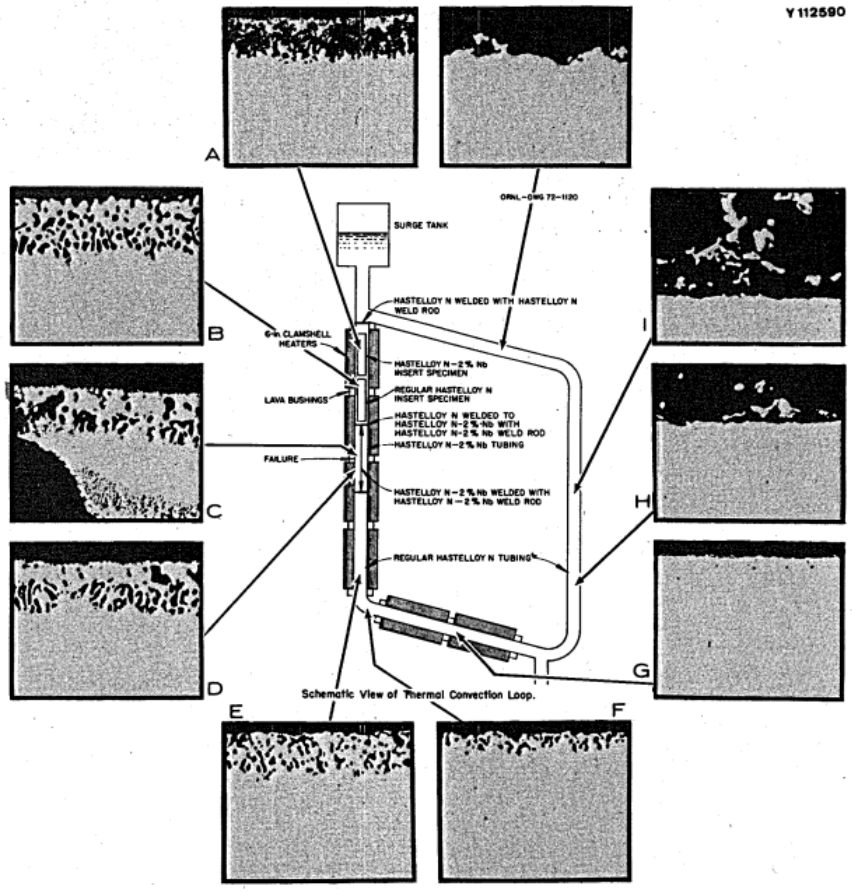

Figure 6. Micrographs of tubing and specimens exposed to molten LiF-BeF_2-ZrF_4-ThF_4-UF_4 (70-23-5-1-1) between 560-700˚C for 30,000 hours (9.2 years). As polished. 500x [53].

1.4.3.3 Dissimilar Material Corrosion

Recent studies suggest that the presence of dissimilar materials in the same molten salt system could affect corrosion. Falconer et al. [55] showed that mass transport of Cr and Fe between 316L stainless

steel and Ni-201 is possible with and without ohmic contact in FLiNaK at 700 ˚C. Under the same conditions, Fe is transported from 316L to TZM, a molybdenum-based alloy, however, neither Fe nor Cr are transported from 316L to copper. It is theorized that the transport is governed by the solubility and activity of the transported element in the new materials matrix [56]. Yang et al. [57] reported that components of Hastelloy-N, such as Ni and Cr, can react with Si in SiC when exposed in FLiNaK at 700 ˚C. Chan et al. [58] demonstrated that pure metals, such as Cr, Fe, W, and Mo, lose weight when exposed to FLiNaK at 700 ˚C in graphite crucibles. Chan et al. [59] also reported that Hastelloy-N that was pre-carburized before exposure to FLiNaK at 700 ˚C suffered less corrosion than non-carburized Hastelloy-N. The corrosion mechanism appeared to be strongly linked to carburization of the metal induced by the capsule material. This suggests that carbon in the environment may play a role in tying up strong carbide formers, such as Cr and Mo. These recent findings have motivated this research to look closely at the effect of capsule environments, such as 316 stainless steel, nickel, graphite (glassy carbon), and pyrolytic boron nitride (PBN).

1.4.4 Rate of Corrosion

In the presence of an adequate constant driving force for corrosion, the corrosion rate depends on the temperature and pathway for alloying elements to migrate to the materials' surface. The pathway is determined by both the materials' microstructure and temperature. For example, after exposing the nickel-based alloy Inconel (14-17Cr, 6-10Fe, 1Mn, 0.15C max) to NaF-ZrF_4 it was concluded that at lower temperatures diffusion occurred preferentially along selective pathways, such as grain boundaries where the rate of diffusion was highest. At higher temperatures homogeneous volume diffusion dominated because the rate of Cr diffusion throughout the bulk became significantly high [60], [61].

At a temperature relevant to today's MSR designs, typically 700 ˚C, alloys investigated in this research, Hastelloy-N, Alloy-3, and Alloy-141 are likely to have phases in the microstructure that could influence the corrosion performance of the alloy. A hypothesis of the proposed research is that the

precipitates at the grain boundaries could act as barriers to Cr diffusion to the material surface via grain boundaries and thus improve corrosion resistance.

1.5 Electrochemistry Theory

Electrochemistry is a branch of science which bridges many fields including physical chemistry, material science, and corrosion. Physical chemistry is the study of the thermodynamics of chemical systems that govern the possible states of matter. Material surface science is the study of chemical phenomena that occur at the interface of the materials and environment and includes topic such as catalysis, nucleation and growth, and corrosion. An issue of great importance to these topics is reaction kinetics, or the rate of the chemical process. Electrochemistry is the study of the energetics and kinetics of the exchange of electrons at the interface between the material and the environment and the corresponding change in chemical equilibrium.

The link between electric potential and the corresponding charge transfer has been well characterized by electrochemistry theory. When two materials (i.e., an anode and a cathode) are separated by an electrolyte, the electrolyte can be a medium for conducting electrical work. The energy to do work comes from a potential difference between the two material surfaces called a *cell potential*. The work is carried out through redox processes occurring at both material surfaces and mass transport through the electrolyte. To simplify the chemical system an electrochemical cell can be divided into two the half-cell reactions occurring at each material. The *redox potential* is the tendency of a single chemical species to acquire or lose electrons at one of the material interfaces. All chemical species have their own inherent redox potentials when measured against a common reference electrochemical reaction. For example, a metal has a redox potential associated with being oxidized by fluorine (fluoridized). A fluoride may have both a reduction potential and an oxidation potential. The following electrochemical theory is used to relate these redox potentials to physical quantities such as activity (concentration), energy, and charge transfer. The relationships form the basis for two electrochemical techniques used in this research potentiodynamic

polarization and cyclic voltammetry (CV). Electrochemical cell design for molten fluoride salts will be discussed in the following sections.

1.5.1 Cell Potential

While the goal in electrochemistry experiments is to study a reaction occurring at a material-electrolyte interface, the current flowing from an electrode into an electrolyte must also pass through a second interface to complete the circuit between the power supply's anode and cathode. Another redox reaction will occur at this second electrode. The potential difference generated by the two different reactions in the same electrolyte is called the *cell potential, E*. The sign of a cell potential is the indicator of the spontaneity of the overall chemical reaction in the cell. Considering the reaction where A and B react to form C and D,

$$\alpha A + \beta B \leftrightarrow \gamma C + \delta D \tag{15}$$

The Gibbs free energy change when the reaction moves to the right is,

$$\Delta G = \Delta G° + RTln\frac{{a_C}^{\gamma}{a_D}^{\delta}}{{a_A}^{\alpha}{a_B}^{\beta}} \tag{16}$$

where $\Delta G°$ is the standard free energy of reaction in (J mol^{-1}). At constant temperature and pressure, the change in Gibbs free energy is equal to the amount of electrical work that can be done by the system [62],

$$\Delta G_{T,P} = -nFE \tag{17}$$

where *n* is the number of electrons per mole or reaction (mol mol^{-1}), *F* is Faraday's constant (96485 C mol^{-1}). *E* is the equivalent work in volts (V). Combining equations 16 and 17 we obtain

$$-nFE = \Delta G° + RTln\frac{{a_C}^{\gamma}{a_D}^{\delta}}{{a_A}^{\alpha}{a_B}^{\beta}} \tag{18}$$

At the condition referred to as *the standard state,* the activities of the reactants and products are all unity and the *standard cell potential, E°*, of the complete cell reaction is,

$$E° = -\Delta G°/nF \tag{19}$$

Rearranging equation 18 we obtain an expression for the *cell potential, E*, via the Nernst equation,

$$E = E^{\circ} - \frac{RT}{nF} ln \frac{{a_C}^{\gamma} {a_D}^{\delta}}{{a_A}^{\alpha} {a_B}^{\beta}} \quad (20)$$

The Nernst equation relates the potential measured across an electrochemical cell to the activities of the chemical species involved in the cell reaction. The cell potential can be a powerful tool for understanding how a chemical species (solid or dissolved) will behave in an electrolyte provided that all the terms of the Nernst Equation are well defined.

1.5.2 Half-Cell Reduction Potential (Redox Potential)

Electrochemical investigation of molten salts is greatly simplified when a complete cell reaction can be separated in to two reactions, called *half-cell reduction reactions*. From Reaction 15 we can write two half-cell reduction reactions as,

$$A + ne^{-} \leftrightarrow C \qquad E^{\circ}_{C/A} \quad (21)$$

$$D + me^{-} \leftrightarrow B \qquad E^{\circ}_{B/D} \quad (22)$$

Each half-cell reaction is written as a reduction reaction in which the reactant gains electrons. In an electrochemical cell, the electrons are typically transferred to or from the electrode interface. From equation 19, each half-cell reaction possesses a standard half-cell reduction potential, $E^{\circ}_{C/A}$ or $E^{\circ}_{B/D}$. The electrode where a species gains electrons (reduction) is called the cathode and the electrode where species loses electrons (oxidation) is called the anode. At the standard state, the standard cell potential, E°, is the sum of the two half-cell reduction potentials corresponding to the cathode and the anode.

$$E^{\circ} = E^{\circ}_{A/C} - E^{\circ}_{D/B} = E^{\circ}_{cathode} - E^{\circ}_{anode} \quad (23)$$

The first term corresponds to the cathode reaction. The sign of the second term is negative to account for the reversal of Reaction 22 at the anode. In aqueous electrochemistry, the *electrochemical series* defines the standard half-cell potential of many reactions with respect to the reduction potential of hydrogen which is set equal to 0 V. All E° are reported for a 1 M ideal solution at a temperature of 25˚C and a pressure of 1 atm. [63][64].

If the standard potential of a half-cell reaction is known for a given set of conditions, the activities of the oxidized and reduced species can be calculated using the Nernst Equation for the half-cell reaction.

$$E_{Ox/Red} = E^{\circ}{}_{Ox/Red} - \frac{RT}{nF} ln \frac{a_{red}}{a_{ox}} \quad (24)$$

With electrochemistry equipment, such as a potentiostat, we can perturb the system in a way that allows us to study the redox potential of a single half-cell reaction, provided the other attributes of the electrochemical cell, such as the other half-cell reaction, are well understood. Note that, in Equation 17, the redox potentials are extrinsic quantities, a characteristic that makes them easy to work with and practical to measure.

1.5.3 Formal Half-Cell Reduction Potential

The Nernst equation in its form in equation 24, is somewhat difficult to use directly for molten fluoride salts. It is inconvenient to deal with activities because little is known about the values of the activity coefficients in fluoride melts [65]. The manner in which activities and activity coefficients must be treated depends on factors including divergences from ideality and whether the species is concentrated or dilute. For very dilute solutions (<0.01 M) it can often be assumed that the activity coefficient is relatively constant and standard potentials can be calculated with a reasonable amount of accuracy. For more concentrated species like Be the activity coefficient must be determined empirically [63][66].

The formal half-cell potential is a device to avoid dealing with activity coefficients of a dilute species and can allow more quantitative studies of corrosion and fission products in molten fluoride salts. Activity coefficients primarily depend on the total electrolyte concentration (ionic strength) of the solution. In general, the inert species in solution with the highest concentrations determine the ionic strength. As a result, the activity coefficients of the dilute species are relatively constant and can be mathematically isolated from concentration [63]. Expanding the Nernst Equation, we have

$$E_{Ox/Red} = E^{\circ}{}_{Ox/Red} - \frac{RT}{nF} ln \frac{\gamma_{Red}}{\gamma_{Ox}} - \frac{RT}{nF} ln \frac{[Red]}{[Ox]} \quad (25)$$

The formal half-cell reduction potential, $E^{\circ\prime}{}_{Red/Ox}$, is defined as the potential when the concentration quotient of the Nernst Equation equals 1 and the last term in the expression is zero.

$$E^{\circ\prime}{}_{Ox/Red} = E^{\circ}{}_{Ox/Red} - \frac{RT}{nF} ln \frac{\gamma_{Red}}{\gamma_{Ox}} \quad (26)$$

Expressing the Nernst equation in terms of $E^{\circ\prime}{}_{Red/Ox}$ gives an expression for the half-cell reduction potential in terms of the concentration of the oxidized and reduced species.

$$E_{Ox/Red} = E^{\circ\prime}{}_{Ox/Red} - \frac{RT}{nF} ln \frac{[Red]}{[Ox]} \quad (27)$$

In many cases, $E^{o\prime}$ is relatively constant and can be consistently measured experimentally. Once $E^{o\prime}$ is known, the electric potential can be related to the concentration of the oxidized and reduced species [63]. An electric potential can also be applied to the interface where the redox reaction occurs to impose a new reaction quotient. The formal potential will be employed in the study of dilute species in FLiBe in this research as discussed in Section 3.4.

1.5.4 Overpotential & Charge Transfer Relationships

The electrochemical techniques used in this research measure the relationship between an applied potential and the resulting charge transfer through an interface (i.e. an electrode). The flow of electrons, or current *I*, to or from a reaction interface is a measure of the reaction rate. The current is related to the mass reacted, *m*, through the proportionality called Faraday's Law,

$$m = \frac{It\mathrm{a}}{nF} \quad (28)$$

where *F* is Faraday's constant (96,500 Coulombs/equivalent), *n* is the number of equivalents exchanged, a is the atomic weight, and *t* is the time. Dividing by t and the surface area, *A*, yields the corrosion rate, *r*.

$$r = \frac{m}{tA} = \frac{j\mathrm{a}}{nF} \quad (29)$$

Where *j* is current density in A cm^{-2}. Corrosion rate is both a mass loss per unit time-area ($mg/dm^2/day$) or a flux of electrons.

When an electrochemically active surface is at the electric potential equal to the half-cell reduction potential (redox potential), $E_{Ox/Red}$, the reaction is at the equilibrium state. The equilibrium state is the condition when the rate of the forward reaction (left to right), r_f, is equal to the reverse reaction rate, r_r.

$$r_f = r_r = \frac{j_o a}{nF} \tag{30}$$

where j_o is the exchange current density equivalent to the reversible reaction rate at equilibrium. The total current density, j, is the sum of the anodic and cathodic reactions

$$j = j_a + j_c \tag{31}$$

j_o is equivalent to j_a when j_a=j_c. Combining equations 29 through 31, the total current density can be written as a function of the electric potential in the form of the Butler-Volmer equation,

$$j = j_o \left\{ exp\left[\frac{\alpha_a nF(E_{app} - E_{Red/Ox})}{RT}\right] - exp\left[\frac{\alpha_c nF(E_{app} - E_{Red/Ox})}{RT}\right]\right\} \tag{32}$$

where E_{app} is the electric potential applied to an electrode. α_a and α_c are the charge transfer coefficients for the anodic and cathodic reactions, respectively. α_a and α_c describe the shape of the activation energy barrier facing the reaction. When E_{app} is applied to an electrode, the Butler-Volmer equation yields the instantaneous current density from a shift in the half-cell redox equilibrium. The *overpotential*, η, is the difference between the applied electric potential of the reactive interface, E_{app}, and the equilibrium reduction potential, $E_{Ox/Red}$.

$$\eta = E_{app} - E_{Ox/Red} \tag{33}$$

The Butler-Volmer equation predicts that there is an exponential relationship of reaction rate (current density) to overpotential.

$$j = j_o \left\{ exp\left[\frac{\alpha_a nF\eta}{RT}\right] - exp\left[\frac{\alpha_c nF\eta}{RT}\right]\right\} \tag{34}$$

The relationship holds under the conditions that there is an infinite supply of oxidized and reduced species that can react instantaneously at the interface. In many electrochemical systems, the reactants are diffuse, and time is required for mass transport to the electrode interface. Mass transport can cause deviation from the Butler-Volmer equation. Potentiodynamic polarization is an electroanalytical technique which applies the Butler-Volmer model to relate overpotential and charge transfer at a specimen surface. The model is also integral to cyclic voltammetry, a technique for investigating systems where mass transport is a significant rate limiting step of the electrochemical reaction.

1.5.5 Potentiodynamic Polarization

The potentiodynamic polarization experiment rapidly evaluates a material's compatibility with an electrolyte by measuring the corrosion kinetics over a broad range of applied potentials. In this experiment, the specimen is exposed to the electrolyte and polarized from a negative (reducing) potential to a positive (oxidizing) potential. The current is related to corrosion rate at each potential. Analysis of the polarization curves under a set of conditions can parameterize the materials corrosion resistance.

The theory discussed in this section is applicable to general corrosion of a uniform surface [67]. Equation 32 is useful for predicting reaction kinetics in various conditions. For instance, if an anodic (oxidizing) potential is applied to the reactive surface, the contribution of the cathodic current from the second term becomes negligible and the anodic current density is approximately,

$$j_a = j_o exp\left[\frac{\alpha_a nF\eta}{RT}\right] \tag{35}$$

Taking the log of the expression and combining constants, gives the anodic overpotential as a function of the anodic and cathodic current density,

$$\eta_a = \beta_a log\frac{j_a}{j_o} \tag{36}$$

Where $\beta_a = 2.3RT/\alpha_a nF$. This is a useful metric that describes the amount of anodic overpotential, η_a, necessary to increase the corrosion rate by a factor of ten. Equation 36 is one form of the Tafel equation.

The corrosion kinetics parameters $E_{Ox/Red}$, j_o, and β_a can be measured with a potentiostat and a three-electrode probe like the one shown in Figure 7(a). The working electrode (WE) is polarized by applying a potential using the counter electrode (CE). Current can only flow between the WE and the counter electrode (CE). The working electrode (WE) is polarized to various electric potentials with respect to the reference electrode (RE) using a feedback loop. The corrosion kinetics parameters in Equation 36 can be obtained by fitting linear curve fits to a plot of log of current density vs. potential plot, as shown in Figure 7(b). Curve fits are applied to the linear regions to either side of where the current is minimized. This is called a *Tafel Plot.* The parameter β is the slope of each linear fit and is called the Tafel slope. The

intersection of linear fits for the anodic and cathodic Tafel regions yields the theoretical values of $E_{Ox/Red}$ and j_o.

The intersection of linear fits for the anodic and cathodic Tafel regions of two different half-cell reactions is denoted by E_{corr} and j_{corr}, call the corrosion potential and corrosion current. These quantities are the theoretical cell potential between the two materials and the rate of corrosion or deposition of a material on one of the materials [67], [68]. These parameters can be used to calculate theoretical reaction rates if two materials (two half-cell reaction) were placed in the same electrolyte.

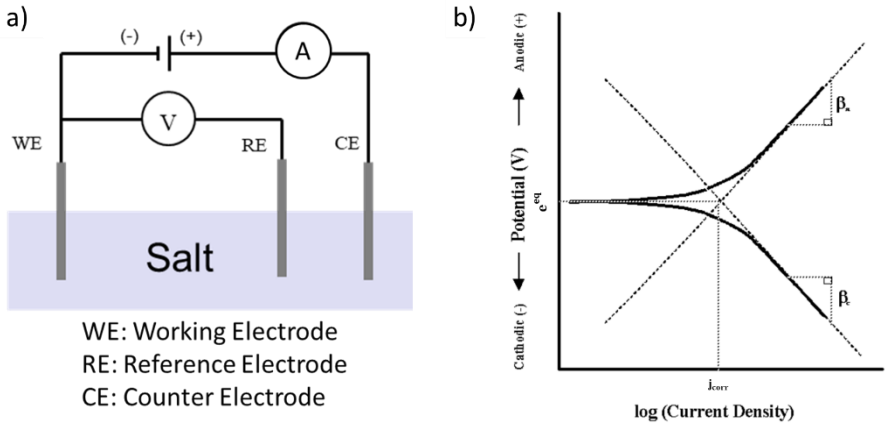

Figure 7. (a) Schematic diagram of a three-electrode electrochemical cell. (b) Analysis of an idealized Tafel plot of potentiodynamic data [69].

The widespread application of the potentiodynamic polarization method for evaluating an alloys' corrosion behavior make up the scientific basis for application of the technique for evaluation of alloys in molten salts. Successful application of the method has been shown in aqueous environments in many industries [70]–[72]. Several specialized ASTM standards for aqueous environments have been published that can be adapted to molten salts [73]. Recently, a few papers [70], [74]–[80] have demonstrated application of the technique to molten fluoride salts such as FLiNaK, but significant work is required to refine these techniques to make them useful to corrosion scientists.

1.5.6 Cyclic Voltammetry

Cyclic voltammetry (CV) is another electrochemical technique that can provide information about both the thermodynamics and reaction kinetics of the system. CV is useful for examining the behavior of

both components of the solvent, such as KF or BeF2, and trace elements, such as salt corrosion products. CV is the application of a linearly varying potential applied in a periodic fashion. The goal is typically to force the reactive soluble species to undergo a redox reaction at the electrode interface. By relating the faradaic current, current corresponding to the redox reaction, to the applied potential, it is often possible to obtain good approximation of a redox couple's half-cell reduction potential. With adequate experimentation to determine these redox potentials, it is possible to identify common dissolved species, such as the corrosion products. In the case of some dissolved species which exhibit multiple oxidation states (e.g. Cr^{2+}/Cr^{3+} and U^{3+}/U^{4+}) it may be possible to distinguish between oxidation states based on the potential at which the corresponding peaks occur. When a chemical species' waveform behavior can be isolated, the method can also offer quantitative data on concentration using prior experiments with known concentration of species for calibration.

The Nernst Equation (Equation 20) and the Butler-Volmer Equation (Equation 32) make up the foundations of CV theory. When CV is applied to analysis of dilute species in an electrolyte mass transport effects of the species through the electrolyte become critical to the observed reaction kinetics. In the case of dilute species, the rate of reaction at the electrode surface can be determined by the rate at which the soluble species migrate to the electrode surface. An expression for the time-dependent current resulting from the instantaneous application of a potential is given by the Cottrell equation,

$$i_D = nFAC_O^*\sqrt{D_O/\pi t} \tag{37}$$

where C_O^* is the initial concentration of the reactive species and D_O is its diffusion coefficient. The concentration gradient at the electrode (i.e. the current density) decreases as $\sqrt{1/t}$.

The combination of the Butler-Volmer relationship and the Cottrell equation give CVs their characteristic peak shapes. Immediately after the potential is changed large current results as dictated by the Bulter-Volmer relationship. At increasing time, the effect of diffusion limits the current in accordance with the Cottrell equation.

The proportionality between the CV peak current density and species concentration have been demonstrated by previous researchers. The Randles-Sevsik equation describes reactions involving two soluble species in the electrolyte,

$$j_{p,soluble-soluble} = 0.446nFAC\sqrt{\frac{nFvD}{RT}} \tag{38}$$

where C denotes the concentration of the reactive species, *A* is the surface area, *v* is the scan rate, and *D* is the diffusion coefficient of the reactive species. A similar relationship for systems consisting of a single soluble reactant and an insoluble product, such as $M^{2+}(d) + 2e^- \rightarrow M^0(s)$ is given by the Berzins-Delahay equation [81], [82].

$$j_{p,soluble-insoluble} = 0.61AC\sqrt{\frac{n^3F^3vD}{RT}} \tag{39}$$

Several studies of soluble-insoluble reactions in molten salts have fit experimental CV data to the Berzins-Delahay equation to demonstrate relationships between species concentration and CV peak current density [81].

Solutes in fluoride salts, such as chromium, europium, gadolinium, plutonium, samarium, and uranium are known to have complex redox behavior involving multiple oxidation states [38], [65], [83]–[87], [87]–[101]. Recent studies of dissolved chromium using cyclic voltammetry in FLiNaK [94] and in FLiBe [102] have shown that it may be possible to measure the prevalence of Cr(II) and Cr(III) oxidation states *in situ*. The change in oxidation state of the reactant is important in determining which peak current-concentration relationship to apply.

1.5.7 Reference Electrodes for Fluoride Salts

Establishing a repeatable reference electrode for voltammetry experiments is a considerable challenge in fluoride salt electrochemistry. The desired qualities of a good reference electrode are measurement repeatability, long term stability, and accuracy in terms of providing thermodynamic information. Other considerations include robustness, manufacturability, and cost. The high-temperature

and corrosive environment of molten fluoride salts often means that compromises need to be made among these requirements. Some common reference electrode concepts for fluoride salts include inert metal, or quasi-reference electrodes (QRE), and thermodynamic reference electrodes, such as the Ni/NiF_2 reference electrode. A relatively new reference electrode concept referred to as the dynamic reference electrode (DRE) has been developed and utilized in this research. A theoretical understanding of these electrodes and their benefits and limitations will be discussed in this section.

The simplest reference electrode is an inert (to molten fluoride salt) metal sucah as Pt or Mo, called a quasi-reference electrode (QRE). Depending on the electrode material QREs are robust and can be easily deployed in a variety of conditions without concerns of failure. A QRE's potential can depend on many factors, but typically their values are relatively stable over periods of hours making them suitable for experiments in which stability is the only requirement. The challenge with a QRE is the soluble species interacting with the electrode in the adjacent phase (molten salt) is unknown and so the reference half-cell reaction is not well defined.

To relate measured half-cell reduction potentials to thermodynamic quantities, a reference electrode in which all components of the reference half-cell reaction have known activities is required. An example of a thermodynamic reference electrode is the Ni/NiF_2 reference electrode. Carotti et al. [103] have published a review of Ni/NiF_2 reference electrode designs and demonstrated a promising prototype. In this electrode, a Ni wire is placed in contact with a fluoride salt containing a known concentration of NiF_2. The salt in the electrode is saturated with NiF_2 to mitigate change in the Ni^{2+} activity. The reference electrode is equilibrated with the molten salt mixture under study by immersing it into the melt. Electrical contact is established between the two salts via a lanthanum fluoride single crystal which can conduct F^- ions. The half-cell reaction and reduction potential predicted by the Nernst Equation are

$$Ni^{2+}{}_{(d)} + 2e^- \leftrightarrow Ni_{(s)} \tag{40}$$

$$E_{Ni^{2+}/Ni} = E^{\circ}{}_{Ni^{2+}/Ni} + \frac{RT}{2F} ln \frac{a_{Ni^{2+}}}{a_{Ni}} \tag{41}$$

For a solid pure Ni electrode, the activity of metallic Ni is unity. Theoretically, the standard reduction potential of another half-cell reaction can be measured with respect to the Ni/NiF_2 reference electrode. The Ni/NiF_2 reference electrode is the only widely used thermodynamic reference electrode. Uncertainties due to material-salt interactions, robustness, and standardization make comparing values obtained with Ni/NiF_2 reference electrodes challenging. Moreover, calibration of a Ni/NiF_2 reference electrode cannot be performed for a given salt mixture because no other repeatable reference electrode is available [103]. Before such as task can be undertaken, other standardized and repeatable reference electrodes must be demonstrated for a given salt mixture.

A dynamic reference electrode (DRE) is a reference half-cell reaction that is created using one of the components of the solution. In effect, the DRE is created *in situ* during the experiment rather than physically introducing a reference electrode. The advantages of a DRE are its simplicity and robustness compared to other reference electrodes. The purpose of a DRE is to create a redox couple for which the activities of the soluble and insoluble components of the half-cell reaction are defined at a constant temperature. A dynamic chemical equilibrium represents a condition in which the rates of the forward reaction and the reverse reaction are equal. The term '*dynamic'* characterizes the method of forming a redox reaction as one that is not far from a thermodynamically reversible (quasi-static) process [104], [105].

In molten FLiNaK and FLiBe, a repeatable DRE can be manufactured using one of the salt components. In FLiNaK, applying a sufficiently negative potential to an electrode can cause the reduction of K^+ ion to potassium metal. When the electrode is completely covered in potassium metal the half-cell reference reaction for the K/K^+ redox couple is established.

$$K^+_{(d)} + e^- \leftrightarrow K_{(s)} \tag{42}$$

where the symbols (d) and (s) denote dissolved and solid species. In FLiBe salt, the Be/Be^{2+} half-cell reference reaction is formed by reducing the Be^{2+} ion to beryllium metal the electrode.

$$Be^{2+}_{(d)} + 2e^- \leftrightarrow Be_{(s)} \tag{43}$$

In each salt mixture, the K/K^+ and Be/Be^{2+} redox couples are attractive choices for a DRE because their reduction potentials are relatively high compared to the Li/Li^+ and Na/Na^+ redox couples. KF and BeF_2 are of the first salt components to be reduced in FLiNaK and FLiBe, respectively, under a sufficiently negative applied potential. Taking the beryllium DRE as an example, Equation 20 gives the DRE's half-cell reduction potential to be,

$$E_{Be^{2+}/Be} = E^{o}_{Be^{2+}/Be} + \frac{RT}{2F} ln\ a_{Be^{2+}} \tag{44}$$

where $E^{o}_{Be^{2+}/Be}$ is the standard potential of the Be/Be^{2+} couple in the molten salt mixture with respect to an arbitrary thermodynamic reference point, *R* is the gas constant, *T* the temperature, n is the number of electrons, and *F* is Faraday's constant. Theoretically, at a given temperature and pressure, the activities of K^+ and Be^{2+} will be relatively constant compared to less concentrated solutes [66]. The well-defined half-cell reaction and constant activity make possible a relatively repeatable reference potential that is simple and inexpensive to measure.

DREs are increasingly being used in molten salts to enable a variety of electrochemistry studies [106]–[108], [104], [109], [90], [83], [102], [110]. The applications and state of the art production methods for DREs vary in the literature. Chronopotentiometry has been used to produce DREs in different salt mixtures. Ema et al. [106] created a K/K^+ and Li/Li^+ DREs on a nickel electrode in the LiF-KF eutectic melt at 570 ˚C and attempted to calibrate their potential using a HF/H_2 electrode. Afonichkin et al. [107] produced a Be/Be^{2+} DRE in a 15LiF–58NaF–27BeF_2 mixture (mol%) in order to measure the potential of an inert indicator electrode in flowing salt loops. Durán-Klie et al. [108] made a K/K^+ DRE in FLiNaK to measure the potential of a Ni wire in equilibrium with salt containing various amounts of NiF_2 to extrapolate the Ni/Ni^{2+} standard potential. A potential pulse followed by an open circuit potential was used by Kelleher et al. [104] to make Be/Be^{2+} DRE in 66.6LiF-33.4BeF_2 (FLiBe) to study the effect of Be metal dissolution on the potential of the indicator electrode. The K/K^+ DRE has been produced in FLiNaK using cyclic voltammetry and used as the reference for voltammetric studies of dissolved LaF_3 [109], EuF_3/EuF_2 [90], and UF_4 [83]. A DRE produced with CV has been used to measure the voltammetric behavior of dissolved

CrF_2 with respect to the Na/Na^+ redox couple in LiF-NaF [111]. In the candidate's previous work [102], a Be/Be^{2+} DRE was produced using a linear sweep voltammogram to form the Be/Be^{2+} electrode. Its potential was measured with a subsequent OCP and theDRE enabled the corrosion products CrF_2 and FeF_2 to be precisely characterized with CV [102]. CV was then applied to corrosion product monitoring before and after exposure of 316H stainless steel at 700 ˚C [110]. Having demonstrated reliable performance in electrochemical studies of the behavior of dissolved species in fluoride salts, DREs are poised to find applications in other voltammetry experiments, such as potentiodynamic polarization.

The characteristics of a DRE are between those of a QRE and thermodynamic reference electrode meaning that they must be carefully applied to molten salt research. DREs are superior to most inert metal reference electrodes in that their half-cell redox reaction can be rationalized. They are not, however, thermodynamic reference electrodes because their potential is still a function of the unknown salt component activity. The measured quantity $E^{o}_{Be^{2+}/Be}$ has been tabulated by Baes [60] and a theoretical Be^{2+} activity has been determined by Hitch & Baes [66] in pure FLiBe as a function of temperature. The activity of Be^{2+} and K^+ are not well characterized when significant salt impurities are present. To address this, experimentation with dissolved corrosion products and polarized specimens have been undertaken to demonstrate the repeatability of measurements taken with respect to the DRE under various conditions. In all instances in this research, the motivation for use of the DRE is to establish a repeatable reference point with which to identify and measure qualitatively the behavior of other species in a molten salt.

2 Experimental Procedures

2.1 Design and construction of molten salt corrosion facilities

2.1.1 Gloveboxes

Corrosion and electrochemistry studies were performed in inert atmosphere argon glove boxes. Glove box atmosphere was maintained below 1 ppm moisture and oxygen levels by an environmental purification system. Gloveboxes used for FLiBe and FLiNaK salt research are shown in Figure 8. The glovebox for FLiBe research was built in a specially designed laboratory with controls to maintain a safe beryllium work area environment. The glovebox for FLiNaK research was built in a separate laboratory. Both labs are located in the premises of the College of Engineering at the University of Wisconsin, Madison.

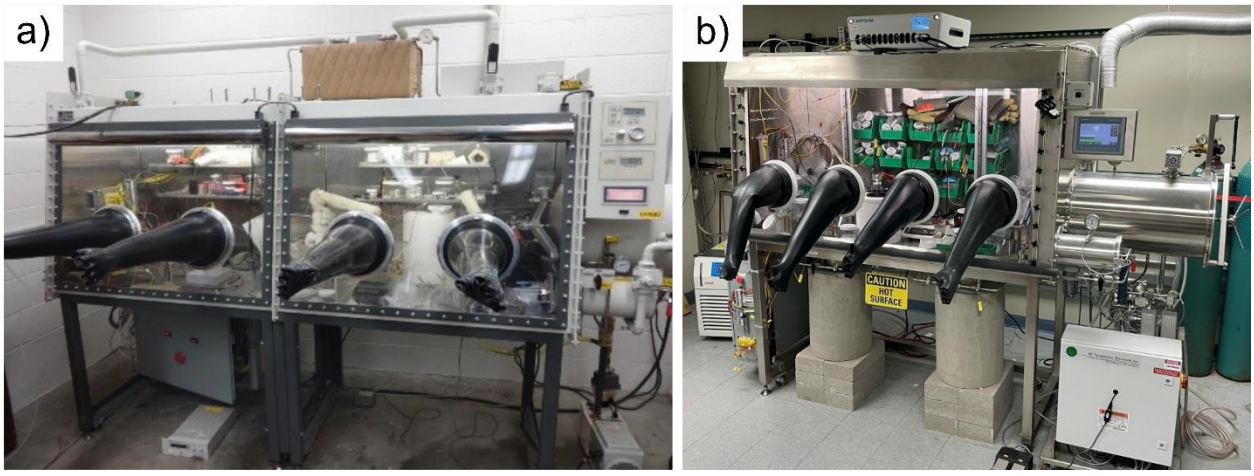

Figure 8. Environment-controlled argon atmosphere gloveboxes for research with (a) FLiBe and (b) FLiNaK.

To meet the needs of corrosion and electrochemistry experiments, the glovebox for FLiNaK research featured advanced custom corrosion testing furnaces that enabled testing of multiple sample materials in separate capsules in single experimental campaigns, thereby allowing for higher throughput static corrosion testing. These furnace wells were designed in collaboration with LC Technology Solutions Inc. A schematic illustration of the furnace is shown in Figure 9(a). The electric heaters and insulation were attached to the outside of the steel vessel as shown in Figure 9 (b). The heaters consisted of two semi-cylindrical ceramic fiber heaters (each 3000 W at 240 VAC) obtained from Watlow Electric Manufacturing

Company. This has the key advantage of isolating the corrosion environment from the heater materials as well as simplifying the maintenance of the furnace. In Figure 9 (c), an assembly which holds the corrosion experiment is raised up and down inside the glovebox by a pneumatic lifting system. To maintain adequate cooling between the glovebox and the furnace a coolant system and heat shield array system [112] were used. With this system, the specimens could be manipulated in and out of the molten FLiNaK at temperature. The ability to remove test samples from the molten salt at the experiment temperature is a significant feature for enhancing the scientific quality of the results of corrosion tests. Cooling of the salt can potentially lead to plate-out of corrosion products on the samples' surface due the strong dependence of their solubilities in molten salt. This can dramatically complicate the evaluation of weight change measurements and post-test microstructural characterization of the near-surface regions on the test samples.

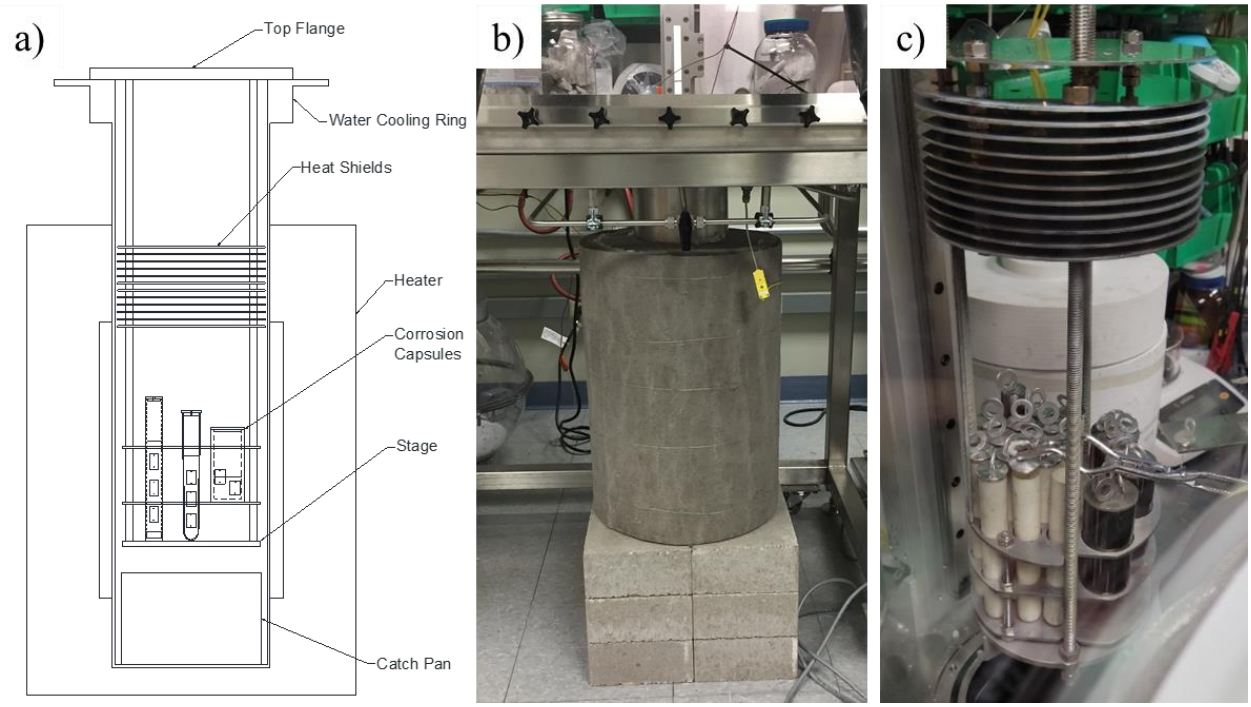

Figure 9. Static corrosion furnace incorporated in environment-controlled glovebox (a) schematic, (b) heaters and well, and (c) corrosion cell assembly.

Two generations of beryllium-designated laboratory work areas that were used in this research. The second-generation beryllium laboratory is shown in Figure 10. The author was instrumental in updating standard operating procedures to reflect changes in OSHA standards and establishing training programs for

operating the new beryllium work area. Unfortunately, the COVID-19 pandemic put a pause on beryllium research in this laboratory.

Figure 10. The FLiBe salt laboratory used for this research.

2.1.2 Beryllium Laboratory Safety

Repeated exposure to beryllium vapor or dust can cause the onset of Chronic Beryllium Disease (CBD), or more rarely, Acute Beryllium Disease (ABD). The University of Wisconsin Beryllium Exposure Control Plan dictates the necessary actions required to protect researchers and the public from the hazards of beryllium. The requirements of this plan are derived from the final rule of document *29 CFR 1910.1024 Beryllium* [113] and supplemented by parts of the final rule of document *10 CFR Part 850 Department of Energy Chronic Beryllium Disease Prevention Program* [114]. This plan meets the requirements of the *OSHA Exposure Control Plan* and actions are considered the basic level of protocol that must be followed. All new laboratory employees are required to read, understand and abide by this document. A training program for employees working in beryllium work areas has been designed by University Health Services in collaboration with the College of Engineering and Environmental Health & Safety.

The OSHA beryllium final rule established an air quality action level of 0.1 $\mu g/m^3$ Be and reduced the permissible exposure limit (PEL) for beryllium, to 0.2 $\mu g/m^3$. Both values are 8-hour time weighted

average concentrations. The standard also established a short-term exposure limit (STEL) of 2.0 μg/m^3 as determined over a sampling period of 15 minutes. OSHA does not set a numerical surface contamination limit but requires employers to establish procedures to maintain all surfaces in beryllium work areas as free of beryllium as practicable. UW-Madison maintains a stringent maintenance and cleaning schedule that reduces the risk of beryllium contamination of the laboratory. Should any of these limits be exceeded, all beryllium handling is stopped while re-evaluations and changes are made to reduce exposures.

Beryllium sensitization (BeS) is an abnormal immune response to exposure to beryllium and indicates that an individual has been exposed to beryllium. All researchers working with beryllium are required to be tested for BeS and CBD. A blood test referred to as the *Beryllium Lymphocyte Proliferation Test (BeLPT)* [115] is administered on a yearly basis by University Health Services at UW-Madison. The test screens for an abnormal immune response to exposure to beryllium. A medical evaluation including BeLPT is administered if a worker experiences symptoms of CBD.

All laboratory workers are medically cleared, trained and annually fit tested in a NIOSH approved full-face respirator with at least P100 filters as a precaution. P100 filters are appropriate for protection against any beryllium particulate. All beryllium workers are trained at Environmental Health & Safety (EOH) on proper respirator use. The employee has to undergo annual on-site training. The employee must be able to demonstrate, among other things, knowledge and understanding of the following: (i) the health hazards associated with airborne exposure to and contact with beryllium, including signs and symptoms of CBD, (ii) the written beryllium exposure control plan, and (iii) donning and doffing of appropriate personnel protective equipment.

2.1.3 Electronics & Labview control systems

To maximize the capabilities of the new glovebox systems, considerable effort was put into design and construction of custom electronics and integrated LabView controls that enable accurate and safe high temperature experimentation. The gloveboxes were outfitted with custom electronics controls and sensors for operating multiple furnaces simultaneously. The electrical distribution boxes, shown in Figure 11, were

designed and built-in house by the author and fellow graduate students. The National Instruments CompactRio hardware was used to interface with LabView Controls software. Custom designed software for user input, temperature data logging, emergency notifications, PID temperature control, and ramp soak capability for controlled heating and cooling were implemented. Switched power circuits and sensors were fed both inside and outside the glovebox. The system could control 3 208 VAC furnaces, two DC power circuits, and two 120 VAC circuits. 16 thermocouples provided input to the control system and monitored the temperature of the furnace, water coolant, furnace well cooling rings, and the ambient glovebox temperature, as well as other devices inside the glovebox.

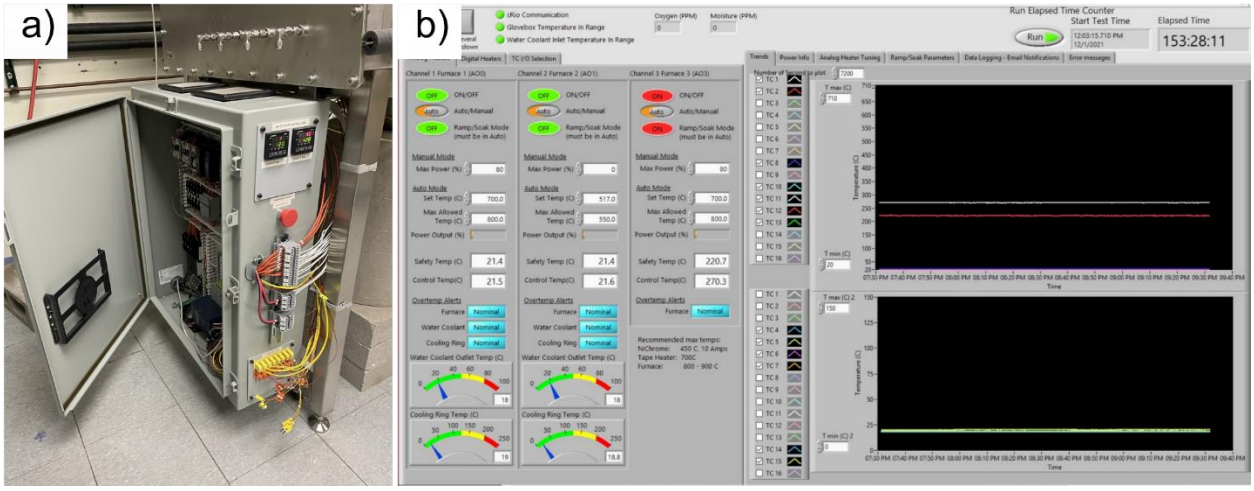

Figure 11. Electronics and LabVIEW software designed and constructed for operation of the glovebox furnaces and sensors.

2.2 FLiBe and FLiNaK salt procurement & purification

FLiBe and FLiNaK salt were procured for molten salt corrosion and electrochemistry experiments. The FLiBe salt production processes has previously been described [116] and is summarized in the next section. A pre-melted eutectic mixture of FLiNaK was obtained from Materion Corporation. A purification process was performed on the salts to remove moisture, oxygen, sulfur, and other trace metals. In this research, purified FLiBe was used for all FLiBe salt experiments. The as-received FLiNaK was used for all FLiNaK experiments. The author made major contributions towards construction of a new fluoride salt purifier in support of future fluoride salt experimentation.

2.2.1 Fluoride salt purification systems

Fluoride salt purification is important for maintaining low concentrations of moisture, oxygen, sulfur, and other trace metals. These impurities can create very corrosive conditions in molten fluoride salts. Upon melting, salt which contains water may undergo hydrolysis and the formation of oxides or hydroxides by the following reactions [117].

$$H_2O + 2F^- \leftrightarrow O^{2-} + 2HF \tag{45}$$

and

$$H_2O + F^- \leftrightarrow OH^- + HF \tag{46}$$

Sulfur is another salt impurity that may interact with structural materials in molten fluoride salts. Sulfates, SO_4^{2-}, may participate in a two-step reduction reaction. First, sulfide ions, S^{2-}, are formed through a corrosion reaction with metals in the system. Second, the sulfide ion can react with HF in the salt to form H_2S gas [118].

$$SO_4^{2-}{}_{(d)} + 4M^0_{(s)} \rightarrow 4MO_{(s)} + S^{2-}_{(d)} \tag{47}$$

$$2HF_{(d)} + S^{2-}_{(d)} \rightarrow H_2S_{(g)} + 2F^-_{(d)} \tag{48}$$

These impurity reactions share the common reactants HF and H_2 meaning that it is theoretically possible to control their reaction equilibrium quotients by controlling the partial pressure of HF and H_2 in the system. This is the basis for the process known as hydrofluorination.

Hydrofluorination is generally a two-step process involving the sparging, or bubbling, of different gas mixtures through the molten salt at a temperature of about 600 ˚C. In the first step, a mixture of HF and H_2 gas is sparged to drive Reactions 45 and 46 towards reactants and Reaction 48 towards products. The resulting water and H_2S are gaseous at the reaction temperature and leave the salt. Ratios of HF and H_2 gas are tuned such that effective removal of these impurities is achieved without excessive corrosion of the reactor vessel.

Some corrosion of the reactor vessel is unavoidable during the first step; therefore, a second reduction step is required. Reduction of some corrosion products is accomplished by sparging pure

hydrogen gas through the salt. The reaction of H_2 gas with metal fluorides liberates a small amount of HF gas which ideally leaves the system as a gas.

$$MF_2 + H_2 \leftrightarrow M + 2HF \tag{49}$$

Despite the engineering difficulties associated with HF and H_2 gas, hydrofluorination is an effective means of purifying fluoride salts and was the primary method used for purification of salt for the MSRE [118].

To support future FLiNaK salt research a fluoride salt purifier was constructed in the second-generation beryllium laboratory. The purifier was designed to sparge hydrogen and hydrogen-fluoride gas through the salt. The parts and instrumentation were designed in collaboration with Erie Shore Engineering Inc. and the unit was constructed in house by the author and fellow graduate student Cody Falconer. Pictured in Figure 12, the system consisted of hydrogen and hydrogen fluoride gas distribution cabinets, a purification reactor vessel, and an effluent gas scrubber system. One novel aspect of this purification system was the implementation of a custom purifier reactor vessel which could be detached from the purifier and connected directly to the glovebox via one of the glovebox furnace wells, as shown in Figure 12(d). This enabled purification to be conducted safely in a dedicated space and enabled the salt to be pumped out of the purifier vessel directly into the inert argon atmosphere. This avoided possible errors due to multivessel salt transfers. The linkage to the glovebox also helped prevent the contamination of the glovebox with materials used to build the heating elements of the purifier vessel. The author's primary contribution to the project was design and construction of the electronics used to safely operate the system and in assisting with purification experiments.

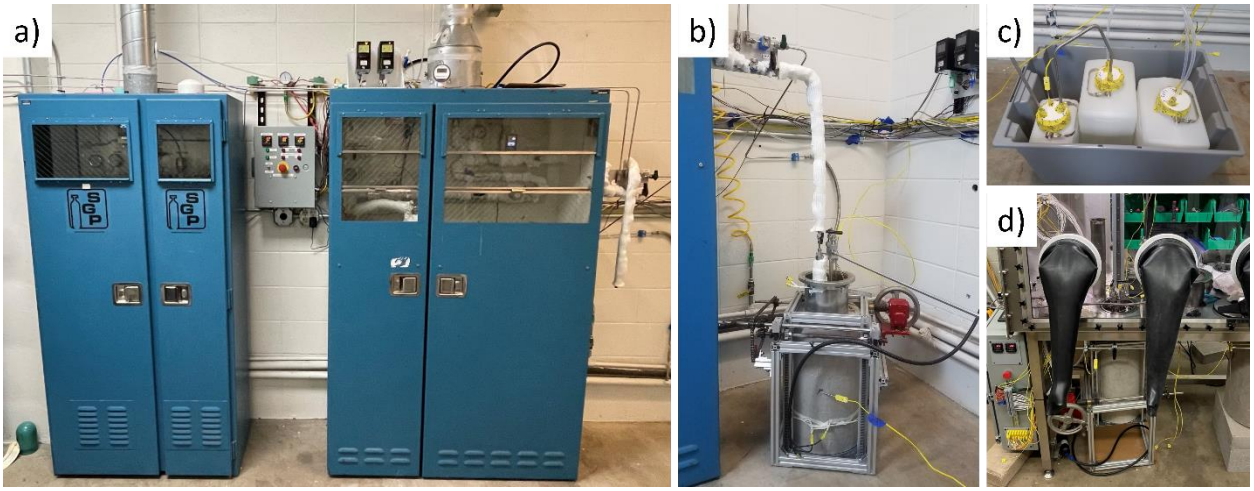

Figure 12. Fluoride salt purification system including (a) gas distribution cabinets for H_2 (left) and HF (right), (b) purification reactor vessel, (c) effluent scrubber baths, and (d) purification reactor vessel attached to the glovebox.

2.2.2 FLiBe salt purification

Lithium fluoride (99.8% purity) was obtained from Noah Technologies and beryllium fluoride (98.8% purity) was procured from Materion Corporation. A 40 kg batch was produced by hydrofluorination, The salt was stored in sealed vessels back pressurized with ultra-high purity argon or helium to 5 psi to ensure that it did not come into contact with water vapor. To retrieve the salt, the salt was first transferred into a smaller nickel containment vessel. The vessel was then brought into the glovebox and heated to 600 ˚C. Gas pressure was applied to push the salt out of the vessel via a nickel transfer line dip tube. The salt was poured into a nickel tray. Figure 13 shows FLiBe salt after being transferred into the tray [105], [116].

Figure 13. FLiBe salt solidified in a nickel tray after being poured from a nickel transfer vessel [105], [116]. The large dendritic structures are a manifestation of the high purity of the salt.

2.2.3 FLiNaK salt procurement and purification

4 kg of LiF-NaF-KF (46.5-11.5-42 mol %) salt was procured from Materion Corporation where it was mixed and melted in a graphite crucible under an argon atmosphere. The initial LiF, NaF, and KF constituents each had a purity level of greater than 99.9 %. Differential scanning calorimetry (DSC) showed the salt's melting temperature to be 456 °C which is close to the theoretical eutectic temperature of the mixture of 454 ˚C. The FLiNaK was sealed in glass jars in argon and shipped to the University of Wisconsin-Madison, as shown in Figure 14. The assessment of this salt was performed in collaboration between UW-Madison and Materion Corporation.

Figure 14. Photograph of FLiNaK produced in collaboration Materion Corporation.

2 kg of FLiNaK procured from Materion were purified in 2020. Figure 15 shows a comparison between as-received and purified FLiNaK. The purified salt turned white indicating that some impurities had been removed. The concentration of trace elements measured by ICP-MS in the as-received FLiNaK and in three salt samples taken after purification are shown in Table 6. While moisture and oxygen are difficult to evaluate, ICP-MS showed decreased levels of Fe and S.

Figure 15. FLiNaK salt before (left) and after (right) purification. The white color generally indicates a higher purity salt.

Table 6. Concentration of trace elements in FLiNaK salt before and after purification.

Element	As-received FLiNaK	Purified FLiNaK 1	Purified FLiNaK 2	Purified FLiNaK 3
Fe	78 ± 5	39 ± 1	30 ± 3	41 ± 2
S	54 ± 3	47 ± 4	36 ± 5	40 ± 6
P	10.3 ± 0.6	7.0 ± 0.5	6.6 ± 0.6	8.9 ± 1.0
Ca	10 ± 3	7 ± 4	7 ± 18	10 ± 31
Al	8.7 ± 0.5	25 ± 2	36 ± 1	11 ± 2
Ni	4.0 ± 0.3	84 ± 3	81 ± 4	83 ± 4
Cr	2.8 ± 0.1	3.7 ± 0.1	3.7 ± 0.2	5.8 ± 0.3
Ti	0.8 ± 0.1	1.6 ± 0.2	2.4 ± 0.3	2.2 ± 0.2
Mo	0.8 ± 0.1	0.1 ± 0.0	0.1 ± 0.0	0.1 ± 0.0
Mn	0.7 ± 0.0	0.7 ± 0.0	0.7 ± 0.1	1.1 ± 0.1

2.3 Static corrosion experimental design

The goal of the static corrosion experiment was to compare the corrosion performance and mechanisms of different candidate structural alloys under a variety of conditions relevant to MSRs. A variety of alloys were investigated including 316L and 316H stainless steel, 16-8-2 weld material, and the nickel-based alloys Hastelloy-N (Alloy N), Alloy 141, and Alloy 3. 316L and 316H were heat treated in a variety of ways to investigate the effects of microstructure on corrosion. The weight change of the samples (per unit area) were determined by measurements of dimensions and weights of samples before and after exposure according to standardized procedures. This was followed by a suite of characterization methodologies to understand the mechanisms of corrosion in various alloys and microstructures. As discussed in other sections of the thesis, corrosion of test samples is strongly influenced by the capsule material used for the tests. Therefore, specimens were exposed in various capsule types (notably glassy carbon, Ni, 316L stainless steel, and pyrolytic boron-nitride) which were procured and used in the tests to investigate the effect of dissimilar materials (i.e., capsule material and test samples) on corrosion.

2.3.1 Procurement & heat treatment of 316L & 316H stainless steel

Table 7. Composition (in wt.%) of 316L and 316H stainless steels used in this study as measured independently by Anderson Laboratory.

Alloy	Spec.	C	Mo	Ni	P	Cr	Mn	Si	Fe
316L (UNS S31603)	Min		2.00	10.0		16.00			Balance
	Max	0.03	3.00	14.0	0.045	18.00	2.0	0.75	
316L		0.018	2.16	9.98	0.032	16.77	1.66	0.35	Balance
316H (UNS S31609)	Min	0.04	2.00	10.0		16.00			Balance
	Max	0.10	3.00	14.0	0.045	18.00	2.0	0.75	
316H		0.04	1.97	10	0.031	16.77	1.5	0.3	Balance

Two variants of type 316 stainless steel with a low (316L) and high (316H) concentration of carbon were tested in static corrosion tests in molten salt. A 14-gauge 316L sheet was purchased from Speedy

Metals. A 1/2-inch-thick plate of 316H was purchased from Sandmeyer Steel. The composition of each alloy was measured by Anderson Laboratory. Carbon was measured with a Leco CS844. A Leco O/N 736 was used to measure nitrogen. All the remaining elements are analyzed using ARL-Spark OES Metals Analyzer. The specification of these two alloys and the composition are shown in Table 7. 316L's carbon concentration was 0.018 wt. %. 316H's carbon concentration was 0.04 wt. % C. Both alloys meet the specification of the stipulated compositions of their grade.

Table 8. 316L & 316H heat treatment times and temperatures investigated for molten FLiNaK salt corrosion experiments.

Batch	Annealing Temp [˚C]	Annealing Time [min]	Sensitization Temp [˚C]	Sensitization Time [min]
As-received 316L	NA	NA	NA	NA
316L batch I	1,100	20	NA	NA
316L batch II	NA	NA	700	24
316L batch III	1,100	20	700	24
As-received 316H	NA	NA	NA	NA
Sensitized 316H	NA	NA	700	24

To investigate the effects of microstructure in a given stainless steel, such as grain boundary character and sensitization, on corrosion, the as-received 316L sheet was cut into smaller sections and heat treated in a box furnace. The heat treatment times and temperatures for the 316L batches are summarized in Table 8 and designated as I, II, and III. This convention will be used in future sections. Images of the four heats of 316L after heat treatment are shown in Figure 16. Specimen coupons were then sectioned from each batch of 316L material using wire EDM. The as-received 316L was annealed at 1,100 ˚C for 5, 20, and 60 minutes to induce grain growth. Samples of the as-received stainless steel samples that was annealed for 20 minutes at 1,100 ˚C were held at 700 ˚C for 24 hours to induce sensitization. To eliminate the effects of oxidation, at least 40 μm of material was removed from each face of the heat-treated specimens using SiC grinding media, prior to molten salt exposures.

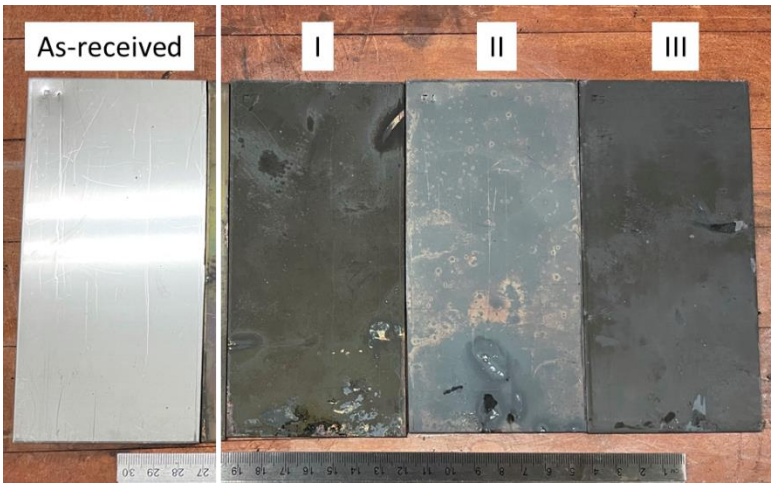

Figure 16. 316L batches before and after heat treatment in ambient environment. Table 8 summarizes the heat treatment parameters. Surface oxide layer was removed prior to testing in molten salt by grinding with SiC grinding media.

The effect of pre-sensitization of the 316H microstructure was also investigated in static corrosion tests in FLiNaK. The as-received 316H was heat treated in a box furnace at 700 ˚C for 24 hours to induce sensitization prior to molten salt exposure. To remove oxidation resulting from the heat treatment, material thickness of 100 μm was removed from the faces of the sensitized bar stock using Wire EDM. Sample coupons were then cut from both bar stock by cutting in the transverse direction. The approximate specimen dimensions were 14 mm x 11 mm x 1.5 mm. Two 1.58 mm diameter holes were drilled in each end of the specimen to facilitate suspension in the molten salt from a steel capsule lid using nickel wire.

2.3.2 Procurement of Alloy-N, Alloy 141, and Alloy 3

Table 9. Composition (in wt.%) of Alloy-N, Alloy 141, and Alloy 3 as measured by Luvak Inc.

Alloy	Ni	Fe	Al	Co	Cr	Mn	Mo
N	71	4	0.5	0.2	7	0.8	16
141	67.9	0.015	0.11	0.016	7	0.78	11.9
3	73.7	0.03	0.11	0.018	6.96	0.82	12.8

Alloy	Ti	Nb	Hf	Ta	W	C	N
N	0.5				0.5	0.06	
141	0.0094	0.015	0.0005	4.03	8.03	0.046	0.002
3	1.12	1.16	1.16	1.22	0.51	0.25	0.001

Alloy-N, Alloy 141, and Alloy 3 were obtained from Oak Ridge National Laboratory (ORNL). Figure 17 shows these alloys in the as received condition. The compositions of Alloy 141 and Alloy 3 were computationally designed at ORNL to achieve superior high temperature strength corrosion compared to Alloy-N but with comparable corrosion resistance. As part of the production process, Alloy 141 and Alloy 3 has a green oxide covering (likely Cr-rich oxide) the surface after being heat treated at 1,100 ˚C for 1 hour. The stocks were machined into square sections with a carbide end mill. As shown in Table 9, the composition of each alloy was analyzed by Luvak Inc. using a Beckman SpectraSpan VI for Directly Coupled Plasma Emission Spectrometry (DCPES) for the metals analyses and an Eltra CS 800 for Combustion-Infrared Detection (CID) for carbon analysis. Specimen were then cut into coupons with the approximate dimensions of 14 mm x 11 mm x 1.5 mm using wire EDM. Two 1.58 mm diameter holes were drilled in each end of the specimen to suspend them from the corrosion capsule lid into the molten salt using a nickel wire.

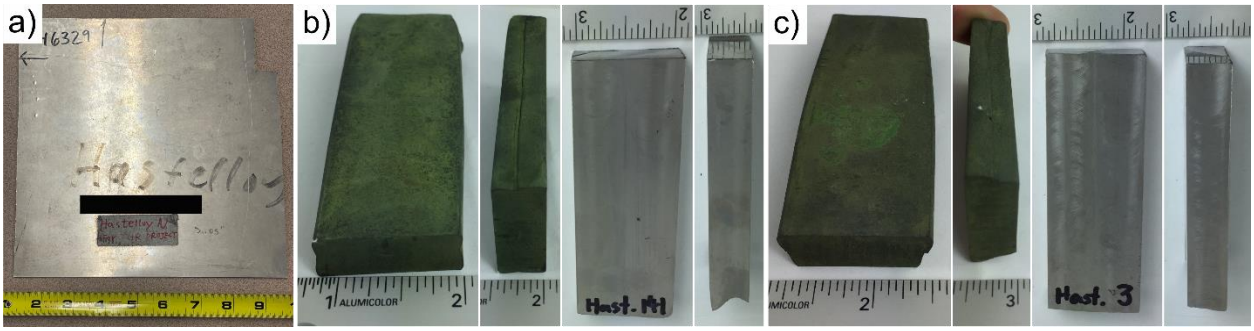

Figure 17. Photographs of (a) Hastelloy-N sheet and the as-received and machined (b) Alloy 141 and (c) Alloy 3 obtained from Oak Ridge National Laboratory.

2.3.3 Procurement of 16-8-2 weld

Table 10. Composition (in wt.%) of the 316H substrate, and 16-8-2 weld material used to produce the 16-8-2 weld pad. The compositions listed are certified by the manufacturer.

Alloy	C	Mo	Ni	P	Cr	Mn	Si	Fe
316H substrate	0.063	2.428	11.469	0.0175	17.409	1.375	0.425	Balance
16-8-2	0.05	1.28	8.45	0.019	15.24	1.42	0.39	Balance

Welded 16-8-2 material was manufactured by building up a weld pad on a 316H stainless steel substrate using gas tungsten arc welding (GTAW). A schematic illustration of the welding process is shown in Figure 18(a). 1.14 mm diameter 16-8-2 filler wire was obtained from Midalloy Performance Welding Products. The 50 mm thick 316H stainless steel substrate (here after referred to as the 316H substrate) was obtained from SeAH Changwon Integrated Special Steel. Figure 18(b) shows the as deposited 16-8-2 weld pad. For comparison, Table 10 shows composition of the 16-8-2 filler wire and the 316H substrate certified by the manufacturer. A sufficient thickness of 16-8-2 was deposited so that coupons could be made entirely from weld material without including the heat affected zone (HAZ). Figure 18(c) & (d) show the as-received 16-8-2 and 316H substrate coupons, respectively. The dimensions of the coupons made from the welded plate were 14.7 mm x 12.2 mm 1.6 mm. Two 1.58 mm diameter holes were drilled in each end of the specimen to allow for them to be suspended from a steel capsule lid into the molten salt using a nickel wire.

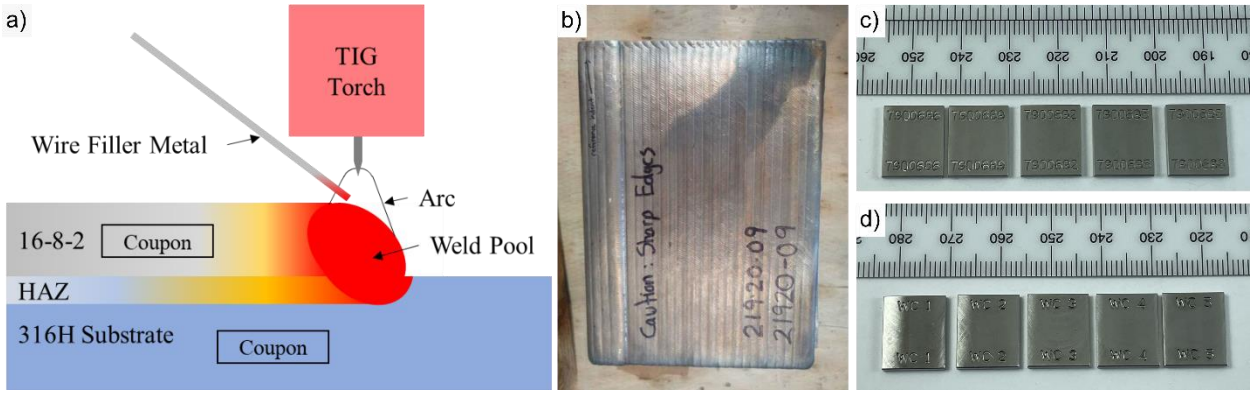

Figure 18. 16-8-2 weld material and 316H substrates (a) a schematic of the GTAW welding process, (b) image of the as-welded plate, c) image of the 316H substrate coupons, and (d) image of the 16-8-2 coupons [119].

2.3.4 Procurement of pyrolytic boron nitride

Pyrolytic boron nitride (PBN) specimen coupons were purchased from QS Advanced Materials. The coupons are produced using a CVD process. They had a compositional purity of 99.99% and did not contain any binder material. The material is deposited on a pyrolytic graphite coated graphite mold. The pyrolytic graphite is removed from the PBN using ultrasonic methods. The purpose of testing these coupons was to better understand the molten fluoride salt interactions with PBN which was used as a capsule material in a number of corrosion experiments.

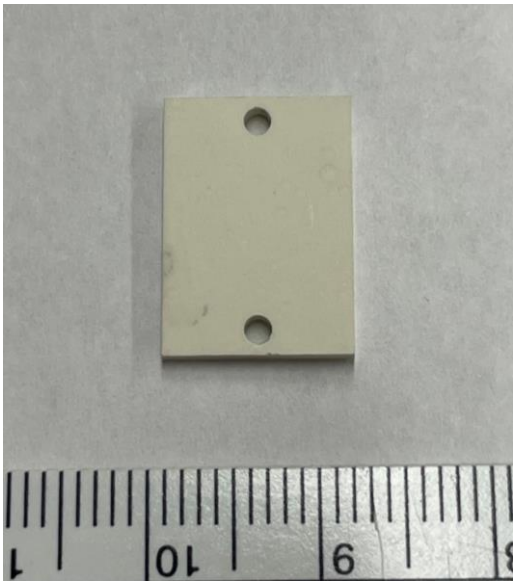

Figure 19. A pyrolytic boron nitride (PBN) specimen used to evaluate PBN as a potential capsule material for static corrosion studies.

2.3.5 Pre-exposure processing of test specimens

All corrosion coupons were gently ground to 1200 grit using SiC abrasive and cleaned by wet ultrasonic cleaning methods. Sample dimensions were measured with a micrometer. Specimen weights were measured to an accuracy of ±2 μg. Specimens were then suspended from capsule lids by wires. Figure 20 shows images of the arrangement for suspending the specimens before exposure in (a) metallic or PBN capsules and (b) glassy carbon capsules (similar arrangements were followed for Ni and stainless steel capsules).

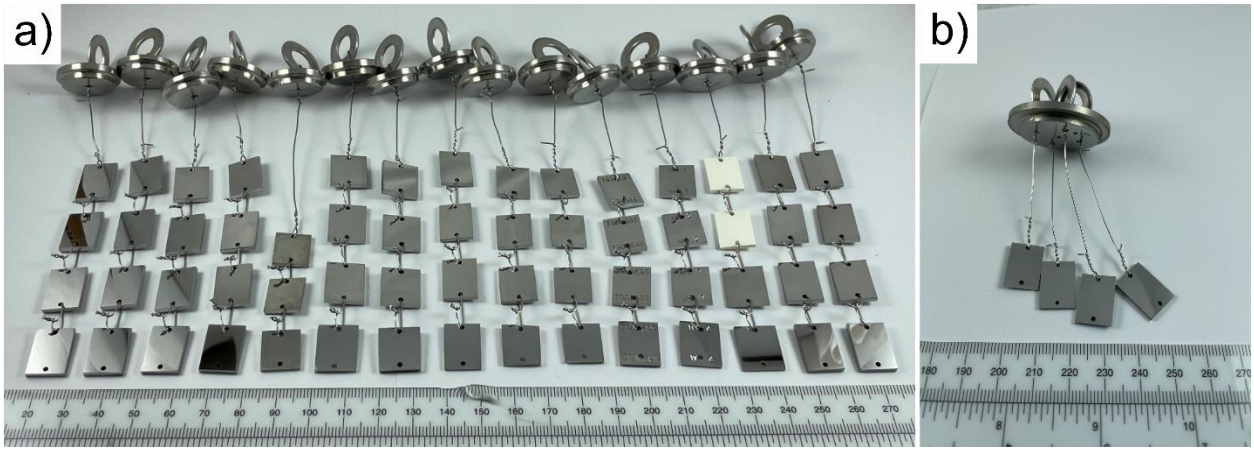

Figure 20. Photograph of static corrosion specimens before exposure to molten FLiNaK salt in (a) PBN capsules and (b) glassy carbon capsules. Specimens are polished and then suspended from capsule lids by 316 stainless steel or nickel wires depending on the test material.

2.3.6 Capsule design & corrosion experiment procedure

To investigate the influence of dissimilar materials on corrosion, each alloy was tested for corrosion in capsules of different materials. As shown in Figure 21, several specimens of a single alloy were exposed in separate capsules made of 316 stainless steel, nickel, pyrolytic boron nitride (PBN), or glassy carbon (GC). The 316 stainless steel and nickel (Ni-201 alloy) capsules were produced by Dynamic Temperature Supplies LLC. The metallic capsules had an inside diameter of 1.6 cm and a depth of 15 cm. A plug composed of the same material was welded on to the bottom of a tube using 316 stainless steel or nickel filler wire. The PBN capsules were procured from QS Advanced Materials Inc. These binder free PBN were manufactured by the CVD process and were of 99.99% purity. The PBN capsules had a lip diameter

of 3.4 cm and depth of 14.1 cm. The layered structure of the CVD manufactured PBN capsules imparted crack propagation resistance, and hence thermal shock resistance to the PBN capsules. The 60 ml glassy (vitreous) carbon crucibles with a diameter of 37 mm and height of 80mm were purchased from SPI Supplies.

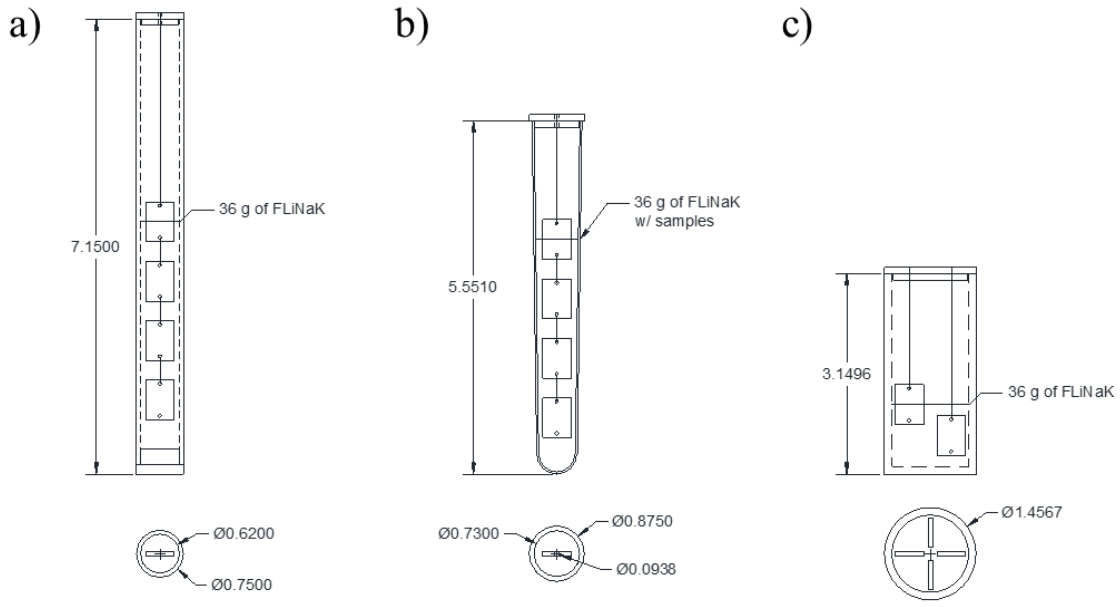

Figure 21. Schematic diagram of (a) 316 stainless steel or nickel capsules, (b) glassy carbon capsules, and (c) pyrolytic boron nitride (PBN) capsules for static corrosion experiments. Dimensions are in inches.

Each capsule was loaded with 36 g of FLiNaK or FLiBe. The salt was first dried in the capsules in a furnace at 250 ˚C for 24 hours inside of an inert atmosphere glovebox to remove any potential moisture that may have been introduced during transport. The salt was then melted, and the test specimens were introduced into the molten salt when its temperature reached 700 ˚C. Specimens were removed from the salt at temperature and air cooled to mitigate solidification of salt on the specimens. Using the density of pure FLiNaK reported by Williams [12] of 2.530-0.00073·T[˚C] g/cm^3, the calculated salt volume was approximately 17.8 mL. The salt volume-sample surface area ratio was approximately 1.5 cm.

2.3.7 Post-exposure treatment of test specimens

2.3.7.1 Weight Change

Specimen coupons exposed to molten FLiNaK were cleaned using ultrasonic cleaning in a 1M aluminum nitrate solution prior to characterization. The specimens were fully dried under low vacuum for about 12 hours. Then the weights of the specimens were measured using a Sartorius CPA26P high accuracy scale with a resolution of 2 μg. Specimen dimensions were measured with a micrometer. In this study weight change is calculated from the difference of the initial and final masses of the samples normalized by the surface area of the specimen. The average and standard deviation of the weight change is calculated from measurement of three coupons in each capsule.

Weight change is the most broadly used metric for materials degradation in molten salts. Often the weight change parameter is used to calculate uniform corrosion rate assuming that Cr dissolution occurs by thermal diffusion outward through the material matrix. It will be shown that in some cases, grain boundary Cr diffusion can be significant compared to diffusion through the grains leading to deep preferential dissolution of Cr along grain boundaries. It will also be shown that in instances where other matter from the environment, such as dissolved C of Fe^{2+}, interact with the specimen the weight change is not a reliable indicator of corrosion. For these reason, other metrics are used to define the depth of corrosion attack more accurately.

2.3.7.2 Materials Characterization

Plan view (normal to the surface) and cross-sectional imaging microscopy were performed using scanning electron microscopy (SEM) with a Zeiss LEO 1530. Compositional analysis was conducted with energy dispersive spectroscopy (EDS) using the Thermoscientific Pathfinder EDS system using an accelerating voltage of 20 kV. EDS is analytical technique in which the X-rays emitted from a sample under an intense electron beam are measured and related to elemental concentration. When an atom within the sample contains ground state electrons in discrete energy shells bound to the nucleus, the incident beam may excite an electron in an inner electron shell, ejecting it from the shell while creating an electron hole.

When an electron from a higher-energy shell fills the hole, an X-ray with a characteristic energy related to that transition between energy shells is emitted. The EDS detector is sensitive to the energies of the X-rays and can relate the counted X-rays to elemental composition.

The surface was examined with two approaches for elemental compositional analysis. EDS area averages that measure the average composition of a broad area were performed. This analysis provides an average composition of an element of the entire microstructure. EDS point scans with an approximate diameter of 1 μm were performed on both the bulk material and the precipitates (if present). The point scan data represents the average and standard deviation of three point scans measured for both the matrix and precipitates.

Cross sections of the exposed materials were analyzed with EDS spectral maps and line scans. The spectral maps depict the distribution of the various alloying elements of interest in the cross section. Line scans were performed normal to the surface through the material matrix. Care was taken to avoid the grain boundaries when placing a line scan so that the EDS profile represents the gradients of alloying elements in the matrix only. For these cross-sectional examinations, the specimens were electroplated with a copper coating before mounting in Bakelite to protect the sample edge during subsequent grinding and polishing. In this research, *bulk grain Cr dissolution* refers to the dissolution of Cr (or other alloying elements) occurring in the homogeneous single phase of a material, such as the austenitic phase in 300-series stainless steel. *Matrix Cr dissolution* refers to the dissolution of Cr (or other alloying elements) occurring in the primary phase of the material, such as the austenitic Ni-rich phase surrounding the precipitates within a single grain.

Topographical data, such as surface recession, was evaluated using optical profilometry, also known as interferometry. Profilometry was performed using a Zygo NewView 9000 scanning white light and optical phase-shifting interferometer. Surface recession measurements are conducted on specimens that were half submerged in the molten salt. Line scans were performed vertically across the vapor-salt interface on the corrosion specimens. The measurement was taken as the difference between the average height of the surface exposed to the vapor phase and the average height of the surface exposed to the molten salt.

X-ray Diffraction (XRD) was conducted with a Bruker D8 Discovery using CuKα radiation (1.542 Angstroms). In order to incorporate a statistically significant number of grains in each material, XRD was conducted over a broad 1 mm x 1mm area by oscillating the XRD stage at 0.2 mm sec^{-1}. Using Bragg's law $n\lambda=2d\sin\theta$ the characteristic d-spacings of each indexed peak were calculated. To obtain precise measurements of the material lattice parameter, the lattice parameter obtained from each peak was plotted against the Nelson-Riley extrapolation function $(\cos^2(\theta)/\sin(\theta) + \cos^2(\theta)/\theta)$. The true lattice parameter was obtained by extrapolation to lattice parameter at $\theta = 90^{\circ}$.

X-ray photoelectron spectroscopy (XPS) is a surface-sensitive spectroscopy technique for measuring elemental composition, chemical state, and electronic state of solids. Surface analysis is performed by irradiating the sample with monoenergetic soft X-rays and measuring the energy of the resulting electrons that are emitted. Because of the limited penetration depth of X-rays, the technique is sensitive to only several nanometers of depth into the materials' surface. The advantage of the technique is that it does not require internal standards for quantitative analysis. A Thermo K alpha X-ray Photoelectron Spectrometer with a monochromatic Al Ka X-ray source was used. With a pass energy of 50 eV and 0.4 eV energy resolution, the X-ray spot size was 400 μm. XPS analysis was used for selecting samples for detection of the elemental depletion in the near-surface regions of samples as well as the chemical state of carbon at the surface in cases where glassy carbon capsules was used and mass transport to the sample surface may have occurred.

2.4 Salt Chemistry Analysis & Metal Fluoride Impurity Additions

Analytical salt chemistry methods were used to support molten salt electrochemistry and materials corrosion research. Over the course of this research a strong relationship was formed with Wisconsin State Laboratory of Hygiene (WSLH) to develop standardized methods of analyzing FLiBe and FLiNaK. Two analytical chemistry methods were used, namely, Inductively Coupled Plasma-Optical Emission Spectroscopy (ICP-OES) and Inductively Coupled Plasma-Mass Spectroscopy (ICP-MS). Early FLiBe research utilized ICP-OES. Later, ICP-MS was used for analysis of trace impurities and ICP-OES was used

for the main salt constituents. In both cases a salt sample of 0.5 g was analyzed. The choice of analysis method was determined by the concentration range of the species to be analyzed and throughput.

2.4.1 Inductively Coupled Plasma-Optical Emission Spectroscopy

Table 11. Concentration of trace metals in purified FLiBe determined by ICP-OES.

Al	Ca	Cr	Mg	Mn	Ni	K	Na
30 ± 20	114 ± 4	6 ± 1	136 ± 6	4.1 ± 0.4	15 ± 2	448 ± 38	493 ± 47

Analysis of metal content of FLiBe was performed at the WSLH using ICP-OES. In ICP-OES, the sample, in solution form, is aerosolized and passed into an argon plasma. In the plasma the sample is atomized and ionized. This raises the energy of the electrons in the sample to an excited state. When the electrons return to the ground state, energy is given off in the form of photons. The photons emitted from a certain element have characteristic emission spectra that is measured with a spectrometer. The intensity of a light spectrum is related to concentration of the element using calibration curves.

The method used to break down the salt is based on EPA 3050B [120]. 0.5 g of the sample was weighed and introduced into a polypropylene hot block digestion tube. 2.5 mL of 16 M HNO_3 was added, and the sample was refluxed at 95 ˚C for 2 hours. 30% H_2O_2 was added in increments of 1.25 mL followed by heating until bubbling subsided. The maximum volume of H_2O_2 that may be added is 5 mL, but the reactivity of the individual sample determines the exact volume that was used. 5 mL of 12 M HCl was added, and the sample was refluxed at 95 ˚C for 15 minutes. The sample was diluted to 50 mL with reagent water. The concentration of trace elements was measured using a dilution ratio of 1:2. Table 11 shows concentration of trace metals in purified FLiBe. In general, the technique excels at quantifying dilute metal impurities such as chromium and nickel in the part per million (weight ppm) concentration range. ICP-OES uses a set of internal standards to convert the intensity of light observed at a given wavelength upon ionization of an element to its concentration. Spectral interference is common and was encountered between Be and Cr for certain wavelengths of light. By adjusting the method for Cr from 205.56 nm to 283.563 nm, the measured value of chromium metal for pure UW FLiBe could be measured more repeatably. Iron was

detected but was below the level of quantification (LOQ) of 65 ppm above which only there is confidence in the measured value. The analysis of salt with intentional addition of FeF_2 (for specific experiments) were able to be analyzed for Fe because LOQ was exceeded in these cases.

2.4.2 Inductively Coupled Plasma-Mass Spectroscopy

Table 12. Composition of FLiNaK salt. The concentrations of the main salt constituents were measured with ICP-OES. The concentrations of trace elements were measured with ICP-MS. All values are in μg/g.

Fe	S	P	Ca	Al	Ni	Cr	Mo	Mn
78 ± 5	54 ± 3	9.9 ± 0.7	9 ± 18	8.7 ± 0.5	4.0 ± 0.2	2.7 ± 0.2	0.7 ± 0.1	0.7 ± 0.0

Very high accuracy measurements of trace impurities (ppb) can be obtained with magnetic-sector inductively coupled plasma mass spectrometer (ICP-MS). In this technique, the sample, in solution form, is aerosolized and passed through a plasma source for atomizing and ionizing the sample. A portion of the ions generated are then accelerated to the mass spectrometer. The mass spectrometer uses a magnetic field to separate the ions based on mass-to-charge ratio. The mass-resolved beams are then directed into collectors where the ions are converted into voltage. Quantification of the isotopes present is performed by comparing the voltages from the different collectors.

Adequate digestion of FLiNaK salt for ICP analysis is challenging. The composition of a small portion of salt (~0.5g) was measured by the WSLH. To breakdown the salts for analysis, samples are first ground in an agate pestle. A mixed acid microwave-aided digestion was performed in Teflon-bombs. The digestion matrix consisted of 7.00 mL of 16M nitric acid, 3.00 mL of 12M hydrochloric acid, 2.00 mL of 28M hydrofluoric acid, 1.00 mL of Milli-Q. The final digested volume was 50 mL. The composition of trace elements was measured using a dilution ratio of 1:5. ICP-OES is better suited for measuring the concentration of the main salt constituents. Aliquots of the digest were diluted 1:200 into a solution that is 0.8 M HNO_3 and 0.6 M HCl (or 5% v/v of each). Analysis was performed in triplicate and the mean values are reported. Table 12 shows the concentration of trace metals in as-received FLiNaK. The reported

uncertainty reflects components from the precision of the ICP-MS analysis, uncertainty in the blank subtraction, and uncertainty in the digestion recovery.

2.4.3 Metal Fluoride Impurity Additions

To simulate the introduction of corrosion products into FLiBe, divalent chromium, iron and nickel fluorides were added to the purified salt. These are considered the predominant stable metal fluorides formed by these metals. The addition of fluorides facilitates fast dissolution of the corrosion product and maintains the fluoride ratio in the melt. Nickel(II)fluoride of 99% purity was obtained from Acros Organic. Iron(II)fluoride with 99.9% purity was obtained from Apollo Scientific. Chromium(II)fluoride of 99% purity was obtained from Synquest Laboratories.

To produce salts with a range of impurity concentrations, a salt dilution method was used. Figure 22 depicts the steps in the dilution process. A large, concentrated sample was produced by dissolving a pure fluoride like CrF_2 or FeF_2 into a large batch of FLiBe. Pure FLiBe was then used to dilute the concentrated salt and produce salts with fractions of the original concentration.

For the electrochemical investigation of corrosion products, beryllium metal flakes (99% pure) were used to further purify the salt. The high stability of beryllium fluoride in the melt, results in a reduction of less stable fluorides such as the common metal fluoride corrosion products.

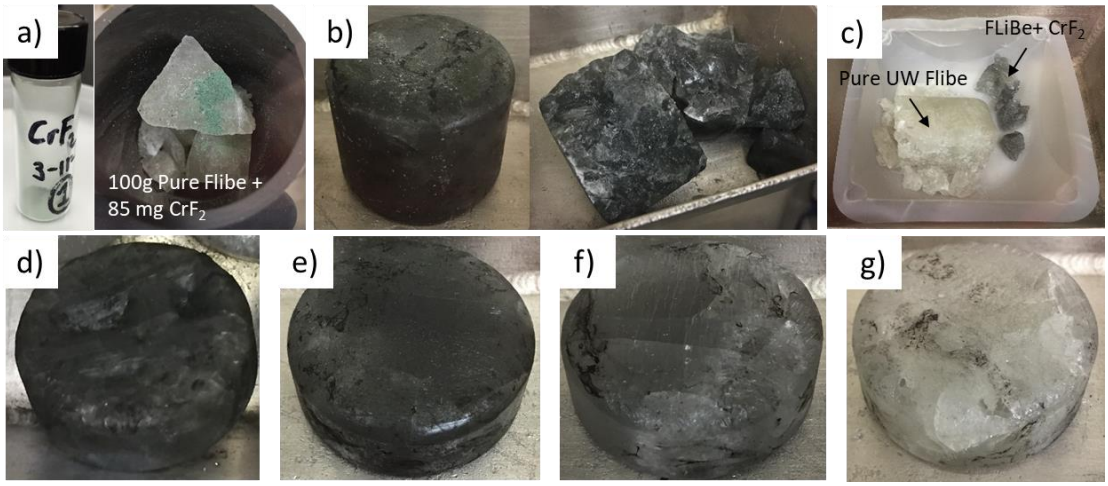

Figure 22. Preparation of FLiBe with varying concentrations of chromium fluoride prepared by dilution. a) 100 g of purified FLiBe with 85 mg of CrF_2 powder in a glassy carbon crucible, b) FLiBe with the added CrF_2, before and after breaking in to small pieces, c) preparation of purified FLiBe and FLiBe with CrF_2 for dilution, d) FLiBe with 352 ppm Cr, e) FLiBe with 286 ppm, f) FLiBe with 185 ppm CrF_2, and g) FLiBe with 100 ppm CrF_2.

2.5 Electrochemistry Experimental Procedures

Electrochemical experiments were conducted using a ceramic furnace in an inert argon atmosphere glovebox with the moisture and oxygen maintained below 1 ppm. A Metrohm Autolab 302N potentiostat was used for potentiodynamic polarization, open circuit potential, and salt potential measurements. The potentiostat has a voltage range of ±10 V (±30 V compliance) and a potential resolution of ±0.2 μV. The maximum current rating is ±2 A with a current accuracy of ±0.2 %. The 1 MHz bandwidth means practically that extremely high data acquisition rates can be achieved, which is important for techniques involving rapid potential or current sweeps.

The most basic electrochemical probe for voltammetry experiments consisted of three electrodes: a working electrode (WE), a reference electrode (RE) and a counter electrode (CE). For this research, a versatile electrochemical probe was constructed which featured ports for additional electrodes as desired. A schematic illustration of the electrochemical cell is shown in Figure 23**.** Images of the probe are shown in Figure 24. The probe was configured with either one or two working electrodes, referred to as primary and secondary working electrodes. The working electrodes and their corresponding potential sense electrodes were controlled using of a Metrohm working electrode multiplexer module (MUX SCNR16) to

automatically switch on and off the working electrodes in sequence. Here the primary (WE1) and secondary working electrodes (WE2) refer to separate electrodes. Each working electrode has its own pair of current conducting and voltage sensing wire leads. To control multiple working electrodes without a multiplexer would require manually moving the current conducting and voltage sensing leads. The counter electrode was a graphite or glassy carbon rod. A K-type thermocouple inside of a nickel or molybdenum sheath was submerged into the salt and used to control the furnace temperature.

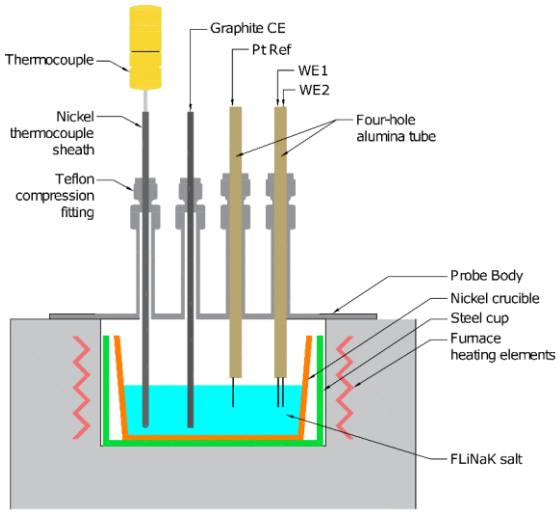

Figure 23. Schematic diagram of the electrochemical cell used in this study.

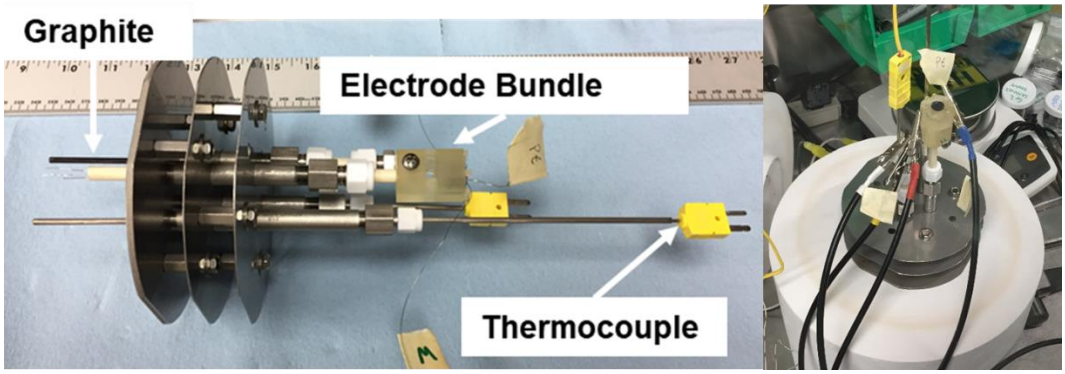

Figure 24. Electrochemical probe for molten salt chemistry and corrosion kinetics studies.

2.5.1 Dynamic Reference Electrodes

The DRE was produced using a three-electrode system: a cathode for forming the DRE, an indicator electrode, and an anode (counter electrode) for providing current to the cathode. A schematic diagram of

the electrode system is shown in Figure 23. The DRE is formed by applying a sufficiently negative potential or current to the cathode to reduce a soluble component of the salt to an insoluble metal which completely covers the surface of the cathode. The reaction's half-cell redox potential should be dependent on the standard potential and activity of the salt component in the melt. The potential of a temporary reference electrode, such as Pt, may be measured while the DRE reference half-cell reaction is present.

One drawback of the DRE is that the reference reaction is inherently unstable due to the tendency for Be and K metal to redissolve back into the salt. If the DRE is formed properly, the imposed reaction quotient will not be far from equilibrium. However, when the applied potential is removed, the imposed reaction quotient will be short lived as the metallic beryllium or potassium will rapidly dissolve back into solution. This means that the DRE can be used for measurements at short time scales but cannot be utilized directly for long term experiments. Instead, its potential relative to another temporary quasi-reference electrode must be acquired separately under the same testing conditions.

Measurement with the DRE involved two steps: a plating step to form the metal-metal fluoride redox couple and a cell potential measurement to measure the relative potential of the QRE. Several authors have proposed potentiostatic and galvanostatic methods for the first step [104], [105], [107], [108]. In this research, linear sweep voltammetry (LSV) was used to scan a significant portion of the usable potential range before forming the DRE. In Figure 25(a), LSV scans were performed on a FLiBe sample containing 286 ppm Cr at temperatures between 500°C and 700°C. The potential of the WE versus the Mo QRE is swept at 100 mV s^{-1} until the reduction of beryllium (reaction 1c) is observed. Due to the large concentration of Be^{2+} in the bulk solution, the reduction of Be^{2+} to Be metal is not limited by mass transport and represents the limit of the usable negative potential range. After completion of the plating step, the potential of the Be coated WE will remain at the Be/Be^{2+} half-cell reduction potential until the electrode is no longer covered with Be. This generally results in a plateau in potential in the open circuit potential measurement (OCP) in Figure 25(b). The potential of the QRE relative to the DRE can be obtained from the magnitude of the OCP plateau potential.

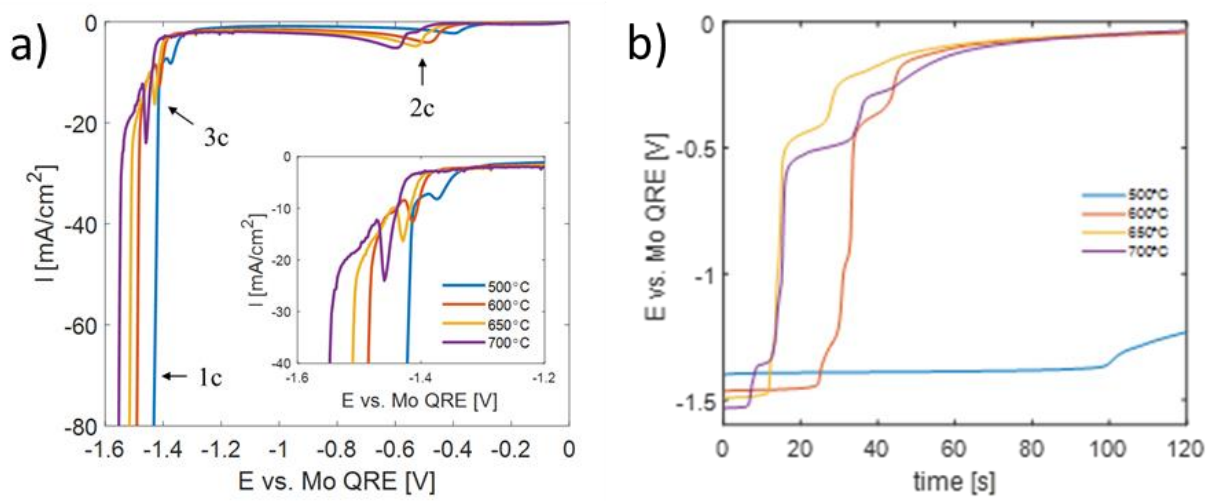

Figure 25. (a) Linear sweep voltammogram (LSV) of FLiBe salt with 286 ppm Cr at various temperatures. Scan rate is 100 mV/sec. (b) Open circuit potential between the beryllium dynamic reference electrode (DRE) and the Mo QRE as a function of time following the LSV [102] (from the author's research).

A similar measurement can also be made using cyclic voltammetry (CV). In Figure 26, CV was conducted using the Mo WE1, the Pt QRE and the graphite CE in FLiNaK salt at 700 ˚C. The WE1 potential was scanned from the WE1-QRE open circuit potential (OCP) in the negative direction. When the K/K^+ reduction potential is reached a large negative current signal occurs. The potassium is dissolved back into the molten salt when the potential is scanned in the positive direction. This causes a large positive current signal. At the positive end of the potential spectrum the oxidation of the WE1 is also observed. The region between these two reactions constitutes the usable potential range of FLiNaK and is on average 2.1 V. Within the usable potential range, there are no other redox peaks indicating that the FLiNaK salt is very pure. The potential of the QRE relative to the DRE can be obtained from a CV by extrapolating the negative K/K^+ reduction curve to the x-axis and then taking the difference of the potentials between the two electrodes. Due to the sudden steep current response, the K/K^+ half-cell reduction potential obtained in this way is practically the same as the potential obtained from the OCP measurement in Figure 25(b).

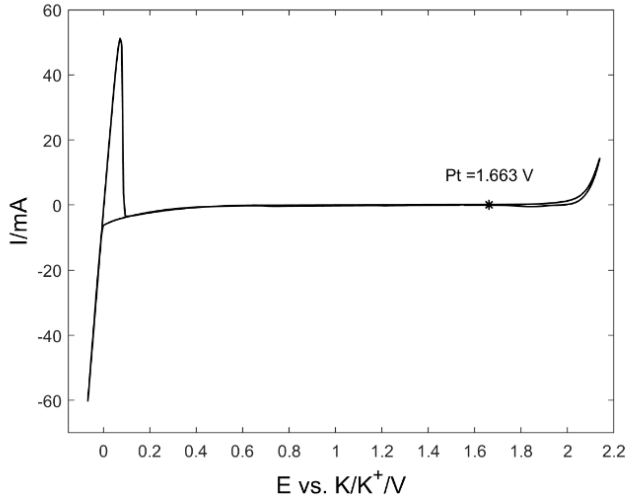

Figure 26. Cyclic voltammogram of FLiNaK salt at 700 ˚C acquired using Mo working electrode, Pt reference electrode, and graphite counter electrode. A scan rate 80 mV/sec was used, and the potential was normalized to the K/K^+ redox couple.

The cell potential between the QRE and the DRE is sometimes referred to as the inherent salt potential (redox potential), however, as previously discussed in Section 1.5.7, the relationship between the QRE's potential to the molten salt impurity chemistry is ambiguous. The intended purpose of the measurement is to provide a means of converting data acquired with respect to the QRE to with respect to the DRE. For example, following acquisition, the data in Figure 26 is normalized with respect to the K/K^+ reference reaction using the Pt-DRE potential difference of 1.663 V. Once this cell potential is known for a given set of conditions, potentials of other electrochemistry data obtained in the same salt can be normalized in a similar manner. In this work, the QRE-DRE cell potential was measured three times to get a good statistical average before conducting another electrochemical experiment.

2.5.2 Potentiodynamic Polarization Experimental Procedure

Potentiodynamic polarization measurements were conducted with the probe configured as described in Figure 24**.** The electrochemical probe consisted of a primary and secondary working electrode, a graphite counter electrode, and a K-type thermocouple. The primary working electrode, WE1, was a 0.5 mm diameter molybdenum (99.95%) wire used for creating the K/K^+ DRE. A 0.5 mm diameter polarization specimen (test material) was the secondary working electrode, WE2. 0.5 mm diameter platinum wire was

used as a quasi-reference electrode (QRE). For consistency, a new Pt QRE and Mo WE1 electrode was used for each test. The graphite counter electrode (99.9995%) was purchased from Fisher Scientific. For each polarization specimen, 15 g of FLiNaK was melted in a nickel crucible obtained from Alfa-Aesar. The thermocouple used to control the furnace was inserted into a nickel sheath (99.5%) and submerged in the salt. Four-hole alumina tubes were used to precisely position the wire electrodes. The surface area of the electrode was determined by measuring the depth of electrode immersion in the molten salt optically after exposure. The WE1 and WE2 were spaced 32 mm away from the QRE. A Metrohm Autolab PGSTAT302N potentiostat was used for open circuit potentials, DRE production and measurement, and potentiodynamic polarization.

Potentiodynamic polarization tests were conducted of Ni, Fe, Cr, 316L, and Ni-20Cr binary alloy specimens. For each test, a new specimen of each material was polarized to a different anodic overpotential to induce various levels of corrosion attack. Unless otherwise specified, the experimental procedure consisted of three measurements: (i) the potential of the Pt QRE with respect to the K/K^+ DRE (measured three times within a duration of 10 minutes), (ii) the open circuit potential of the specimen (WE2) relative to Pt QRE (recorded for 50 minutes), and (iii) potentiodynamic polarization of the specimen (WE2) with respect to the Pt QRE.

The results from measurement No. i were used to convert the result from measurement No. iii with respect to the K/K^+ DRE. In most cases, polarization was initiated 1 hour after insertion of the specimen. In theory, the exposure time before polarization is intended to allow the specimen to come to thermal equilibrium with the electrolyte [73].

A considerable effort was made to find a single set of potentiodynamic polarization parameters to investigate all materials, however, the corrosion characteristics of some materials investigated necessitated the use of different parameters to achieve precise results. The selection of scan rate of the applied potential was particularly important in these polarization experiments. It is desirable to select a scan rate that is sufficiently slow to minimize the effect of concentration polarization [67]. However, a reasonably fast scan

rate is needed to ensure the experiment is executed in a time frame over which the potential of the QRE with respect to the DRE is valid. It was assumed that while the specimen is polarized cathodically, there is no change in salt composition that could affect the potentials of either the QRE or the DRE. A scan rate of 0.166 mV sec^{-1} was used in all cases except for Cr for which a scan rate of 1 mV sec^{-1} was used (to be discussed in a later section).

The final applied anodic overpotential was the primary variable investigated in this study. Overpotential, η, is the difference between the applied potential and the specimen's apparent redox potential, $E_{apparent}$.

$$\eta = E_{applied} - E_{apparent} \qquad (50)$$

The start and finish overpotentials of polarization η_{Start}, and η_{Finish}, respectively, were applied relative to the specimen's open circuit potential (OCP). In all cases, the nominal start overpotential was -300 mV vs. the OCP and the nominal finish overpotential were varied between 250 mV to 850 mV vs. the OCP. The actual η_{Start} and η_{Finish} varied because the OCP and the measured $E_{apparent}$ with respect to the Pt QRE are rarely the same. The nominal anodic overpotential, η, the actual η_{Start}, and actual η_{Finish} for each specimen material are tabulated in Table 24 to Table 28. Prior to starting the polarization sweep, the potential was held at the start potential for 30 seconds to allow current from the potential step to subside.

It is assumed that while the applied potential is below $E_{apparent}$ there is no change in salt composition that could alter the potential of the K/K^+ DRE or Pt QRE. Potentiodynamic polarization tests were corrected for uncompensated solution resistance (please see Appendix). The precision of the redox potential measurements represents the multiple measurements taken for each material and the precision of the DRE.

2.5.3 Cyclic Voltammetry Experimental Procedure

Cyclic voltammetry experiments in FLiBe were conducted with an electrochemical probe designed by Kelleher [104], [116] and further researched by Dolan [105]. The probe was configured with three-electrodes. The working electrode and quasi-reference electrode (QRE) were a 1.58 mm diameter

molybdenum rod (99.95%) purchased from H.C. Starck Inc. The WE served a dual purpose as the electrode for investigation of dissolved species and for creating the K/K+ redox couple. The molybdenum WE and QRE were polished to 1200 grit with SiC abrasive before each test. The counter electrode (CE) was a 2mm glassy carbon rod purchased from Hochtemperatur-Werkstoffe GmbH (HTW). Experiments were carried out in a GAT13 glassy carbon crucible purchased from HTW. The thermocouple used to control the furnace was inserted into a molybdenum sheath purchased from H.C. Starck Inc. and submerged in the salt. The surface area of the electrode was determined by measuring the depth of electrode immersion in the molten salt optically after exposure.

3 Results & Discussion

3.1 Corrosion Studies of 316L & 316H Stainless Steel

3.1.1 Overview

Molten salt facing materials in an MSR must endure high-temperatures, high radiation doses, and corrosive environments. Figure 1 showed MSRs will operate at a higher temperature and experience higher displacements per atom than LWRs and most other advanced reactor concepts. The present targeted operation temperature for MSRs by industry is 700C, although higher temperatures are conceivable if appropriate structural materials become available. These conditions will place increased demands on current standard structural materials in use by the nuclear industry. There are currently only a limited number of ASME Boiler and Pressure Vessel Code Section III Division 5 qualified alloys for operation at MSR operating temperatures. 316H, a variant of type 316 stainless steel with 0.04-0.1 wt. % carbon, is currently one of the only widely available and economical codified alloys suitable for construction of MSR. The properties of 316H have been extensively validated for applications in high stress and high radiation dose environments, but the alloy has not been optimized as a molten salt facing material. Unfortunately, there are not yet any code standards for coatings or claddings to improve the corrosion resistance of structural materials in salts. While corrosion resistance is not specified under the ASME code, the thickness of the material affected by corrosion will likely not be within the specification of the code. Understanding the degree to which molten salt corrosion affects the near-surface composition and microstructure of 316H stainless steel will help address what design rules are required to ensure adequate MSR vessel design.

To adequately understand and predict corrosion in molten salts, material degradation must be described by a precise set of metrics, such as weight loss, the depth of preferential dissolution of an element from the bulk grain or grain boundaries, surface recession, and phase transformations in the near-surface regions of the material. Standard practices for weight change and alloying element depletion measurements are used in the literature [121], however, the majority of molten salt material corrosion research does not always report these measurements. Some of these measurements are only possible through materials

characterization techniques, such as XRD and SEM/EDS. Degradation by surface recession is usually not reported which can lead to discrepancies in the assessment of corrosion. The present work utilizes a profilometry method for quantifying surface recession occurring at the molten salt-vapor interface on the structural material. SEM and EDS are used to quantify changes in near surface elemental composition and determine whether preferential dissolution of certain alloying elements in a material occurs in the bulk grains or the grain boundaries.

The specification, quality and production methods of type 316 stainless steel vary globally. The alloy composition and microstructure are pivotal to establishing the mechanical properties of the material and are dictated largely by the composition (including impurity content) of the feed material and thermo-mechanical processing routes utilized. In addition to understanding the corrosion resistance of commercially available 316H stainless steel, there is interest in evaluating the performance of other type 316 stainless steel variants, such as the more common low carbon variant 316L (<0.03 wt. % carbon). The minor differences in specification could affect not only high temperature creep resistance, but also the long-term corrosion of the structural material. Recent literature suggests that microstructural features such as high angle grain boundaries can accelerate corrosion by providing fast diffusion pathways for Cr from the alloy into the molten salt [122]. Microstructural features, such as grain boundary character and second phases such as carbides, could alter the rate of corrosion by affecting the mass transport of alloying elements susceptible to corrosion to the alloy surface.

3.1.2 Comparison of as-received 316L and 316H corrosion resistance in FLiNaK

The present study is aimed at evaluating the effect of variations in composition, microstructure and capsule material on the corrosion resistance of type 316 stainless steels in molten FLiNaK salt at 700 ˚C, the maximum design temperature of current fluoride salt-cooled MSR designs. Two compositional variants, 316L and 316H stainless steel, are compared. The effect of capsule environment was investigated by exposing the samples in molten salt in 316L stainless steel, pyrolytic boron nitride (PBN), and glassy carbon capsules. All tests were performed for 500 hours at 700 ˚C.

3.1.2.1 Weight Change after exposure to molten FLiNaK

In all capsule environments, as-received 316L and 316H experienced varying amounts of weight loss when exposed to FLiNaK. Figure 27 summarizes the resulting of weight changes during these exposure tests. When exposed in 316L capsules, the weight changes of 316L and 316H were -0.210 ± 0.002 mg cm^{-2} and -0.119 ± 0.001 mg cm^{-2}, respectively. In PBN capsules the two alloys had statistically the same weight change of -1.5 ± 0.1 mg cm^{-2}. More weight loss was observed in glassy carbon capsules than in PBN capsules where the weight change of 316L and 316H were -2.0 ± 0.2 mg cm^{-2} and -1.7 ± 0.1 mg cm^{-2}, respectively.

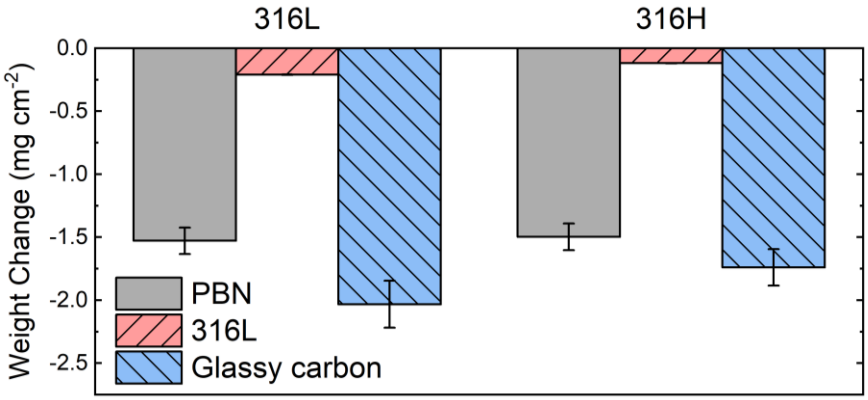

Figure 27. Weight change for 316L and 316H stainless steels after exposure to FLiNaK for 500 hours at 700 ˚C in pyrolytic boron nitride (PBN), 316 stainless steel (316L), and glassy carbon (GC) capsules.

Understanding the role of capsule material on corrosion was an important focus of the present research. From a practical standpoint, it is important to understand the role of dissimilar materials (as

presented by the diversity in test sample and capsule materials), and from a more fundamental side to understand corrosion of the test material in isolation, i.e., without the effects of the capsule material environment. It is noted here that in an MSR multiple materials coexist in the vicinity of each other in a molten salt medium. In both 316L and glassy carbon capsules, 316L lost more weight than 316H indicating that compositional or microstructural differences may be important factors in these environments. It was speculated that the small weight change in 316L capsules, compared to other capsule materials, was due to both the specimen-capsule similarity and the high material surface area-to-salt volume ratio. The specimen-capsule similarity means that there is no inherent driving force for mass transport due to compositional differences. A high value of the above ratio could result in the attainment of concentration of species such as Cr near their solubility limit in the salt, thereby reducing the driving force for corrosion. This would decrease overall corrosion attack in the test samples. Ultimately, it was determined based on the performance of the as-received alloys, that PBN had the least influence (i.e., was the most inert) on corrosion of test alloys of a wide range of compositions and microstructures.

3.1.2.2 Alloy surface morphology after molten salt exposure

Photographs of the 316L and 316H specimens before and after exposure in capsules of various materials are shown in Figure 28. The specimens turned a dull grey color after exposure to molten salt. For each set of specimens exposed in PBN and glassy carbon capsules, the top specimen in each sample chain was half submerged in the molten salt. This specimen shows a transition from the original polished surface to the corroded surface at the vapor-salt interface. 316H specimens exposed in the 316L capsule were fully submerged so no vapor-salt interface is observed in Figure 28 (e).

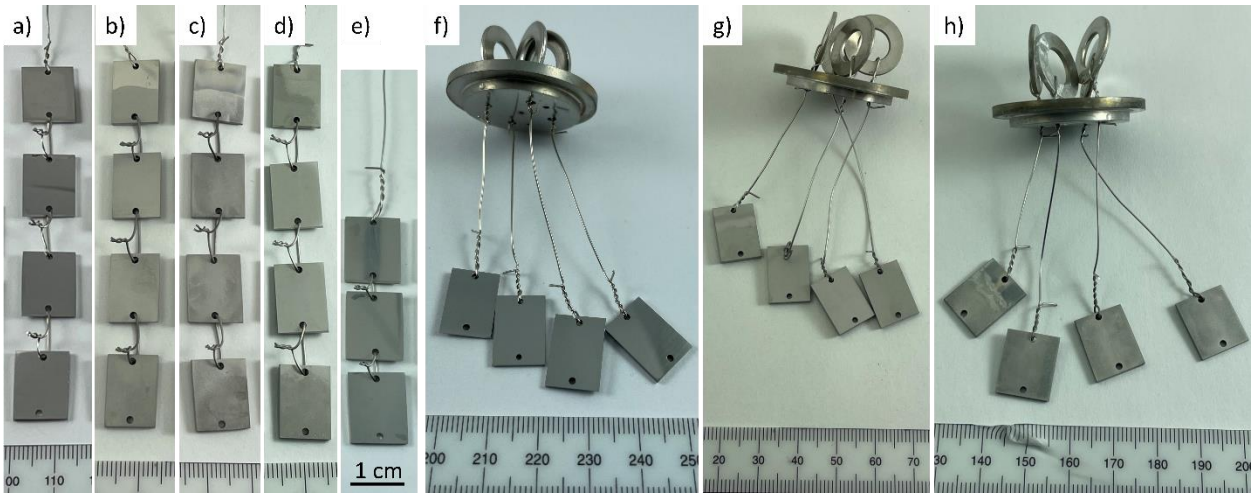

Figure 28. Photographs of (a)(b)(d)(f)(g) 316L and (c)(e)(h) 316H specimens (a) before exposure in PBN or 316L capsules, (b-c) after exposure in PBN capsules, (c-d) after exposure in 316L capsules, (f) before exposure in glassy carbon capsules, and (g-h) after exposure in glassy carbon capsules.

The effect of molten salt exposure on the surface topography of the as-received 316L and 316H exposed in different capsule materials was studied with SEM. Figure 29 shows (a) the polished 316L before exposure and 316L exposed in (b) PBN, (c) 316L, and (d) glassy carbon. Figure 29 also shows (e) the as-polished 316H before exposure and 316H exposed in (f) PBN, (g) 316L, and (h) glassy carbon. After exposure to FLiNaK in PBN and glassy carbon capsules, 316L and 316H showed clear signs of grain boundary attack, indicative of preferential dissolution of alloying elements along grain boundaries. Results pertaining to grain size differences are discussed in later sections. When exposed in 316L capsules, both 316L and 316H do not show significant grain boundary attack. Instead, there is an emergence of facets on the surface which could dramatically increase the specimen surface area. In addition to the facets, a uniform dispersion of second phase particles emerged on the surface of the sample. It is speculated that the formation of these precipitate phases is promoted by depletion of elements, notably Cr, from the grains which alters the phase equilibria in the grains. Elemental analysis of the sample will be discussed in a later section. Comparison of the corroded sample SEM images reveals striking differences between the modes of corrosion attack and possibly the types of corrosion mechanisms occurring in the different capsule environments. These modes of corrosion attack will be quantified in terms of uniform surface recession,

preferential dissolution of elements from grain boundaries, and preferential dissolution of elements within the grains.

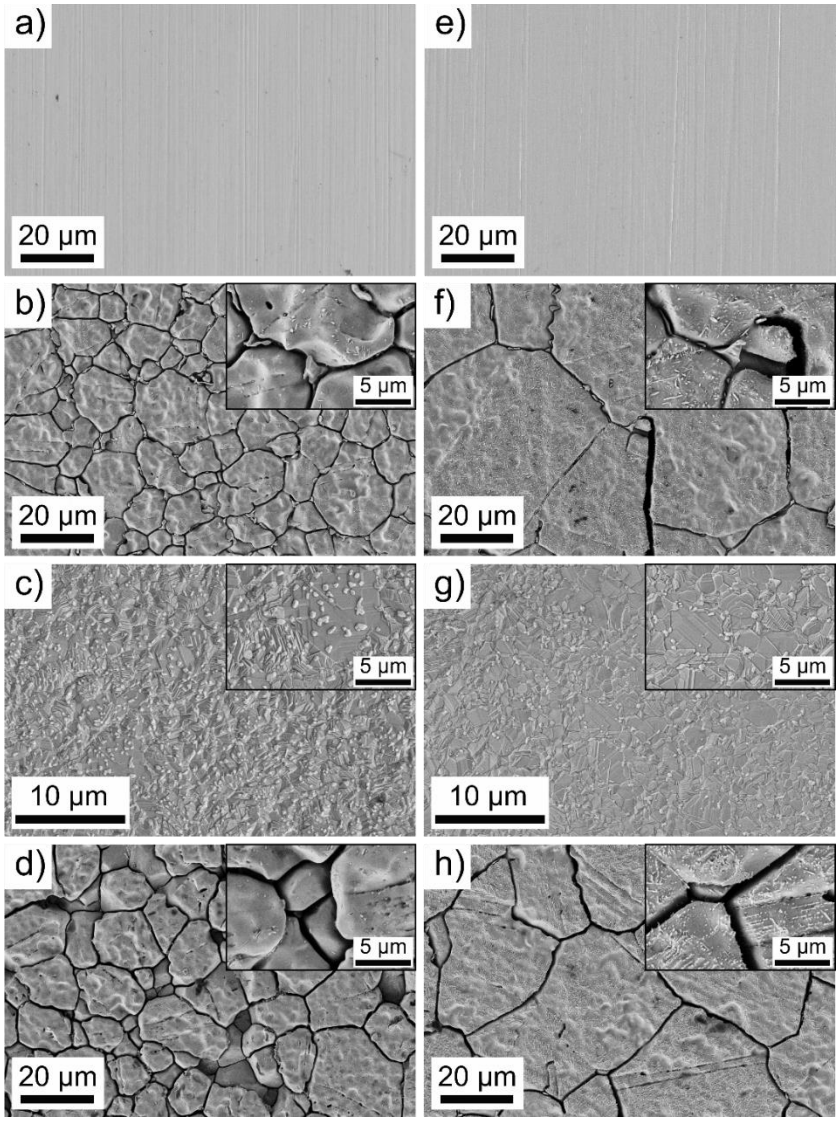

Figure 29. SEM images of the surface of (a-d) 316L and (e-h) 316H (a)(e) before exposure, and after exposure to FLiNaK for 500 h at 700 ˚C in (b), (f) PBN capsules, (c), (g) 316L capsules, and (d), (h) in a glassy carbon capsules.

For comparison, the surface roughness of the steels exposed in different capsules was quantified with profilometry as shown in Figure 30. The average root mean square (RMS) surface roughness of the as-polished specimens were 0.006 µm. The surface roughness of the specimen after corrosion increased dramatically in PBN and glassy carbon capsules. In PBN capsules, the RMS roughness of 316L and 316H were 0.496 µm and 0.392 µm, respectively. The roughness of 316L (0.925 µm) was much higher than 316H

(0.497 μm) after exposure in glassy carbon. It is speculated that this effect is due to the higher prevalence of grain boundaries in 316L. There is some apparent removal of small grains on the surface that leave behind voids (blue regions) that are nearly 2 μm in depth. Although facets were found on the surface of the steels exposed in 316L capsules, the RMS roughness was only 0.049 μm and 0.041 μm for 316L and 316H, respectively. This is due to the lack of obvious deep grain boundary attack or voids in the specimen surfaces.

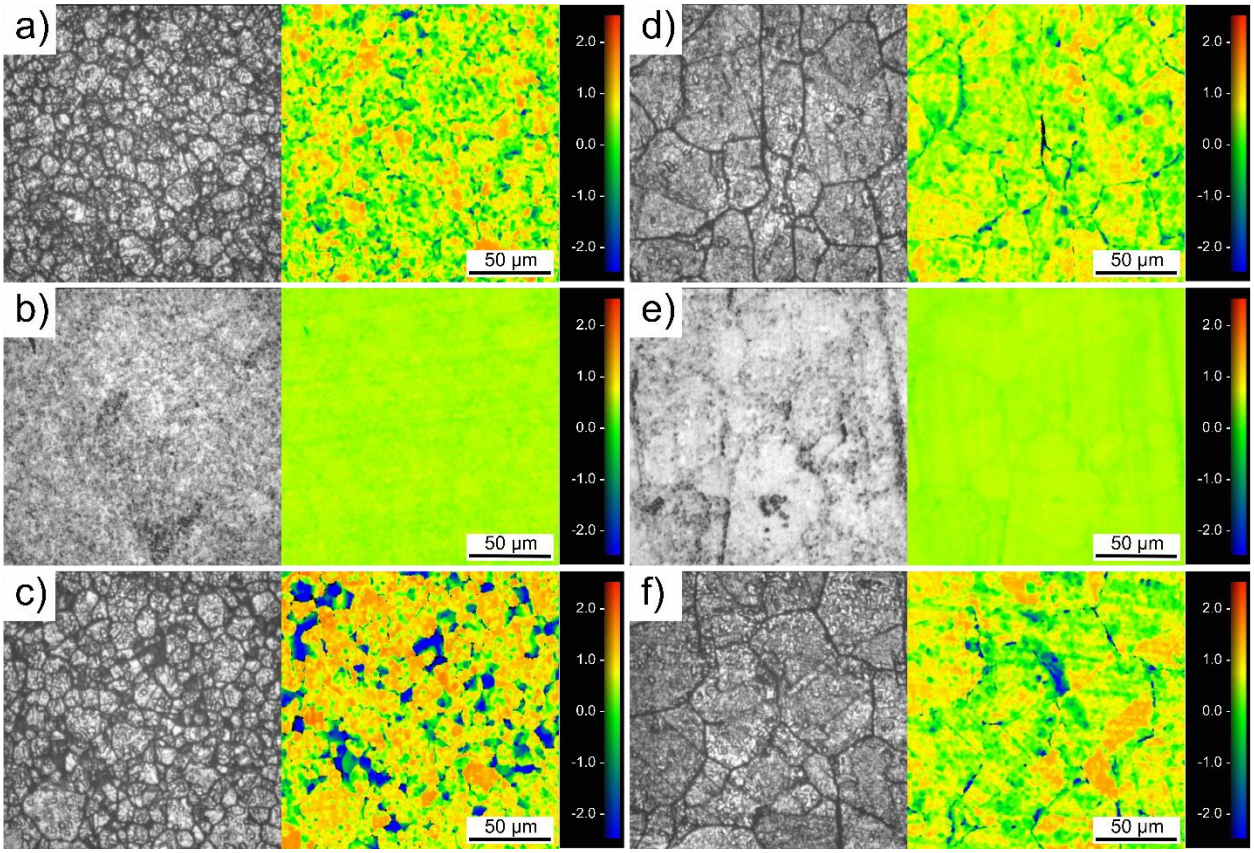

Figure 30. Profilometry of the surface of (a-c) 316L and (d-f) 316H after exposure to FLiNaK for 500 hours at 700 ˚C in (a),(d) PBN capsules, (b),(e) 316L capsules, and (c),(f) in a glassy carbon capsules (units are μm).

To investigate surface recession, profilometry was used to measure the surface topography of the vapor-salt interface on specimens of as-received 316L and 316H that were half submerged in PBN and glassy carbon capsules. Figure 31 shows profilometry topographical maps where the surface submerged in the salt is in the bottom of the image. In most cases, the vapor-salt interface shows a sharp drop to a lower average surface height indicating uniform surface recession of the material. The surface recession measurement is the difference between the average surface heights of the area exposed to the salt and the

area exposed to the vapor phase (where it is assumed no corrosion has occurred). In the case of, 316L and 316H exposed in PBN capsules and 316H exposed in glassy carbon the interface is discrete and could be readily measured with a single scan at 5x magnification. The surface recession of the 316L and 316H in PBN capsules were 1.13 μm, 1.14 μm, respectively. The surface recession of the 316L and 316H in glassy carbon capsules were 3.70 μm, 1.79 μm, respectively. 316L in glassy carbon was challenging to measure because the recession at vapor-salt interface had a large gradient, as shown in Figure 31(c). This required a broader scan comprised of several stitched profilometry measurements. The specimen's thickness varied along the entire length of the specimen. The corrosion mechanisms that lead to uniform surface recession were investigated with electrochemical methods and will be discussed in Section 3.3. The detectable surface recession of samples exposed in PBN and glassy carbon capsules are summarized in Table 14.

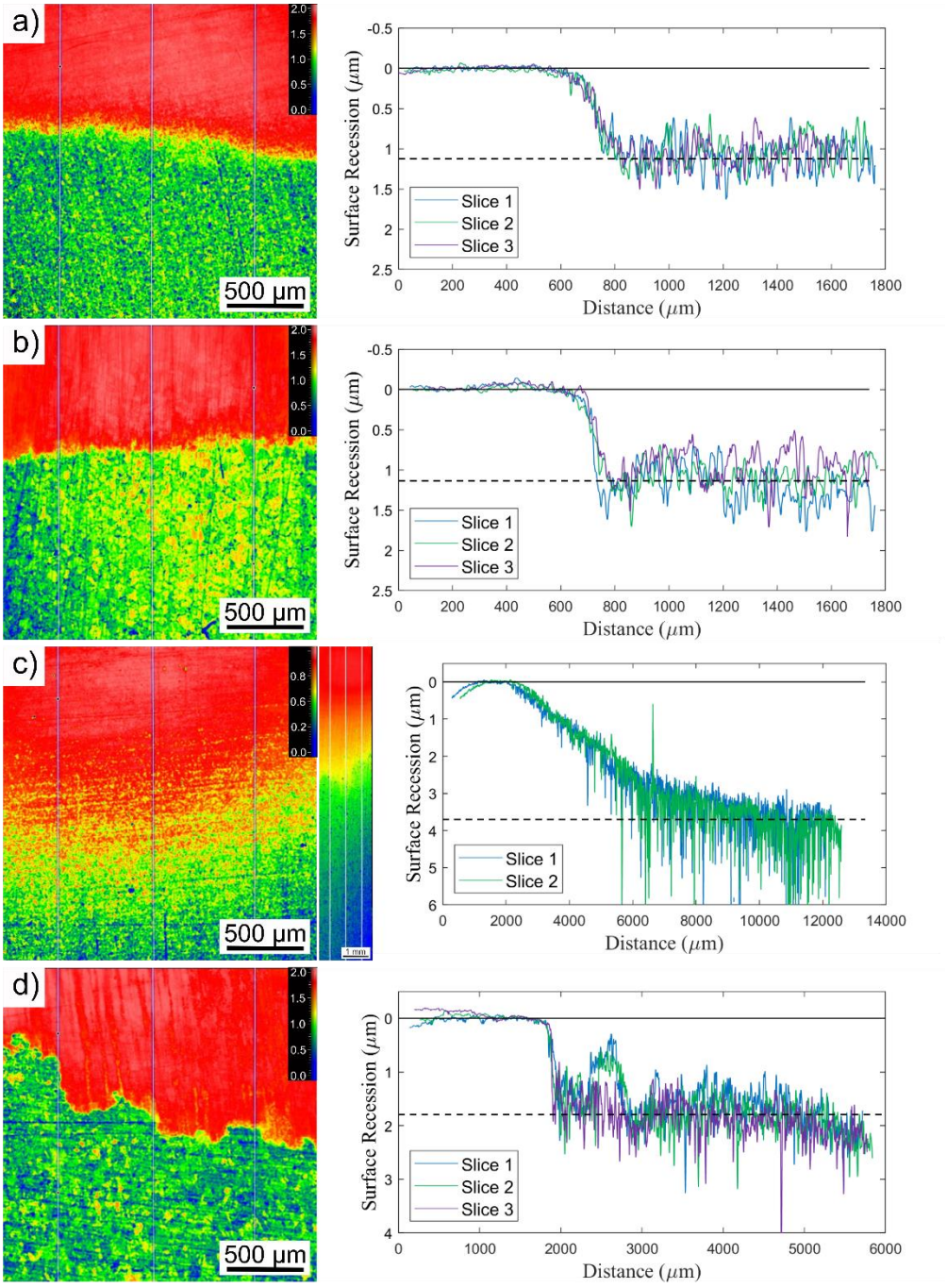

Figure 31. Profilometry topographical maps and linear slice plots of the salt-vapor interface of (a) 316L in pyrolytic boron nitride (PBN), (b) 316H in pyrolytic boron nitride (PBN), (c) 316L in glassy carbon, and (d) 316H in glassy carbon. The bottom region of the topographical map was submerged in molten salt and the top region was exposed to the vapor phase (units are µm).

3.1.2.3 Elemental analysis of the corrosion surface

Compositional changes in the surface of the 316L and 316H specimens exposed in the different capsule environments were initially evaluated using EDS area average composition scans. The usefulness of the area average composition measurement approach is the ability to detect the overall preferential dissolution of elements, averaged over the entire microstructure, in the near surface regions of the specimen. Area averages however do not detect preferential dissolution of elements along grain boundaries or other microstructural heterogeneities. Figure 32 shows the as-received composition of the surface and the net change in average composition of the surface after corrosion. In general, the surfaces of the as-received 316L and 316H show a net decrease in Cr after exposure. Enrichment of Ni and Mo is observed due to Cr dissolution. Specimens experienced about the same net decrease in Cr concentration in PBN capsules. This may partially explain the similarity in the weight change between the two alloys in PBN capsules. A slightly higher net decrease in Cr concentration was observed in 316L than in 316H when the specimens were exposed in 316L and glassy carbon capsules. This effect may be attributed to the higher carbon concentration in 316H which binds partially Cr in the alloy. When exposed in 316L capsules, the 316L specimen showed that the Mn concentration had dropped almost to zero. The results suggest that in these environments, the corrosion mechanisms may be different for 316L and 316H. The effect of differences in material microstructure will be investigated in Section 3.1.3.

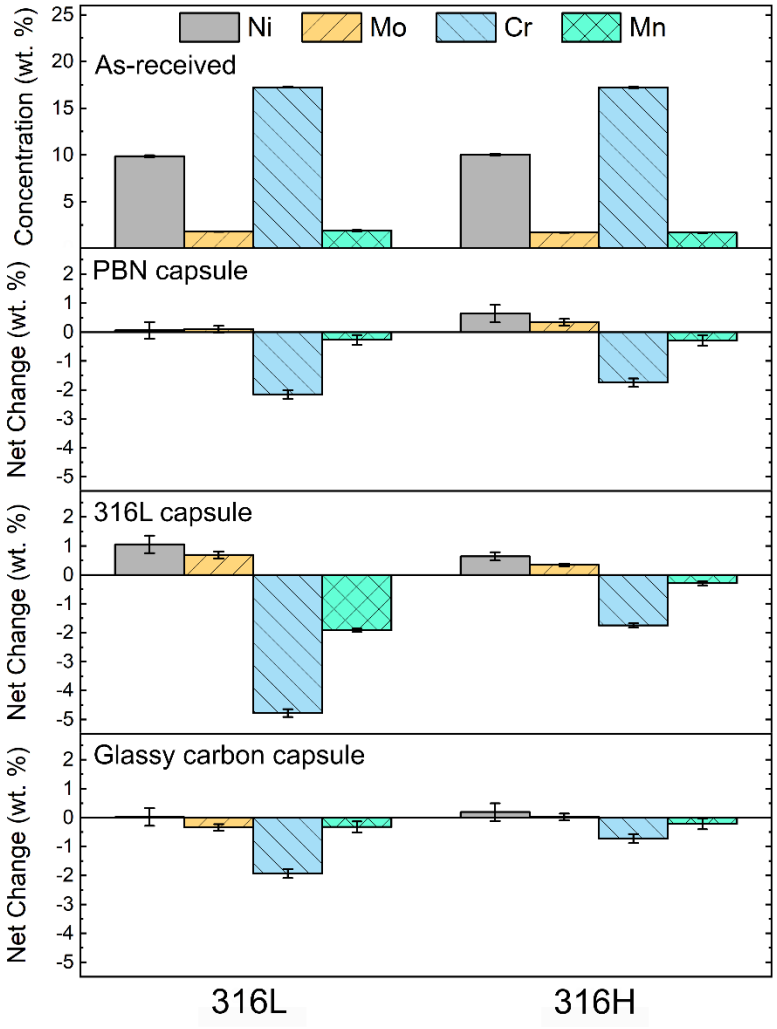

Figure 32. EDS large area average compositional analysis of the as-received 316L and 316H specimens and the net change in composition after exposure to FLiNaK salt in different capsules for 500 hours at 700 ˚C. Fe makes up the balance of the composition.

EDS cross-sectional analysis was performed on the specimens to determine the most dominant modes of corrosion attack occurring in each capsule environment. All specimens for cross-sectional examination were first coated with Cu before mounting in Bakelite to protect against edge rounding effect of the thin corrosion layer during metallographic sample preparation. Figure 33 through Figure 36 show the EDS spectral maps along with the distribution of Cr in the near surface region. It is noted here that the test temperature of 700 ˚C falls within the sensitization range of 316 stainless steel. When 316 stainless steel becomes sensitized, the grain boundaries become enriched in Cr due to nucleation of chromium carbide phase at the grain boundaries [19]. The grain boundaries are highlighted in the Cr spectral maps indicating

sensitization. In general, 316H shows more continuous and thicker Cr-rich regions in the grain boundaries in the bulk material after exposure. This is due to the higher C content of the alloy. When the Cr is dissolved from the grain boundaries the grain boundaries appear dark in the spectral map. The *depth of grain boundary Cr dissolution* is measured by taking the maximum projected depth of the depleted grain boundary normal to the exposed surface. The yellow arrow in the SEM image indicates the path of the EDS line scan. The line scans are placed so that they extend from the Cu coating directly into the grains, avoiding grain boundaries. The *depth of bulk grain Cr dissolution* is measured from the Cu coating interface (dotted line) to the approximate distance where the Cr drops approaches the bulk Cr concentration (dashed line).

Figure 33 shows the grain boundary Cr dissolution for 316L and 316H to a depth of 5.8 μm and 6.3 μm, respectively, when the testing was performed in PBN capsule. 316L did not show considerable Cr dissolution in the grains. 316H, however, showed a depth of matrix Cr dissolution of 3 μm. Another difference between the alloys in PBN capsule is the width of the grain boundary void created by grain boundary attack. The corroded grains boundaries in 316L appear much wider than in 316H. This is consistent with regions of grain removal in 316L samples in profilometry images shown earlier. In general, the corrosion of the two 316 stainless steels is quite similar when tested in PBN capsule. This contrasts with aqueous environments, where higher carbon contents in stainless steel results in a markedly lower corrosion resistance.

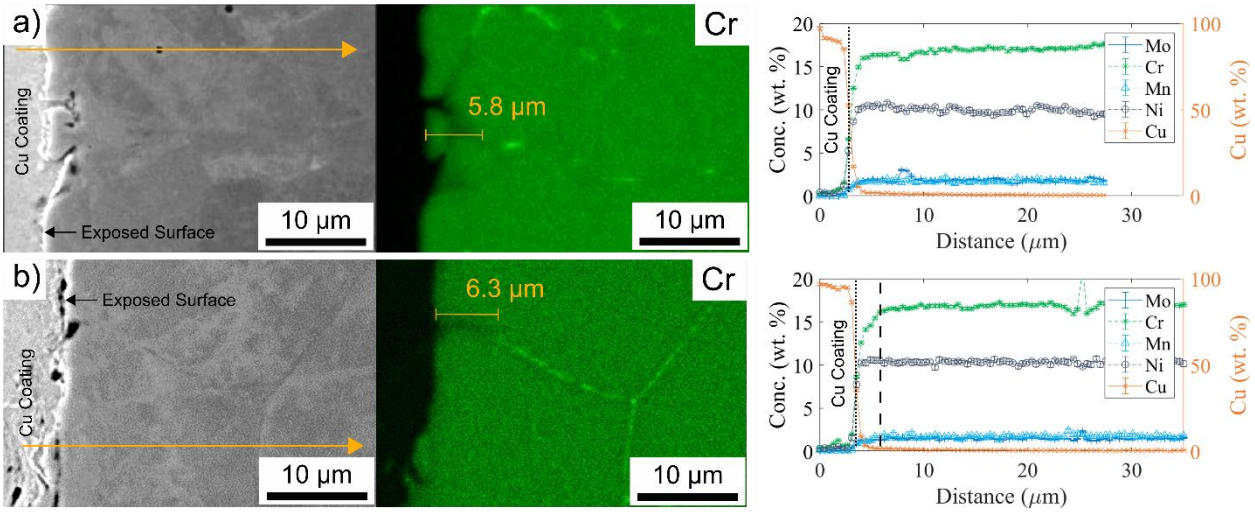

Figure 33. Cross-sectional EDS compositional analysis of (a) 316L and (b) 316H surfaces exposed to FLiNaK in pyrolytic boron nitride (PBN) capsules for 500 hours at 700 ˚C. A Cu coating was electroplated on the sample surface prior to mounting and polishing. Yellow arrow in the SEM image denotes the path of the EDS line scan.

Cross sections of 316L and 316H exposed in 316L capsules did not show aggressive Cr dissolution. There is minimal grain boundary Cr dissolution in both materials. EDS line-scans, however, reveal dissolution of Cr in the bulk grains. The depths of bulk grain Cr dissolution in 316L and 316H were 6.0 μm and 3.0 μm, respectively. While the measured depth of bulk grain Cr dissolution is different, it should be noted that the apparent concentration of Cr at the surface of each alloy decreased to different levels. The total Cr dissolved, therefore, may be approximately the same in both alloys. It is speculated that since 316L may have more prevalent grain boundaries than 316H, the Cr in 316L may be transported from the bulk more quickly via these faster diffusion paths. The effect of grain boundaries character will be investigated in Section 3.1.3.

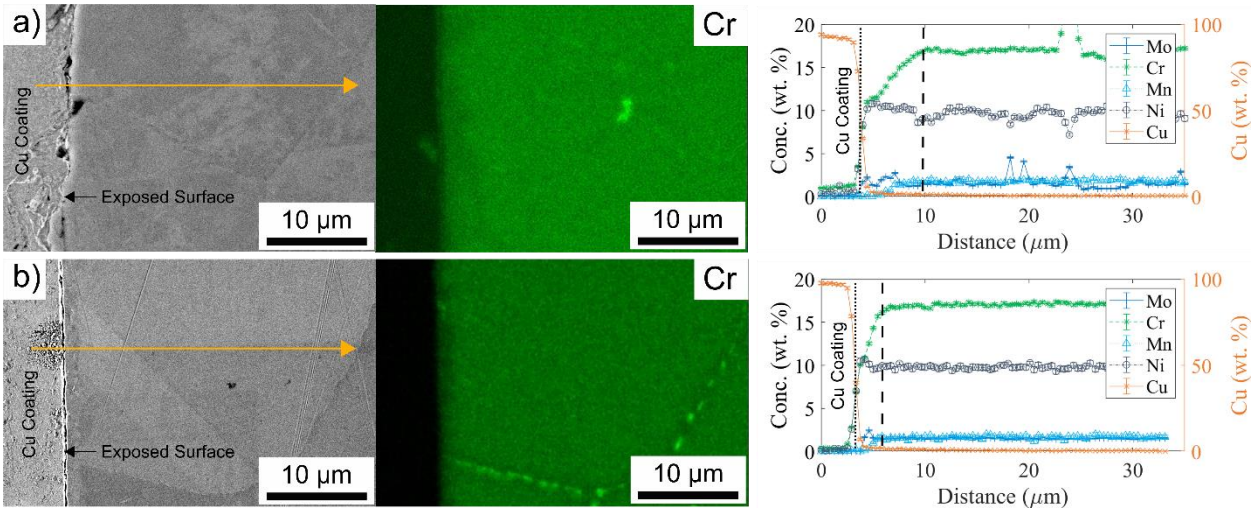

Figure 34. Cross-sectional EDS compositional analysis of (a) 316L and (b) 316H surfaces exposed to FLiNaK in 316L capsules for 500 hours at 700 ˚C. A Cu coating was electroplated on the sample surface prior to mounting and polishing. Yellow arrow in the SEM image denotes the path of the EDS line scan.

High magnification SEM images ans EDS point scans were performed on the stainless steels exposed in 316L capsules to investigate the small precipitate particles which were observed on the surface of the steels after salt exposure in these capsules. While accurate phase identification is challenging using SEM or XRD, the point scans over the particles reported between 8 and 12 wt. % Mo. Considering that the point scan also picks up the bulk material, it was concluded that these particles are molybdenum-rich phases.

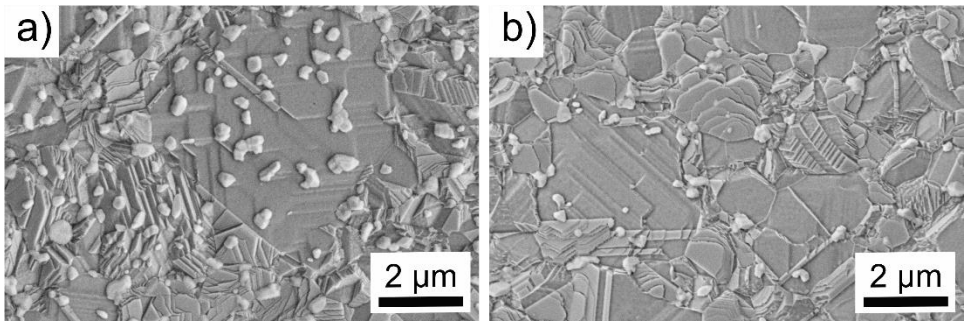

Figure 35. High magnification SEM images of the surface of (a) 316L and (b) 316H exposed to FLiNaK in 316L capsules for 500 hours at 700 ˚C.

In contrast to 316L capsules, 316L and 316H specimens exposed in glassy carbon capsules experience considerable dissolution of Cr along the grain boundaries only. In Figure 36, the EDS line scans show that there is minimal depth of bulk grain Cr depletion. Instead, there is extensive dissolution of Cr from the grain boundaries that leaves considerable sized voids in the near surface region. In 316L and 316H,

the depth of grain boundary Cr dissolution was 6.3 μm and 7.7 μm, respectively. One possible explanation for the higher weight loss in 316L is that the as-received material contains more salt facing grain boundaries than the 316H. Graphite is highly cathodic with respect to stainless steel [77]. The galvanic corrosion cell created by 316 stainless steel and glassy carbon may provide an additional driving force that could change the corrosion mechanism and or the corrosion rate of 316 stainless steel. 316 stainless steel corrosion mechanisms were investigated further using electrochemical methods in Section 3.3.

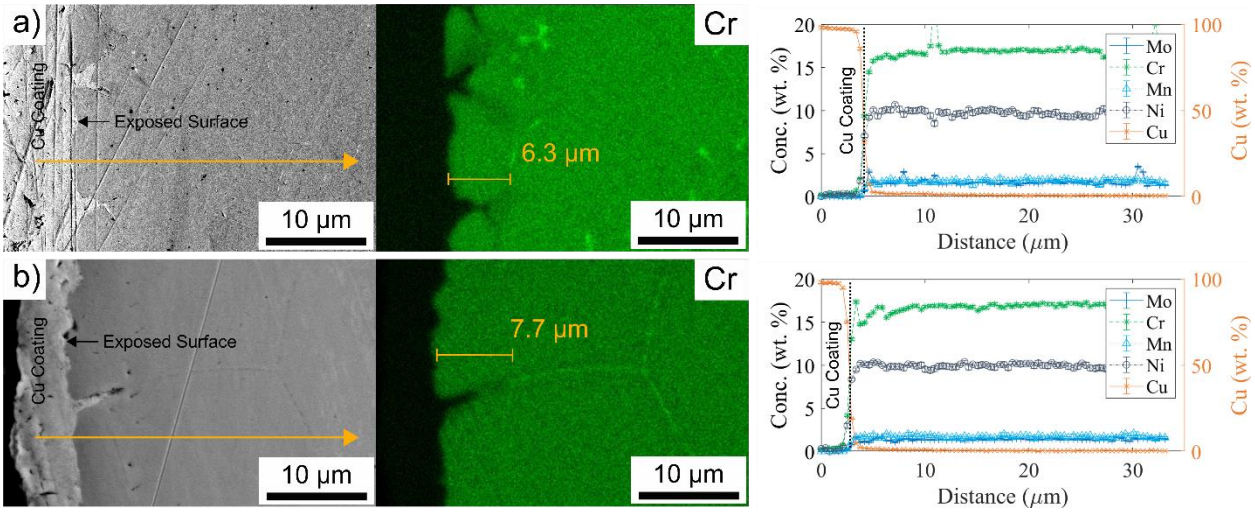

Figure 36. Cross-sectional EDS compositional analysis of (a) 316L and (b) 316H surfaces exposed to FLiNaK in glassy carbon capsules for 500 hours at 700 ˚C. A Cu coating was electroplated on the sample surface prior to mounting and polishing. Yellow arrow in the SEM image denotes the path of the EDS line scan.

3.1.2.4 XRD analysis of the corrosion surface

XRD was performed to identify the near-surface corrosion-induced phase changes in the alloy microstructure due to exposure to molten salt. Figure 37 shows XRD patterns for (a) 316L and (b) 316H both as-received and after exposure to PBN, 316L and glassy carbon. Both 316L and 316H showed strong (111), (200), (220), and (311) γ-austenite peaks corresponding to the face-centered-cubic (FCC) bulk material. To precisely calculate the lattice parameter, Bragg's Law was first used to calculate the d-pacing followed by calculation of lattice parameter for the individual γ-austenite peaks.

$$n\lambda = 2dsin\theta \tag{51}$$

The lattice parameters obtained from the (200), (220), and (311) γ-austenite and the Nelson-Riley extrapolation function ($\cos^2(\theta)/\sin(\theta) + \cos^2(\theta)/\theta$) were used to extrapolate to theta = 90 degrees to determine the accurate lattice parameter. In Figure 38, the lattice parameter is obtained from the y-intercept of the linear fit to the data. The lattice parameters of as-received 316L and 316H were 360.13 pm and 360.05 pm, respectively. According to Vegard's law, the lattice parameter of mixtures of two alloying elements is roughly approximated by the weighted mean of the two constituents' lattice parameters [123]. When Cr is depleted from the austenite matrix, the alloy's lattice parameter is expected to shrink, due to the depletion of Cr from the γ-austenite solid solution. The net change in lattice parameters of the exposed alloys were also calculated and are shown in Table 13. The lattice parameter of the γ-austenite phase decreases after exposure to molten salt because of out-diffusion of Cr from the alloy solid solution into the molten salt. This is consistent with the finding that the alloys experience some matrix Cr dissolution.

Both materials showed a faint peak around $2\theta = 45$ degrees corresponding to ferrite. It was concluded that the heats of steel naturally have some small amount of ferrite. The changes in the ferrite content of the alloys after exposure to molten salts remains a topic of ongoing investigation. It has been proposed that a austenite to ferrite transformation can occur by a vacancy injection mechanism due the excess vacancies created by the out-diffusion of Cr into the molten salt.

The signal strength of any Mo-rich phases were too weak to be observed above the background of the XRD pattern. It was therefore not possible to determine the exact phase or composition of the Mo-rich phases observed on the surface of 316L and 316H after exposure in 316L capsules.

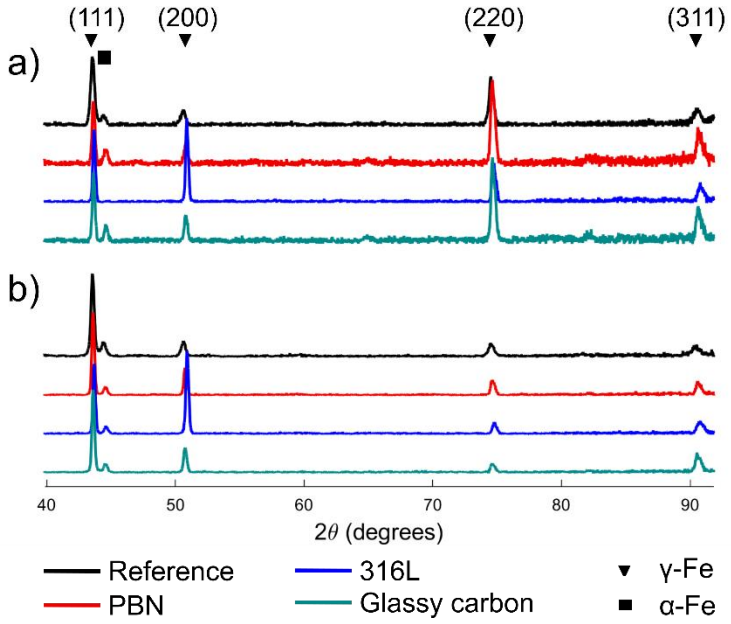

Figure 37. XRD patterns for (a) 316L and (b) 316H reference specimens and specimens exposed to FLiNaK in pyrolytic boron nitride (PBN), 316L, and glassy carbon capsules for 500 hours at 700 ˚C.

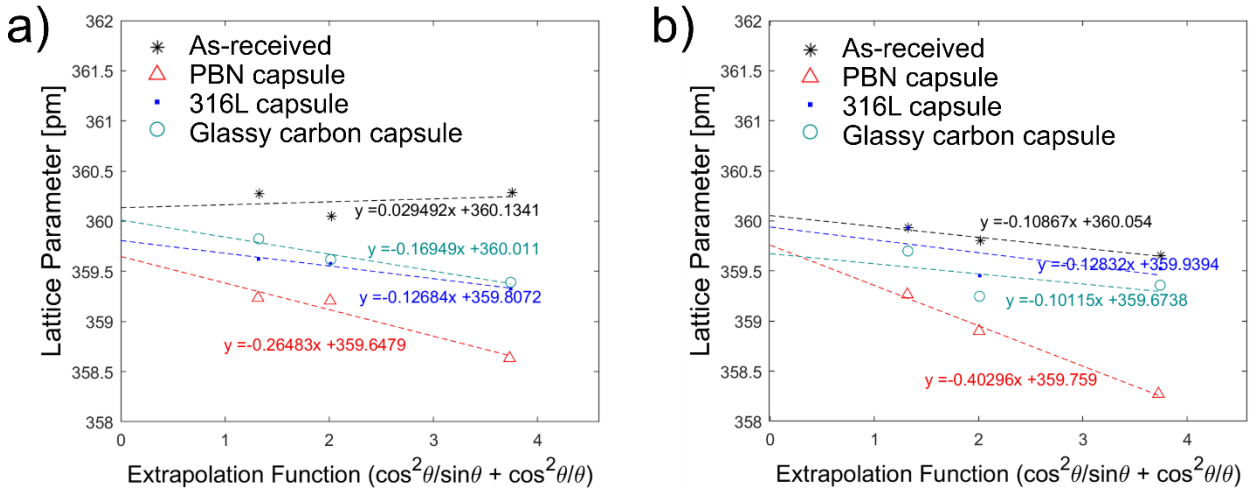

Figure 38. Calculated lattice parameter as a function of the Neslon-Riley extrapolation function $(\cos^2(\theta)/\sin(\theta) + \cos^2(\theta)/\theta)$ for (a) 316L and (b) 316H specimens exposed in different capsule materials.

Table 13. Net change in lattice parameter of 316L and 316H specimens exposed in pyrolytic boron nitride (PBN), 316L, and glassy carbon capsules measured by Nelson-Riley function extrapolation. Units are in pm.

Specimen	316L	316H
PBN	-0.49	-0.29
316L	-0.33	-0.11
Glassy Carbon	-0.12	-0.38

3.1.2.5 Salt Analysis

Salt chemistry analysis was performed using ICP-MS before and after exposure by the Wisconsin State Laboratory of Hygiene. The results for sulfur, chromium, and manganese are reported in Figure 39. In general, the sulfur concentration, which has been shown to adversely affect nickel-based alloys [124], did not change significantly during exposure to steels. The salts showed significant increases in Cr and Mn after exposure. The salts which contained 316L showed more Cr than their 316H counterparts. This is consistent with less corrosion in 316H compared to 316L. In salts tested in 316L capsules, there was a noticeable increase in Mn in the salt after exposure. It is believed that Mn is also corroded from the 316L capsules. The higher surface area to salt volume ratio means that there is a greater supply of Mn to the salt.

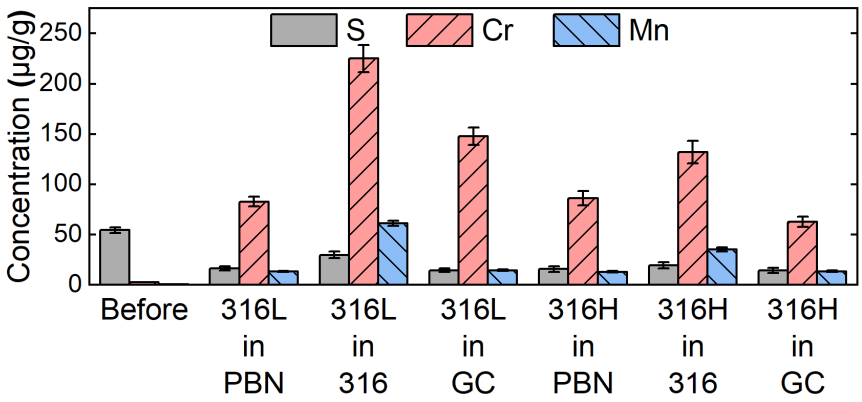

Figure 39. Concentration of trace impurities in FLiNaK salt before and after exposure to 316L and 316H stainless steel in pyrolytic boron nitride (PBN), 316 stainless steel (316L), and glassy carbon (GC) capsules for 500 hours at 700 ˚C.

3.1.2.6 Discussion

Comparison of the surface topography, composition, and near-surface microstructural changes of 316L and 316H specimens in different material capsules revealed striking differences between the corrosion mechanisms occurring in each capsule environment. Three quantifiable types of corrosion attack are observed in 316 stainless steels in molten fluoride salt environments: surface recession (uniform corrosion), preferential elemental dissolution within the bulk grains, and preferential elemental dissolution along grain boundaries. Table 14 summarizes the results obtained from this experiment. Total depth of corrosion is calculated by summing the measured surface recession and either the depth of grain boundary Cr dissolution or the depth of bulk grain Cr dissolution depending on which depth is greater. This metric is likely more useful for reactor design where ultimately the total material lost to corrosion is of most importance.

Table 14. Analysis of as-received 316L and 316H corrosion after exposure to FLiNaK for 500 hours at 700 ˚C in various capsule materials.

Specimen	Capsule	Weight Change (mg cm-2)	RMS Surface Roughness (μm)	Surface Recession (μm)	Depth of Grain Boundary Cr Dissolution (μm)	Depth of Bulk Grain Cr Dissolution (μm)	Total Depth of Corrosion (μm)	Types of Corrosion
316L	PBN	-1.5 ± 0.1	0.496	1.13	5.8	0.0	6.9	Surface recession & grain boundary Cr dissolution
316H	PBN	-1.5 ± 0.1	0.392	1.14	6.3	3.0	7.5	Surface recession & grain boundary Cr dissolution
316L	316L	-0.210 ± 0.002	0.049	ND	0.0	6.0	6.0	Bulk grain Cr dissolution*
316H	316L	-0.119 ± 0.001	0.041	ND	0.0	3.0	3.0	Bulk grain Cr dissolution*
316L	Glassy carbon	-2.0 ± 0.2	0.925	3.70	5.8	0.0	9.5	Surface recession & grain boundary Cr dissolution
316H	Glassy carbon	-1.7 ± 0.1	0.497	1.79	7.7	0.0	9.5	Surface recession & grain boundary Cr dissolution

*It was not possible to quantify surface recession

The capsule environment has an important effect on the dominant types of corrosion observed. The tendency towards grain boundary Cr dissolution as in the case of glassy carbon capsules could mean that grain boundaries become prone to stress corrosion cracking in the presence of tensile stress. Cr dissolution

via homogeneous diffusion through the bulk grains as in the case of 316 stainless steel capsules could lead to void formation in the bulk as a result of the Kirkendall effect [125]. The stainless steels exposed in PBN capsules show a combination of surface recession, preferential bulk grain Cr dissolution, and preferential grain boundary Cr dissolution. This indicates that PBN may be a promising capsule environment to study materials corrosion effects in isolation without significant capsule effects.

A collective examination of the above results suggests that corrosion performance of 316H is slightly superior to 316L by some metrics and quite comparable by others. This is of considerable significance to the MSR application, given that, of the two materials, only 316H is ASME codified and can be utilized for the manufacture of structural components of MSRs. A closer examination of individual metrics for corrosion of the two materials revealed subtle microstructural differences. For example, EDS spectral maps after extended exposure at 700 ˚C reveal that the grain boundaries of 316H contain more continuous and often thicker Cr-rich carbide precipitates at the grain boundaries. The formation of these carbides is promoted by higher carbon content augmented by sensitization effects at the test temperature. The average grain size of the two materials is also different, leading to some stochastic uncertainties. To further understand the corrosion phenomena, the as-received 316L and 316H stainless steels were heat-treated in a variety of ways and then subjected to similar corrosion tests.

3.1.3 Microstructural effects on corrosion of 316L & 316H in FLiNaK

To investigate the effect of microstructure on corrosion, a variety of microstructures were produced in these stainless steels by heat treating. The heat treatment parameters are summarized in Table 8. 316L Batch I was annealed at 1,100 ˚C for 20 minutes to produce a batch with comparable grain size to 316H. 316L batch II was heat treated at 700 ˚C for 24 hours to pre-sensitize the stainless steel prior to corrosion tests to investigate the effect of the presence of chromium carbide at the alloy grain boundaries on corrosion. In short, the latter experiment was performed to seek the net effects of the competition between the kinetics of sensitization and the corrosion rate of the stainless steels, given that sensitization would occur during the corrosion test. 316L batch III was annealed at 1,100 ˚C for 20 minutes and heat treated at 700 ˚C for 24 hours to both increase the grain size and pre-sensitize the material. 316H was heat treated at 700 ˚C for 24 hours to induce sensitization. Specimens were then exposed in PBN capsules for 500 hours at 700 ˚C.

3.1.3.1 Initial microstructure characterization

Figure 40 depicts polished and etched cross sections of the various 316L and 316H heat treatments. Annealing of 316L was performed at 1,100 ˚C for 20 minutes to induce grain growth from about 10 μm to about 70 μm. This was primarily done to make the grain size comparable for both stainless steels. Compared to the as-received or annealed specimens, the sensitized steel etched quickly, revealing the grain boundaries, implying that the local corrosion resistance of the alloy to aqueous corrosion (a form of etching) was reduced.

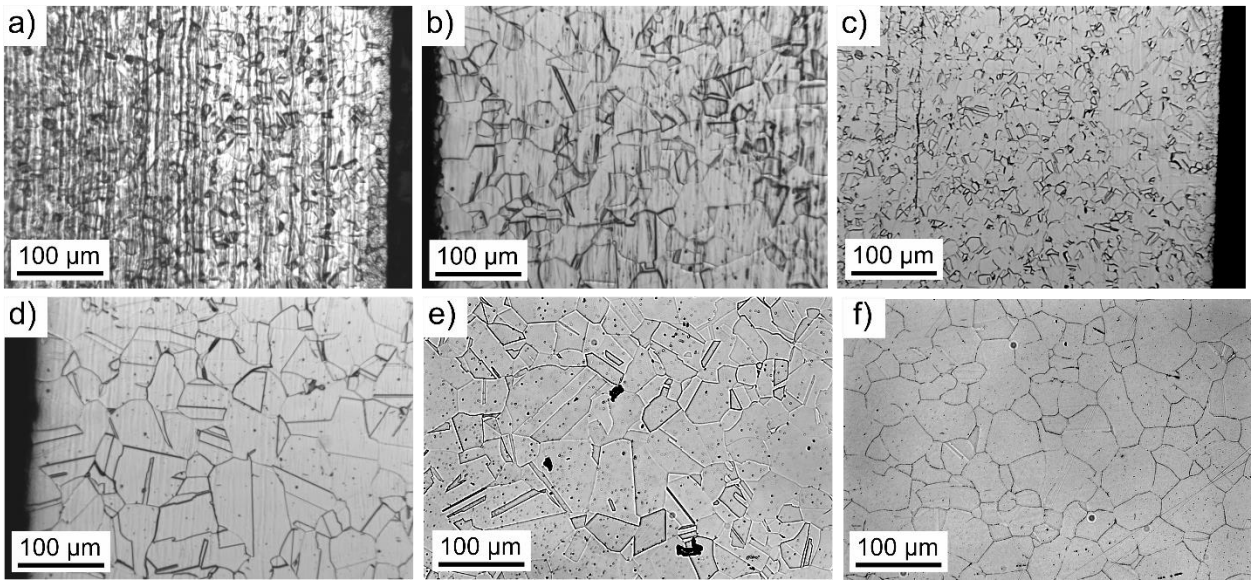

Figure 40. Optical cross section images of etched (a) 316L, (b) 316L annealed 20 minutes at 1,100 ˚C, (c) 316L sensitized 24 hours at 700 ˚C, (d) 316L annealed 20 min at 1,100 ˚C & sensitized 24 h at 700 ˚C, (e) 316H, and (f) 316H sensitized 24 h at 700 ˚C. Specimens are etched by swabbing with 3:1 (by volume) $HCl:HNO_3$ for 1 minute.

316H was pre-sensitized for 24 h at 700 ˚C. Figure 41 shows etched cross sections of as-received 316H, 316H that was sensitized, and as-received 316H after exposure to salt for 500 h at 700 ˚C. While minimal grain growth occurs at this temperature, the morphology of the grains changes slightly as the grain boundaries become sensitized.

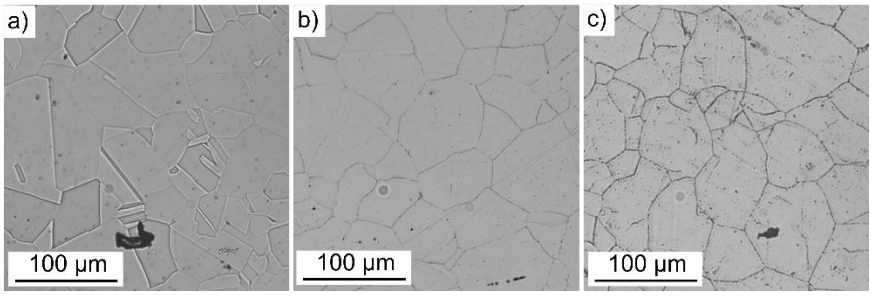

Figure 41. Optical images of etched (a) as-received 316H, (b) 316H sensitized for 24 h at 700 ˚C, and (c) as-received 316H after 500 h at 700 ˚C in FLiNaK. Etchant is aqua regia solution

3.1.3.2 Weight Change after exposure to molten FLiNaK

The weight change of the as-received and heat treated specimens are shown in Figure 42. In general, all 316L batches and the as-received 316H showed statistically the same weight change of about -1.5 ± 0.1 mg cm^{-2}. In the case of 316L neither the increase in grain size (reduction in total length of high angle

grain boundaries per volume) nor sensitization appeared to dramatically affect the corrosion. Sensitization of 316H, however, caused slightly higher weight change of -1.8 ± 0.1 mg cm^{-2} compared to the as-received 316H. The results indicate that, in this instance, the corrosion of 316L was not strongly dictated by the grain boundary character of the alloys. The higher carbon content could lead to greater sensitization effects in 316H and alter the transport of Cr along grain boundaries. Characterization, such as profilometry, SEM, and EDS, was needed to determine what the rate limiting corrosion step was in this instance.

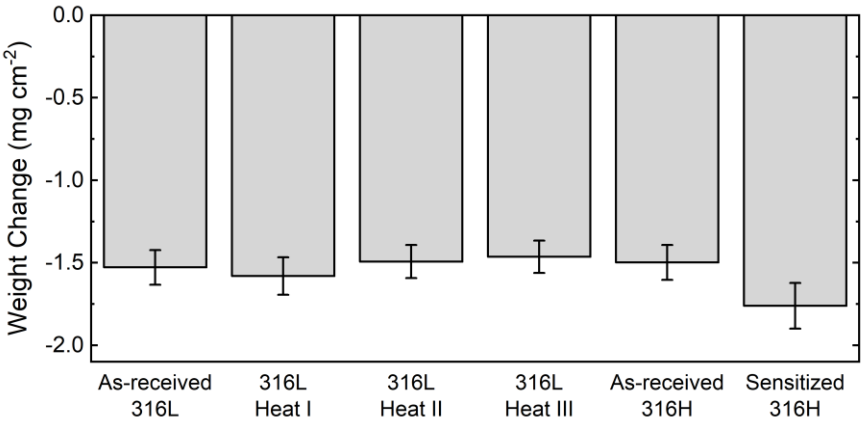

Figure 42. Weight change of as-received and heat treated 316L and 316H after exposure to FLiNaK for 500 hours at 700 ˚C in pyrolytic boron nitride (PBN).

3.1.3.3 Alloy surface morphology after molten salt exposure

Photographs of the as-received and heat treated 316L and 316H specimens before and after exposure in PBN capsules are shown in Figure 43. Much like the as-received stainless steels, the heat-treated specimens turned a dull grey color after exposure to molten salt. The top specimen in each chain of specimens was half submerged in the molten salt. This specimen shows a transition from the original polished surface to the corroded surface at the vapor-salt interface that was examined for surface recession.

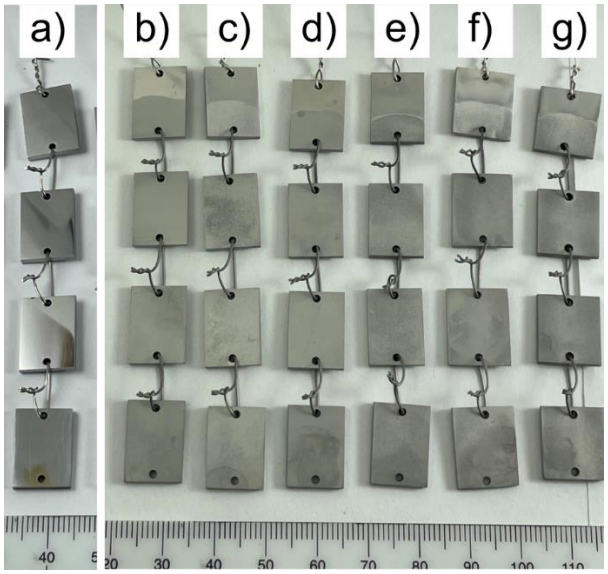

Figure 43. Photographs of (a) as-polished 316L and (b) 316L, (c) 316L batch I, (d) 316L batch II, (e) 316L batch III, (f) 316H, and (g) Sensitized 316H after exposure to molten FLiNaK for 500 hours at 700 ˚C in pyrolytic boron nitride (PBN) capsules.

SEM was used to study the surface morphology of the heat-treated steels after exposure. Figure 44 and Figure 45 show the heat treated 316L and 316H specimens, respectively. In all specimens, the corrosion has led to extensive grain boundary attack and general roughening of the surface. The difference in material grain size and prevalence of grain boundaries in each material can plainly be seen. Comparison of the as-received 316L and the 316L annealed for 20 minutes at 1,100 ˚C (batch I), in Figure 44(a) and (b) shows much less apparent grain boundary attack. Cross-sectional analysis was required to determine if there was a difference in the thickness of the specimen affected by corrosion. Less grain boundary attack is visible in the pre-sensitized 316L (batch II) than in the as-received 316L, suggesting that the kinetics of depletion of Cr into molten salt supersedes the kinetics of sensitization. The 316L that was both annealed and sensitized (batch III) appears to have the same level of grain boundary attack as the annealed 316L (batch I). Comparison of Figure 44(b) and Figure 45(a) shows that the grain size and grain boundary attack are comparable in annealed 316L and as-received 316H. Comparison the 316H samples from two conditions in Figure 45(a) and (b) suggests that pre-sensitization may have an effect on the width of the corroded grain boundary after exposure to molten FLiNaK for 500 hours, due to the preponderance of Cr-carbide phase at the grain boundary prior to the corrosion test. Comparison of the sensitized 316L and 316H also suggests

that sensitization affects the width of the corroded grain boundaries in 316H more than it does in 316L, an effect attributed to the larger quantity of chromium carbide accumulation at the grain boundaries in 316H.

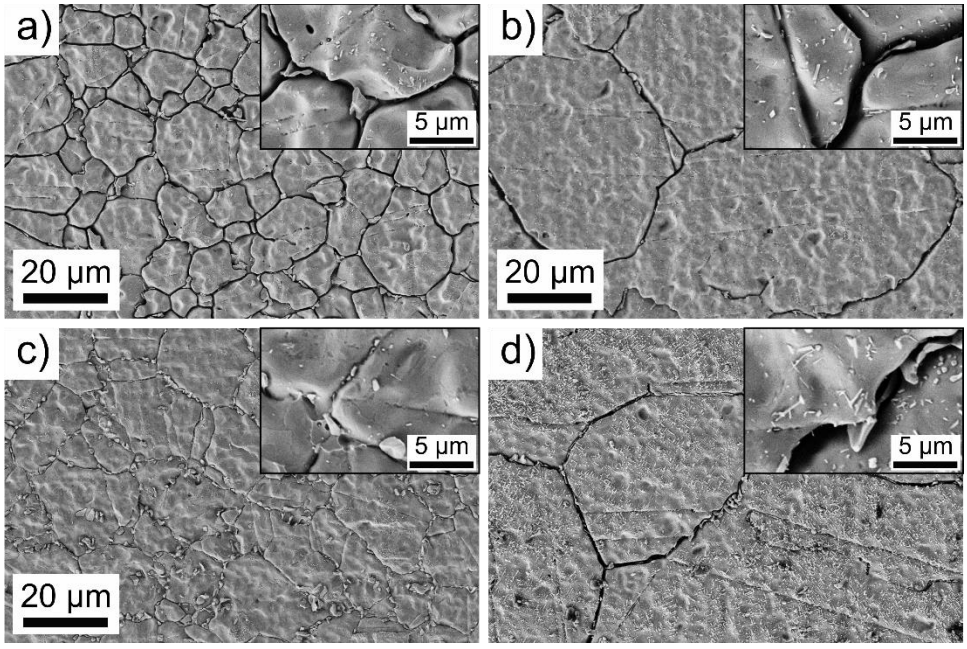

Figure 44. SEM images of the surface of (a) as-received 316L, (b) 316L batch I, (c) 316L batch II, and (d) 316L batch III after exposure to FLiNaK in pyrolytic boron nitride (PBN) capsules for 500 hours at 700 ˚C.

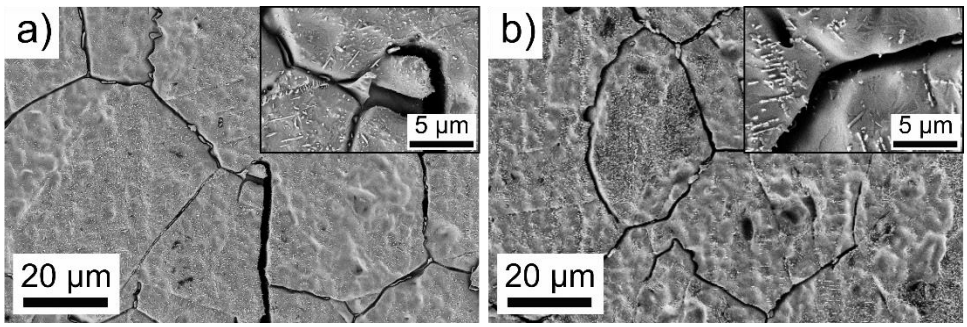

Figure 45. SEM images of the surface of (a) as-received 316H and (b) pre-sensitized 316H after exposure to FLiNaK in pyrolytic boron nitride (PBN) capsules for 500 hours at 700 ˚C.

The surface roughness of the heat-treated steels after exposure to molten FLiNaK was quantified with profilometry in Figure 46 and Figure 47. The RMS roughness of as-received 316L, the annealed 316L (batch I), the pre-sensitized 316L (batch II), and the annealed and pre-sensitized 316L (batch III) were 0.496 µm, 0.476 µm, 0.432 µm, and 0.375 µm, respectively. The roughness of as-received 316H and pre-sensitized 316H were 0.392 µm, 0.541 µm, respectively. While not a direct measurement of the amount

of grain boundary attack, specimens that showed more severe grain boundary attack have on average higher roughness than specimens with less grain boundary attack.

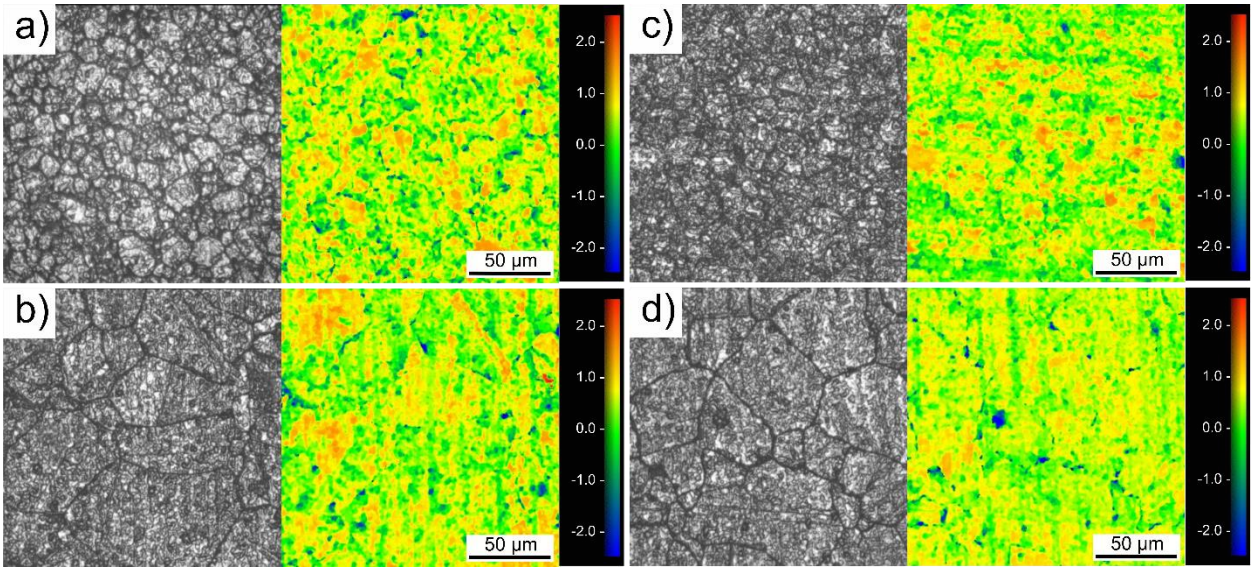

Figure 46. Profilometry of the surface of (a) as-received 316L, (b) 316L annealed for 20 minutes at 1,100 ˚C (batch I), (c) 316L sensitized for 24 hours at 700 ˚C (batch II), and (d) 316L annealed for 20 minutes at 1,100 ˚C (batch III), and sensitized for 24 hours at 700 ˚C after exposure to FLiNaK for 500 hours at 700 ˚C in PBN capsules (units are µm).

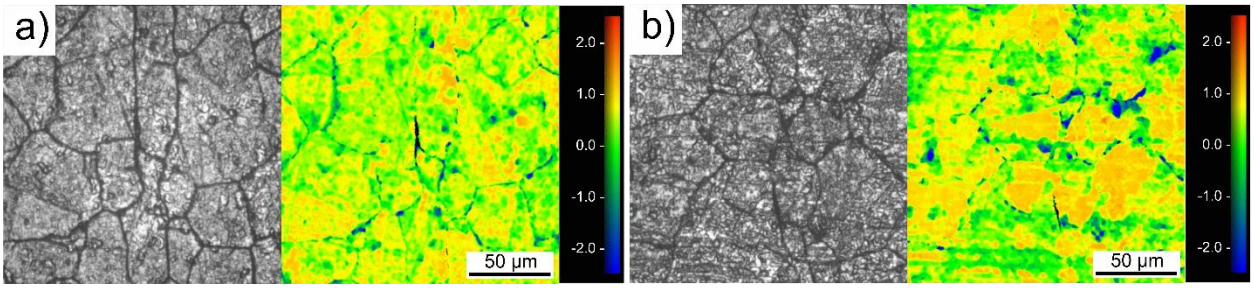

Figure 47. Profilometry of the surface of (a) as-received 316H, and (b) 316H sensitized for 24 hours at 700 ˚C after exposure to FLiNaK for 500 hours at 700 ˚C in PBN capsules (units are µm).

Profilometry was used to measure the surface topography of the vapor-salt interface on specimens of as-received and heat-treated steel specimens that were half submerged in PBN. Figure 48 and Figure 49 show maps of the vapor-salt interface. Again, the amount of surface recession is measured using vertical slices of the topographical map. The height of the three slices in the vapor and the salt regions are averaged and the surface recession is calculated by taking the difference in height between the two regions. The average height of the salt exposed region is indicated by the dotted line in the plots. The surface recession

of as-received 316L, the annealed 316L (batch I), the pre-sensitized 316L (batch II), and the annealed and pre-sensitized 316L (batch III) were 1.13 μm, 1.35 μm, 0.92 μm, and 0.92 μm, respectively. These results suggest that even in the low carbon 316L stainless steel, pre-sensitization is beneficial for corrosion resistance. The surface recession of as-received 316H and sensitized 316H were 1.14 μm, 1.05 μm, respectively. Here again pre-sensitization reduces surface recession. The results also show that for the same grain size, 316H still exhibits lower surface recession than 316L. The surface recedes more quickly than preferential grain boundary Cr dissolution. The surface recession of the annealed 316L and the annealed and sensitized 316L are similar.

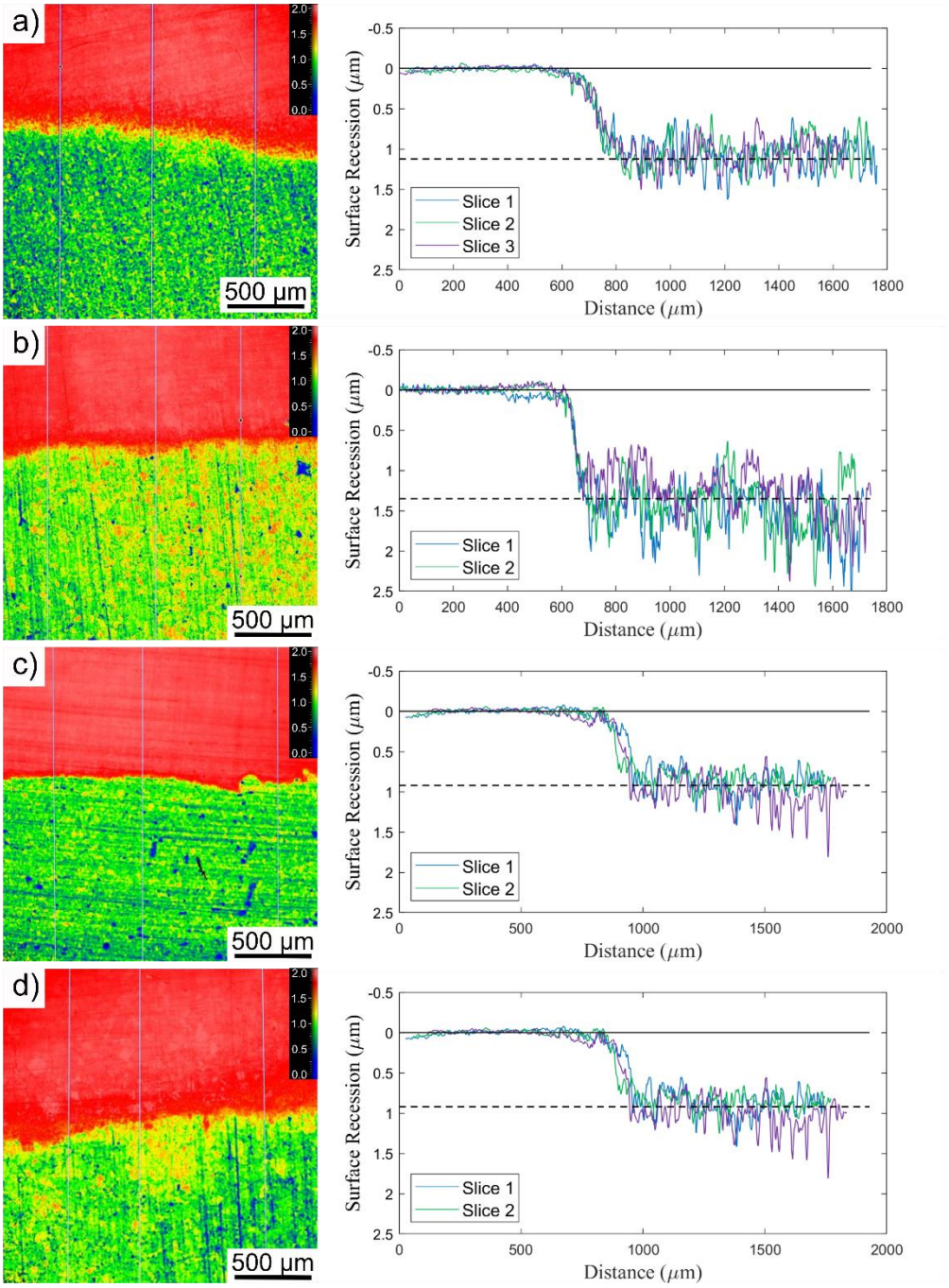

Figure 48. Profilometry topographical maps and linear slice plots of the salt-vapor interface of (a) as-received 316L, (b) 316L annealed for 20 minutes at 1,100 ˚C (batch I), (c) 316L sensitized for 24 hours at 700 ˚C (batch II), and (d) 316L annealed for 20 minutes at 1,100 ˚C and sensitized for 24 hours at 700 ˚C (batch III) after exposure to FLiNaK for 500 hours at 700 ˚C in PBN capsules (units are µm).

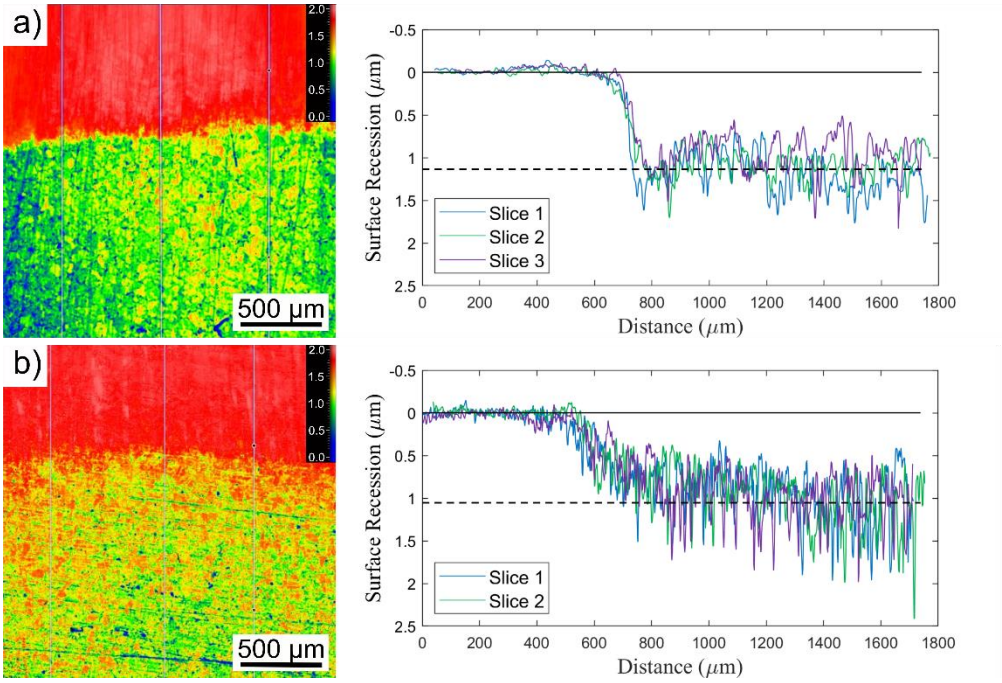

Figure 49. Profilometry topographical maps and linear slice plots of the salt-vapor interface of (a) as-received 316H, and (b) 316H sensitized for 24 hours at 700 ˚C after exposure to FLiNaK for 500 hours at 700 ˚C in PBN capsules (units are µm).

3.1.3.4 Elemental analysis of the corrosion surface

Compositional changes in the surface of the heat-treated 316L and 316H specimens exposed in the PBN capsules were initially evaluated using EDS area average composition scans of the specimen surfaces. Figure 50 shows the net change in average composition of the specimen surfaces after exposure in PBN capsules. The reference composition is the corresponding as-received 316L or 316H before exposure. The heat-treated alloys show comparable changes in surface elemental composition. The sensitized 316L (batch II) showed slightly higher Cr loss on average than the other steels. It is speculated that the higher prevalence of grain boundaries and pre-sensitization may lead to increased Cr transport to the surface of the sensitized 316L. The net change in Cr concentration in the sensitized 316H was not significantly different than the as-received 316H after exposure. Specimens with comparable grain size all showed similar net changes in surface Cr concentration. It should be noted that the decrease in surface Cr concentration may not necessarily correlate to surface recession discussed earlier.

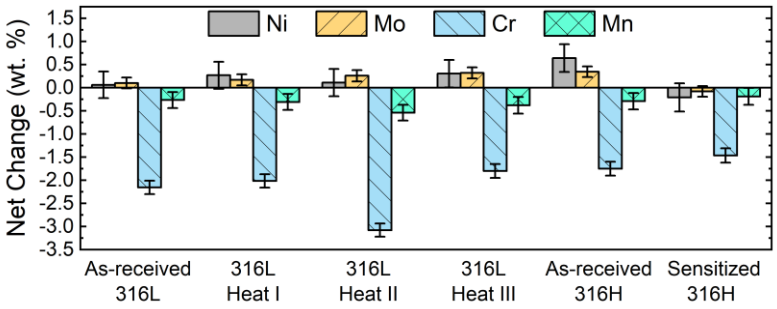

Figure 50. EDS large area average compositional analysis showing the net change in composition of as-received and heat treated 316L and 316H specimens after exposure to FLiNaK salt in pyrolytic boron nitride (PBN) capsules for 500 hours at 700 ˚C. Iron makes up the balance of the composition.

EDS cross-sectional analysis was performed to determine the most dominant types of corrosion attack occurring in each heat treated specimen. Figure 51 shows the EDS spectral maps of the distribution of Cr in the near surface region and a line scan of the bulk grains for the 316L specimens. The grain boundary Cr dissolution in as-received 316L, the annealed 316L (batch I), the sensitized 316L (batch II), and the annealed and sensitized 316L (batch III) were 5.8 μm, 10.0 μm, 6.4 μm, and 6.4 μm, respectively. The annealed 316L (batch I) was the only 316L heat that showed considerable Cr dissolution in the grains. The depth of bulk grain dissolution for batch I was 4.0 μm. It is possible that the measurement of bulk grain boundary Cr dissolution may be affected by the prevalence of Cr deficient grain boundaries near the surface. The combination of the higher, surface recession and grain boundary Cr dissolution suggest that for similar grain sizes the performance of 316H is superior to 316L.

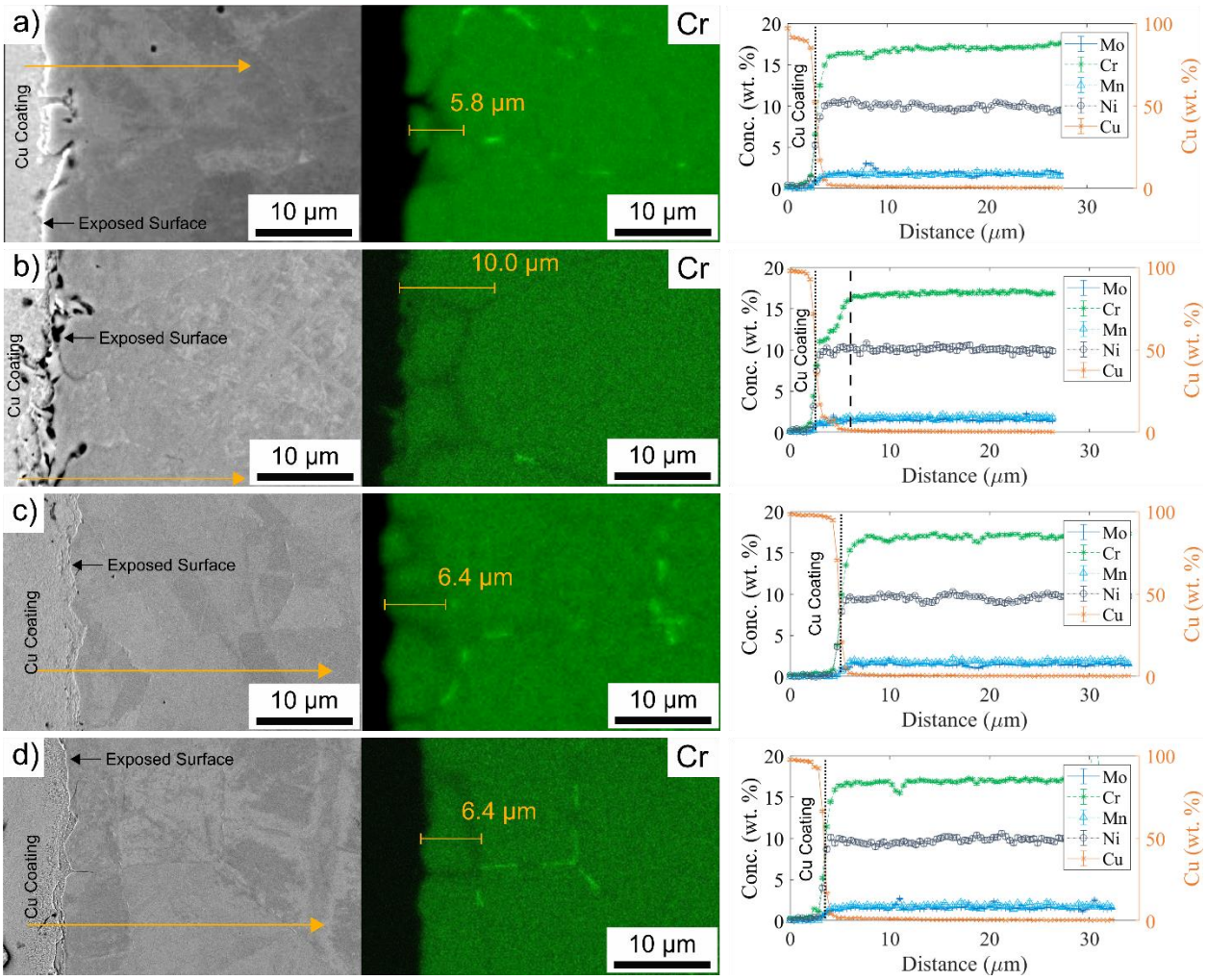

Figure 51. Cross-sectional EDS compositional analysis of (a) as-received 316L, (b) 316L annealed for 20 minutes at 1,100 ˚C (batch I), (c) 316L sensitized for 24 hours at 700 ˚C (batch II), and (d) 316L annealed for 20 minutes at 1,100 ˚C and sensitized for 24 hours at 700 ˚C (batch III) exposed to FLiNaK in pyrolytic boron nitride (PBN) capsules for 500 hours at 700 ˚C. A Cu coating was electroplated on the sample surface prior to mounting and polishing. Yellow arrow in the SEM image denotes the path of the EDS line scan.

Unlike the as-received 316H, the sensitized 316H did not show bulk grain Cr dissolution in Figure 52(b). The measured depths of grain boundary Cr dissolution for as-received 316H and sensitized 316H were 6.3 μm and 3.8 μm, respectively. While the depths of grain boundary attack are similar, the width of the corroded grain boundary is much larger in the sensitized 316H than in the as-received 316H. This suggests a difference in initial corrosion mechanisms or reaction kinetics occurring in grain boundaries when the grain boundaries initially contain more chromium carbide.

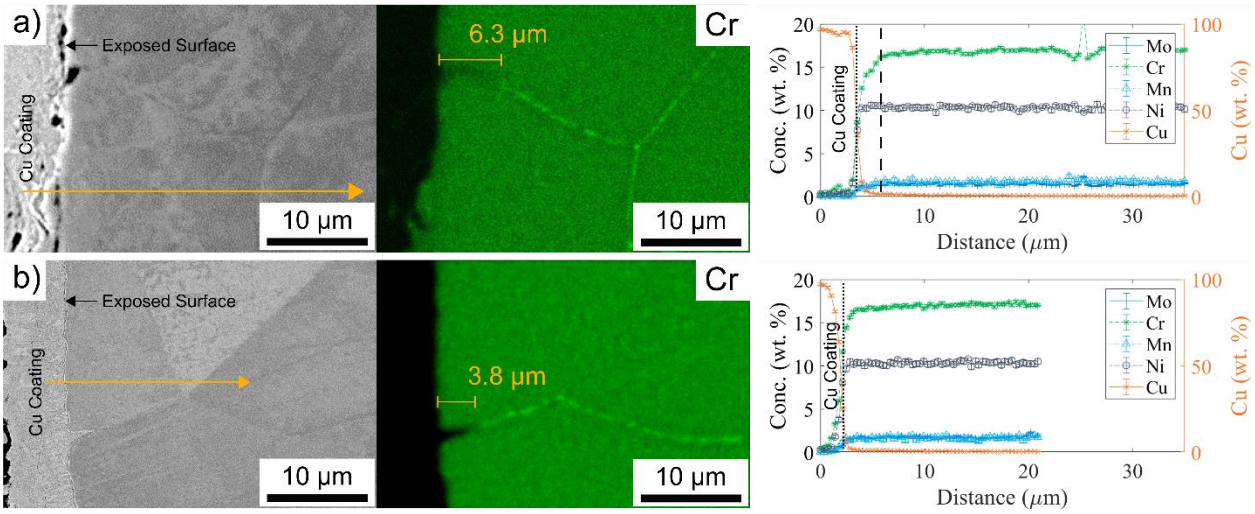

Figure 52. Cross-sectional EDS compositional analysis of (a) as-received 316H, and (b) sensitized 316H exposed to FLiNaK in pyrolytic boron nitride (PBN) capsules for 500 hours at 700 ˚C. A Cu coating was electroplated on the sample surface prior to mounting and polishing. Yellow arrow in the SEM image denotes the path of the EDS line scan.

3.1.3.5 Salt Analysis

Salt chemistry analysis using ICP-MS showed no differences in trends in alloying elements that were dissolved heat-treated stainless steels compared to the as-received stainless steels. Figure 53 shows the results for sulfur, chromium, and manganese. The concentration of chromium and manganese increased in each capsule salt. The concentration of chromium and manganese in the salts were all approximately the same. This was a good indicator that the salt environment was consistent in each capsule.

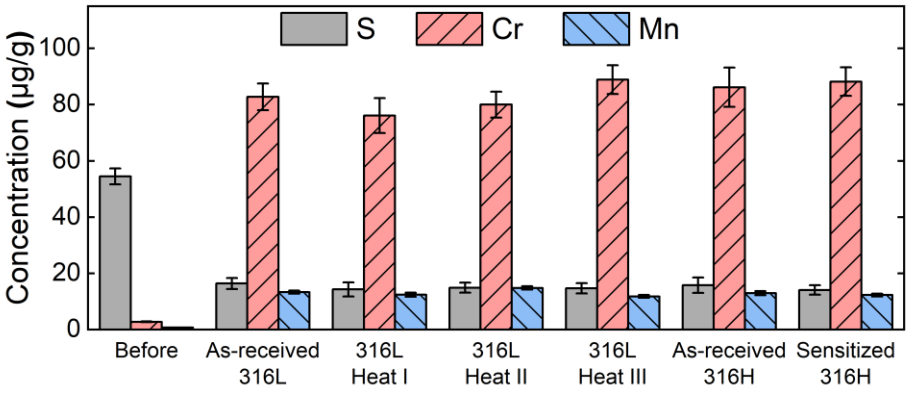

Figure 53. Concentration of trace impurities in FLiNaK salt before and after exposure to as-received and heat treated 316L and 316H for 500 hours at 700 ˚C in pyrolytic boron nitride (PBN).

3.1.3.6 Discussion

The results of annealed and pre-sensitized 316L and 316H indicate that these modifications to the microstructure do not significantly alter the magnitude of corrosion, although they affect the corrosion mechanism. Table 15 summarizes of each type of corrosion observed: surface recession (uniform corrosion), preferential elemental dissolution within the bulk grains, and preferential elemental dissolution along grain boundaries. In PBN capsules, the amount of surface recession of the steels was consistent. The annealed 316L with larger grain size showed the highest surface recession. The sensitized versions of 316L and 316H all showed lower surface recession than the as-received steels. Grain boundary Cr dissolution was the most significant type of corrosion attack in each stainless steel. The annealed 316L specimen again showed the highest depth of grain boundary Cr dissolution due to the direct path offered by the grain boundaries in larger grained materials, compared to the smaller grained materials.

The experiment illustrates the complicated relationship between the weight change and the total depth of corrosion (i.e. the unusable material thickness). The weight change of the heat-treated 316L specimens were all the same, however there were significant differences in surface recession and depth of grain boundary Cr dissolution. In the case of as-received and heat treated 316H, the total depth of corrosion attack was marginally higher for as-received 316H but the sensitized specimen lost more weight. Here it seems that the character of grain boundaries initially containing large amounts of chromium carbide influences the depth and width of the depleted grain boundaries. The kinetics of chromium and chromium carbide corrosion are no doubt different and as a result a different surface morphology may arise if the salt facing material is sensitized prior to exposure to molten salt.

Table 15. Analysis of heat treated 316L and 316H corrosion after exposure to FLiNaK for 500 hours at 700 ˚C in PBN capsules.

Specimen	Capsule	Weight Change (mg cm^{-2})	RMS Surface Roughness (μm)	Surface Recession (μm)	Depth of Grain Boundary Depletion (μm)	Depth of Bulk Grain Cr Dissolution (μm)	Total Depth of Corrosion (μm)	Type of Corrosion
316L	PBN	-1.5 ± 0.1	0.496	1.13	5.8	0.0	6.9	Surface recession & grain boundary Cr dissolution
316L batch I	PBN	-1.5 ± 0.1	0.476	1.35	10.0	4.0	11.4	Surface recession & grain boundary Cr dissolution
316L batch II	PBN	-1.5 ± 0.1	0.432	0.92	6.4	0.0	7.4	Surface recession & grain boundary Cr dissolution
316L batch III	PBN	-1.5 ± 0.1	0.375	0.92	6.4	0.0	7.3	Surface recession & grain boundary Cr dissolution
316H	PBN	-1.5 ± 0.1	0.392	1.14	6.3	3.0	7.5	Surface recession & grain boundary Cr dissolution
Pre-sensitized 316H	PBN	-1.8 ± 0.1	0.541	1.05	3.8	0.0	4.9	Surface recession & grain boundary Cr dissolution

3.1.4 Corrosion resistance of 16-8-2 weld material in FLiNaK

Appropriate welding materials and methods for 316H stainless steel will be required for the construction of MSR. 16-8-2 weld material is a candidate welding filler material for joining 316H stainless steel. Although the material is code qualified and has a composition very close to that of 316H, its corrosion behavior in molten fluoride salts is not understood. It is therefore necessary to test the corrosion resistance of 16-8-2 in molten fluoride salts. To accomplish this, specimens entirely made from 16-8-2 and 316H were procured. As described in Section 2.3.3, the 16-8-2 material was deposited on top of a 316H substrate to a thickness sufficient to make coupons entirely out of the filler rod material that did not contain the heat affected zone between the weld and the 316H substrate. This enabled separate effects tests to be conducted on the weld material without the influence of the substrate material. The substrate and weld material were exposed to molten FLiNaK salt for 500 hours at 700 ˚C in PBN capsules. Following exposure, weight change, microstructural and compositional analysis were performed on the weld and substrate materials to understand their corrosion behavior.

3.1.4.1 Initial microstructure characterization

After polishing to 1200 grit, the 316H substrate and 16-8-2 weld specimens were examined with SEM and EDS to analyze their composition and microstructure. EDS area averages showed that the alloys were within the specification of the alloy composition, however, inhomogeneity was observed in the 16-8-2 weld specimens. Figure 54 shows SEM and EDS compositional maps of the as-polished 316H substrate and 16-8-2 weld specimens. The 316H substrate was very homogeneous. The 16-8-2 weld, on the other hand, showed variations in composition across the surface, most noticeably in the Cr and Ni concentrations. The effect of this compositional inhomogeneity on corrosion was investigated.

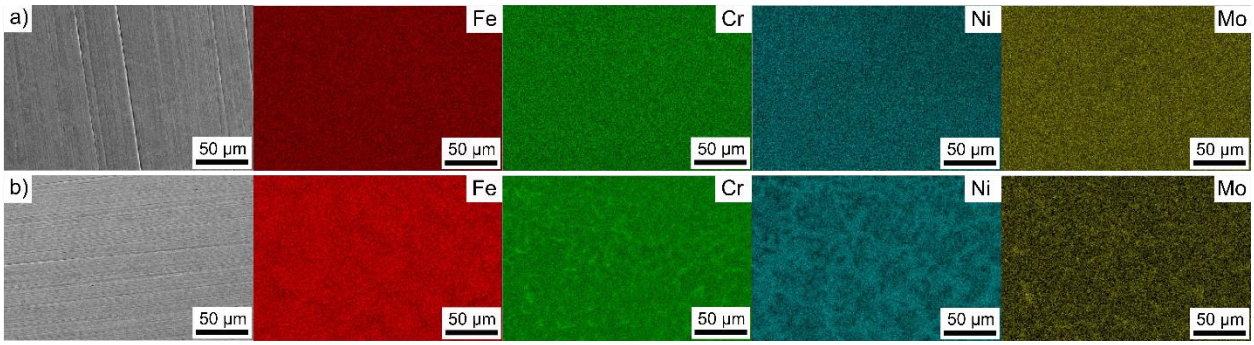

Figure 54. SEM and EDS compositional maps of as-polished (a) 316H substrate and (b) 16-8-2 weld specimen surfaces.

3.1.4.2 Weight Change after exposure to molten FLiNaK

Both the 316H substrate and the 16-8-2 weld material lost weight when exposed to FLiNaK. Figure 55 summarizes the weight changes during these exposure tests. The weight changes of the 316H substrate and the 16-8-2 weld were -1.6 ± 0.1 mg cm^{-2} and -2.6 ± 0.3mg cm^{-2}, respectively. The weld lost significantly more weight than the 316H substrate despite having a slightly lower chromium concentration.

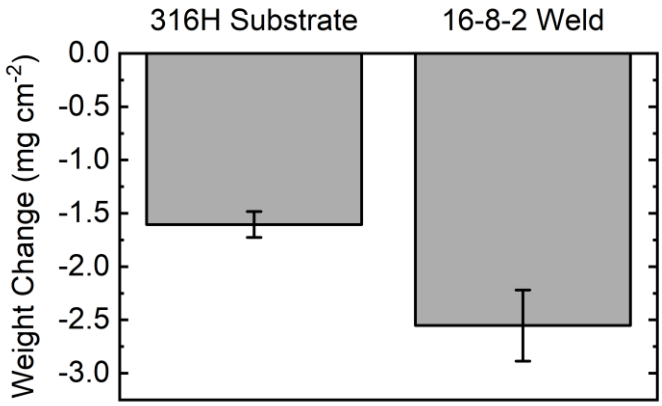

Figure 55. Weight change for 316H substrate and 16-8-2 weld specimens after exposure to FLiNaK for 500 hours at 700 ˚C in pyrolytic boron nitride (PBN) capsules.

3.1.4.3 Alloy surface morphology after molten salt exposure

Photographs of the 316H substrate and 16-8-2 weld specimens before and after exposure in PBN capsules are shown in Figure 56. The specimens turned a dull grey color after exposure to the molten salt. The top specimen in each chain of specimens was half submerged in the molten salt. This specimen shows

a transition from the original polished surface to the corroded surface at the vapor-salt interface that was examined for surface recession.

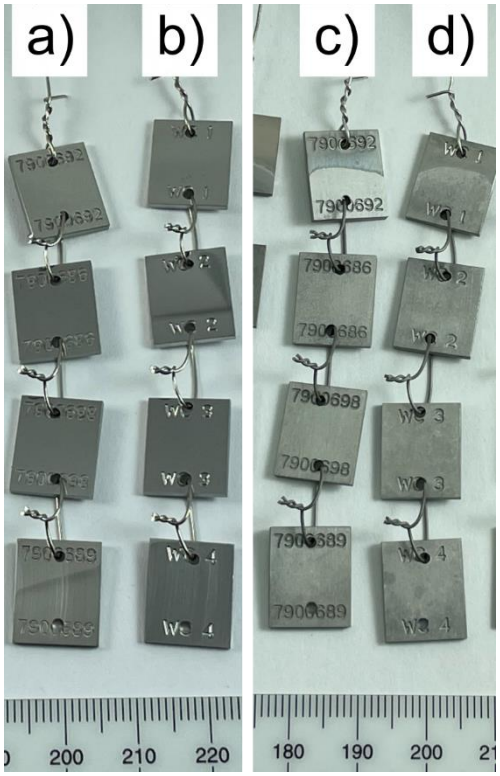

Figure 56. SEM images for (a)(c) 316H substrate and (b)(d) 16-8-2 weld specimens (a)(b) before and (c)(d) after exposure to FLiNaK for 500 hours at 700 ˚C in pyrolytic boron nitride (PBN) capsules.

The surface morphology of the 316H substrate and 16-8-2 weld specimens after exposure was examined with SEM as shown in Figure 57. The corrosion led to grain boundary attack and general roughening of the surface. The surface roughening was measured using profilometry in Figure 58. The RMS roughness of the 316H substrate and 16-8-2 weld specimens were 0.338 μm and 0.386 μm, respectively.

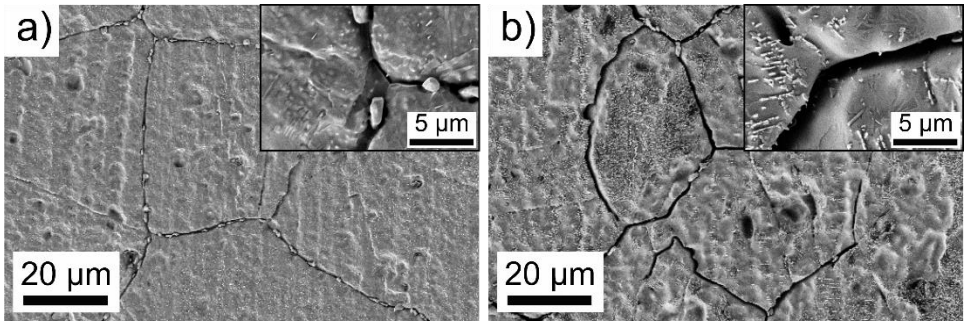

Figure 57. SEM images for (a) 316H substrate and (b) 16-8-2 weld specimens after exposure to FLiNaK for 500 hours at 700 ˚C in pyrolytic boron nitride (PBN) capsules.

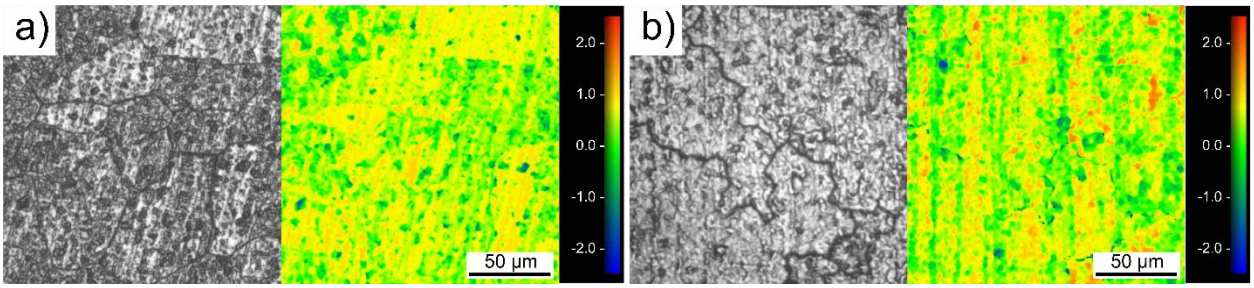

Figure 58. Profilometry of the surface of (a) 316H substrate and (b) 16-8-2 weld specimens after exposure to FLiNaK for 500 hours at 700 ˚C in pyrolytic boron nitride (PBN) capsules.

Profilometry was used to measure the surface topography of the vapor-salt interface on the 316H substrate and 16-8-2 weld specimens that were half submerged, using the procedures discussed earlier. Figure 59 shows topographical maps of the vapor-salt interface. The average height of the salt exposed region is indicated by the dotted line in the plots. The surface recession of the 316H substrate and the 16-8-2 weld were 0.80 µm and 1.70 µm, respectively. 16-8-2 experienced more than twice the amount of surface recession as the 316H substrate. This largely explains why 16-8-2 experienced a higher weight loss compared to the 316H substrate and underscores the importance of measuring surface recession.

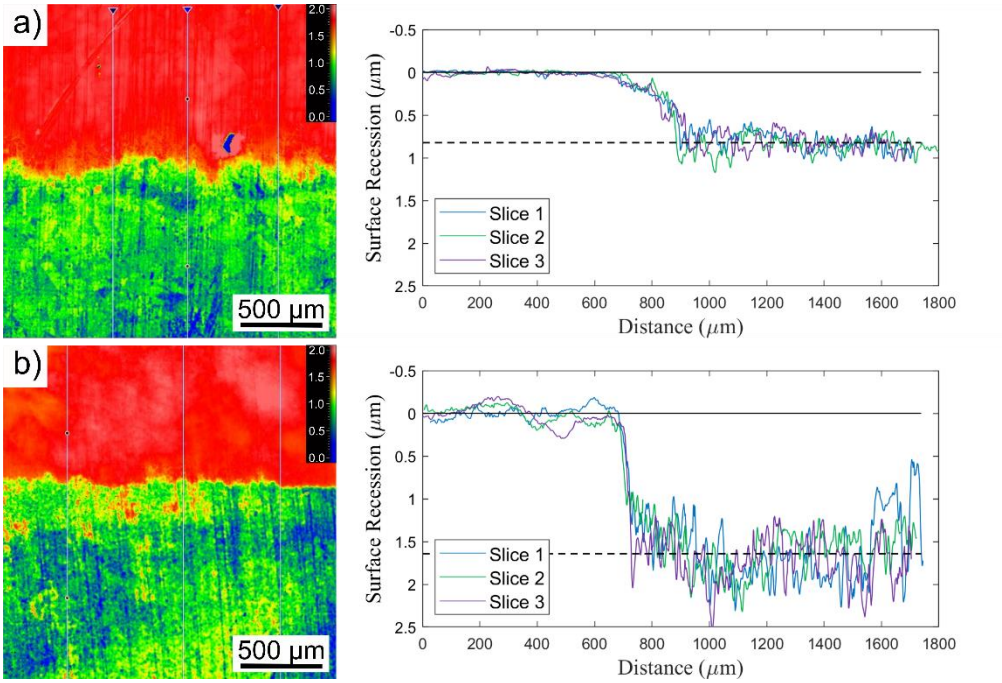

Figure 59. Profilometry topographical maps and linear slice plots of the salt-vapor interface of (a) 316H substrate and (b) 16-8-2 weld specimens after exposure to FLiNaK for 500 hours at 700 ˚C in pyrolytic boron nitride (PBN) capsules.

3.1.4.4 Elemental analysis of the corrosion surface

Compositional changes in the surface of the 316H substrate and 16-8-2 weld specimens were evaluated using EDS area average composition scans of the specimen surfaces. Figure 60 shows the as-received composition and the net change in average composition of the two materials after exposure. The 16-8-2 weld specimen showed higher net loss of chromium than the 316H substrate despite having a lower initial concentration of chromium.

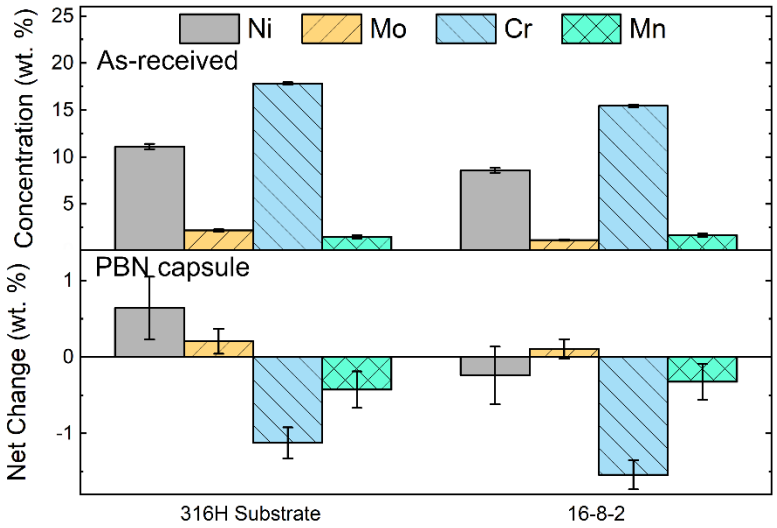

Figure 60. EDS large area average compositional analysis of the 316H substrate and 16-8-2 weld specimens and the net change in composition after exposure to FLiNaK salt in PBN capsules for 500 hours at 700 ˚C. Iron makes up the balance of the composition.

EDS cross-sectional analysis was performed to determine the most dominant types of corrosion attack occurring in the 316H substrate and 16-8-2 weld specimens. Figure 61 shows the EDS spectral maps of the distribution of Cr in the near surface region and a line scan of the bulk grains. Grain boundary Cr dissolution was only evident in the Cr spectral maps for 316H which was depleted to a depth of 4.6 μm. Neither material showed appreciable bulk grain Cr dissolution in the line scan data. While 16-8-2 did not show appreciable signs of preferential element dissolution, the distribution of alloying elements in the cross section was also not homogeneous. Figure 62 shows, a lower magnification EDS spectral map of the corroded 16-8-2 weld specimen that depicts compositional banding, particularly in the nickel concentration. Some correlation between the topography of the specimen and the apparent nickel concentration oscillations at the specimen surface was observed. In Figure 62, the white arrows indicate regions where the surface nickel concentration is relatively high due to the compositional banding. These regions of the cross section are slightly thicker than the regions which contain less nickel. This was an indication that surface recession and possibly chromium dissolution is highly dependent on the local concentration of nickel in the surface.

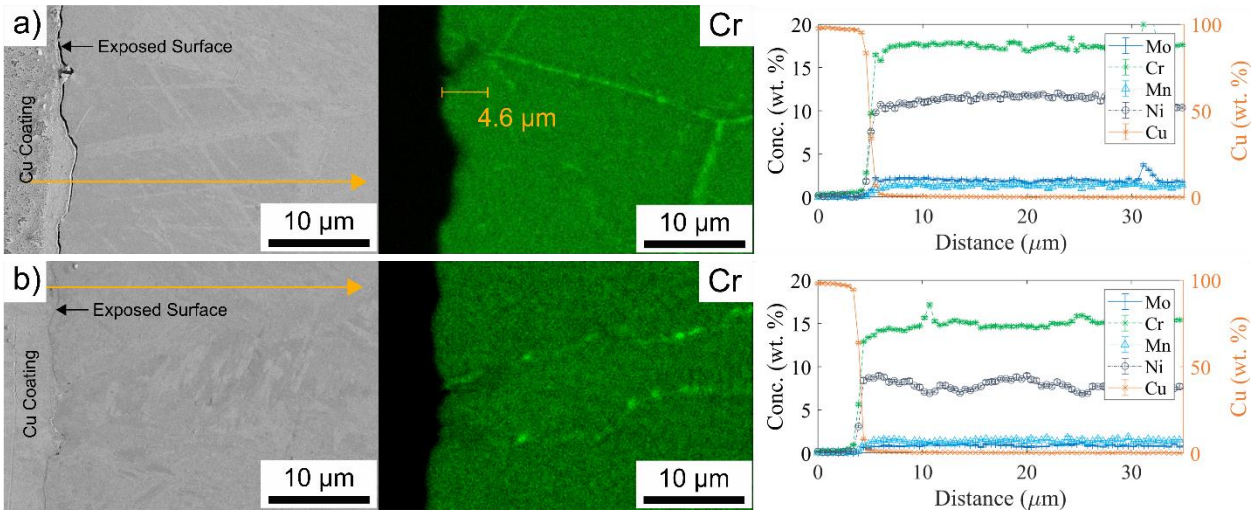

Figure 61. Cross-sectional EDS compositional analysis of (a) 316H substrate and (b) 16-8-2 weld specimens exposed to FLiNaK in pyrolytic boron nitride (PBN) capsules for 500 hours at 700 ˚C. A Cu coating was electroplated on the sample surface prior to mounting and polishing. The yellow arrow in the SEM image denotes the path of the EDS line scan.

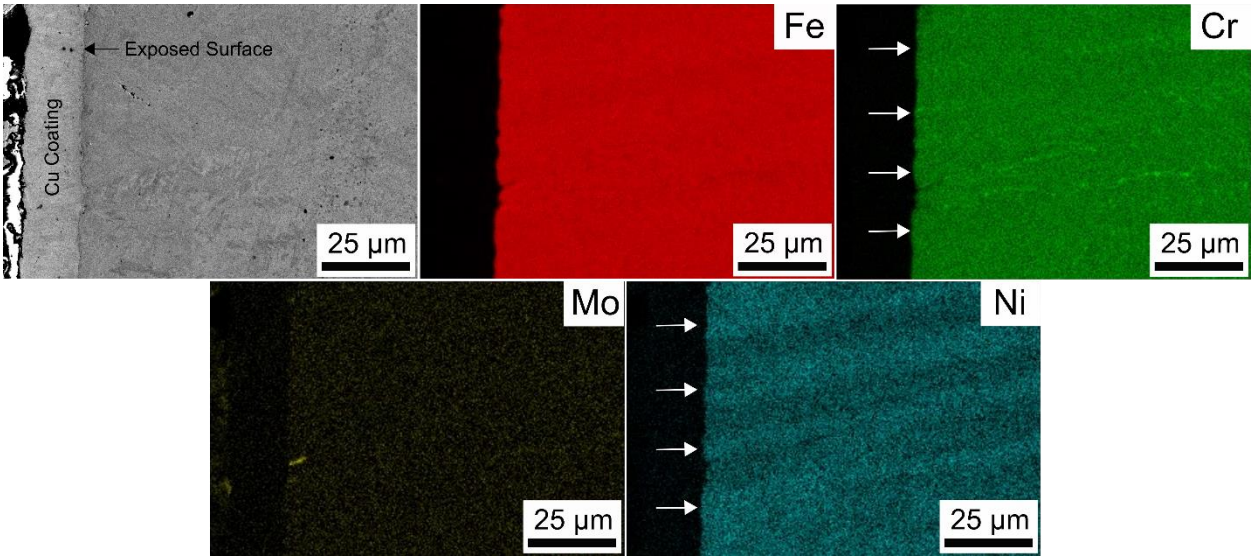

Figure 62. Cross-sectional EDS compositional analysis of a 16-8-2 weld specimen exposed to FLiNaK in pyrolytic boron nitride (PBN) capsules for 500 hours at 700 ˚C. A Cu coating was electroplated on the sample surface prior to mounting and polishing. The yellow arrow in the SEM image denotes the path of the EDS line scan.

To investigate the effects of local surface elemental composition on the surface recession of the material, profilometry and EDS lines scans were performed. Figure 63(a) shows a profilometry topographical map and a slice of the surface to reveal the horizontal surface topography. Figure 63(b) shows an SEM image and an EDS line scan of the composition in the same area as the topographical slice.

Comparison of the topographical profile to the nickel concentration profile shows that the composition variation and surface peaks and valleys have roughly the same periodicity. This is evidence that the local surface nickel concentration is influential over the rate of surface recession. From Figure 62 and Figure 63 it was concluded that regions of higher nickel concentration exhibit less surface recession in 16-8-2.

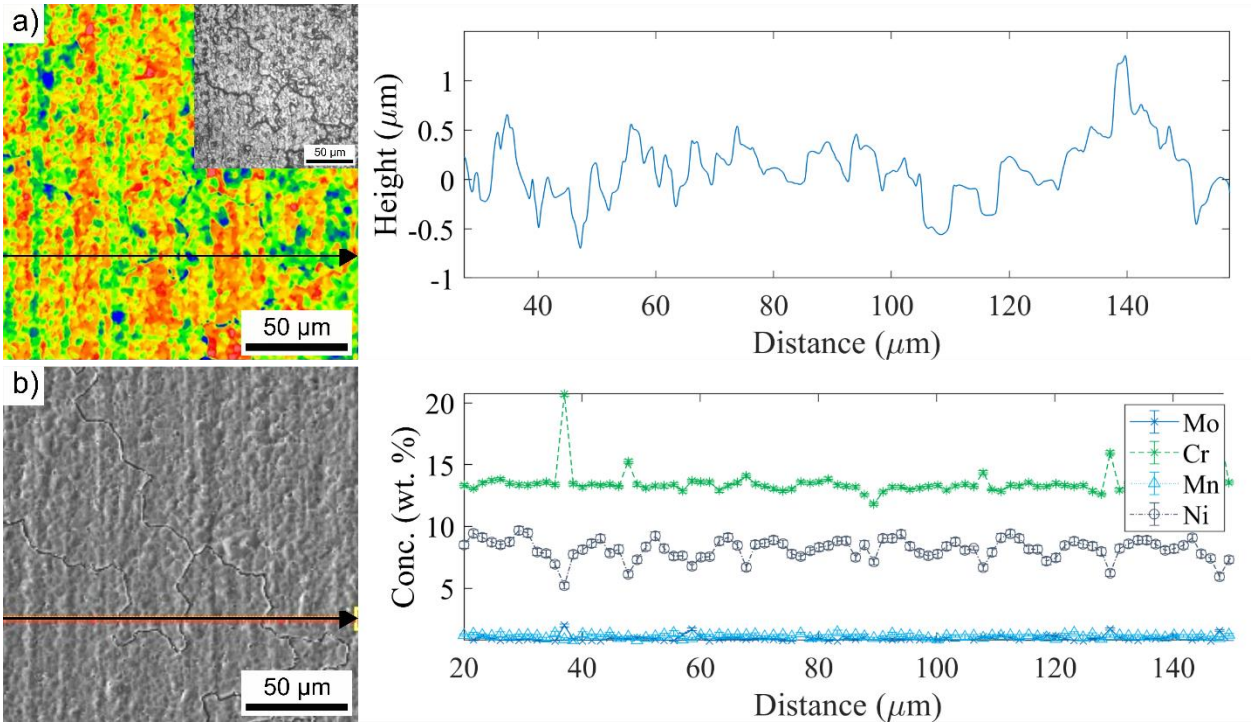

Figure 63. 16-8-2 surface (a) topographical map and linear slice and (b) compositional line scan after exposure to FLiNaK for 500 hours at 700 ˚C in a PBN capsule. The black arrow indicates the path of the slice and the line scan. The inset image in the topographical map is an optical image of the analyzed area.

3.1.4.5 XRD analysis on corrosion surface

XRD was performed to characterize the microstructure of the 316H substrate and the 16-8-2 weld before and after exposure to molten salt. Figure 64 shows the XRD patterns for the two materials before and after exposure. The as-received specimens showed strong (111), (200), (220), and (311) γ-austenite peaks corresponding to the face-centered-cubic (FCC) bulk material. In the 316H substrate a small peak emerged corresponding to the (110) α-Ferrite phase (indicated by the black square). In the 16-8-2 weld material the (111) γ-austenite peak was not observed. Large peaks at 2θ ~ 44 degrees and 2θ ~ 82 degrees

indicate the formation of (110) and (211) α-Ferrite phase, respectively. It is not clear if the phase transformation is driven by thermal effects or corrosion effects.

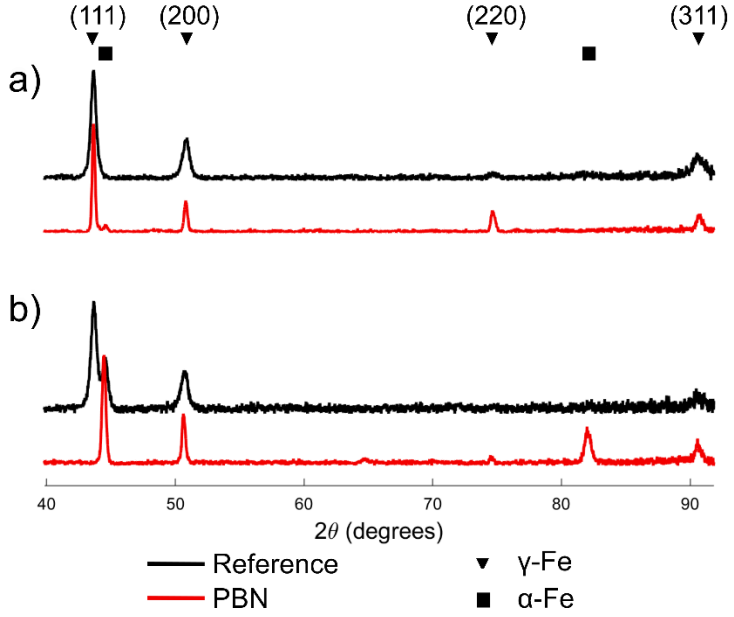

Figure 64. XRD patterns for (a) 316H substrate and (b) 16-8-2 weld before (reference) and after exposure to FLiNaK in pyrolytic boron nitride (PBN) for 500 hours at 700 ˚C.

3.1.4.6 Salt Analysis

Analysis of the test salts for 316H substrate and 16-8-2 was performed. Figure 65 shows ICP-MS concentration measurements of important trace elements in the salt. Chromium was again depleted from both alloys.

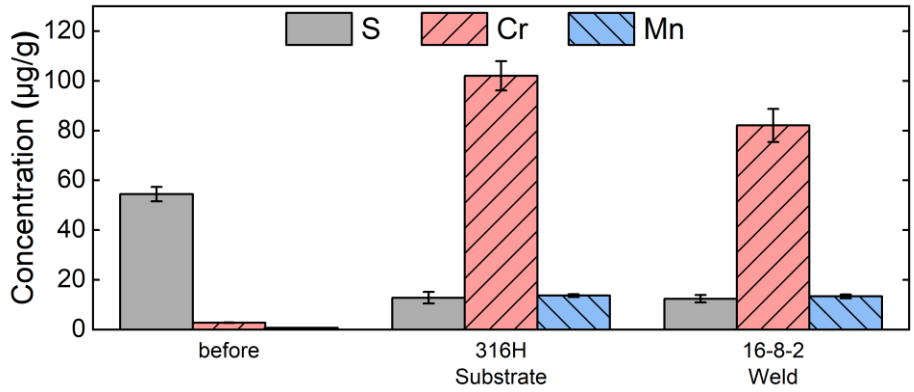

Figure 65. Concentration of trace impurities in FLiNaK salt before and after exposure to 316H substrate and 16-8-2 weld specimens for 500 hours at 700 ˚C in pyrolytic boron nitride (PBN).

3.1.4.7 Discussion

The results of corrosion testing of 16-8-2 weld material and the 316H substrate show important differences between the two materials that are pertinent to MSR design and construction. Quantifiable corrosion, such as weight loss, surface recession, depth of grain boundary Cr dissolution, and depth of bulk grain Cr dissolution are shown in Table 16. The 316H substrate performed on par with other 316H specimens that were tested in this research. The 16-8-2 weld material, which was manufactured by repeated passes of a gas tungsten arc welding (GTAW) process, showed considerable compositional banding. This is presumably the result of the melting and solidification (and thermal cycling) cycles that occurred during manufacturing that may have led to compositional partitioning. The material not only showed more substantial thickness loss but also showed somewhat non-uniform surface recession. The variations in nickel concentration may change the alloy's local resistance to corrosion. As a result, it was very difficult to accurately evaluate the depth of bulk grain Cr depletion. Of note is the prominent evolution of BCC ferrite/martensite peaks after exposure to molten salt which may also influence the mechanical properties of the weld.

Table 16. Analysis of the 316H substrate an 16-8-2 weld corrosion after exposure to FLiNaK for 500 hours at 700 ˚C in PBN capsules.

Specimen	Capsule	Weight Change (mg cm^{-2})	RMS Surface Roughness (μm)	Surface Recession (μm)	Depth of Grain Boundary Depletion (μm)	Depth of Bulk Grain Cr Dissolution (μm)	Total Depth of Corrosion (μm)	Type of Corrosion Attack
316H Substrate	PBN	-1.6 ± 0.1	0.338	0.80	4.6	0.0	5.4	Surface recession & grain boundary Cr dissolution
16-8-2	PBN	-2.6 ± 0.3	0.386	1.70	0.0	0.0	1.7	Surface recession

3.2 Corrosion Studies of Alloy N, 141 & 3

3.2.1 Overview

As shown earlier in Figure 4, nickel is very thermodynamically stable in molten fluoride salts, and consequently Ni-based alloys are among the leading candidate structural materials for fluoride salt-cooled MSRs. However, alloying elements added to Ni for high temperature creep strength may not necessarily exhibit similar corrosion stability in this environment. Moreover, the chemical state (e.g., solid solution, intermetallic compounds, and interstitial compounds) of these alloying elements in the Ni-alloy matrix will also influence their corrosion stability. The depletion of these alloying elements over long periods of exposure to molten fluoride salts can be detrimental to the creep behavior of the overall system and also lead to contamination of the molten salt. Therefore, understanding the influence of molten fluoride salt on the Ni-based alloys' microstructure and distribution of alloying elements during corrosion is paramount to ensuring structural integrity over the service life of an MSR. In many cases, corrosion can modify a material surface in situ to form a corrosion-resistant layer on the surface or compositionally graded material. However, there are no ASME BPVC codification standards for coated or compositionally graded materials. The corroded region must in effect be neglected while accounting for specified minimum tolerances for an MSR vessel and other components. To ensure that the vessel stays within specifications, data for corrosion rate including thickness loss and attack depth are required. In addition, mechanisms of corrosion must be understood to assess the long-term corrosion behavior. It has also become apparent from recent literature that environmental factors, such as dissimilar materials, can strongly influence several metrics of corrosion [55]. To address these issues, 500-hour static materials exposure tests were undertaken with the goal of studying the following questions: (i) which alloying elements are most susceptible to corrosion? (ii) which phases in the microstructure are resistant to corrosion? (iii) what is the effect of dissimilar materials on corrosion? Addressing these issues will allow for an improved understanding of the corrosion mechanisms which in turn would provide the direction for down selection of alloys for longer-term tests and eventual application in MSRs.

3.2.2 Initial microstructure and composition characterization of alloys

Materials characterization was performed on the as-received alloys to understand the compositional and microstructural differences between the alloys. Figure 85 shows cross-sectional SEM images of as-received Alloy N, Alloy 141, and Alloy 3. The grain size was analyzed using the Abrams three-circle procedure [126]. Randomly selected regions of 10 micrographs of each alloy were analyzed and the results averaged. The grain size of Alloy-N, Alloy 141, and Alloy 3 was 34 ± 3 μm, 48 ± 8 μm, and 29 ± 5 μm, respectively.

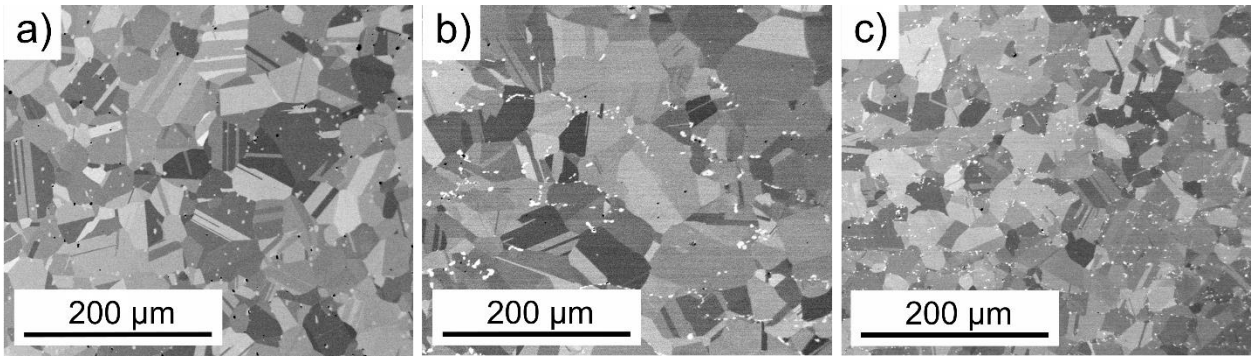

Figure 66. SEM images of Alloy N, Alloy 141, and Alloy 3. Specimens are prepared by 3 hours of vibratory polishing with 0.02 μm colloidal silica. An accelerating voltage of 5 kV and an aperture of 120 μm was used.

As described in Section 1.3, and visually noted here, Alloy 141 and Alloy 3 contain a higher number density of precipitates than Alloy N. The precipitates in Alloy 3 are finer in size and more uniformly distributed than Alloy N and Alloy 141. It is expected that the higher alloy content and higher carbon concentration in Alloy 3 will increase the volume fraction of precipitates and the variety of precipitate chemistries, particularly the carbide phases.

The composition of the phases in the as-received alloy were measured semi-quantitatively by EDS. Figure 67 shows two metrics for compositional analysis of the alloys. Figure 67(a)-(c) depict EDS averages in which the average composition within a larger pre-defined selected area is measured (this represents the overall composition of the alloy). Figure 67(d)-(e) show EDS point scans centered on identifiable precipitate phases and the surrounding precipitate-free alloy matrix. Figure 68 summarizes the compositional analysis of each alloy based on these metrics. The point scan data represents the average of

the data from three point scans measured for both the matrix and the precipitates. The large area compositional averages agree with each alloys' composition measured by DCPES in Table 9. The area averages show that each alloy contains approximately 7 wt. % Cr. Point scans confirmed that most of the Cr resides in the matrix, which is important for understanding its diffusion to the surface in the bulk alloy and its eventual exit into the molten salt. In each alloy, both the matrix and the precipitates contain significant amounts of Mo, suggesting the presence of Mo in solid solution and as Mo-rich compound precipitates such as molybdenum carbide. Molybdenum carbide (as well as other carbides) precipitates leads to significant high temperature creep strength because by virtue of acting as obstacles to dislocation movement.

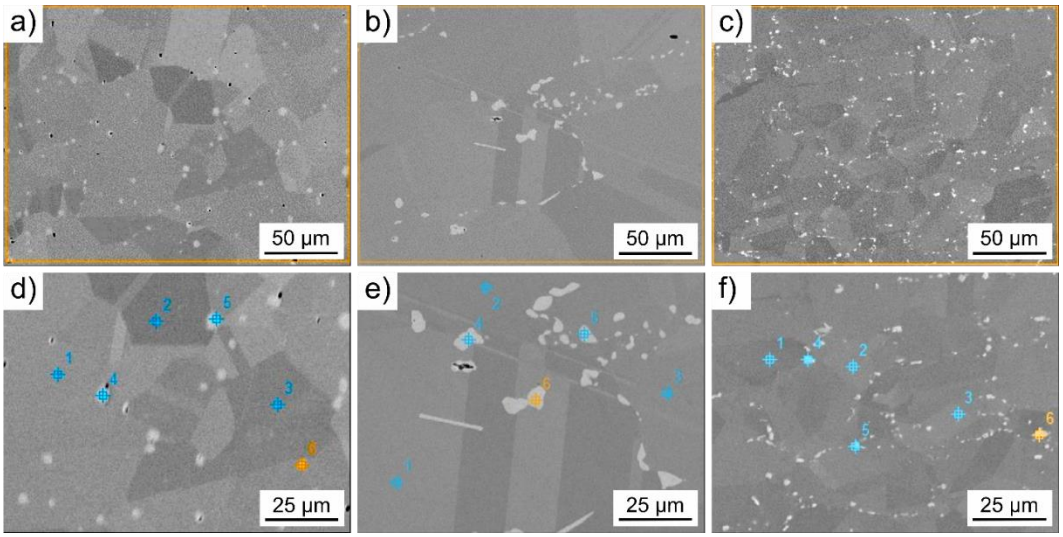

Figure 67. EDS (a-c) large area average composition and (d-e) point scans of the matrix material and precipitates for as-received (a)(d) Alloy N, (b)(e) Alloy 141, and (c)(f) Alloy 3.

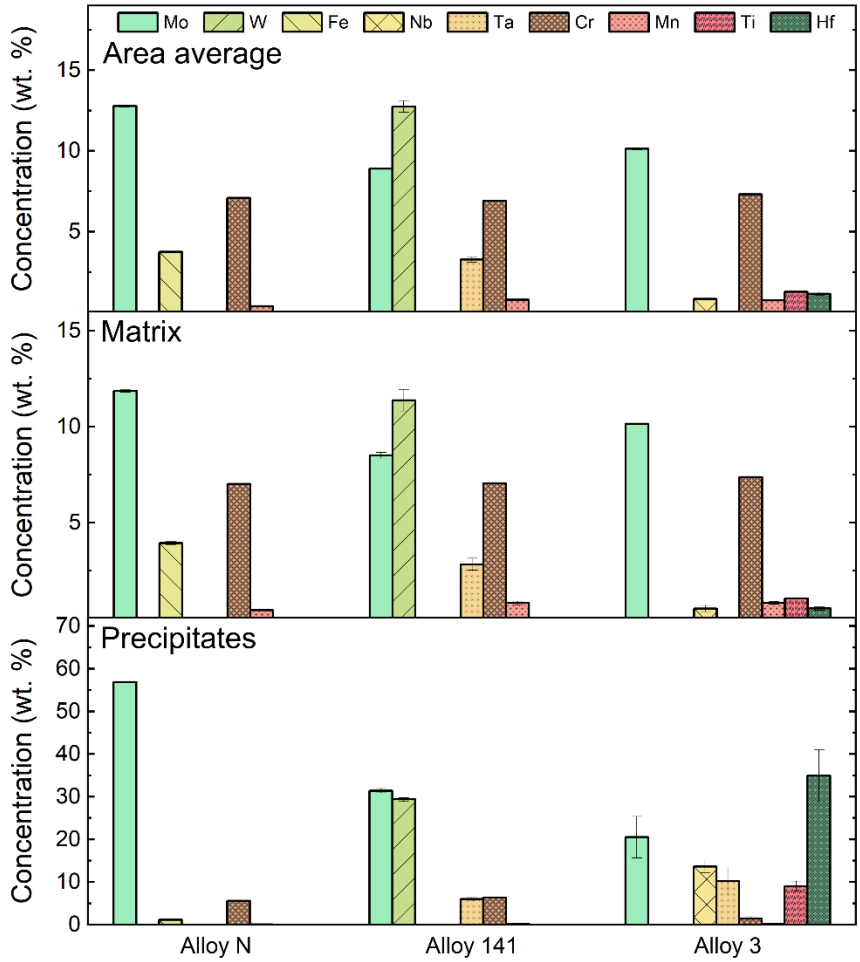

Figure 68. EDS compositional analysis of the Ni-based alloy specimens before exposure to molten salt (balance Ni).

The major alloying elements in Alloy N are Ni, Fe, Cr, and Mo. In Figure 68, all the Fe is retained in the matrix material. The precipitates are deficient in Ni and rich in Mo with some solubility for Cr.

The composition and microstructure of Alloy 141 is similar to Alloy N with a few key differences. The alloy does not contain Fe, however, it contains additions of Ta and W while maintaining a relatively low concentration of C (0.046 wt. %) similar to Alloy N. Figure 68 shows that the matrix for this alloy contains the majority of the Cr and Ta. The precipitates are deficient in Ni and rich in Mo and W, suggesting the formation of molybdenum and W carbides or intermetallic compounds (a future section will discuss phase prediction using Pandat software).

Alloy 3 presents the most complex composition and microstructure of the nickel-based alloys in this study. The alloy contains additions of Mo, Ta, Hf, Nb, and Ti, and relatively high C (0.25 wt. %). In Figure 68 the matrix is shown to also contain approximately 1 wt. % of Nb, Ti and Hf. In general, Ta was difficult to quantify with EDS given its low concentration of ~<1 wt. %. The precipitates are deficient in Ni and rich in Mo, Ta, Hf, Nb, and Ti. With the high concentration of carbon and alloying elements, these precipitates are likely M_6C carbide phases. As will be discussed later, it is possible that Hf in this alloy may also form an intermetallic phase with Ni, such as Ni_5Hf . The microstructure of the phases present in these alloys will be further discussed in a future Section 3.2.8.

3.2.3 Weight Change after exposure to molten FLiNaK

Static corrosion tests were carried out in molten FLiNaK on specimens of Alloy N, Alloy 141, and Alloy 3 for 500 hours at 700 ˚C. Tests were conducted in capsules composed of nickel, PBN, and glassy carbon to simulate and study the effects of dissimilar materials on corrosion. Figure 69 summarizes the weight change of the alloys after exposure. The alloys lost weight when exposed in all capsule environments. Alloy 141 and Alloy 3 lost more weight compared to Alloy N when exposed in Ni capsules. In PBN capsules, the alloys lost a nearly equal amount of weight. In glassy carbon capsules, Alloy 141 and Alloy 3 lost less weight compared to Alloy N.

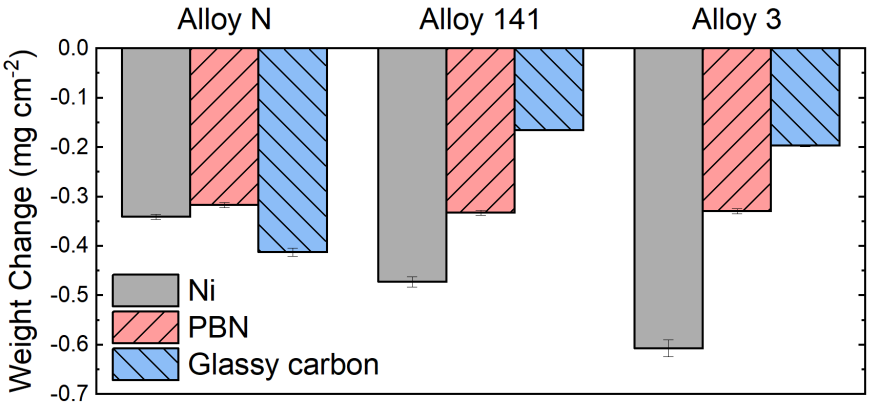

Figure 69. Weight change of Ni-based alloys after exposure to FLiNaK for 500 hours at 700 ˚C in nickel (Ni), pyrolytic boron nitride (PBN), and glassy carbon capsules.

3.2.4 Exposed alloy surface morphology

Photographs of the nickel alloys before and after exposure in various capsules are shown in Figure 78. In general, the specimens appear a dull grey color after exposure to molten salt. For each set of specimens exposed in PBN and glassy carbon capsules, the top specimen in each sample chain was half submerged in the molten salt. This specimen shows a transition from the original polished surface to the corroded surface at the vapor-salt interface in Figure 78(b)(e) and (f). Specimens exposed in nickel capsules were fully submerged so no vapor-salt interface is observed in Figure 78(c).

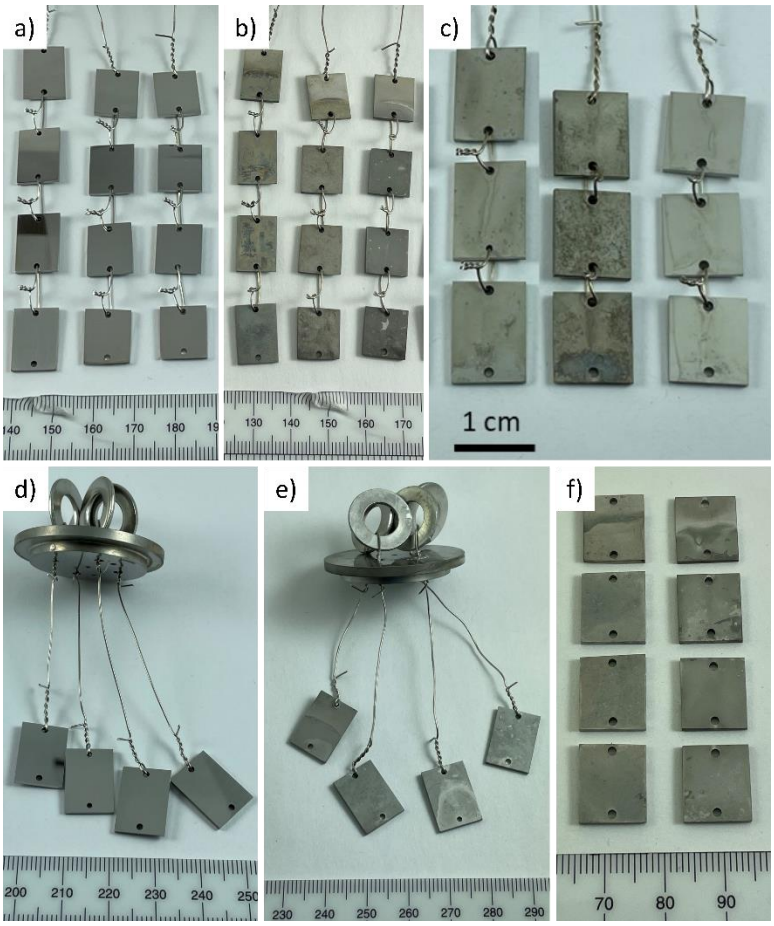

Figure 70. Photographs of nickel alloy specimens before and after exposure to molten FLiNaK salt for 500 hours at 700 ˚C. Alloy N (left), Alloy 141, and Alloy 3 (right) are shown (a) before exposure, and after exposure in (b) pyrolytic boron nitride (PBN) capsules, and (c) nickel capsules. Alloy N is shown (d) before and (e) after exposure in a glassy carbon capsule. Alloys 141 (left) and Alloy 3 (right) are shown (f) after exposure in glassy carbon capsules.

The effect of salt exposure on the surface topography of the alloys was investigated with SEM. Figure 71 shows the three alloys before and after exposure in molten FLiNaK salt in various capsule materials. Figure 71(a)(e) and (i) show the as-polished (1200 grit) Alloy N, Alloy 141, and Alloy 3, respectively. Specimens exposed in the PBN, nickel, and glassy carbon capsules are shown in Figure 71 (b),(f),(j), Figure 71(c),(g),(k) and Figure 71(d),(h),(l), respectively. Alloy N in PBN and glassy carbon capsules shows more pronounced exposed precipitates on the surface than the Alloy N in the nickel capsule. In each capsule type, Alloy 141 showed exposed carbides on the specimen's surface. Alloy 3 showed pits in the surface after exposure in all capsule environments. This pitting may be occurring in the matrix phase

in the region devoid of carbide or it may indicate that certain carbide compositions are selectively dissolved leaving behind a void.

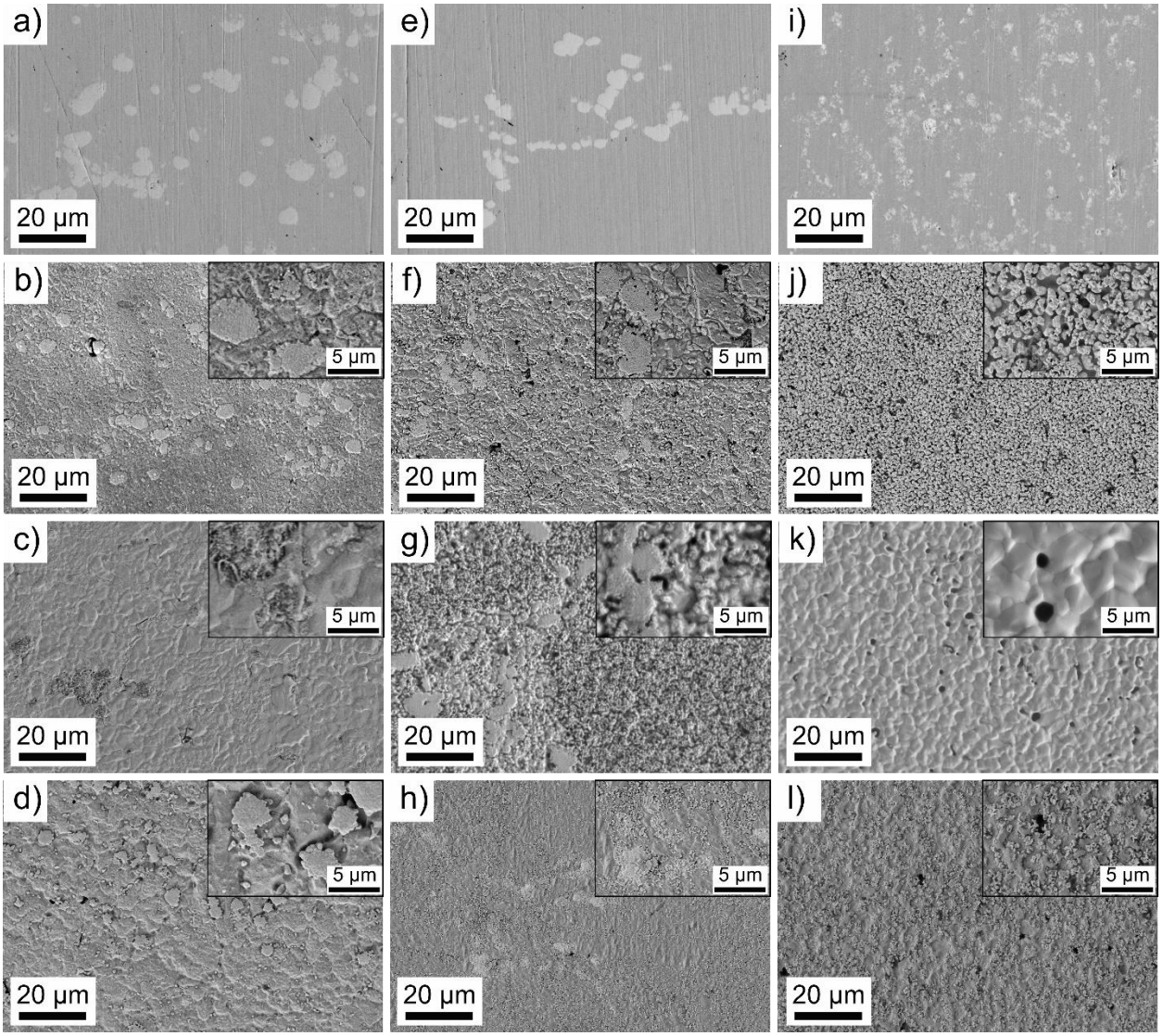

Figure 71. SEM images of the surface of (a-d) Alloy N, (e-h) Alloy 141, and (i-l) Alloy 3 (a),(e),(i) before exposure, and after 500 h exposure at 700 ˚C in (b),(f),(j) pyrolytic boron nitride (PBN) capsules, (c),(g),(k) nickel capsules, and (d),(h),(i) in a glassy carbon capsules.

The surface roughness of the alloys exposed in different capsules was quantified with profilometry in Figure 72. The average root mean square (RMS) surface roughness of the as-polished specimens was 0.006 µm. As shown in Table 22, the surface roughness of the specimens increased to 0.07-0.3 µm after exposure to the molten salt. Alloy 141 exposed in a nickel capsule had the highest surface roughness after exposure. Alloy N in PBN showed the lowest roughness.

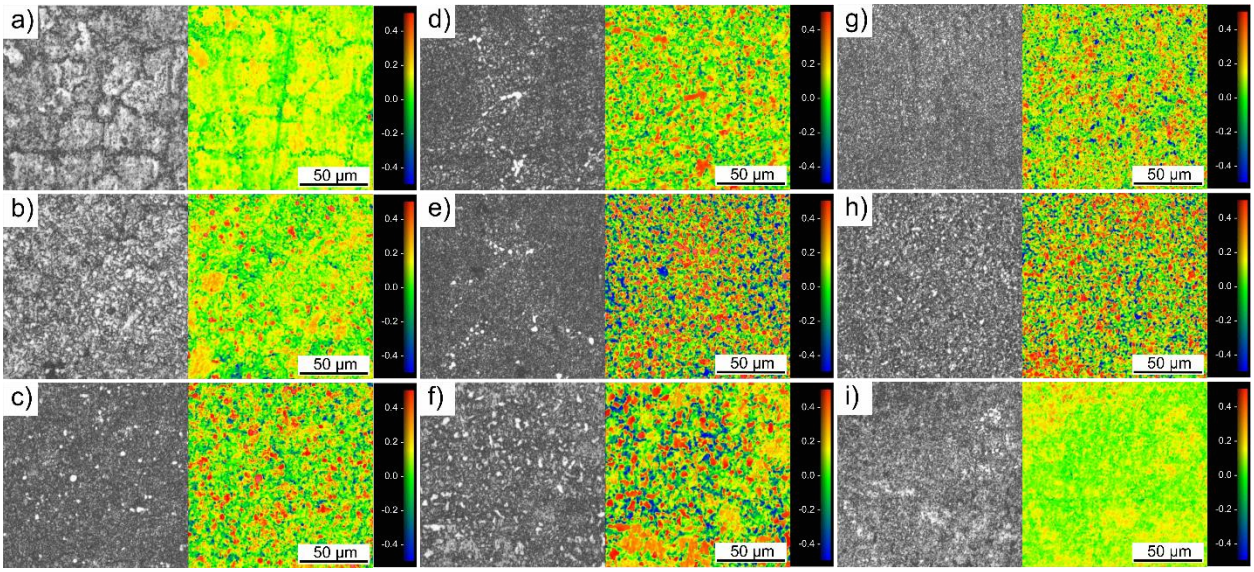

Figure 72. Profilometry of the surface of (a-c) Alloy N, (d-f) Alloy 141, and (g-i) Alloy 3 after 500 h exposure at 700 ˚C in (a),(d),(g) pyrolytic boron nitride (PBN) capsules, (b),(e),(h) nickel capsules, and (c),(f),(i) in a glassy carbon capsules.

Profilometry was used to measure the surface recession at the vapor-salt interface on nickel alloy specimens that were half submerged in molten salt. Figure 73 shows profilometry topographical maps where the surface submerged in the salt is in the bottom of the image. The detectable surface recession of samples exposed in PBN and glassy carbon capsules are shown in Table 22. The vapor-salt interface was barely detectable in these nickel-based alloys after exposure. The amount of surface recession was very small and it was challenging to distinguish corrosion attack from the natural curvature of the specimen surface. The average surface recession measured for the nickel-based alloys in all capsule environments was 0.27 µm. This was almost 10 times less than the surface recession measured for stainless steels in the same capsule environments. Higher surface recession was observed in glassy carbon capsule than in PBN capsules, suggesting that the corrosion mechanisms are different in these two environments. In general, the carbide phase strengthened Alloy performed very well in both capsule environments. The corrosion mechanisms that lead to uniform surface recession were investigated with electrochemical methods and will be discussed in Section 3.3.

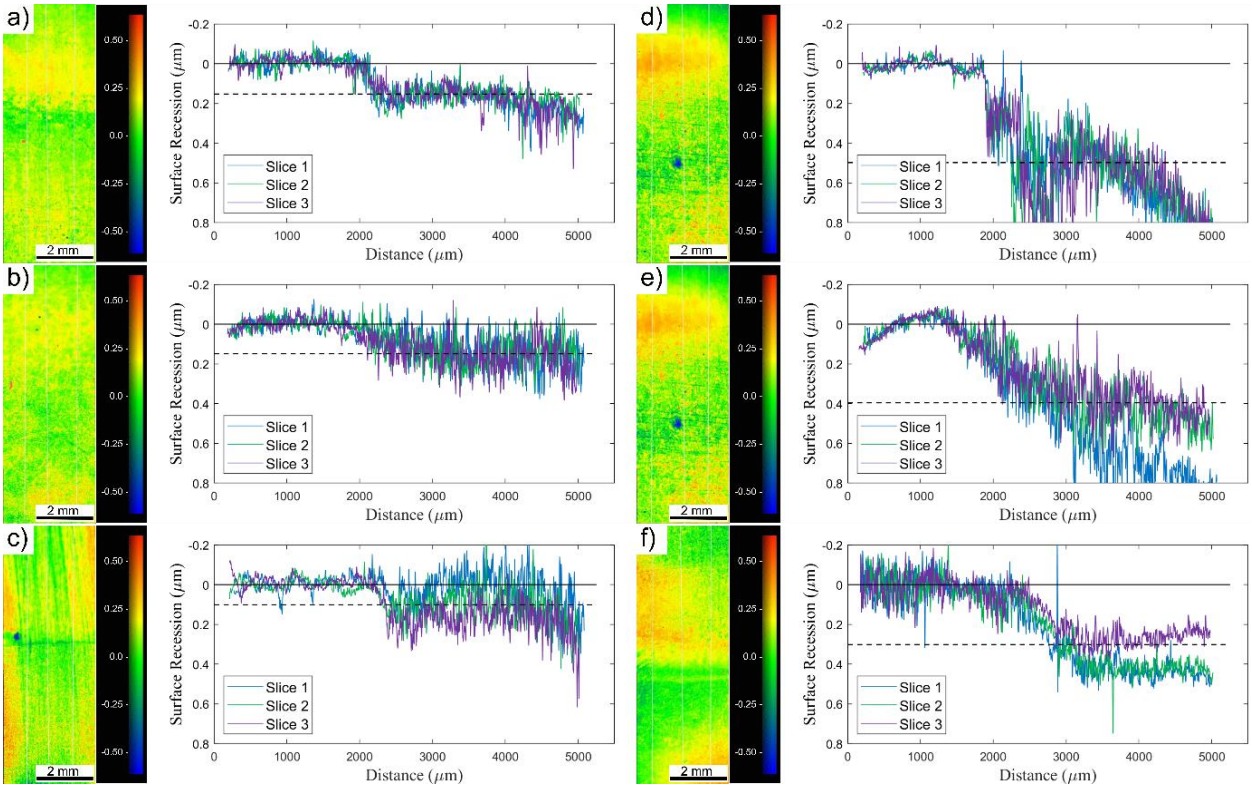

Figure 73. Profilometry topographical maps and linear slice plots of the salt-vapor interface of (a) Alloy N, (b) Alloy 141, and (c) Alloy 3 in pyrolytic boron nitride (PBN) and (d) Alloy N, (e) Alloy 141, and (f) Alloy 3 in glassy carbon. The bottom region of the topographical map was submerged in molten salt and the top region was exposed to the vapor phase (units are μm).

3.2.5 Elemental analysis of the corrosion surface exposed in PBN capsules

The impetus for investigating materials corrosion in PBN capsules was that the relatively inert material may afford the opportunity to study corrosion without dissimilar materials effects coming from the capsule material. Alloy N, 141, and 3 lost comparable amounts of weight during the 500 hour exposure in PBN capsules, however, differences in surface topography in Figure 71 indicate that the corrosion mechanism may not be the same for the three alloys.

EDS elemental analysis was performed on the exposed alloy surfaces to determine which elements and phases were prone to corrosion attack. Utilizing EDS area averages of the alloy surface, shown in Figure 74, the net change in elemental composition over a large area of the microstructure was measured and the results are shown in Figure 75. Depletion of Cr and enrichment of Mo were observed. Depletion of Cr is highest in Alloy N and lowest for Alloy 3. Examining the net change in Alloy 141's Ta and Alloy 3's

Nb, Ti, and Hf it was observed that other alloying elements are also contributing to dissolution of mass from the alloy. The change in the composition of the matrix point scans follows the same trend as the area averages. The precipitate point scans show that a considerable quantity of the Ta, Nb, Ti, an Hf are lost specifically from the precipitates in Alloy 141 and Alloy 3. The corrosion of other alloying elements may partially explain why there is less change in Cr concentration in Alloy 141 and Alloy 3.

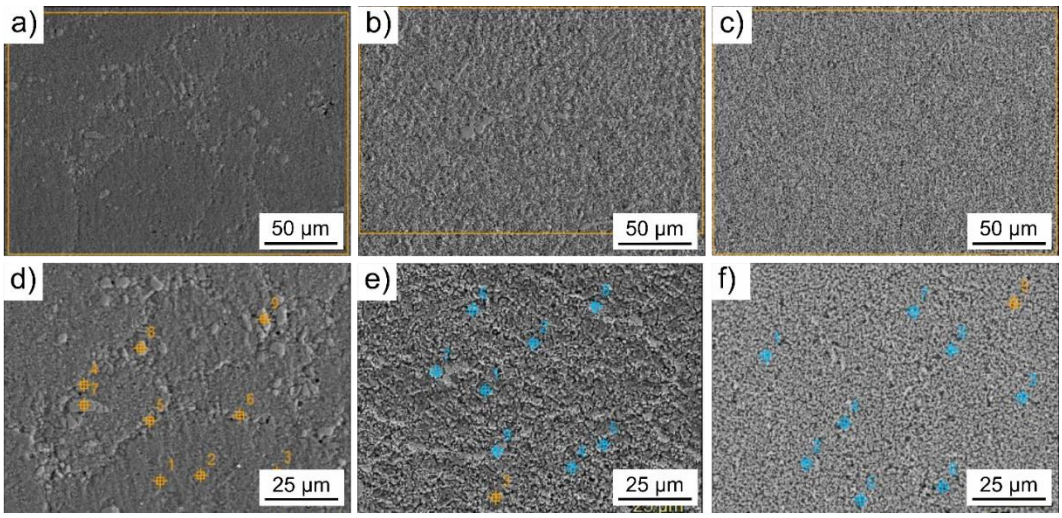

Figure 74.EDS (a-c) area average composition and (d-e) point scans of the matrix and precipitates for (a)(d) Alloy N, (b)(e) Alloy 141, and (c)(f) Alloy 3, exposed to FLiNaK in PBN capsules for 500 hours at 700 ˚C.

Figure 76 shows cross sections of each alloy following exposure to FLiNaK in PBN capsules. The EDS Cr compositional maps indicate that Alloy N experienced preferential grain boundary Cr dissolution. Alloy 141 and Alloy 3 experienced matrix Cr dissolution. In Figure 76(a), the EDS line scan shows that Alloy N does not experience bulk grain Cr or Fe dissolution in the PBN capsule. Figure 76(b) shows that, the Alloy 141 matrix experienced dissolution of Cr to a depth of 12 µm. The matrix also appears to lose some Ta, but the Ta dissolution is not as severe as Cr. In Figure 76 (c), Alloy 3 experienced depletion of Cr, Hf, Nb, and Ti. The depth of matrix Cr dissolution in Alloy 3 was 15 µm. These results show that, in PBN capsules, some alloying elements, such as Fe and Ta are resistant to corrosion, while others, most notably Cr are preferentially dissolved.

The surface SEM images of Alloy 3 in PBN, shown in Figure 71(j), show particulates on the surface of the specimen. In Figure 77, EDS point scan analysis showed a higher concentration of Mo (20-30 wt.

%) for points scans (points 4-6) of the particles. Since the point scans detect both the particle and the matrix underneath, the measurement is semi-quantitative. It is speculated that these Mo-rich precipitates are exposed by corrosion. Additional characterization to determine the elemental makeup of the Mo rich phase will be discussed in Section 3.2.1.

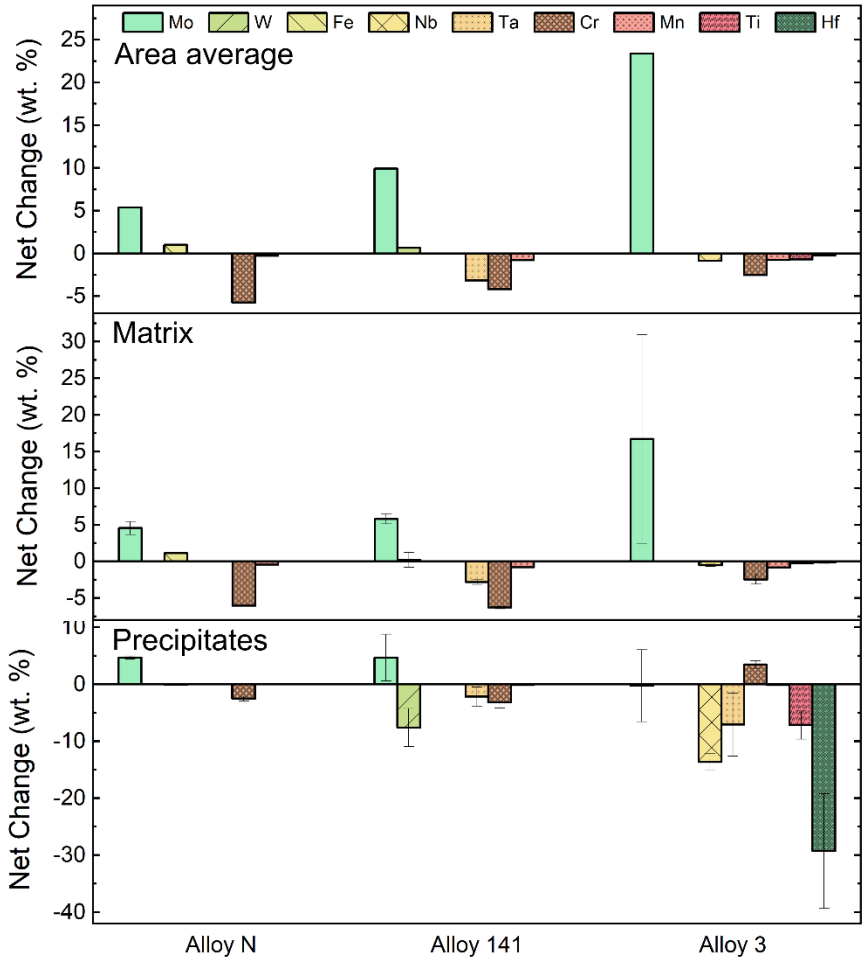

Figure 75. EDS compositional analysis of the net change in composition of the area average, matrix point scans, and precipitates point scans after exposure to FLiNaK salt in a PBN capsule for 500 hours at 700 ˚C.

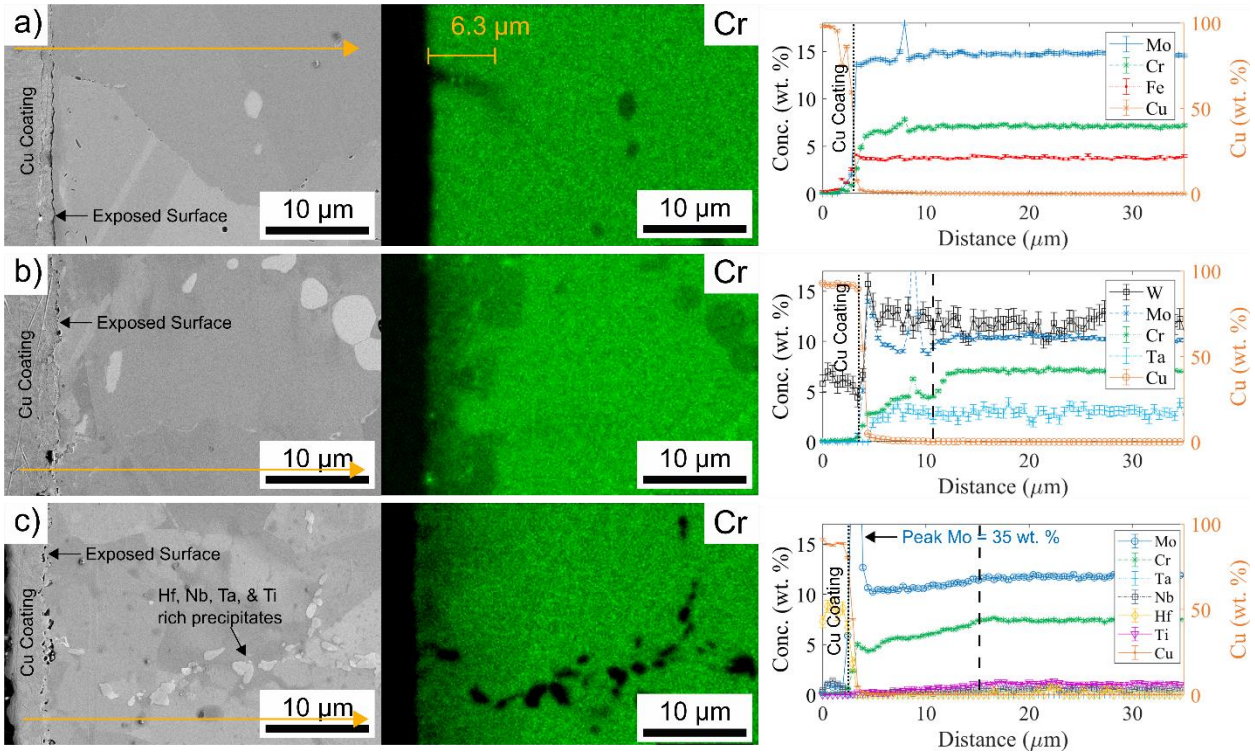

Figure 76. SEM image, EDS compositional maps, and EDS line scans of cross sections of (a) Alloy N, (b) Alloy 141, and (c) Alloy N in FLiNaK in pyrolytic boron nitride (PBN) capsules for 500 hours at 700 ˚C. A Cu coating was electroplated on the sample surface prior to mounting and polishing. Yellow arrow in the SEM image denotes the path of the EDS line scan. Cross sections were etched during 0.2 µm colloidal silica polishing.

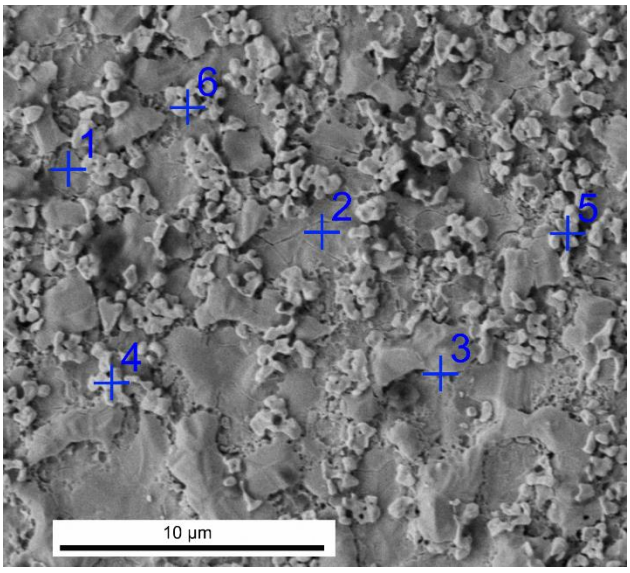

Figure 77. EDS point scan analysis of Alloy 3 exposed to FLiNaK in a PBN capsule for 500 hours at 700 ˚C. Point scans 1-3 are located on the matrix. Point scans 4-6 are located on Mo-rich surface precipitate particles.

3.2.6 Elemental analysis of the corrosion surface exposed in nickel capsules

Compositional changes in the surface of the nickel-based alloys exposed in nickel capsules were measured using SEM-EDS, as shown in Figure 78. The net change in concentration of each element in the various regions of the microstructure is shown in Figure 79. The average surface composition indicated that all three alloys experience depletion in Cr and enrichment in Mo. The enrichment of Mo is a result of depletion of elements such as Cr which raises the relative concentration of Mo. It testifies to the outstanding corrosion resistance of Mo and possibly Mo-rich carbides in molten fluoride salts. In addition to Cr depletion, each alloy lost some minor alloying elements from the bulk grains to the molten salt due to corrosion. Alloy N's Fe concentration (initially 4 wt. %) was reduced by half at the corroded surface. The Ta concentration in Alloy 141's surface was reduced to near zero. In Alloy 3 nearly all the Nb, Ti, and Hf in the near surface was depleted. Ta was difficult to quantify accurately at such a low concentration in Alloy3

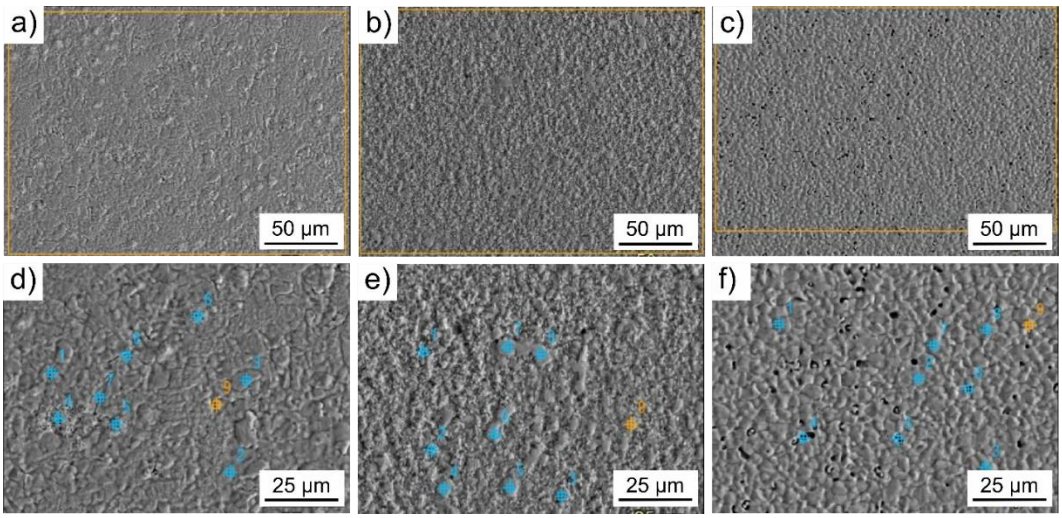

Figure 78. EDS (a-c) area average composition and (d-e) point scans of the matrix and precipitates for (a)(d) Alloy N, (b)(e) Alloy 141, and (c)(f) Alloy 3, exposed to FLiNaK in nickel capsules for 500 hours at 700 ˚C.

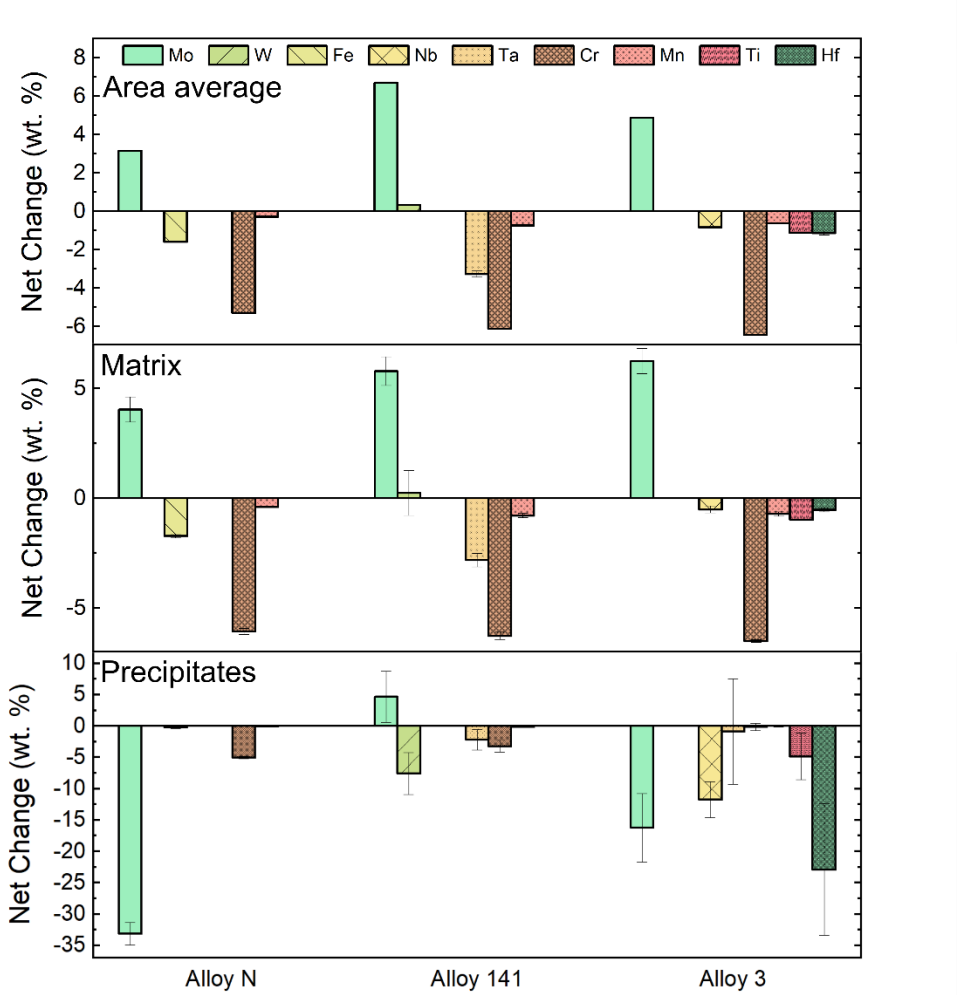

Figure 79. EDS compositional analysis of the net change in composition of the area average, matrix point scans, and precipitates point scans after exposure to FLiNaK salt in a nickel capsule for 500 hours at 700 ˚C.

Changes in the alloys' precipitate composition were also observed after exposure to FLiNaK in nickel capsules. In Figure 79, the Mo concentration in many precipitates in Alloy N and Alloy 3 dropped significantly. At the same time the area average concentration of Mo increased. In Alloy 141 the concentration of W in the precipitates decreased, however, it is unclear how much variation exists in the precipitate W concentration. According to Figure 67 , the majority of the Nb, Ti, and Hf in Alloy 3 is initially bound in the precipitates. In Figure 79, the large net change in Nb, Ti, and Hf concentration in the precipitates indicates that they are susceptible to being removed from the alloy in the Ni capsule environment.

Figure 80 shows cross-sectional SEM images, EDS elemental maps, and EDS line scans of each alloy following exposure to FLiNaK in nickel capsules. Pits are visible in the cross-section of the surface of Alloy 3. The chromium distribution maps indicate that all alloys experienced primarily matrix Cr dissolution when exposed in a Ni capsule. In Figure 80(a), the line scan shows that both Cr and Fe in Alloy N are depleted to a depth of 9 μm in the matrix. A similar effect is observed with the Cr and Ta in Alloy 141, in Figure 80(b), which are depleted to the same depth in the matrix. In Figure 80(c), the depth of matrix Cr dissolution was 12 μm in Alloy 3. The minor alloying elements Hf, Nb, and Ti were also depleted by exposure to molten FLiNaK. The surface pitting in Alloy 3 is thought to be caused primarily by corrosion of precipitate phases leaving behind voids in the material. There is a moderate increase in Mo in the near surface region of all the alloys consistent with the surface EDS compositional analysis. This is attributed to the relative depletion of other alloying elements. The dissolution of Cr appears to be the largest change in near surface chemistry and the depth of Cr dissolution is considered the thickness of material affected by corrosion.

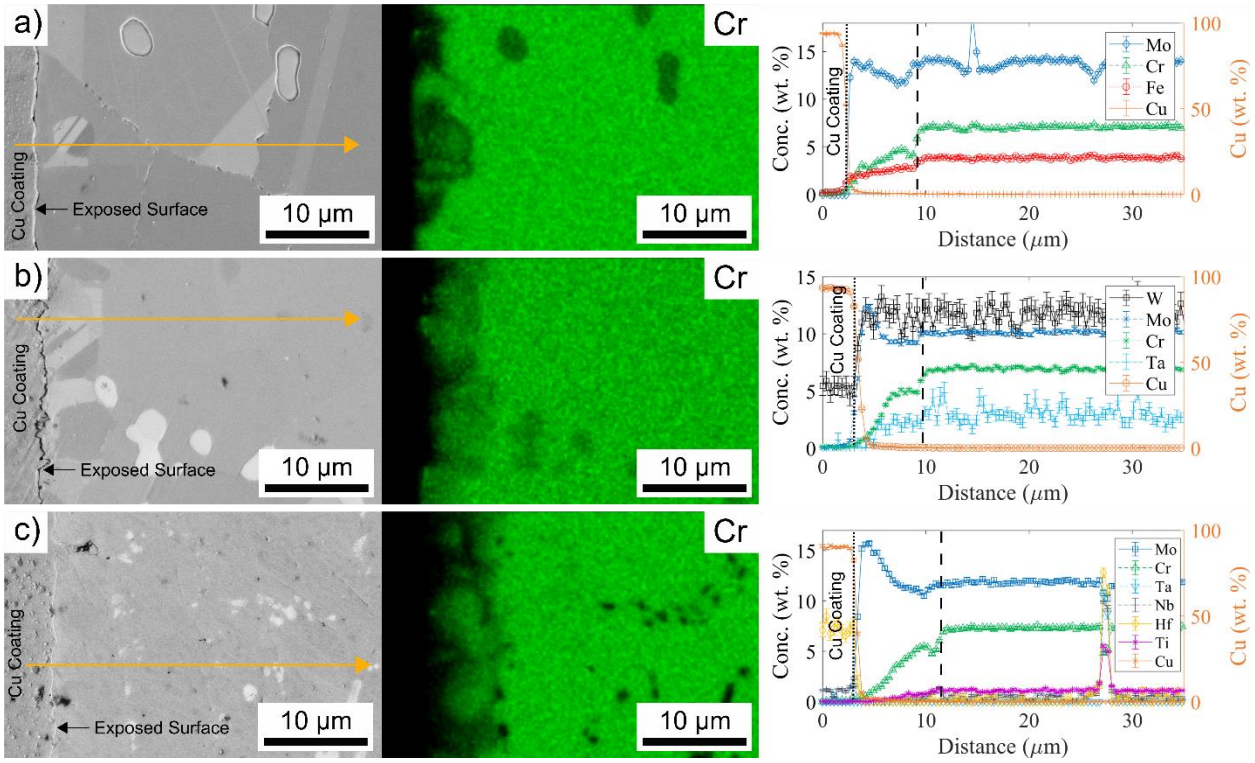

Figure 80. SEM image, EDS compositional maps, and EDS line scans of cross sections of (a) Alloy N, (b) Alloy 141, and (c) Alloy N in FLiNaK in nickel capsules for 500 hours at 700 ˚C. A Cu coating was electroplated on the sample surface prior to mounting and polishing. Yellow arrow in the SEM image denotes the path of the EDS line scan. Cross sections were etched during 0.2 μm colloidal silica polishing.

3.2.7 Elemental analysis of the corrosion surface exposed in glassy carbon capsules

Based on the weight change, surface microscopy, and XRD data, the corrosion of the nickel alloys in glassy carbon capsules appears to be quite different than Ni or PBN capsules. Elemental analysis was performed to investigate the compositional changes occurring in this environment. Figure 81 shows EDS area averages and point scans of the bulk and precipitates found in the exposed surface. In Figure 82, area averages and bulk point scans again show that all alloys lose a significant amount of Cr from the bulk grains. Alloy N appears to have retained the Fe in the matrix after exposure. Ta is again depleted from Alloy 141, however, the net change in Ta is less than in Ni or PBN capsules. The surface of Alloy 3 experience the most negative net change in Cr of the three alloys. Again, Alloy 3 experiences depletion of Nb, Ta, Ti and Hf. Cross sectional EDS examination was required to determine why the alloy lost less weight despite the changes in near surface chemistry.

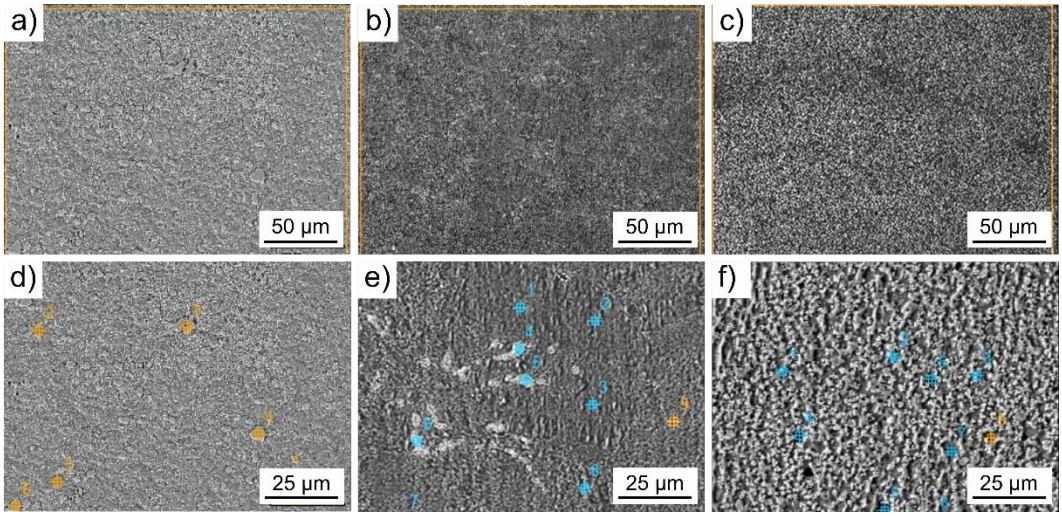

Figure 81. EDS (a-c) area average composition and (d-e) point scans of the matrix and precipitates for (a)(d) Alloy N, (b)(e) Alloy 141, and (c)(f) Alloy 3, exposed to FLiNaK in PBN capsules for 500 hours at 700 ˚C.

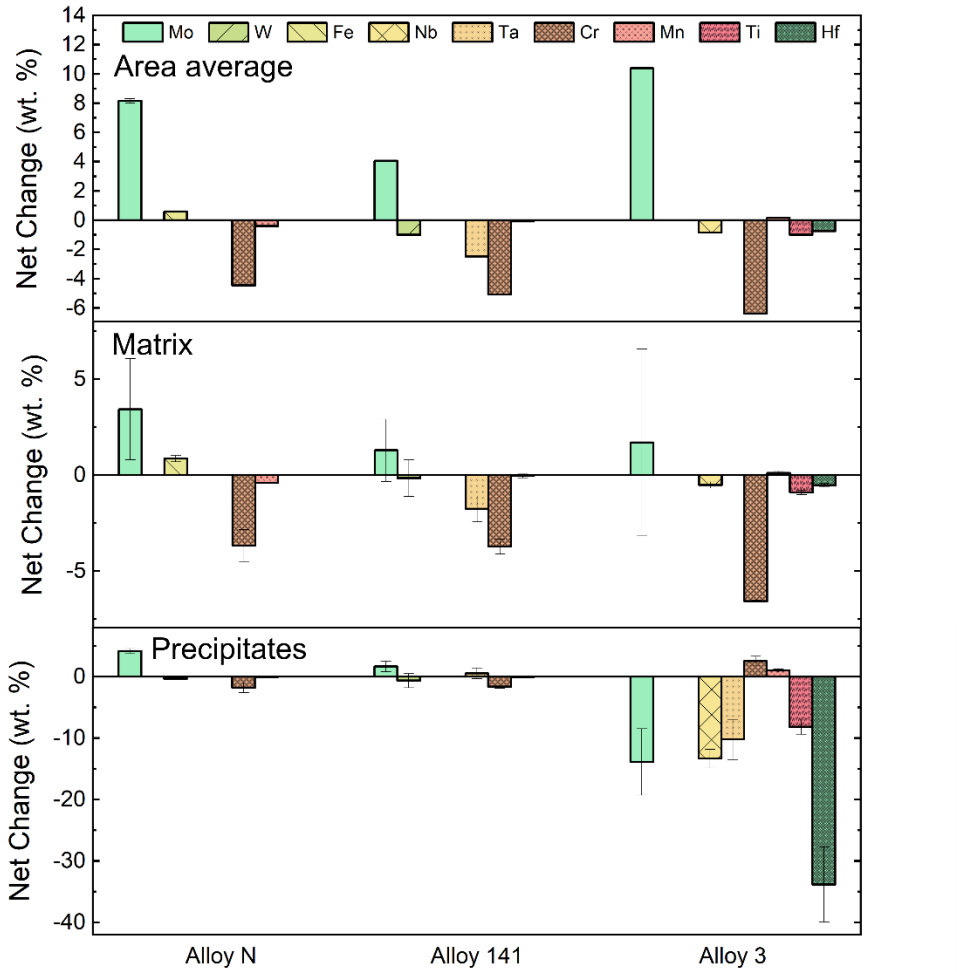

Figure 82. EDS compositional analysis of the net change in composition of the area average, matrix point scans, and precipitates point scans after exposure to FLiNaK salt in a glassy carbon capsule for 500 hours at 700 ˚C.

Figure 83 shows cross-sectional SEM images, EDS elemental maps, and EDS line scans of each alloy following exposure to FLiNaK in glassy carbon capsules. The most noticeable difference between the alloys in this environment was the apparent depth of matrix Cr dissolution. Alloy N experience the highest matrix Cr dissolution to a depth of 7.0 μm. The depths of matrix Cr dissolution in Alloy 141 and Alloy 3 were 4.0 μm and 3.0 μm, respectively.

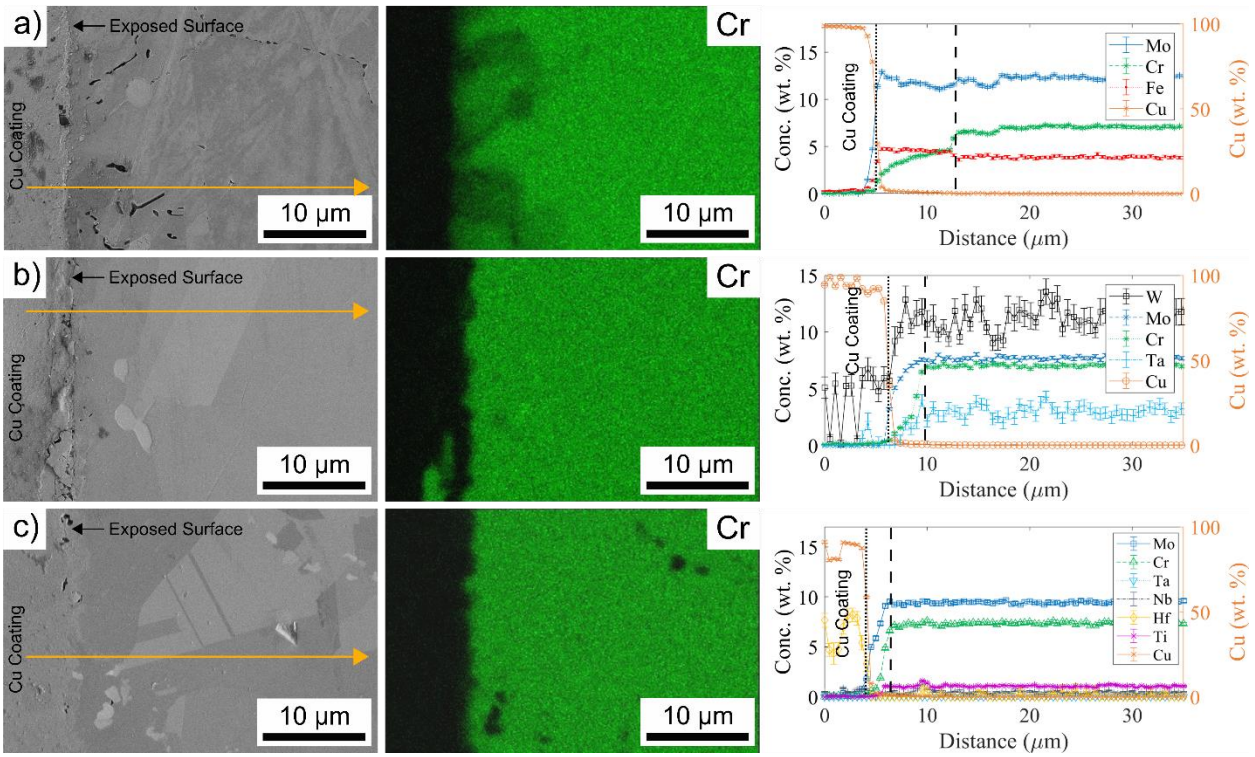

Figure 83. SEM image, EDS compositional maps, and EDS line scans of cross sections of (a) Alloy N, (b) Alloy 141, and (c) Alloy N in FLiNaK in glassy carbon capsules for 500 hours at 700 ˚C. A Cu coating was electroplated on the sample surface prior to mounting and polishing. Yellow arrow in the SEM image denotes the path of the EDS line scan. Cross sections were etched during 0.2 μm colloidal silica polishing.

Precipitate particles were also observed on the surfaces of the nickel-based alloys exposed in glassy carbon capsules. The particles were largest and most abundant on the surface of Alloy 3 shown in Figure 84. The composition of the particles (points 4-6) shows Mo concentrations between 20 and 50 wt. %. Considering that the point scan also picks up signal from the matrix below the concentration of these precipitates are expected to highly enriched in Mo. The depletion of Mo observed in near surface EDS line scans of the specimen cross sections may be a result of partitioning of Mo to these precipitates. The elemental makeup of the Mo rich precipitates was further investigated, and the results are presented in Section 3.2.1.

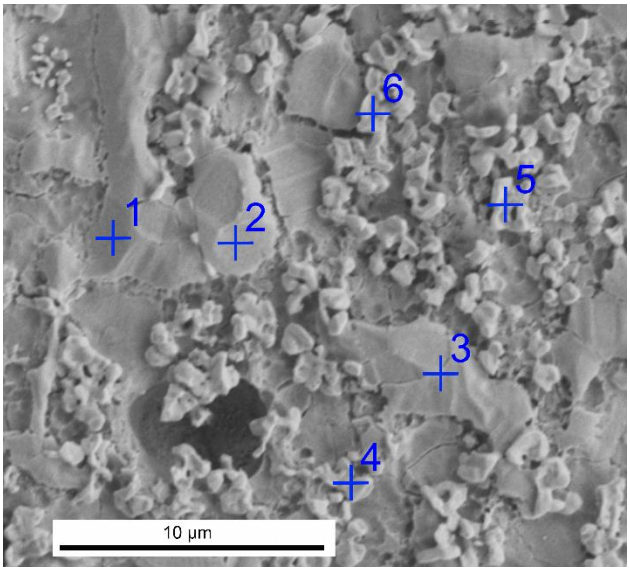

Figure 84 EDS point scan analysis of Alloy 3 exposed to FLiNaK in a glassy carbon capsule for 500 hours at 700 ˚C. Point scans 1-3 are located on the matrix. Point scans 4-6 are located on Mo rich surface particulate.

3.2.8 Compositional and phase stability calculations

Given that the MSR will operate for long periods of time at temperatures between 700 ˚C to 850 ˚C (the present targeted maximum temperature is 700 ˚C), it is reasonable to expect that the most thermodynamically stable phases will be present in the alloy microstructure during much of the reactor operation period. Figure 85, Figure 86, and Figure 87 show plots of the mass fraction of various thermodynamically feasible phases and the concentration of Cr in each phase as a function of temperature calculated using Pandat for Alloy N, Alloy 141, and Alloy 3, respectively. It is important to note that as the near-surface composition of the alloy changes continually due to corrosion, the thermodynamically feasible phases in this region will also change through elemental redistribution facilitated by diffusion kinetics at these high temperatures. The phases in the interior regions of the alloy will be dictated by purely thermal effects. Since the chemical state of the element in each alloy could influence chromium's susceptibility to corrosion, the concentration of Cr in each phase was calculated. In all three alloys most of the chromium is in solid solution at 700 ˚C. Some Cr in these alloys partitions to the M_6C and the p-phases, a Mo and Ni rich carbide, respectively, at 700 ˚C. Although the overwhelming majority of Cr resides in solid solution, the presence of precipitates at grain boundaries may impede alloying element diffusion along the grain

boundaries. The effects of a more complex solid solution chemistry and different microstructures during exposure to molten salts at 700 ˚C will influence mass transport of Cr to the corrosion surface from the bulk and warrants investigation.

Table 17. Composition of nickel-based alloys used in phase stability calculations.

Alloy	Ni	Fe	Al	Co	Cr	Mn	Mo	Ti
Alloy N	71	4	0.5	0.2	7	0.8	16	0.5
Alloy 141	67.9	0.015	0.11	0.016	7	0.78	11.9	0.0094
Alloy 3	73.7	0.03	0.11	0.018	6.96	0.82	12.8	1.12

Alloy	Nb	Hf	Ta	W	C	B	N	Total
Alloy N				0.5	0.06			100
Alloy 141	0.015	0.0005	4.03	8.03	0.046		0.002	100
Alloy 3	1.16	1.16	1.22	0.51	0.25		0.001	100

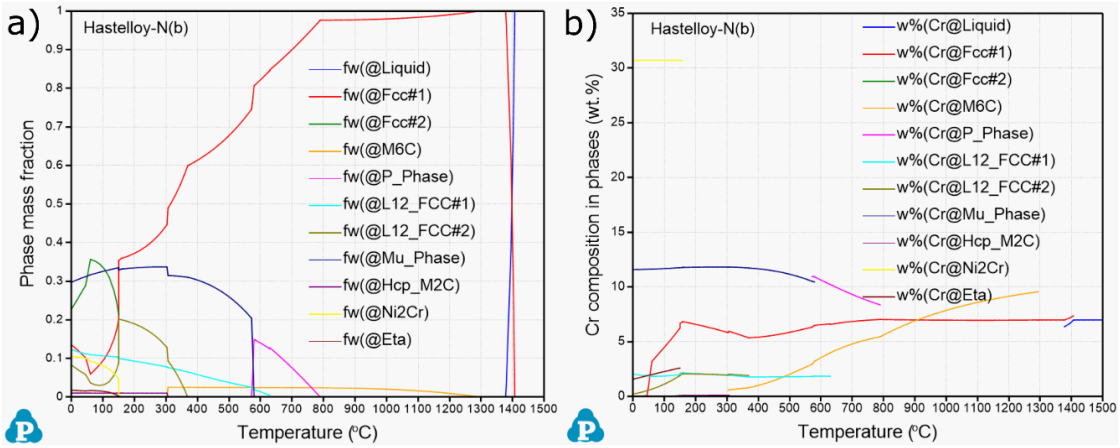

Figure 85. The calculated Hastelloy-N microstructure (a) phase mass fraction and (b) concentration of Cr in each phase as a function of temperature.

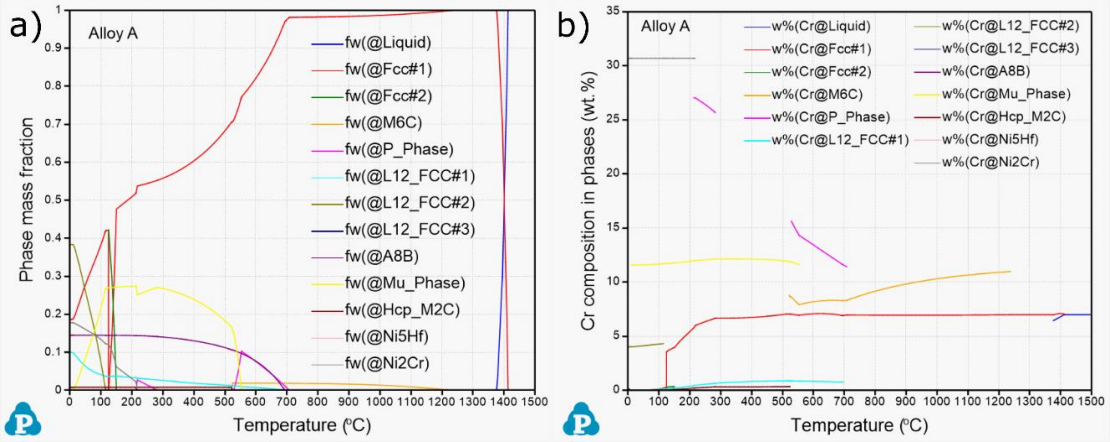

Figure 86. The calculated Alloy A microstructure (a) phase mass fraction and (b) concentration of Cr in each phase as a function of temperature.

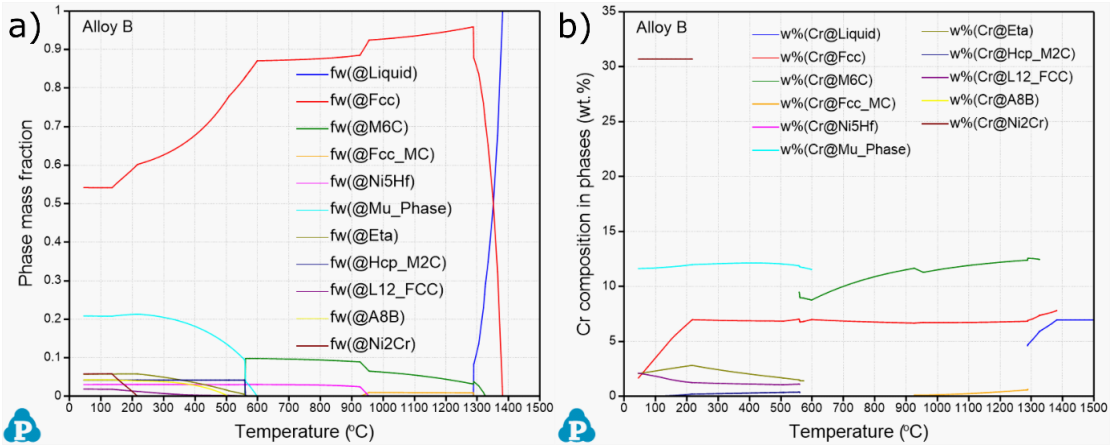

Figure 87. The calculated Alloy B microstructure (a) phase mass fraction and (b) concentration of Cr in each phase as a function of temperature.

To predict the microstructural behavior of the Alloy N, Alloy 141 and Alloy 3 used in this research, the thermodynamically stable phases present at 700 ˚C were calculated. M_6C type carbides were predicted to form in each alloy. The composition of this phase will largely depend on the amount of Cr and other alloying elements available. A Mo and Ni-rich carbide phase referred to as the p-phase is also predicted to occur in Alloy N and Alloy 141. In Table 18, the percentage of the p-phase in Alloy N and Alloy 141 is 7.56 wt.% and 0.61 wt.%, respectively. This is significant for Alloy N because, as seen in Figure 85(b), the p-phase has some solubility for Cr (10 wt. % at 700 ˚C). This could potentially alter the chemistry and therefore the Cr corrosion kinetics in the alloy. It is not clear how significantly this would affect corrosion

of Alloy N as the p-phase potentially makes up only a small fraction of the total alloy microstructure. Given that Hf is susceptible to corrosion, the Ni_5Hf phase predicted to occur in Alloy 3 may sequester Hf.

Table 18. Phase concentration (wt. %) in new advanced nickel-based alloys at 700 ˚C.

Alloy	M_6C	MC	Ni_5Hf	p-phase
Alloy N	2.43%	0.00%	0.00%	7.56%
Alloy A	1.85%	0.00%	0.00%	0.61%
Alloy B	9.67%	0.00%	3.03%	0.00%

To assess the effect of carbide phase on corrosion, , the thermodynamic stability of carbide phases formed from relevant alloying elements was calculated using HSC 7.0 [40]. Figure 88 shows the Gibbs free energy of formation of some of the most stable carbide phases. The spontaneity of the reaction of each carbide with F_2 gas was calculated in Table 19 to predict which carbides most readily experience corrosion in molten fluoride salt. It is assumed here that the reaction is between pure carbide and F_2 gas to form a solid fluoride and carbon. In general, this reaction is spontaneous for all carbides considered. $Mn_{23}C_6$ and all the Cr carbides have the most negative free energies of fluoride formation. In the presence of corrosive trace impurities, such as HF, it is unlikely that a Mn or Cr carbide will be resistant to corrosion in molten fluoride salts. The carbides formed by the other alloying elements in the nickel-based alloys, such as Hf, Nb, Ta, and Ti are marginally more thermodynamically stable than their pure elemental for and may also be susceptible to corrosion. The reactions of Mo and W carbides with F_2 gas have relatively positive free energies of reaction compared to other carbides. If these other carbide, such as Ta_2C are present in the alloy they may be preferentially corroded before Mo and W carbides are attacked.

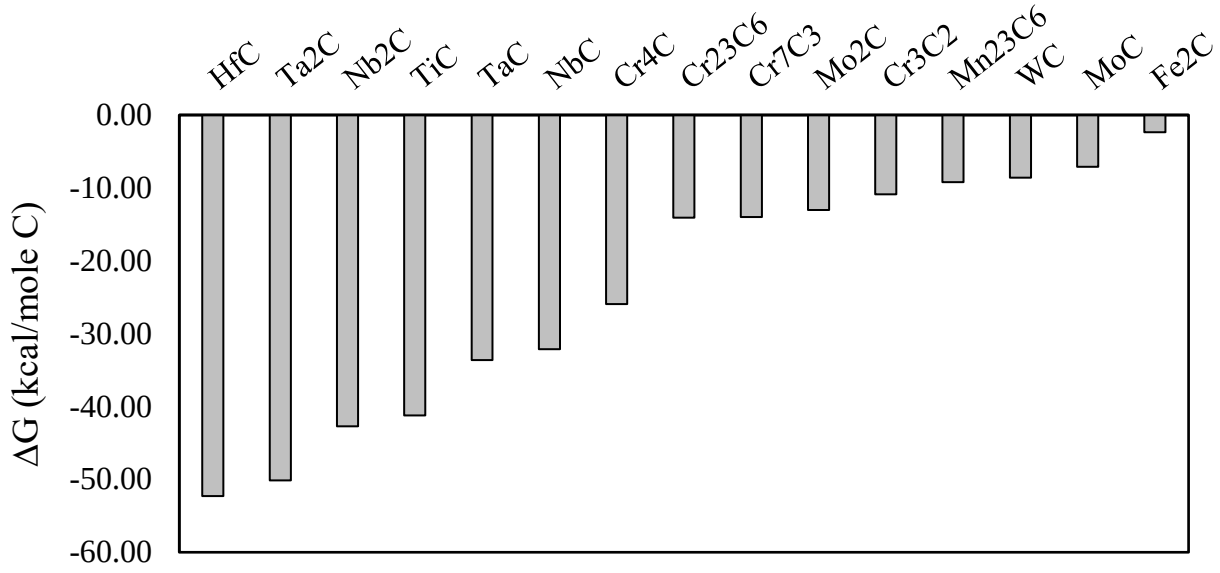

Figure 88. Gibbs free energy of carbide formation at 700 ˚C calculated using HSC 7.0 [40].

Table 19. Gibbs free energy of reaction between carbides and F_2 gas at 700 ˚C calculated using HSC 7.0 [40].

Reaction	ΔG(700 ˚C) (kcal/mole F_2)
0.3MoC + F2(g) = 0.3MoF6(g) + 0.3C	-99.9
0.16Mo2C + F2(g) = 0.3MoF6(g) + 0.16C	-100.1
0.5WC + F2(g) = 0.5WF4 + 0.5C	-111.6
TaC + F2(g) = TaF2 + C	-114.8
0.5Ta2C + F2(g) = TaF2 + 0.5C	-123.4
0.4NbC + F2(g) = 0.4NbF5 + 0.4C	-128.8
0.2Nb2C + F2(g) = 0.2NbF5 + 0.2C	-133.1
TiC + F2(g) = TiF2 + C	-143.1
HfC + F2(g) = HfF2 + C	-144.0
0.3Cr3C2 + F2(g) = CrF2 + 0.6C	-148.8
.25Cr4C + F2(g) = CrF2 + 0.25C	-149.6
0.25Cr4C + F2(g) = CrF2 + 0.25C	-149.6
0.14Cr7C3 + F2(g) = CrF2 + 0.43C	-150.1
0.04Cr23C6 + F2(g) = CrF2 + 0.26C	-152.4
0.04Mn23C6 + F2(g) = MnF2 + 0.26C	-169.9

3.2.9 XRD analysis on corrosion surface

XRD analysis was performed to identify the phases present in the nickel-based alloys. Figure 89 show XRD patterns for the as-received Hastelloy-N, Alloy A and Alloy B. All alloys show strong (111), (200), (220), and (311) γ-austenite peaks corresponding to the face-centered-cubic (FCC) nickel matrix. Several smaller peaks match well with a variety of M_6C type metal carbides. This suggests that the precipitates characterized with SEM & EDS are M_6C carbides. Some peaks cannot be associated with either of these phases. Zhu et al. [127] reported similar peaks in Hastelloy N after exposure to FLiNaK in graphite crucibles and concluded that these peaks corresponded to the $Cr_9Mo_{21}Ni$ phase. The signal strength of peaks corresponding to Ni_5Hf were of insufficient intensity and could not be identified.

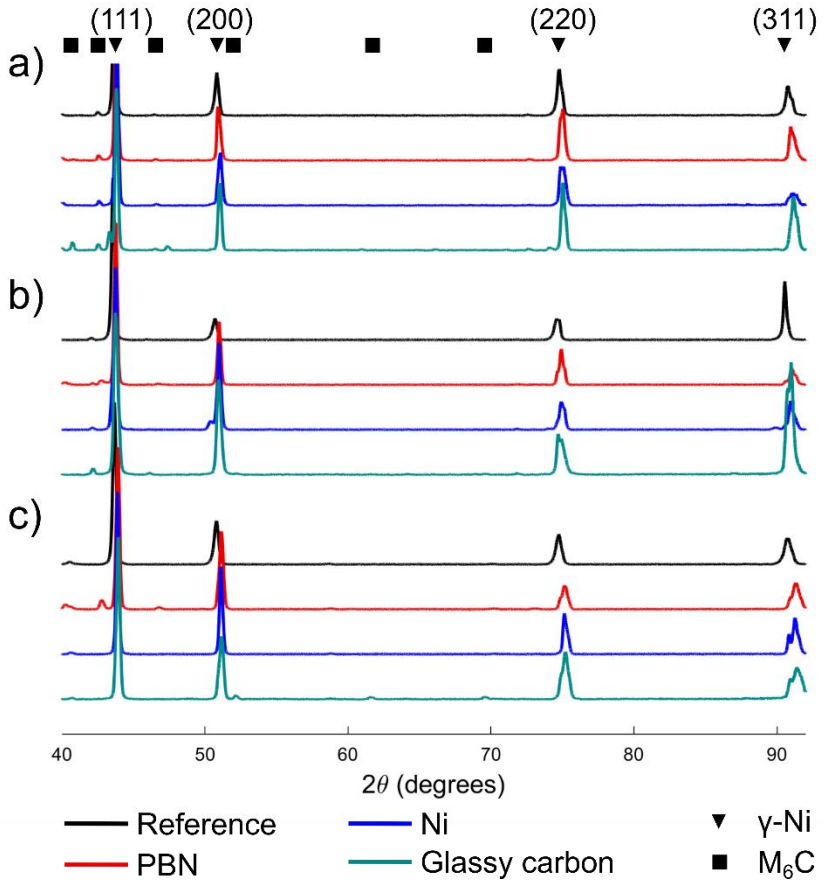

Figure 89. XRD patterns of (a) Alloy N, (b) Alloy 141, and (c) Alloy 3 before and after exposure to FLiNaK in nickel, PBN, and glassy carbon capsules for 500 hours at 700 ˚C.

To investigate the relationship between the alloys' microstructures and compositional changes, the lattice parameter of γ-austenite phase was determined. In Figure 90, a linear regression of the calculated lattice parameter for the (200), (220), and (311) γ-Ni peaks vs. the Nelson-Riley extrapolation function ($\cos^2(\theta)/\sin(\theta) + \cos^2(\theta)/\theta$) was performed. The measured lattice parameter was obtained from the y intercept of the regression. The lattice parameter of the reference Alloy N, 141, and 3 were 358.90 pm, 359.47 pm, and 359.05 pm, respectively. The net change in lattice parameters of the exposed alloys were also calculated and are shown in Table 20. All the alloys experience a decrease in lattice parameter after exposure to molten salt, suggesting that elements in solid solution are being depleted and entered the molten salt.

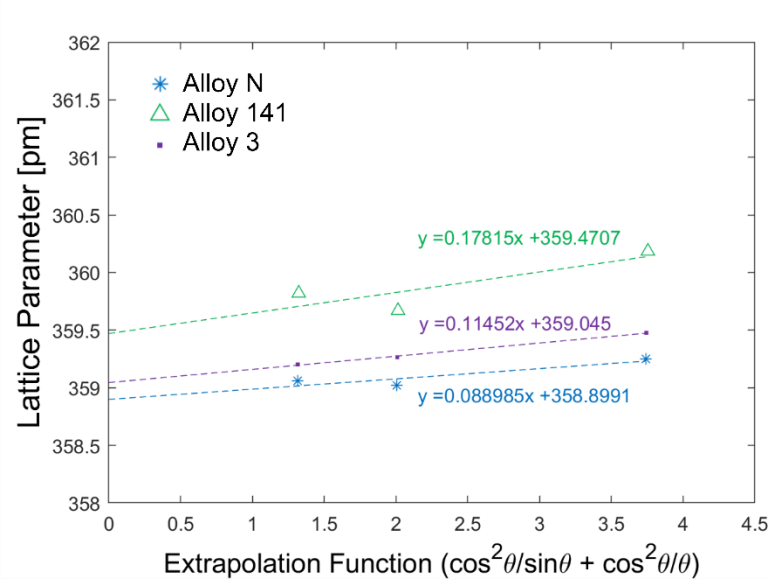

Figure 90. Calculated lattice parameter as a function of the Neslon-Riley extrapolation function ($\cos^2(\theta)/\sin(\theta) + \cos^2(\theta)/\theta$) for Alloy N, 141, and 3 reference specimens.

Table 20. Net change in lattice parameter measured by Nelson-Riley function extrapolation. Units are in pm.

Capsule	Alloy N	Alloy 141	Alloy 3
PBN	-0.73	-1.07	-1.28
Ni	-0.60	-0.92	-1.25
Glassy carbon	-0.96	-0.40	-1.61

3.2.10 Salt analysis

The change in FLiNaK salt composition as a result of exposure of the specimens in various capsules was investigated with ICP-MS. Figure 91 shows the concentration of S, Cr, and Fe in the salt after the 500-hour corrosion test. Trace sulfur in fluoride salts is known to cause corrosion in nickel based alloys [124]. The sulfur concentration in all capsules decreased significantly indicating that the sulfur has reacted with the alloys. The exact reaction is not clear. The concentration of Fe that was initially in the salt (78 ± 5 μg/g) dropped significantly indicating that Fe may undergo a reaction with the Ni-based alloys, possibly leading to corrosion. Even in the case of Alloy N exposed in PBN, which showed dissolution of Fe from the matrix, the concentration of Fe in the salt remained low. The accuracy of Fe ICP-MS data requires further investigation. The concentration of chromium in the salt increased significantly in PBN and glassy carbon capsules. The highest measured chromium concentration occurred in the glassy carbon capsule that held Alloy N which showed 80 ± 7 μg/g. This was consistent with the deep matrix Cr dissolution observed in the specimen cross section. The concentration of Cr in the salts that were contained in Ni capsules is notably lower than in the PBN capsules (<16 μg/g). The influence of Ni capsules was investigated and is presented in Section 3.2.12.

Other minor alloying elements in Alloy 141 and Alloy 3 were found in the salt. In the capsules that contained Alloy 141, there was 20 to 32 μg/g of Ta, indicating that the element is readily dissolved. In PBN and Ni capsules that held Alloy 3, significant levels of Ta, Ti, and Hf were measured. The salt in the glassy carbon capsule that contained Alloy 3 also contained 8.2 ± 0.8 μg/g. This was the only capsule in which Nb appeared to be present after the experiment. EDS shows that Nb may have been depleted from Alloy 3 in PBN and Ni capsules also. The PBN and Ni capsules were investigated for signs of Nb in Sections 3.2.11 and 3.2.12. These results were consistent with the thermodynamic calculations in Figure 4 which showed that these alloying elements have comparable free energies of fluoride formation to Cr and thus may also be susceptible to corrosion.

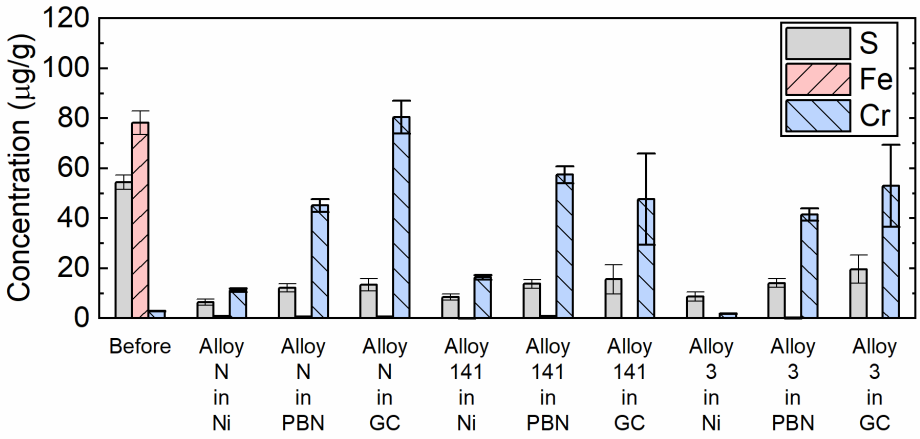

Figure 91. ICP-MS measurements of the S, Fe, and Cr concentration in FLiNaK salt before and after exposure to Alloys N, 141, and 3 in nickel, pyrolytic boron nitride (PBN), and glassy carbon (GC) for 500 hours at 700˚C.

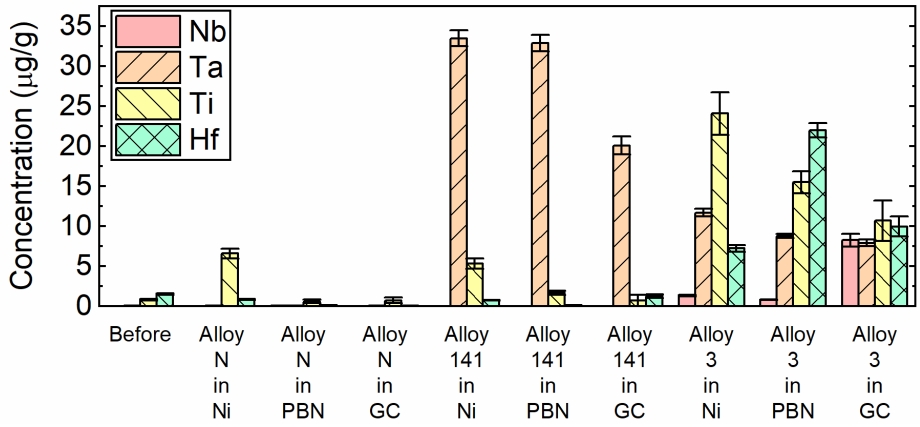

Figure 92. ICP-MS measurements of the Nb, Ta, Ti, and Hf concentration in FLiNaK salt before and after exposure to Alloys N, 141, and 3 in nickel, pyrolytic boron nitride (PBN), and glassy carbon (GC) for 500 hours at 700˚C.

3.2.11 Pyrolytic boron nitride (PBN) capsules

To understand if the PBN capsules play a role in Ni-based alloy corrosion, the inside diameter of a section of the capsules were examined with SEM & EDS for corrosion product mass transfer. The inside of the PBN capsules which held Alloy N for 500 hours at 700 ˚C is shown in Figure 93(a). After exposure, the capsule showed minimal sign of deposits and the salt remaining on the surface after exposure was easily removed with the 1 M aluminum nitrate solution. To improve the conductivity of the PBN surface so that

SEM and EDS analysis could be performed, the PBN capsules were sputter coated with 10 nm of Au. The Au coated specimens are shown in Figure 93(b). EDS analysis was performed on the three PBN capsules used for the three nickel-based alloys' exposure tests. Figure 94(a) and (b) show SEM images of a PBN coupon produced by the same manufacturer and methods and the capsule that contained Alloy N, respectively. Figure 94(c) shows the typical EDS area average spectra for the Au coated PBN. The average composition is dominated by Au which is greater than 96 wt. % of the measured elements on the PBN surface. The concentration of other minor alloying elements relevant to the nickel alloys which are found in addition to Au are plotted in Figure 94(c). Accurate quantification of these minor alloying elements on the surface is challenging with this technique. Considering that the concentration of these elements is below 3 wt. % in a Au coating that is only 10 nm thick, the concentration of the alloying elements deposited on the surface of the PBN is negligible. It was concluded that the PBN capsules do not have an affinity for certain alloying elements that may influence the corrosion of nickel alloys, as in the case of other capsule materials.

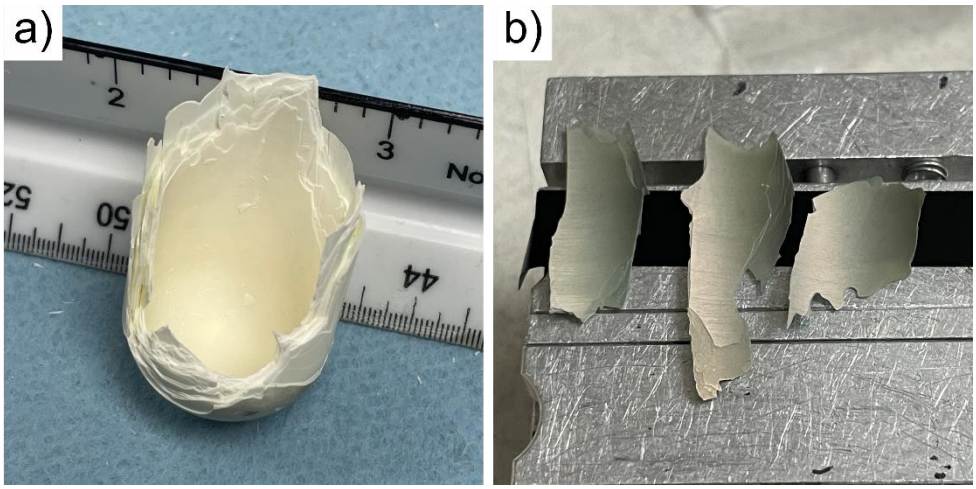

Figure 93. Images of (a) the inside of the bottom of the PBN capsule that contained Alloy N and (b) the PBN capsules specimens after sputter coating with 10 nm of Au to impart conductivity. Capsules were exposed to FLiNaK for 500 hours at 700 ˚C.

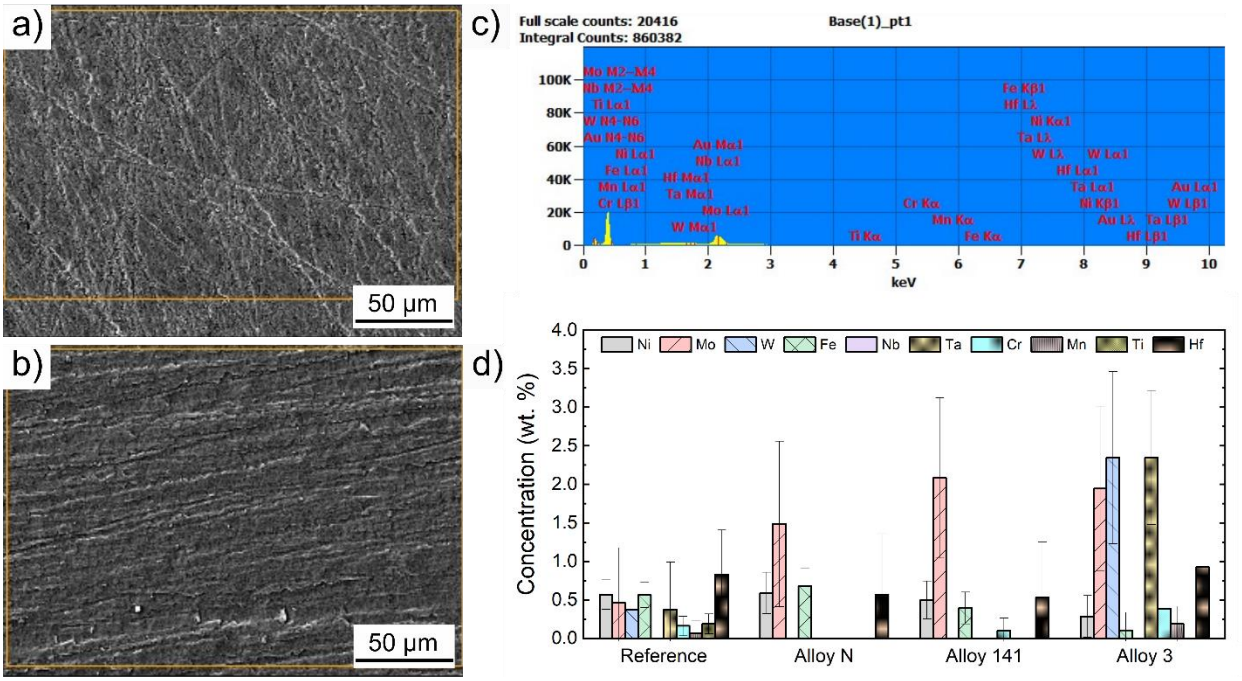

Figure 94. Compositional analysis of (a) the PBN reference coupon, (b) the inside diameter of the PBN capsule which contained Alloy N, (c) the EDS spectra for the capsule which contained Alloy N, and (d) the concentration of various alloying elements detected on the PBN capsules before and after exposure. The PBN is sputter coated with 10 nm of Au to improve conductivity. Au makes up the balance of the area average composition.

The results show that PBN capsules provide a relatively inert environment in the context of promoting corrosion of alloying elements in the test samples. This allows for a comparison of the corrosion of alloys with widely varying compositions, in isolation, without the influence of dissimilar materials effects. However, study of dissimilar materials effect is important for MSR applications given the multiple materials may coexist in the MSR in the molten salt medium.

3.2.12 Nickel capsules

In response to recent findings by Falconer et al. [55], the possible influence of capsule materials on the corrosion of the test specimens was investigated with EDS. Figure 95 shows SEM images of the inner salt-facing surface of the nickel capsules which contained the three alloys, Alloy N, 141, and 3. EDS area averages of the surfaces are shown in Figure 95(a)-(c). This test revealed that there as a net increase of Cr of about 1 wt. % in all exposed nickel capsule surfaces. In the case of the capsule which held Alloy N there was also 1 wt. % net increase in Fe concentration. While the effect is subtle, the Cr and Fe transported are

likely spread out over the entire capsules surface. The net transport of these alloying elements from the specimen to pure nickel is therefore quite significant.

To investigate possible driving forces for the observed mass transport in nickel capsules, cross sectional EDS analysis was performed to examine for evidence of diffusion of Cr and Fe into the nickel matrix. Figure 95(d) shows a photograph of the cross sectioned nickel capsule. To protect the capsule surface during polishing, it was sputter coated with Au, and electroplated with Cu prior to mounting and polishing. EDS cross-sectional analysis shows that there is some diffusion of Cr and Fe into the nickel at the exposed surface.

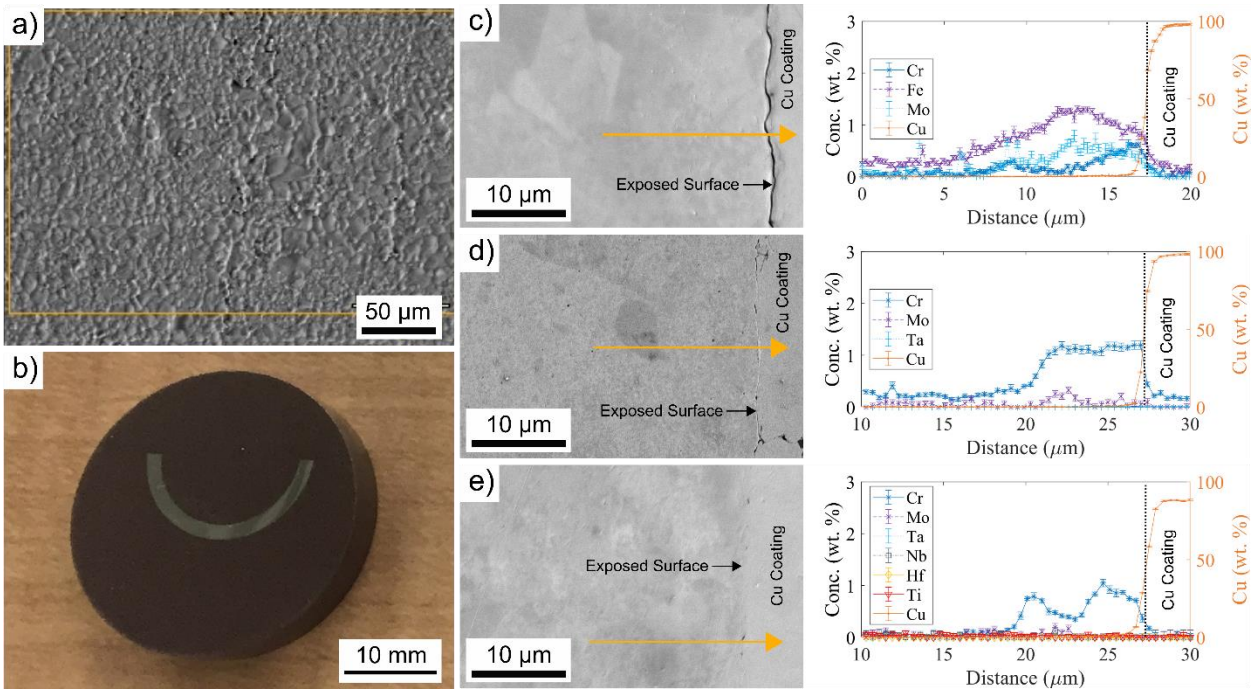

Figure 95. Nickel capsule SEM and EDS analysis of (a) the inside diameter of the nickel capsules that contained Alloy N, (b) photograph of a mounted capsule cross section. EDS line scan of cross sections of the nickel capsules which contained (c) Alloy N, (d) Alloy 141, and (e) Alloy 3 in FLiNaK for 500 hours at 700 ˚C. Cross sections were etched during 0.2 µm colloidal silica polishing.

It is speculated by Falconer et al. [55] that the affinity of the nickel matrix for these alloying elements leads to an activity gradient driven mass transport mechanism. The solubility of various alloying elements in the dissimilar material is one way to evaluate whether mass transport of certain alloying elements is likely to occur. Table 21 shows the solubility limit of various alloying elements in Ni. Iron and

chromium have the highest solubilities. The other refractory metals Nb, Hf, Ti, and Ta have poor solubility. This may explain why only Fe and Cr are observed diffusing into the nickel capsules. If corrosion of Fe and Cr occurs, the nickel capsule may act as a sink establishing a concentration gradient of corrosion products within the salt and providing a driving force for further corrosion. This also explains why there is a lower concentration of Cr in the salts contained in Ni after exposure despite the alloy showing higher weight loss.

Table 21. Solubility of alloying elements in the nickel matrix obtained from phase diagrams.

Alloy Element	Solubility in Ni matrix (at.%)	Solubility in Ni matrix (wt.%)	Reference
Fe	88	87.5	[128]
Nb	8	12.1	[129]
Ta	4	11.4	[130]
Cr	25	22.8	[131]
Ti	9	7.5	[132]
Hf	2	5.8	[133]

3.2.13 XPS analysis of Alloy 3

There are two hypotheses about why alloys like Alloy 3 lose less weight in glassy carbon capsules than they do in PBN capsules. The first is that while extensive corrosion may be occurring, mass transport of carbon from the capsule material to the specimen surface may be mitigating the net weight change of the specimen. The second is that the corrosion reactions taking place are fundamentally different resulting in different magnitudes of weight loss per mole F_2(g). Depending on if the species undergoing corrosion is in a metallic or carbide phase, the quantity, chemical state, and location of carbon on the specimen surface could be indicative of what reactions are occurring. While EDS can detect carbon, the accuracy of the carbon measurement is insufficient and deemed only qualitative. XPS is a an accurate and surface sensitive analysis technique, described in Section 2.3.7.2, is an effective method to detect the chemical state of carbon and other elements in the near-surface region of a material.

XPS was used to measure the elemental composition, chemical state, and electronic state Cr, Mo, and C on the surface of Alloy 3 before and after exposure to molten FLiNaK in PBN and glassy carbon

capsules as shown in Figure 96. By sputtering for increments of 30 seconds, layers of the surface were removed and the scans were repeated in order to obtain a depth profile. The specimen was sputtered for 30 seconds before acquiring the first scan to remove naturally occuring surface contamination that mainly constitutes carbon. By scanning select ranges of binding energies, peaks corresponding to the characteristic photoelectrons from the elements Cr, Mo, and C were detected. In Figure 96(a), the as-polished Alloy 3 specimen before exposure showed peaks at 583 eV and 574 eV corresponding to the Cr $2p_{1/2}$ and Cr $2p_{3/2}$ photoelectrons, respectively. Peaks at 231 eV and 228 eV corresponded to the Mo $3d_{3/2}$ and Mo $3d_{3/2}$ photoelectrons, respectively. Elemental carbon typically shows a peak at 285 eV corresponding to the C 1s photoelectron. This was not present in the as-received Alloy 3 which showed a peak labeled A in Figure 96 at around 283 eV. A number of carbides have photoelectron binding energies in this range including Cr_3C_2 (282.8 eV), Mo_2C (282.7 eV), NbC (281.9 eV), Ni_3C (283.9 eV), TaC (281.9 eV), and TiC (281.6 eV) [134]. Given the high concentration of Mo in Alloy 3 it is likely that peak A corresponds to Mo_2C. In the case of Cr and C, the depth profiles had a constant intensity with depth. Mo increased slightly as a function of depth in the first few scans but settled at a constant value.

XPS of Alloy 3 exposed in PBN capsules shows signs of compositional changes in the near surface region compared to the specimen before exposure in Figure 96(b). The magnitude of the peaks corresponding to Cr decreased slightly. This is consistent with the cross-sectional EDS lines scan, in Figure 76, which showed that the Cr had been depleted to a significant depth but that the composition of Cr at the surface had not gone to zero. The intensity of the Mo peaks also increases. This is also consistent with the EDS line scan in Figure 76 which showed a thin layer of Mo enrichment at the specimen surface. Examining the peaks corresponding to the carbide phase, there also appears to be a new peak at the surface corresponding to C 1s. There is a gradual shift from a peak dominated by the C 1s to a peak dominated by the carbide phase as a function of depth. This seems to indicate carbonization had occurred on the specimen surface during corrosion. The source of carbon in the PBN capsule system remains unclear. It is speculated that an oxidation reaction involving the Nb-, Hf-, Ta-, or Ti- rich carbides, such as the reactions in Table

19, could liberate carbon at the specimen surface which can remain as a free carbon film or react partially with Mo in solid solution to reform a Mo-carbide.

The corrosion process occurring in glassy carbon is differentiated from corrosion occurring in PBN capsules by a lower net weight loss and smaller depth of matrix Cr depletion. In glassy carbon, EDS indicates that the surface concentration of Cr is close to zero. This was confirmed with XPS in Figure 96(c) which does not show Cr peaks. The lower activity of Cr at the alloy surface will likely influence the alloys apparent redox potential and could make different corrosion mechanism favorable. The effects of apparent redox potential will be discussed in more detail in Section 3.3. EDS and ICP also indicate that more Nb and less Hf is oxidized. Based on the higher concentration of Nb found in the salt in glassy carbon, there is a difference in the oxidation potential that Alloy 3 experiences in this capsule environment that provides a driving force for Nb dissolution. The difference in oxidation potential may be the result of galvanic effects from the glassy carbon capsule.

The oxidation of different carbides depending on the capsule environment has important implications for the alloys surface chemistry and long-term corrosion resistance. Hf It should be noted that certain metals have preferred oxidation states when converted to a fluoride. For example, Hf is one of the primary corrosion products of Alloy 3 in PBN. If it is assumed that the dissolved fluoride of Hf, is HfF_2 then the reaction between HfC and $F_2(g)$ would be

$$HfC + F_2(g) = HfF_2 + C \quad (52)$$

Here one mole of $F_2(g)$ reacts to form one mole of HfF_2 dissolved in FLiNaK and one mole of solid carbon. The net weight loss would be equivalent to one Hf atom (178.49 a.m.u.). Now consider the case where Nb (92.90 a.m.u.) is preferentially depleted as in Alloy 3 in glassy carbon. The exact oxidation state of Nb is not known in FLiNaK but NbF_5 has a very high negative free energy of formation. If Nb exists in Alloy 3 as NbC, the corrosion reaction is

$$0.4NbC + F2(g) = 0.4NbF5 + 0.4C \quad (53)$$

and 2.5 moles of $F_2(g)$ are required to produce one mole of NbF_2. If the corrosion reaction is

$$0.2Nb_2C + F_2(g) = 0.2NbF_5 + 0.2C \quad (54)$$

then 5 moles of $F_2(g)$ are required to produce one mole of NbF_5. Since the amount of $F_2(g)$ can be considered the finite reactant in this case, clearly the number of moles and mass of the metal depleted will differ greatly. Assuming the corroded carbide is Nb_2C, one mole of F_2 gas will reduce the mass by 0.2*92.90 a.m.u. = 18.58 a.m.u. This is a large difference in mass loss per mole of reacting F_2 gas. Note that the amount of carbon liberated is 5 times less for the Nb_2C reaction than the HfC reaction.

Comparing the carbon peaks in Figure 96 (b) and (c), there is a lower amount of carbon on the surface of Alloy 3 in the glassy carbon capsule than there is on the specimen in a PBN capsule. This suggests that some transport of carbon from the glassy carbon to the sample that could explain the difference in weight loss has not occurred. Carbon would be liberated in the corrosion carbides. This is believed to be the reason why elemental carbon and carbides are present in the near surface region of Alloy 3 in glassy carbon.

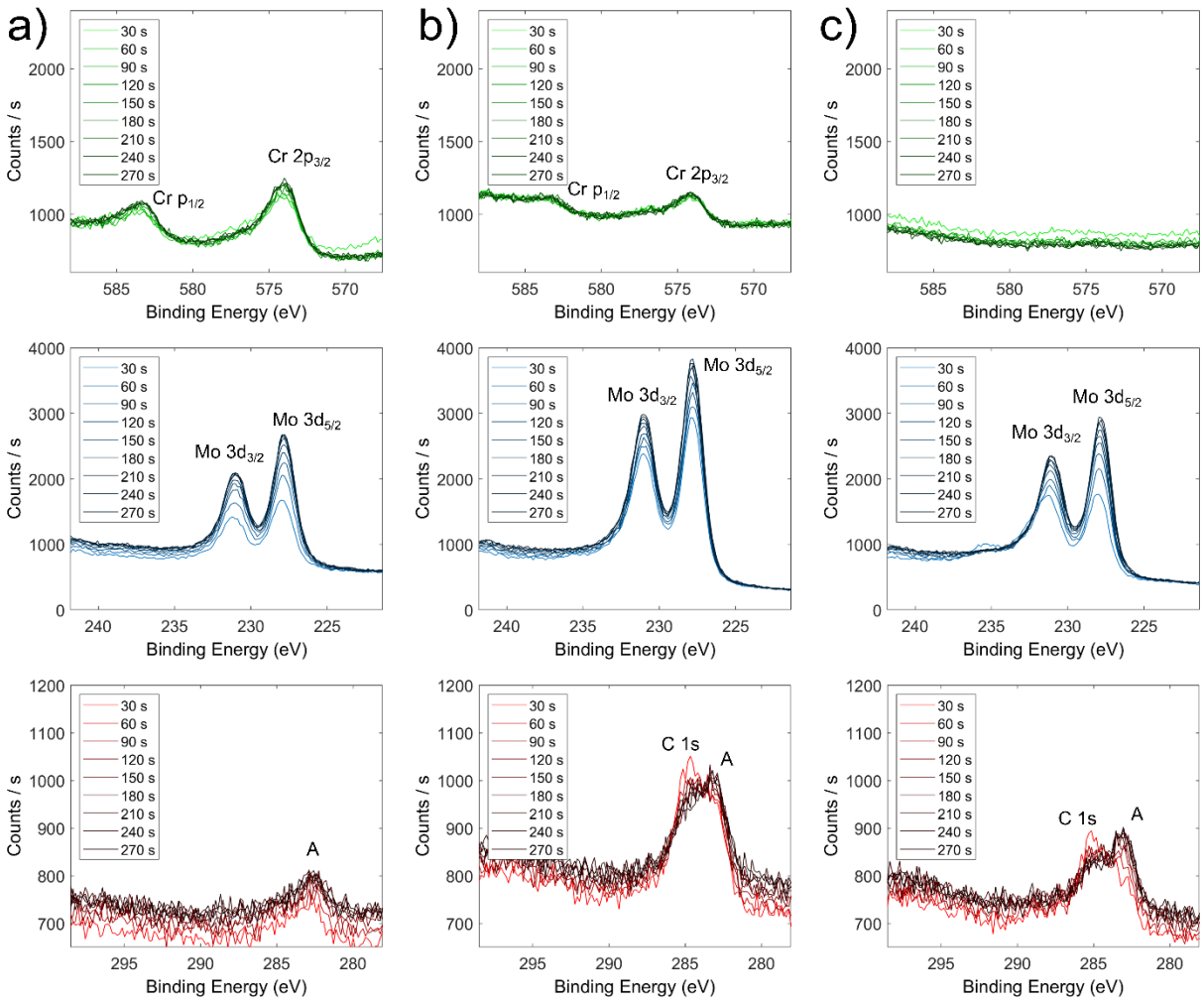

Figure 96. XPS spectra of Alloy 3 surface (a) before exposure, and after exposure to FLiNaK in (b) a PBN capsules, and (c) a glassy carbon capsules for 500 hours at 700 ˚C.

3.2.14 Discussion

The goals of the above corrosion study were to determine which elements are most susceptible to corrosion in candidate advanced concept nickel-based alloys, which microstructural phases are stable, and the effect of dissimilar materials on corrosion. As previously discussed, the weight change after exposure to molten salts, while an important engineering metric, does not shed light on corrosion mechanisms in play in the molten salt environment. Compared to the tested iron-based stainless steels, the nickel-based alloys experience negligible surface recession. Instead, corrosion manifested more strongly as compositional and microstructural changes in the near surface region. Detailed materials characterization was required to

reveal the differences in alloy behavior. The specimens experienced differences in the type of corrosion, the elements depleted, the phases in which corrosion occurred, and dissimilar materials effects.

Comparison of the surface topography, composition, and near-surface microstructural changes of the nickel-based alloys in different capsules revealed striking differences between the corrosion mechanisms occurring in each capsule environment. Three quantifiable types of corrosion are observed: surface recession (uniform corrosion), preferential elemental dissolution within the matrix, and preferential elemental dissolution along grain boundaries. Table 22 summarizes the results obtained from this experiment. Total depth of corrosion is calculated by summing the measured surface recession and either the depth of grain boundary Cr dissolution or the depth of matrix Cr dissolution depending on which is greater. It should be noted that corrosion of precipitates is possible, however, this type of corrosion was not easily quantified and is thought to be less severe than Cr dissolution from the matrix or grain boundaries.

Table 22. Summary of Alloy N, Alloy 141, and Alloy 3 corrosion rate and corrosion mechanisms in various capsule materials after exposure to FLiNaK for 500 hours at 700 ˚C.

Specimen	Capsule	Weight Change (mg cm^{-2})	RMS Surface Roughness (μm)	Surface Recession (μm)	Depth of Grain Boundary Depletion (μm)	Depth of Matrix Cr Dissolution (μm)	Total Depth of Corrosion (μm)	Type of Corrosion Attack
Alloy N	PBN	-0.317 ± 0.005	0.072	0.15	6.6	0.0	6.8	Grain boundary Cr dissolution
Alloy 141	PBN	-0.333 ± 0.005	0.163	0.15	0.0	12.0	12.1	Matrix Cr dissolution
Alloy 3	PBN	-0.330 ± 0.005	0.204	0.10	0.0	15.0	15.1	Matrix Cr dissolution
Alloy N	Ni	-0.34 ± 0.01	0.129	ND	0.0	9.0	9.0	Matrix Cr dissolution
Alloy 141	Ni	-0.47 ± 0.01	0.299	ND	0.0	9.0	9.0	Matrix Cr dissolution
Alloy 3	Ni	-0.61 ± 0.02	0.258	ND	0.0	12.0	12.0	Matrix Cr dissolution
Alloy N	Glassy carbon	-0.41 ± 0.01	0.182	0.50	0.0	7.0	7.5	Matrix Cr dissolution
Alloy 141	Glassy carbon	-0.165 ± 0.001	0.220	0.40	0.0	4.0	4.4	Matrix Cr dissolution
Alloy 3	Glassy carbon	-0.197 ± 0.002	0.253	0.30	0.0	3.0	3.3	Matrix Cr dissolution

The capsule environment has an important effect on the dominant types of corrosion attack observed. In most cases, the type of corrosion attack tended to be matrix Cr dissolution. This type of

corrosion could lead to void formation in the bulk as a result of the Kirkendall effect [125]. Nickel alloys exposed in nickel showed higher weight loss than in other capsule environments. This is explained by the dissimilar materials effect discussed in Section 3.2.12. The nickel alloys exposed in glassy carbon capsules showed slightly more surface recession than in PBN capsules, however, only Alloy N experienced more weight loss in glassy carbon than it did in a PBN capsule. This indicates that glassy carbon may have a dissimilar materials effect on the nickel alloys. ICP and EDS indicated that Hf was the primary corrosion product of Alloy 3 in PBN, while significantly more Nb was oxidized when Alloy 3 was exposed in glassy carbon. The XPS surface chemical analysis performed on Alloy 3 exposed to glassy carbon and PBN may indicated that mass transport of carbon from glassy carbon was not a significant factor in determining the weight loss, however, the conditions imposed by glassy carbon led to more corrosion of Nb. The formation of elemental carbon and or increased concentrations of molybdenum carbides on the surface may give rise to a protective coating on the surface of the alloy that could help slow or prevent outward diffusion and oxidation of chromium. These changes in material surface chemistry and bonding have important implications for the long-term corrosion resistance of the alloy.

A collective examination of the above results suggests that corrosion performance of Alloy N, Alloy 141, and Alloy 3 are quite comparable. This is important to the innovation of MSR technology as the new creep resistant alloys could enable the reactor to operate safely for longer periods of time. However, closer examination of individual metrics for corrosion of the two materials has revealed subtle differences in the corrosion mechanisms. Certain alloying additions, such as Hf, Nb, Ti and Ta appear to be susceptible to corrosion in certain circumstances. To deploy these alloys, the conditions under which each of these alloying elements is preferentially corroded must be understood and salt chemistry control methods must be implemented to prevent severe corrosion.

Some additional corrosion metrics may be important for enhancing the understanding of corrosion mechanisms and kinetics. For instance, when Cr is depleted from the matrix the concentration of Cr at the alloy surface does not always go to zero. For example, for Alloy 3 tested in a PBN capsule, the Cr

concentration did not go to zero at the alloys surface, however, this specimen showed the deepest matrix Cr depletion and one of the lowest surface recessions. On the other hand, Alloy 3 in glassy carbon showed a very small depth of matrix Cr dissolution, but the concentration of Cr went to zero at the alloy surface.

Corrosion of the nickel-based alloys is influenced heavily by compositional and microstructural changes in the near surface region. These changes are summarized in Table 23. Approximate thermodynamic calculations in Figure 4 predicted that Cr, Hf, Ta, and Ti could possibly be susceptible to corrosion in molten fluoride salts. Assessment of corrosion of specific alloying elements were performed using a combination of SEM-EDS and ICP-MS, and to a limited extent XPS. In all capsule environments, Cr was the dominant corrosion product dissolved from the alloy surface and measured in the salt after exposure. Other additional alloying elements added for creep strength also experienced dissolution depending on the capsule environment. In the Ni capsule, Fe preferentially corroded in Alloy N to a comparable depth as Cr. In Ni and PBN capsules, Ta experienced preferential corrosion in Alloy 141 in addition to Cr. Salt analysis for Alloy 3 showed increased concentrations of Ta, Nb, Ti, and Hf, which are commonly found in Alloy 3's precipitates. These alloying elements are dissolved primarily from the precipitates in all capsule environments tested.

Table 23. Summary of types of corrosion attack, phase stability predictions and observations, and effects of dissimilar capsule materials on the nickel alloys exposed to molten FLiNaK for 500 hours.

Alloy	Type of corrosion and element(s) corroded	Phase stability predictions (Observed corrosion effects on predicted phases)	Effect of dissimilar capsule materials
N	Grain boundary and or matrix Cr dissolution	Mo rich M_6C & p-phase (Mo and Ni rich carbide) were predicted. (Carbides were stable before and after corrosion.)	Fe in the alloy matrix: • Was stable in PBN and glassy carbon capsules • Showed dissolution Ni capsules Deposited Fe and Cr showed alloying effects with nickel capsules
141	Matrix Cr dissolution	Mo and Ta rich M_6C phase was predicted. (Mo carbides were stable before and after corrosion. Some Ta was dissolved from precipitates.)	Ta in the alloy matrix: • Was stable in PBN capsules • Showed dissolution in Ni and glassy carbon capsules Deposited Cr showed alloying effects with nickel capsules Weight loss was suppressed in the glassy carbon capsule due to carbide and other secondary phases
3	Matrix Cr dissolution Precipitate Hf, Nb, Ta, & Ti dissolution	A large volume fraction of M_6C were predicted due to higher carbon. Precipitates are rich in Mo, Hf, Nb, Ta, & Ti (The majority of Hf, Nb, Ta, & Ti that was corroded came from the precipitates.)	Deposited Cr showed alloying effects with the nickel capsules Weight loss was suppressed in the glassy carbon capsule

The phase stability has been investigated with computational and materials characterization methods. The precipitate phases, such as M_6C, were predicted to be thermodynamically stable in the bulk alloy at 700 ˚C using Pandat software. Thermodynamic calculations showed that most carbides have a low Gibbs free energy of formation. In Alloy N and 141, the precipitate phases remained stable in the molten fluoride salt environment. The matrix experiences the majority of alloying element depletion. In Alloy 3, the Nb, Ti, Ta, and Hf rich carbides of the type M_6C are depleted from the near surface region of the alloy

after exposure. Increased concentrations of Mo on the surface of these alloys indicates that a Mo rich carbide or silicide may have been stable, suggesting a path for future research on alloy design or protective coatings.

Dissimilar materials effects on corrosion stemming from using different capsule materials were clearly evident in nickel-based alloys. For the nickel capsule tests, Cr and Fe deposition was observed on the capsule's inners surface. This suggests that the depletion of these elements was promoted by the capsule material. The PBN capsule was relatively inert in regard to inducing selective corrosion of alloying elements with minimal evidence of elemental deposition on the capsule's inner surface. The fact that Alloy N in glassy carbon retained its iron suggests that glassy carbon does not have a significant impact on Fe depletion from the alloy surface. The deposition and alloying elements on the capsule surface in effect removes the dissolved alloying elements in the salt providing a greater driving force for corrosion. For example, the removal of dissolved Cr by its plating on the Ni capsule surface, as observed in this study, may also enhance the driving force for the dissolution of other alloying elements into the molten salt, as may be the case for Alloy 141 and Alloy 3.

3.3 Potentiodynamic Polarization for Understanding Metals and Alloys Corrosion Performance in Molten FLiNaK Salt

The motivation for development of electrochemical potentiodynamic polarization methods was to develop a more fundamental understanding of the electrochemical parameters governing corrosion and for the rapid assessment of the corrosion behavior of pure metals and alloys. Most studies of structural alloys corrosion in molten fluoride salts have been performed using long-term (up to a few thousand hours) static capsule or flow-loop tests followed by characterization of near-surface regions of the samples [121]. These types of experiments, while prototypical to MSR environment, are limited in terms of opportunities for detailed study of corrosion mechanisms and reaction rates that could help better understand the interplay between material and the environment in corrosion. Indeed, the highly corrosive nature of molten fluoride salts coupled with high temperatures warrants the examination of the material-environment system, rather than the material alone, to understand and combat corrosion. Examining the corrosion results presented in the preceding sections, many questions remain about the corrosion mechanisms and corrosion resistance of structural materials in molten salts. For example, what factors and conditions lead to surface recession? When do alloys experience preferential dissolution of alloying elements from the grain boundaries versus the bulk? Besides chromium, do other alloying elements also participate in corrosion? Under what conditions will they experience corrosion? These questions would be prohibitively expensive to answer with traditional static corrosion testing. Under controlled circumstances, potentiodynamic polarization (here-after referred to as polarization in this section) can provide basic electrochemical parameters that describe corrosion in prototypical conditions.

The redox potential of individual alloying elements and the apparent redox potential of alloys, fundamental properties of materials which govern corrosion, can be measured with polarization. A standardized and repeatable set of reference electrodes are pivotal to obtaining meaningful redox potentials using polarization. The lack of availability of suitable robust reference electrode systems for fluoride salts has made it challenging to achieve repeatable results that enable interpretation of corrosion data of metals

and alloys. Most previous studies utilize the Ni/NiF_2 reference electrode [74]–[76], [135]–[138]; however, there are uncertainties associated with this approach due to material-salt interactions, standardization, and calibration [103]. In this research, performed using the eutectic salt mixture LiF-NaF-KF (46.5-11.5-42 mol %, FLiNaK) at 700 ˚C, a K/K^+ dynamic reference electrode (DRE) has been developed and implemented to conduct potentiodynamic polarization measurements of pure metals Ni, Fe, Cr and alloys Ni-20Cr and 316L. Discussion of the theory and state of the art methods for DREs was discussed in Section 1.5.7 and Section 2.5.1. Referencing polarization data with respect to the DRE enabled comparisons of corrosion behavior of pure metals and alloys and interpretation of the oxidation reactions occurring for an alloy at an applied potential.

3.3.1 Measuring the K/K^+ Reference Potential

The potential difference between the Pt QRE and the K/K^+ reference half-cell reaction was measured using cyclic voltammetry (CV), as described in Section 2.5.1. The potential of the QRE, E_{QRE}, is defined as the potential difference between a Pt QRE and the K/K^+ redox couple,

$$E_{QRE} = E_{Pt} - E_{K^+/K} \quad (55)$$

In this experiment, $E_{K^+/K}$ was measured by extrapolating the negative K/K^+ reduction curve to the x-axis. At a given temperature, pressure, and when no significant changes in the salt composition occur, E_{QRE} enables normalization of subsequent data acquired using the Pt QRE, such as polarization data, to the K/K^+ DRE. For each polarization experiment, the E_{QRE} was measured three times prior to polarization and the average value was used. The average salt potential of each molten salt solution used for each material is shown in Tables 24-26. For each metal the standard deviation of E_{QRE} was about 10 mV. In the 316L SS and Ni-20Cr tests, the standard deviation of E_{QRE} measurements were 30 mV and 100 mV, respectively. The reactions which influence E_{QRE} are not well characterized making it necessary to convert data acquired with a Pt QRE with respect to an electrode whose potential can be more easily rationalized. It will be shown that variation in E_{QRE} did not considerably influence the precision of redox potential measurements obtained by polarization.

3.3.2 Specimen Open Circuit Potential

In most polarization experiments, the specimen was exposed to the salt for 100 to 120 minutes depending on the final applied overpotential. To determine the stability of the electrochemical cell over this time, open circuit potential measurements between each specimen and the Pt QRE were measured for at least 2 hours as shown in Figure 97. In general, the OCP of Fe and Ni quickly stabilized and did not change significantly over this time. Chromium, however, showed an initial stable period lasting 15 minutes followed by a large change in OCP. 316L and Ni-20Cr showed slight but constant drifts in potential over time. Factors that may lead to specimen OCP drift will be discussed in later sections.

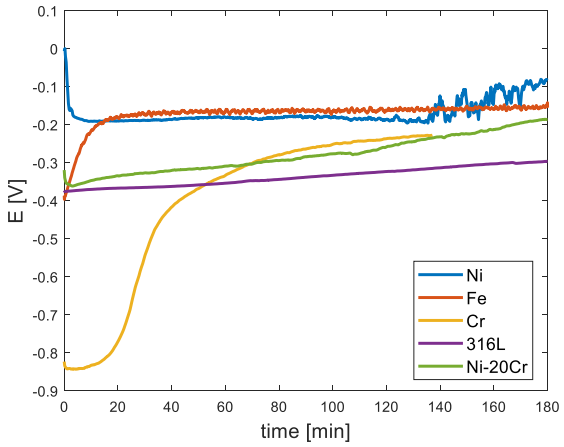

Figure 97. Open circuit potential of Ni, Fe, Cr, the binary alloy Ni-20Cr, and 316L vs. Pt QRE in FLiNaK at 700 ˚C.

3.3.3 FLiNaK Solution Resistance

The solution resistance of the molten FLiNaK was measured to determine whether it is an important factor that could affect the accuracy of these potentiodynamic polarization experiments. The solution resistance, R_s, is the resistance of the electrolyte between the working electrode and reference electrode and induces a potential drop, iR_s, in the measured potential.

$$E_{measured} = E_{applied} - iR_s \tag{56}$$

R_s can be influenced by solution conductivity and cell geometry, such as distance between WE and RE as well as electrode size (double layer capacitance) [139]. Solution resistance was determined by the

current interruption method. A potential was applied to WE2 for one second, after which the current was measured, following which the applied potential was removed. The electrode does not immediately retract to the initial potential because of double layer capacitance. The change in potential after removing the applied potential is calculated by extrapolating the data linearly. The change in applied potential after removing the applied potential is iR_s as the current momentarily drops to zero. The value of the solution resistance is automatically calculated by the Metrohm Nova Software used in this research.

Using an applied potential of -1.5 V vs. Pt and a current range of 10 mA, the average R_s was determined to be $1.3 \pm 0.2\ \Omega$. This compares well with reported values obtained by electrochemical impedance spectroscopy [138],[76],[140]–[142]. FLiNaK therefore has excellent conductivity and introduces minimal error in potential measurements. All potentiodynamic polarization scans yielded currents below 10 mA. At the highest observed current using this cell design, the largest possible iR_s error would be approximately 13 mV. The error near the specimen's redox potential, where the current is small, would be negligible. For comparison, the average standard deviation of salt potential measurements was 18 mV, so the effect is comparable to the precision of salt potential measurement. Nevertheless, iR_s correction was applied to all potentiodynamic polarization scans assuming R_s equals $1.3\ \Omega$.

3.3.4 Potentiodynamic Polarization of Pure Metals

Polarization of the pure metals was performed to obtain the reduction potential, $E_{M^{2+}/M}$, with respect to the K/K^+ reference. The experimental approach including scan parameter was discussed in Section 2.5.2. The final applied anodic overpotential was the primary variable for inducing different amounts of corrosion attack investigated in this study. Overpotential, η, is the difference between the applied potential and the specimen's apparent redox potential, $E_{apparent}$. Ni, Fe and Cr electrodes were polarized to the nominal final overpotentials of 100, 200, and 300 mV to induce varying amounts of corrosion. Tafel plots of the iR_s-corrected polarization data are shown in Figure 98. Assuming that the anodic charge transfer corresponds to the reverse of the half-cell reduction reaction,

$$M^{2+}(d) + 2e^- \rightarrow M(s) \tag{57}$$

where (d) and (s) denote dissolved and solid species, the half-cell reduction potential of each pure metal is

$$E_{M^{2+}/M} = E^{\circ}{}_{M^{2+}/M} + \frac{RT}{nF} ln \frac{a_{M^{2+}}}{a_M} \quad (58)$$

where $E^{\circ}{}_{M^{2+}/M}$ is the standard reduction potential and $a_{M^{2+}}$ is the activity of the dissolved metal fluoride. For pure metals, the activity of the metal, a_M, is unity. The observed $E_{Ni^{2+}/Ni}$ and $E_{Fe^{2+}/Fe}$ were 1.65 ± 0.01 V vs. K/K^+ and 1.29 ± 0.03 V vs. K/K^+, respectively.

The tendency for Cr to dissolve in FLiNaK after just a few minutes necessitated a special approach to obtain repeatable polarization scans. Figure 97 shows that after 15 minutes of exposure for Cr, significant drift in the OCP occurred due to dissolution of the specimen. To address this issue two significant modifications were made to the procedure discussed in Section 2.5.2 to enable the polarization to be completed before significant drift occurred: (i) the total time for measurements (i) & (ii) was reduced to 5 minutes and (ii) measurement 3 was conducted using a higher scan rate of 1 mV s^{-1}.

In Figure 98(c) two Cr electrodes exposed for 5 minutes were polarized to overpotentials of 200 and 300 mV. The average $E_{Cr^{2+}/Cr}$ was 0.842 ± 0.003 V vs. K/K^+. The modifications to the procedure enabled precise measurement of the Cr redox potential. The dependence of $E_{Cr^{2+}/Cr}$ on the exposure time was challenging to quantify. The true value of $E_{Cr^{2+}/Cr}$ at the start of exposure may depend strongly on the Cr^{2+} concentration in the melt and may be only possible to measure by extrapolating from data obtained from subsequent exposure times. The apparent redox potentials of Ni, Fe, and Cr follow a trend that is consistent with the approximate calculations made using the available thermodynamic data [41] and trends reported in literature [138].

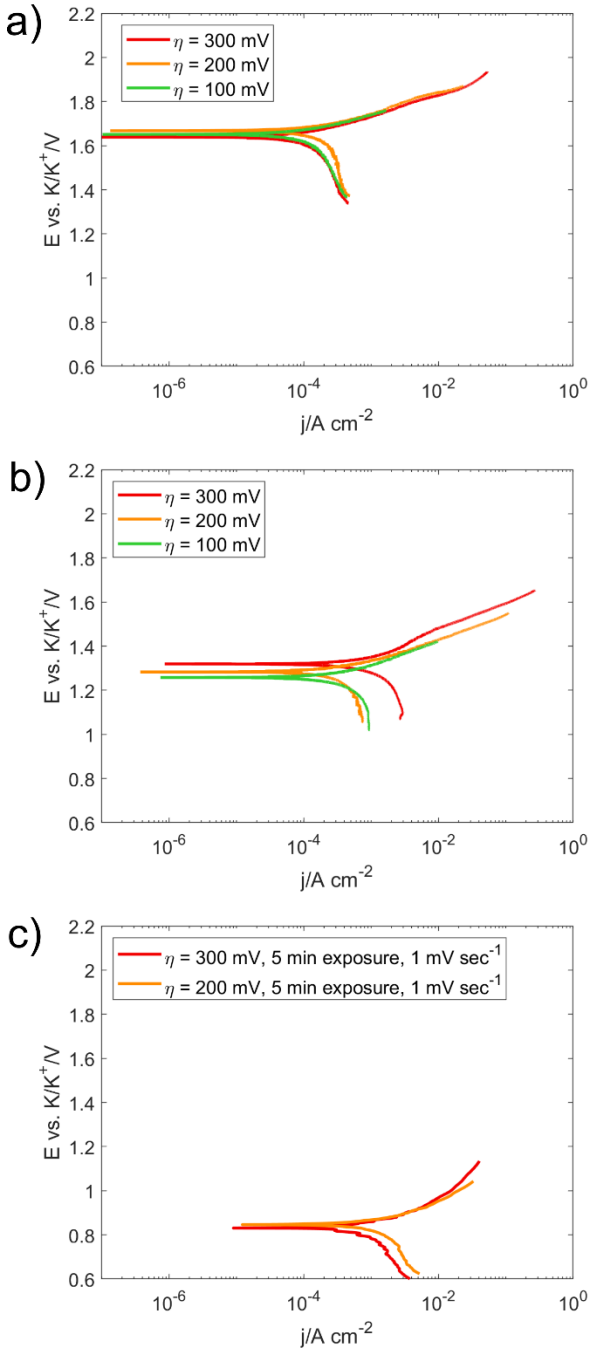

Figure 98. Polarization curves for (a) Ni, (b) Fe, and (c) Cr polarized to various anodic overpotentials, η, in FLiNaK at 700 ˚C.

Tafel extrapolations to measure exchange current density, j_o, and the corresponding Tafel slopes were performed. It is expected that the anodic reaction corresponds to the reverse of Reaction 57 and is activation controlled due to the large quantity of *M* at the interface. In Figure 98, at sufficient anodic

polarization, the curves show linearity confirming that the oxidation processes are activation controlled. The cathodic reaction, on the other hand, is more challenging to determine. Shaffer [118] postulated that several salt impurity-driven reduction reactions may be possible in fluoride salts. Hydrogen fluoride may be reduced to H_2 gas.

$$2HF_{(d)} \rightarrow H_{2\,(g)} + 2F^-_{(d)} \tag{59}$$

Sulfates, SO_4^{2-}, may participate in a two-step reduction reaction. First, dissolved sulfide ions, $S^{2-}_{(d)}$, are formed through a corrosion reaction with metals in the system. Second, the sulfide ion can react with HF in the salt to form H_2S gas.

$$SO_4^{2-}{}_{(d)} + 4M^0_{(s)} \rightarrow 4MO_{(s)} + S^{2-}_{(d)} \tag{60}$$

$$2HF_{(d)} + S^{2-}_{(d)} \rightarrow H_2S_{(g)} + 2F^-_{(d)} \tag{61}$$

Some metal fluoride impurities may undergo either soluble-soluble reduction reactions,

$$M'F_{3(d)} \rightarrow M'F_{2(d)} + F^-_{(d)} \tag{62}$$

or soluble-insoluble reduction reactions.

$$M'F_{2(d)} \rightarrow M'^0_{(s)} + 2F^-_{(d)} \tag{63}$$

Here M' indicates that this cation is native to the salt not the specimen. Reactions 59 and 62 should not affect the specimen surface composition because their products are either gaseous or soluble. Reactions 60 and 63, on the other hand, could change the surface topography and or composition of the specimen. While the exact reaction is not known, it is assumed that the cathodic reaction is Reaction 59. If other impurities, such as dissolved metals fluorides or sulfur are taking part in the cathodic reaction, Table 12 indicates that they are likely very dilute. Despite the low potential scan rate used, the cathodic curves are often not linear due to concentration polarization. For this reason, the reported cathodic Tafel extrapolations should be treated qualitatively.

Tafel analysis was performed by linear Tafel extrapolation of the experimental polarization data. In Figure 99, the Tafel extrapolations are fitted programmatically using a regression of both anodic and cathodic data. Different slopes were selected for the anodic and cathodic data at a plausible values of j_o. The estimate of j_o is the set of coefficients which yielded the smallest combined root-mean-squared error

for both the fitted anodic and cathodic data, weighting both data sets equally. The regions of the anodic and cathodic curves which yielded the optimal fit are highlighted in red. The results for each pure metal are tabulated in Tables 24-26. For each scan, the exchange current density, j_o, the anodic Tafel slope, β_a, and the cathodic Tafel slope, β_c, and their associated coefficient of determination, R^2, are also tabulated. The average j_o values of Ni, Fe, and Cr are 130 ± 40 μA·cm^{-2}, 330 ± 50 μA·cm^{-2}, and 1200 ± 300 μA·cm^{-2}, respectively. Ni showed the lowest exchange current density.

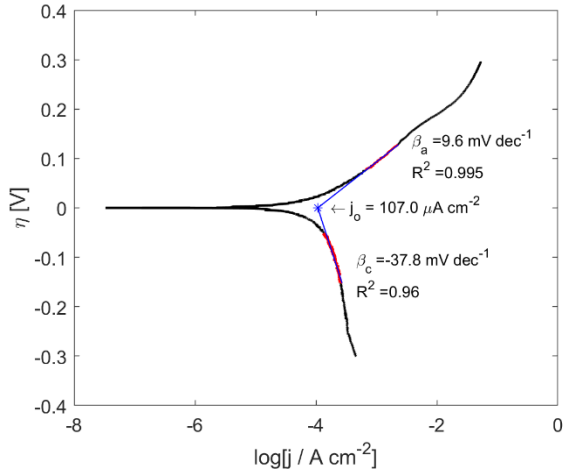

Figure 99. Experimental and fitted polarization curves for Ni polarized to a final anodic overpotential of 300 mV in FLiNaK at 700 ˚C. The regions highlighted in red indicate the portion of the experimental data that is fitted. The blue lines indicate the fitted Tafel extrapolation.

Table 24. Electrochemical parameters for nickel obtained by linear fitting of iR_s-corrected polarization curves in FLiNaK at 700 ˚C.

η	η_{Start}	η_{Finish}	E_{QRE}	$E_{Ni^{2+}/Ni}$	β_a	$R^2{}_a$	β_c	$R^2{}_c$	j_o
[mV]	[mV]	[mV]	[V vs. K/K$^+$]	[V vs. K/K$^+$]	[mV dec^{-1}]	[%]	[mV dec^{-1}]	[%]	[μA·cm^{-2}]
100	-284	109	1.895 ± 0.004	1.652 ± 0.004	8.8	99.5	-40.3	63.4	97.6
200	-295	203	1.908 ± 0.001	1.668 ± 0.001	10.4	99.6	-58.5	86.1	177.7
300	-301	296	1.879 ± 0.006	1.639 ± 0.006	9.6	99.5	-37.8	96.0	107.0
Average			1.89 ± 0.01	1.65 ± 0.01	9.6 ± 0.7		-50 ± 10		130 ± 40

Table 25. Electrochemical parameters for iron obtained by linear fitting of iR_s-corrected polarization curves in FLiNaK at 700 ˚C.

η	η_{Start}	η_{Finish}	E_{QRE}	$E_{Fe^{2+}/Fe}$	β_a	R^2_a	β_c	R^2_c	j_o
[mV]	[mV]	[mV]	[V vs. K/K$^+$]	[V vs. K/K$^+$]	[mV dec^{-1}]	[%]	[mV dec^{-1}]	[%]	[μA·cm^{-2}]
100	-236	163	1.644 ± 0.017	1.25 ± 0.02	11.7	99.7	-37.0	90.8	376.5
200	-225	267	1.638 ± 0.007	1.258 ± 0.007	9.0	98.9	-35.6	92.0	278.6
300	-249	334	1.67 ± 0.03	1.32 ± 0.03	17.5	99.0	-42.8	38.7	1055.9
Average			1.65 ± 0.01	1.29 ± 0.03	13 ± 4		-38 ± 3		330 ± 50*

*The exchange current density from η = 300 mV is considered an outlier and has been excluded from the average.

Table 26. Electrochemical parameters for chromium obtained by linear fitting of iR_s-corrected polarization curves in FLiNaK at 700 ˚C.

η	η_{Start}	η_{Finish}	E_{QRE}	$E_{Cr^{2+}/Cr}$	β_a	R^2_a	β_c	R^2_c	j_o
[mV]	[mV]	[mV]	[V vs. K/K$^+$]	[V vs. K/K$^+$]	[mV dec^{-1}]	[%]	[mV dec^{-1}]	[%]	[μA·cm^{-2}]
200	-223	197	1.67 ± 0.02	0.85 ± 0.02	12.9	98.5	-46.5	97.7	1470.3
300	-230	304	1.687 ± 0.009	0.839 ± 0.009	12.8	98.1	-42.5	98.0	956.1
Average			1.68 ± 0.01	0.842 ± 0.003	12.85 ± 0.09		-45 ± 2		1200 ± 300

SEM in conjunction with EDS was performed on the test specimens (i.e, electrodes) before and after polarization tests as well as after exposure without an applied potential. The surface of as-received specimens of the metal electrodes are shown in Figure 100 (a),(d), and (g) for reference. SEM images of Ni in Figure 100(b), and Fe in Figure 100 (e) show that there is minimal corrosion at the specimen surface after 3 hours of exposure without polarization. As shown in Figure 100 (h) Cr was mostly dissolved after 2.3 hours of exposure. Based on Equation 58 , it is hypothesized that the dissolution increases the apparent half-cell potential of Cr. As will be discussed in Section 3.4.1, adding CrF_2 to 2LiF-BeF_2 caused the reduction potential of the Cr^{2+}/Cr reaction to increase [102]. For this reason, and as already discussed, the polarization test parameters for Cr were changed to achieve a polarization result for a salt with a dissolved chromium concentration closer to the salts used for the other pure metals. The Ni, Fe, & Cr specimen polarized to the nominal overpotential of 300 mV are shown in Figure 100 (c),(f), and (i), respectively. Comparison of the polarized electrodes to the as-received electrode shows that appreciable corrosion had occurred at η = 300 mV and there is a significant reduction in electrode thickness. Ni showed less thickness

loss at η = 300 mV than iron confirming that nickel is more resistant to corrosion under a given applied overpotential than Fe. For both Ni and Fe, the mode of corrosion attack is uniform surface corrosion.

The modified polarization procedure for Cr enabled study of the corrosion parameters without interference from significant dissolution. In Figure 100(i), the polarized Cr electrode shows that the faster 1 mV sec^{-1} scan rate resulted in less thickness loss than the Cr electrode exposed for 2.3 hours shown in Figure 100(h). Less thickness loss at a given final overpotential is observed because faster scan rates reduce the residence time in oxidizing conditions leading to lower total anodic charge transfer.

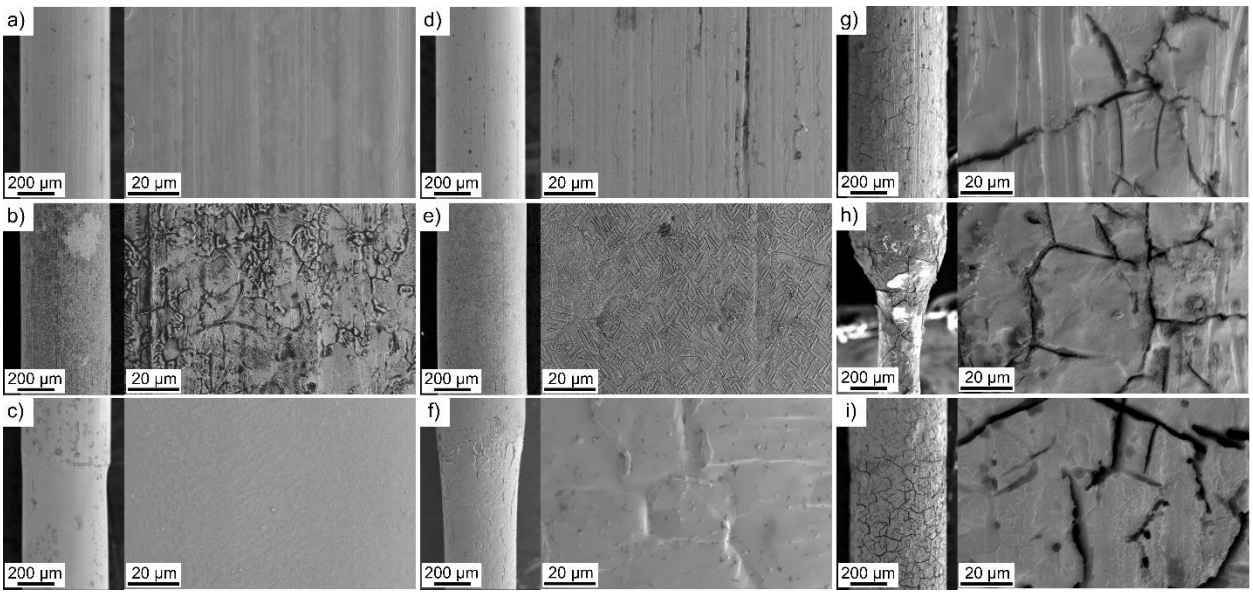

Figure 100. SEM images of (a) as-received Ni, (b) Ni exposed to FLiNaK for 3 hours, (c) Ni polarized to η = 300 mV at 0.166 mV s^{-1} after exposure for 1 hour, (d) as-received Fe, (e) Fe exposed to FLiNaK for 3 hours, (f) Fe polarized to η = 300 at 0.166 mV s^{-1} after exposure for 1 hour, (g) as-received Cr, (h) Cr exposed to FLiNaK for 2.3 hours, (i) Cr polarized to η = 300 mV at 1 mV s^{-1} after exposure for 5 minutes.

3.3.5 Potentiodynamic Polarization of Ni-20Cr

The Ni-20Cr electrodes were polarized to nominal overpotentials of 300, 400, 500, and 800 mV. The iR_s-corrected Tafel plots of this alloy are shown in Figure 101. As shown in Table 27, the average apparent redox potential was 1.33 ± 0.02 V vs. K/K^+. This value is between the average values for Cr and Ni. The result agrees with the trend previously reported in the study by Wang et al. [75] that showed the apparent redox potential of Ni-Cr alloys approaches the redox potential of pure Cr with increasing Cr concentration.

The Ni-20Cr electrodes that were exposed for 3 hours showed noticeable corrosion that may explain the drift in OCP as well as the apparent redox potential. Surface and cross section SEM analysis of Ni-20Cr, in Figure 102(b) and (e), revealed that significant depletion of Cr led to porosity in the near-surface regions of the alloy. The drift of the specimens' OCP is attributed to dissolution of the specimen that may affect the metal's apparent half-cell potential. Increasing the activity of the dissolved metal fluoride in the melt or decreasing the activity of an alloying element could cause a positive drift in the material's apparent corrosion potential.

The anodic polarization curve is characterized by a broad linear region that extends up to η = 500 mV. The average exchange current density was 320 ± 70 $\mu A \cdot cm^{-2}$. The Tafel slopes β_a and β_c were 40 ± 10 $mV\ dec^{-1}$ and -10 ± 3 $mV\ dec^{-1}$, respectively. Qualitatively, Ni-20Cr's exchange current density is lower than for pure Cr and is consistent with the previously reported trend that the exchange current density of the Ni-Cr alloy increases with increasing alloy Cr concentration [75]. The region has relatively high slope compared to the pure elements indicating that greater overpotential is required to achieve the same increase in anodic current as pure Ni or Cr. It is speculated that this behavior is caused by limitations on the reaction rate imposed by diffusion of Cr in the bulk alloy. While Tafel extrapolation is performed, it is less certain if the anodic reaction is truly activation controlled. The parameters are therefore difficult to relate to thermodynamic and kinetic properties of a defined redox reaction at all anodic overpotentials.

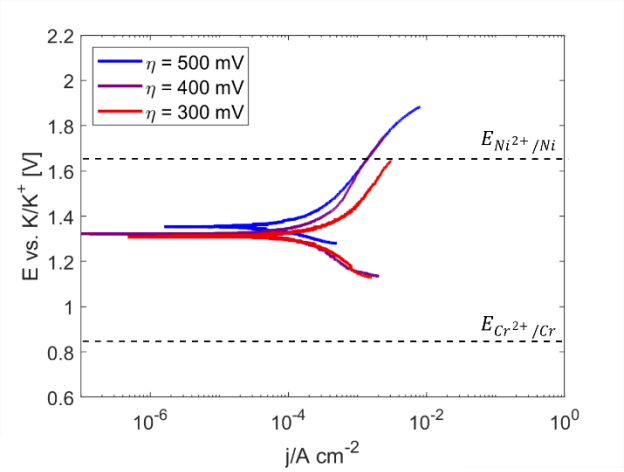

Figure 101. Polarization curves for Ni-20Cr polarized to various anodic overpotentials in FLiNaK at 700 ˚C.

Table 27. Electrochemical parameters for Ni-20Cr obtained by linear fitting of iR_s-corrected polarization curves in FLiNaK at 700 ˚C.

η	η_{Start}	η_{Finish}	E_{QRE}	$E_{apparent}$	β_a	R^2_a	β_c	R^2_c	j_o
[mV]	[mV]	[mV]	[V vs. K/K+]	[V vs. K/K+]	[mV dec^{-1}]	[%]	[mV dec^{-1}]	[%]	[μA·cm^{-2}]
300	-178	337	1.72 ± 0.07	1.31 ± 0.07	39.0	98.6	-14.7	96.6	433.7
400	-189	433	1.849 ± 0.007	1.322 ± 0.007	55.4	99.6	-8.2	97.8	331.6
500	-73	530	1.67 ± 0.02	1.36 ± 0.02	39.2	99.8	-8.6	97.6	239.8
Average			1.70 ± 0.10	1.33 ± 0.02	45 ± 8		-10 ± 3		340 ± 79

Polarization of Ni-20Cr to different potentials relative to the redox potentials of its pure components revealed information related to the dominant redox reaction occurring at a given applied overpotential. The specimen polarized to η = 300 mV was terminated at 1.647 V vs. K/K$^+$ while the η = 500 mV specimen was brought to a final potential of 1.89 V vs. K/K$^+$. As shown in Figure 101, these two scans terminate at potentials above and below $E_{Ni^{2+}/Ni}$. Surface and cross-sectional SEM & EDS of the two polarized specimens are shown in Figure 102. Comparing the specimen polarized to η = 300 to the as-received specimen, there is minimal surface recession. Figure 102(f), shows that the specimen experienced severe depletion of Cr and the formation of deep voids that extend approximately 20 μm into the alloy surface. The attack is much more pronounced than the void formation observed in the specimen exposed to FLiNaK for 3 hours shown in Figure 102(e). As shown in Figure 102(d), the specimen polarized to η = 500 mV experienced pronounced thickness loss. The surface appeared slightly less porous than at lower

overpotentials. As shown in Figure 102(g), the cross section revealed very little depletion of Cr in the remaining material. The result indicates that at potentials below the Ni^{2+}/Ni redox potential the anodic reaction is dominated by Cr oxidation (i.e., dissolution). Above $E_{Ni^{2+}/Ni}$, the oxidation of Ni becomes much more significant to the overall charge transfer process and the surface of the specimen begins to rapidly recede due to simultaneous oxidation of both Cr and Ni. It is speculated that at these high anodic potentials, the rates of Cr and Ni oxidation are comparable and no noticeable selective depletion of an element from the bulk occurs.

Based on the above results, it is concluded that Ni-Cr alloys may experience two modes of corrosion attack in fluoride salts: preferential oxidation of Cr or uniform corrosion. The mode of corrosion attack clearly depends on the anodic potential that the alloy experiences during exposure. More oxidizing salts may essentially impose a higher anodic potential on the alloy that could lead to oxidation of the matrix in addition to alloying elements. There are several examples in which modifying the FLiNaK salt chemistry has reduced the amount of mass transport or intergranular Cr depletion of Ni-based alloys [143]–[146]. For example, Zhou et al. [147] reported that Ni-20Cr foils in contact with FLiNaK containing 5wt% UF_3 showed less intragranular corrosion in the salt facing surface when the material was proton irradiated. It is speculated that irradiation of the salt in the local area may cause it to be so oxidizing that uniform corrosion of the matrix occurs rather than intragranular corrosion. It is challenging to measure surface recession of materials during exposure tests. The possibility that an alloy can experience either surface recession or intragranular depletion of alloying elements has important implications for corrosion studies of Ni-based alloys in static capsule or flow loop tests where the depth of corrosion attack, rather than overall surface recession, is often deemed to be the primary metric of corrosion, an approach that underestimates total magnitude of corrosion.

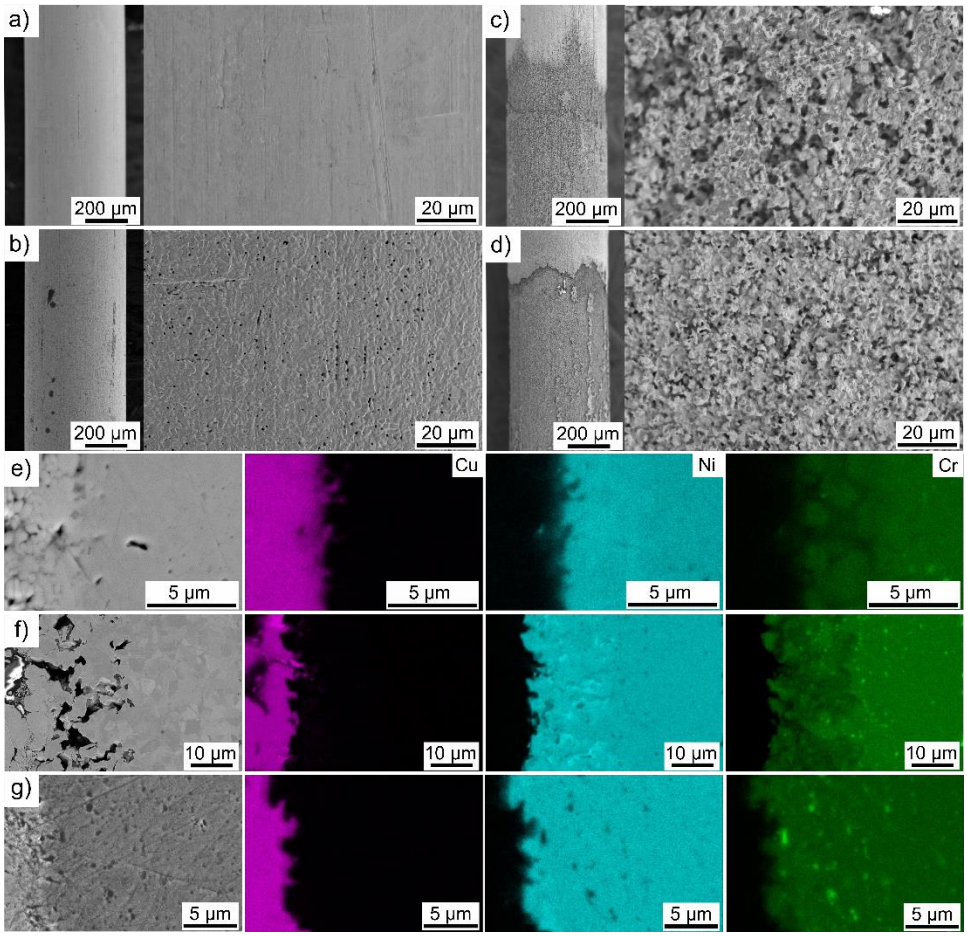

Figure 102. Surface SEM images of a) as-received Ni-20Cr, b) Ni-20Cr exposed to FLiNaK for 3 h, c) Ni-20Cr polarized to η = 300 mV, and d) Ni-20Cr polarized to η = 500 mV. Cross-sectional EDS composition maps of e) Ni-20Cr exposed to FLiNaK for 3 h, f) Ni-20Cr polarized to η = 300 mV, and g) Ni-20Cr polarized to η = 500 mV. Polarization was conducted at 0.166 mV s^{-1} after exposure for 1 hour.

3.3.6 Potentiodynamic Polarization of 316L

In the case of 316L, the redox behavior of the matrix, in addition to that of the alloying elements, may be important to long term corrosion performance of the alloy. Tafel plots of 316L polarized to nominal overpotentials of 250, 300, 500, and 550 mV are shown in Figure 103. The average apparent redox potential of 316L after 1 hour exposure to molten salt was 1.29 ± 0.02 V vs. K/K^+. It was expected that apparent redox potential of the alloy would be regulated by the more electrochemically active Cr. 316L's apparent redox potential after 1 hour of exposure to the salt was statistically the same as the redox potential of pure Fe. This suggests that it is energetically favorable for oxidation of Fe to occur in addition to Cr.

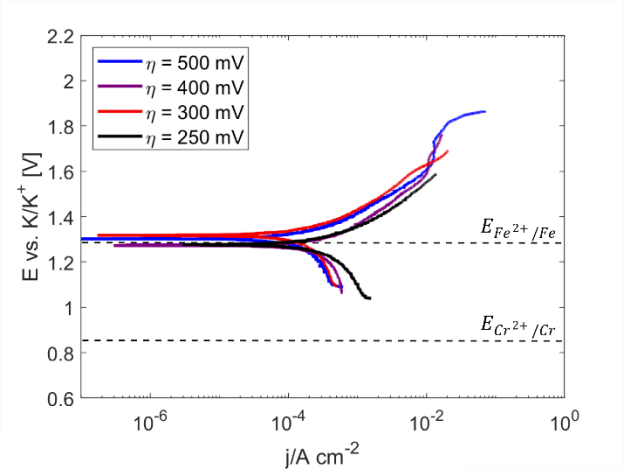

Figure 103. Polarization curves for 316L polarized to various anodic overpotentials in FLiNaK at 700 ˚C.

For the purpose of Tafel extrapolation it is assumed that the anodic reaction occurs by a single activation-controlled reaction (Cr/Cr^{2+} or Fe/Fe^{2+}), however, this is almost certainly not the case. 316L's anodic Tafel slope was 16 ± 3 mV dec^{-1} which is close to the values for pure Fe and Cr. The average j_o on the other hand was 600 ± 500 μA·cm^{-2}.

Table 28. Electrochemical parameters for 316L stainless steel obtained by linear fitting of iR_s-corrected polarization curves in FLiNaK at 700 ˚C.

η	η_{Start}	η_{Finish}	E_{QRE}	$E_{apparent}$	β_a	R^2_a	β_c	R^2_c	j_o
[mV]	[mV]	[mV]	[V vs. K/K+]	[V vs. K/K+]	[mV dec^{-1}]	[%]	[mV dec^{-1}]	[%]	[μA·cm^{-2}]
250	-238	311	1.68 ± 0.02	1.27 ± 0.02	16.7	99.1	-39.3	97.0	358.9
300	-224	374	1.65 ± 0.03	1.32 ± 0.03	16.5	99.8	-60.3	97.9	1605.7
500	-208	491	1.73 ± 0.02	1.28 ± 0.02	19.0	99.3	-66.0	93.0	320.0
550	-213	562	1.653 ± 0.008	1.303 ± 0.008	12.1	97.3	-29.0	94.3	123.5
Average			1.68 ± 0.03	1.29 ± 0.02	16 ± 2		-50 ± 20		600 ± 500

316L experienced noticeable surface corrosion both after exposure to the salt for 3 hours and at all applied overpotentials. Figure 104 shows the surface of (a) the as-received 316L, (b) the 316L exposed for 3 hours without an applied overpotential, and (c) the polarized to anodic overpotential of 300 mV. The electrode that was exposed for 3 hours without polarization shows evidence of surface corrosion attack. The specimen that was polarized experienced more pronounced corrosion in the form of grain boundary attack, similar to the observations made in traditional static capsule corrosion tests [38]. In Figure 104(d) and (e), cross-sectional examination in conjunction with EDS showed attack around grain boundaries in

both the specimens exposed for 3 hours and the sample polarized to η = 300 mV, however, it appears that neither Cr nor Fe were preferentially depleted from the remaining bulk material.

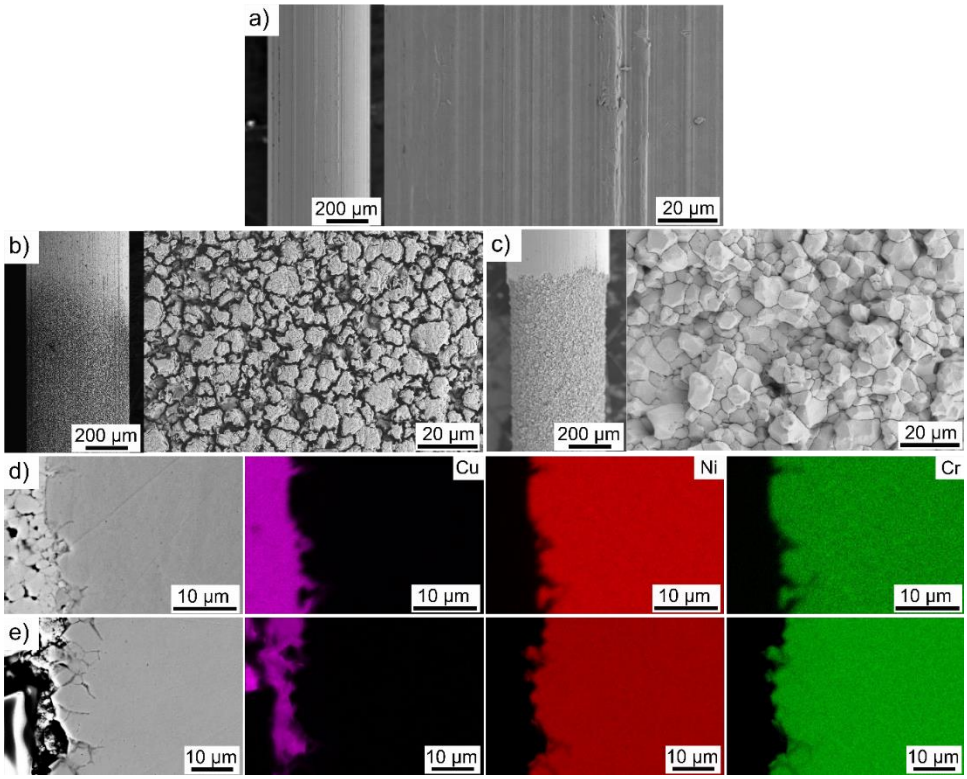

Figure 104. Surface SEM images of a) as-received 316L, b) 316L exposed to FLiNaK for 3 h, and c) 316L polarized to η = 300 mV at 0.166 mV s^{-1} after exposure for 1 hour. Cross-sectional EDS compositional maps of d) 316L exposed to FLiNaK for 3 hours and e) 316L polarized to η = 300 mV at 0.166 mV s^{-1} after exposure for 1 hour.

The corrosion of 316 stainless steel in FLiNaK salt reported in the literature manifests as either preferential dissolution or uniform surface recession. Selective dissolution of Cr is frequently observed [34], [38], [148]. The tendency for Fe and Cr to be corroded simultaneously is consistent with recent observations of Fe-based alloy corrosion in FLiNaK conducted in Section 3.1, in other static corrosion tests [55], [149] and in non-isothermal thermal convection flow tests [54]. A few studies have shown varying levels of preferential dissolution Cr from 316 stainless steel when the chemistry of the salt was modified [146], [150]–[152]. It is speculated that preferential dissolution or dealloying of Cr occurs when the apparent redox potential of 316L is between the redox potentials of the Cr^{2+}/Cr and Fe^{2+}/Fe reactions.

3.3.7 Thickness loss calculations

The thickness loss of the electrode specimens was calculated by integrating the total anodic charge of each scan and using the molar mass and density of Ni, Fe, and Cr for the respective materials. The molar mass and density of Fe and Ni were used for 316L and Ni-20Cr, respectively. This was a reasonable approximation considering the relative molar masses and densities of the two metals. The thickness loss as a function of the applied anodic overpotential are summarized in Figure 105. In all cases, increasing η led to a greater thickness loss of material. For the pure metals Ni and Fe, the relationship is exponential, consistent with Tafel behavior. The Ni-20Cr on the other hand shows a delayed thickness loss with increasing final anodic overpotential compared to the pure metals, due to preferential grain boundary attack. At sufficiently high anodic overpotentials appreciable thickness loss is observed in the alloy due to matrix dissolution.

The thickness loss results based on electrochemical data show that placing each material in an anodic environment (i.e. galvanic cell) will result in different rates of thickness loss at a given galvanic cell potential. Pure metals experience more rapid thickness loss in increasingly anodic environments likely because they experience uniform surface corrosion. Alloys may experience more delayed thickness loss because the selective dissolution of alloying elements takes precedence. At sufficiently high anodic potentials, dissolution of the alloy's matrix becomes energetically favorable, and the rate of thickness loss increases dramatically.

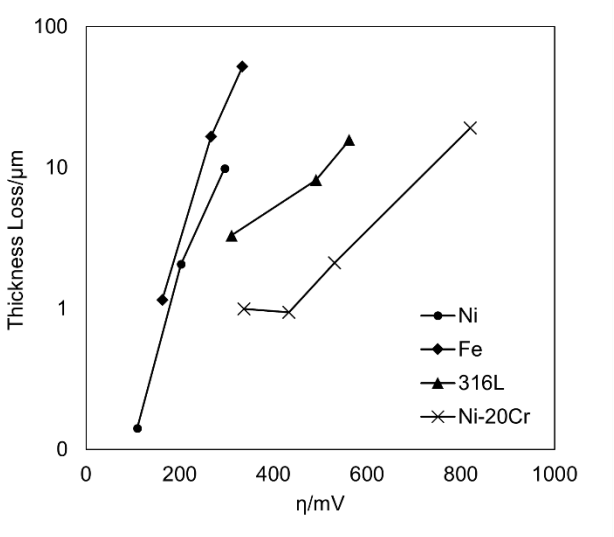

Figure 105. Thickness loss of Ni, Fe, 316L, and Ni-20Cr specimens after polarization to various anodic overpotentials at a scan rate of 0.166 mV sec^{-1} in FLiNaK salt at 700 ˚C.

3.3.8 Driving forces for galvanic corrosion

The reported redox potential and kinetic parameters serve as useful tools for predicting galvanic corrosion in molten salt environments. Table 29 shows the cell potentials, $E_{cell} = E_{cathode} - E_{anode}$, for hypothetical galvanic cells in FLiNaK salt for various materials investigated using the electrochemical data from this study. A positive cell potential indicates that galvanic corrosion is spontaneous. In some cases, the corrosion potentials of materials such as Fe, 316L, and Ni-20Cr are similar resulting in a low driving force for galvanic corrosion in either direction.

Table 29. Electrochemical Cell potentials generated by combination of an anode and cathode material in FLiNaK at 700 ˚C. Positive cell potential indicates reaction spontaneity.

		Anode				
		Ni	Fe	Cr	316L	Ni-20Cr
Cathode	E_{corr} vs. K/K^+ [V]	1.65	1.29	0.84	1.29	1.32
Ni	1.65	0	0.36	0.81	0.36	0.33
Fe	1.29		0	0.45	0	-0.03
Cr	0.84			0	-0.45	-0.48
316L	1.29				0	-0.03
Ni-20Cr	1.32					0

3.3.9 Thermodynamic analysis

To illustrate the effects of the changing alloy and salt composition on the corrosion processes occurring at the alloy-salt interface, the redox potentials of each alloying element under various conditions can be calculated. The standard reduction potentials were obtained from the Gibbs free energy of formation, ΔG_f, for the reaction,

$$M(s) + F_2(g) \rightarrow MF_2(d) \tag{64}$$

The fluorides dissolve in the liquid phase of the salt at temperatures below their melting points. Therefore, the free energy of formation for the supercooled liquid fluoride is obtained from Outotec HSC 7.0 [40]. At 700 ˚C, the cell potential, ΔE, is obtained from the expression,

$$\Delta G_f = -nF\Delta E \tag{65}$$

where n is the number of electrons per mole of reaction and F is the Faraday constant. Choosing the $F_2/2F^-$ reference reaction, the standard half-cell reduction potential, $E°_{M^{2+}/M}$, of Reaction 57 is the opposite of the fluoride formation reaction's cell potential, ΔE. The half-cell reduction potentials are then calculated using Equation 58. Figure 106 shows the calculated half-cell reduction potential of the Ni^{2+}/Ni, Fe^{2+}/Fe, and the Cr^{2+}/Cr redox couples at 700 ˚C. The hypothetical reduction potentials of Ni^{2+}/Ni and Fe^{2+}/Fe are calculated assuming that the activity of the fluoride is 10^{-6}. The redox potential of the Cr^{2+}/Cr redox couple is plotted as a function of the alloy's Cr activity for three hypothetical molten salt compositions containing different activities of dissolved Cr^{2+}. The simultaneous increase in chromium fluoride activity in the salt and decrease in the activity of Cr in the near surface region causes the redox potential of the Cr^{2+}/Cr reaction to increase.

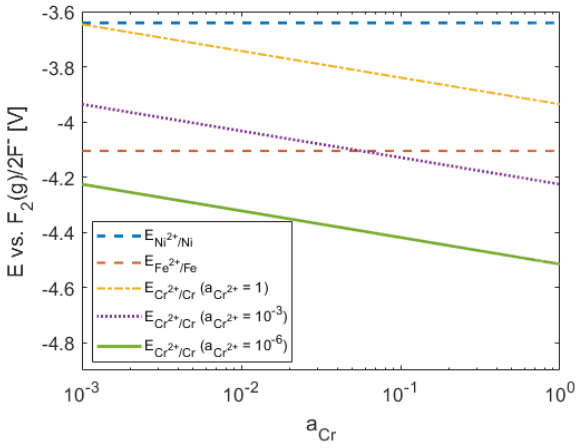

Figure 106. Redox potential of the Ni^{2+}/Ni, Fe^{2+}/Fe, and the Cr^{2+}/Cr redox couples. For Ni^{2+}/Ni and Fe^{2+}/Fe, the activity of the dissolved fluoride is 10^{-6} and the activity of the metal is unity. The redox potential of the Cr^{2+}/Cr redox couple is plotted as a function of the alloy's Cr activity for three hypothetical molten salt compositions containing different activities of dissolved Cr^{2+}.

Theoretically, corrosion of Cr will dominate alloy corrosion until the apparent redox potential of the surface exceeds the redox potential of the bulk metal provided that the kinetics of both reactions are reasonably fast. In the case of Ni-20Cr, for the Cr^{2+}/Cr redox potential to exceed that of the Ni^{2+}/Ni reaction, the activity of Cr in the alloy must be very small (10^{-3}) and the Cr^{2+} activity must be very close to unity. For 316L, there are many more realistic combinations of Cr and Cr^{2+} activities that could raise the Cr^{2+}/Cr redox potential to the same potential as the Fe^{2+}/Fe reaction and cause oxidation of the alloy bulk material. At this redox potential, the corrosion of both elements would continue to proceed, but the corrosion of Cr would likely be regulated by the competition with the Fe oxidation reaction.

3.3.10 Polarization research in the context of static corrosion experiments and alloys development

The corrosion behavior of Ni-20Cr was dependent on the applied potential relative to the redox potential of Ni and Cr. Preferential dissolution of Cr was observed at potentials below the Ni^{2+}/Ni redox potential, however more uniform corrosion of the alloy surface was observed when the potential exceeded the Ni^{2+}/Ni redox potential due to dissolution of both elements. 316L, on the other hand, had the same redox potential as the Fe^{2+}/Fe reaction due to near-surface dissolution of Cr prior to application of the overpotential. Both Cr and Fe experienced comparable corrosion rates, which led to an overall surface

recession at all anodic overpotentials, with no evidence of preferential dissolution of individual alloying elements.

The results of this study are useful for interpreting some of the observations of static corrosion experiments in previous sections. As in static corrosion experiments, the 316L material surface recedes due to oxidation of both Fe and Cr. The polarization method used has allowed direct comparison of the Fe, Cr, and 316L's apparent redox potentials in molten FLiNaK. This showed that after 1 hour of alloy exposure, simultaneous corrosion of Cr and Fe is energetically feasible if corrosive trace impurities are present in the salt. Similarly, comparing Cr, Ni, and Ni-20Cr, there is a range of potential between the redox potential of Cr and Ni in which preferential dissolution of Cr is favorable without oxidation of Ni. This likely explains why the nickel-based alloys, in Section 3.2, showed selective dissolution of Cr without significant surface recession.

The above experiments clearly demonstrate the ability to accelerate or suppress corrosion of pure metals or elements in an alloy by the imposition of a positive or a negative potential, respectively with respect to the equilibrium corrosion potential. As shown in the above experiments for the Ni-20Cr alloy, it is possible to selectively corrode Cr by imposing a potential that is above the equilibrium corrosion potential of Cr, but below that nickel's equilibrium corrosion potential. Application of a negative potential below the equilibrium corrosion potential of alloying elements that are prone to corrosion is an effective approach to mitigate the corrosion of these elements in molten salt environments. This approach known as cathodic protection is wide used for corrosion control in aqueous environments and this study has demonstrated its applicability to molten salt systems.

3.4 Electrochemical Methods for Relating Salt Chemistry & Corrosion

Salt chemistry is an understudied variable in all molten salt corrosion studies. Given the complex relationship between trace impurities and materials degradation in molten fluoride salts it is necessary to develop rapid techniques that can be deployed *in situ* to measure impurities in the salt and the salt's redox potential. Electrochemical analysis techniques provide the basis the development *in situ* molten salt chemistry sensors because the apparatus needed to probe the salt can be made robust, nondestructive, and provide adequate environmental sealing.

A versatile electrochemical method called cyclic voltammetry (CV) can be used to probe the chemistry of some dissolved species in molten salts. The basic methods used in this research were described in Section 1.5.6 and 2.5.3. The aims of the research were to develop an analytical method for measuring relative concentrations of corrosion products, such as CrF_2 and FeF_2, and apply the method towards static molten salt corrosion studies of 316H in FLiBe salt at 700 ˚C. like solids in contact with an electrolyte, some dissolved species in molten fluoride salts can undergo electrochemical reactions (redox reactions) that result in charge transfer at an electrode surface. These electrochemically active species have inherent redox potentials that describe the potential at which the rate of oxidation and reduction reactions are equal. The redox potentials of dissolved species were measured using a Be/Be^{2+} DRE (analogous to the K/K^+ DRE discussed earlier) to measure over a range of potentials in which they occur repeatably. This enabled some dissolved species such as Cr and Fe to be easily identified in a FLiBe salt CV. The magnitude of the cathodic peak current density was then related to the relative concentrations of CrF_2 and FeF_2 intentionally added in FLiBe salt. Application of the CV method to salts before and after exposure to 316H was used to observe changes in the relative concentrations of these impurities in a static corrosion experiment.

3.4.1 Cyclic Voltammetry for measuring metal fluoride impurities

CV is sensitive to trace electroactive species such as chromium and iron fluoride, common corrosion products of structural alloys in molten fluoride salts. The accuracy of identification of various salt impurities using CV is greatly improved by the DRE. In Figure 107, the potential of the WE is varied

at a rate of 80 mV/sec at 650°C. The potential starts at the open circuit potential and moves in the cathodic direction first. The current-potential waveforms for salts with added CrF_2 and FeF_2 are different from purified FLiBe and from one another when normalized to the DRE. In FLiBe containing 286 ppm Cr, peaks 2a and 2c are attributed to oxidation and reduction reactions involving dissolved chromium according to the reaction,

$$Cr^{2+} + 2e^- \leftrightarrow Cr^0 \tag{66}$$

Similarly, peaks 4a and 4c is the reduction of dissolved iron in a salt containing 111 ppm Fe according to the reaction

$$Fe^{2+} + 2e^- \leftrightarrow Fe^0 \tag{67}$$

The assumed charge number of each of the ions are supported by literature which indicates that these cations are mainly divalent in FLiBe [65].

Some interesting electrochemical behavior of dissolved chromium needed to be understood prior to developing quantitative methods. In Figure 108, voltammograms of FLiBe containing 286 ppm Cr at 650˚C show subtle differences between the first and second scan cycle. The potential was varied at 80 mV/sec beginning at the open circuit potential. In general, the first scan cycle showed one complete set of redox peaks (2a and 2c). These peaks are attributed to the redox couple Cr/Cr^{2+} (reaction 66). The small peak 5a was observed upon the anodic sweep of the first scan cycle. The corresponding reduction peak 5c usually appeared only in the second cathodic sweep. Sometimes peak 5c was observed in the first scan cycle if extensive reduction and re-oxidation of solid chromium metal had been achieved immediately prior to the cathodic sweep. Generally, peaks 5a and 5c were most prominent at higher temperatures.

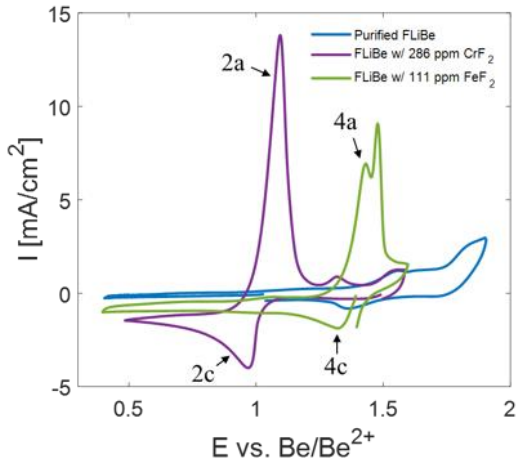

Figure 107. Cyclic voltammograms of molten FLiBe salt samples with various impurity additions at 650˚C. Scan rate was 80 mV/sec.

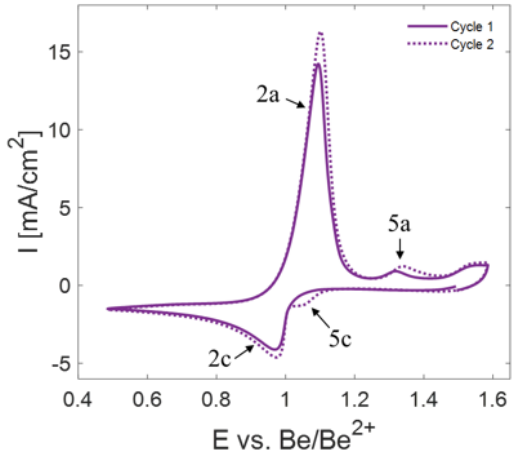

Figure 108. Cyclic voltammogram showing the first and second scan cycles of FLiBe containing 286 ppm Cr at 650˚C. Scan rate is 80 mV/sec.

Previous authors have reported similar behavior for reactions involving the deposition of a metallic species in molten salts. In chloride salts, actinide deposition at potentials higher than the equilibrium potential has been observed. These peaks are generally attributed to be underpotential deposition (UPD) of a monolayer of the reacting species [98], [99], [153]–[158]. This speculation is often made despite the unusually large potential difference between peaks like 5a and 5c. The influence of UPD on quantitative CV methods has been studied only to a limited extent and therefore remains speculative [99].

In other fluoride salts, it has often been suggested that peaks similar to 5a and 5c are the result of a Cr^{2+}/Cr^{3+} couple [83], [93], [100]. It is well known that chromium and iron can exist in both II and III oxidation states in many liquid fluoride salts [159]. In a molten FLiBe solution containing chromium fluoride, one could expect the reaction,

$$Cr^{3+} + e^{-} \rightleftarrows Cr^{2+} \tag{68}$$

The equilibrium concentration of Cr^{3+} in FLiBe is not well understood. The degree to which Cr^{2+} disproportionate in FLiBe has been studied by Redman [159]. It is shown to be low and to depend on the concentration of the acidic fluoride BeF_2.

Analysis of redox peaks 5a and 5c to determine the exact redox mechanism was inconclusive. They have an apparent reduction potential approximately 100-300 mV positive of the reaction 66. To the best of the author's knowledge, no reliable measurement of the equilibrium reduction potential of Cr^{2+}/Cr^{3+} couple with respect to a repeatable reference electrode in FLiBe has been reported. Comparing the peak potentials of peaks 5a and 5c, it is difficult to imagine a reversible reaction with the observed behavior. For a reversible heterogeneous electron transfer process involving a soluble-soluble reaction, the peak potential separation is,

$$\Delta E_p = 2.218 \frac{RT}{nF} \tag{69}$$

At 650˚C, ΔE_p equals 176 mV for a one-electron transfer step. With a peak potential separation larger than a one-electron transfer process, the reaction resulting in peaks 5a and 5c is not reversible. This presents a challenge for analysis of peaks 5a and 5c. It therefore, remains challenging to confidently attribute these peaks to the Cr^{2+}/Cr^{3+} couple.

It is possible that when chromium metal is oxidized in the CV anodic sweep, both Cr^{2+} and Cr^{3+} are formed. The appearance of peak 5c after the system has already been perturbed may indicate that the concentration of Cr^{3+} near the electrode is higher than the initial equilibrium concentration before CV. Peak 5c usually vanishes if the salt is left alone for several minutes. It is unclear whether the disappearance of

the peak is due to the dissolution of a Cr coating as in UPD or reduction of Cr^{3+} to Cr^{2+} as the system returns to chemical equilibrium.

The superposition of the two cathodic peaks 2c and 5c could cause errors for quantitative methods. While the effects of these peaks on each other is sufficiently subtle to enable qualitative conclusions to be drawn about reaction 66, quantitative analysis will require careful acquisition of the cathodic peak. To improve accuracy and repeatability, it is important to allow the system to re-equilibrate following a CV scan. It is not easy to predict the length of time required, which was generally between 5 and 30 minutes in the static solution. As a result, some scans reported in this study show cathodic peak 2c with a slight distortion that is attributed to superposition with peak 5c. Detailed in the experimental methods section, an electrode conditioning step was used to reduce time between scans and prevent the occurrence of peak 5c. The influence of peak 5c on quantitative methods will be discussed.

3.4.1.1 Reduction Potential of the Cr/Cr^{2+} Couple

The behavior of the dissolved Cr^{2+} redox couple under a variety of conditions was compared to electrochemical theory. The apparent reduction potential of Cr^{2+} was observed at temperatures between 500°C to 700°C and at concentrations between 6 ppm and 286 ppm Cr with respect to the Be/Be^{2+} DRE. While quantitative methods using electric potential may prove difficult, the DRE is a useful reference electrode for species identification and qualitative observations related to corrosion.

In this work, the equilibrium reduction potential of the Cr/Cr^{2+} couple, $E^{eq}_{(Cr^o/Cr^{2+})}$, is observed with respect to the Be/Be^{2+} reference reaction. For the reduction of soluble Cr^{2+} to insoluble Cr^0, the equilibrium potential with respect to the DRE is,

$$E^{eq}_{Cr^{2+}/Cr} = E_{Cr^{2+}/Cr} - E_{Be^{2+}/Be} \tag{70}$$

where $E_{Be^{2+}/Be}$ is determined by equation 44. In the case of the soluble-insoluble a half-cell reaction involving chromium, an approximate solution to the Nernst equation can be derived by assuming that the activity of the deposit is equal to unity. Assuming the electrode surface is covered entirely by chromium metal, the half-cell reduction potential of reaction 66 is determined by,

$$E_{Cr^{2+}/Cr} = E^{o}_{Cr^{2+}/Cr} - \frac{RT}{nF}\ln\frac{1}{\gamma_{Cr^{2+}}} - \frac{RT}{nF}\ln\frac{1}{[Cr^{2+}]} \quad (71)$$

where $E^{o}_{Cr^{2+}/Cr}$ would be the standard half-cell reduction potential of chromium fluoride dissolved in a molten FLiBe salt mixture. The activity coefficient, $\gamma_{Cr^{2+}}$, is not known at this time. Sometimes in the case of a very dilute species (<0.01 M), the activity coefficient may be assumed relatively constant, and the first two terms are simplified to,

$$E_{Cr^{2+}/Cr} = E^{o\prime}_{(Cr^{0}/Cr^{2+})} - \frac{RT}{nF}\ln\frac{1}{[Cr^{2+}]} \quad (72)$$

where $E^{o\prime}_{Cr^{2+}/Cr}$ is the formal half-cell potential. $E^{o\prime}_{Cr^{2+}/Cr}$ is a measurable quantity given a reference reaction where all terms in the Nernst equation are defined.

Aside from the challenges in defining the DRE's thermodynamic potential, experimental challenge was encountered in acquiring CVs that could enable accurate determination of $E^{o\prime}_{Cr^{2+}/Cr}$. Quantitative analysis of the equilibrium reduction potential is hindered by the sensitivity to the superposition of the two cathodic peaks discussed in the previous section. Conventional techniques for quantifying the apparent reduction potential, such as the half-peak potential, are moved to more positive potentials by this waveform distortion. This introduces a subtle error which makes quantitative comparison of each half-peak reduction potential challenging. Therefore, the discussion of the reliability of measuring the equilibrium reduction potential of the Cr/Cr^{2+} couple with respect to the DRE is limited to analysis of the peak potentials of the prominent redox peaks.

The reduction potential of the Cr/Cr^{2+} couple is shown as a function of temperature in Figure 109 a) and concentration in Figure 109 b). When normalized to the Be/Be^{2+} couple, redox peaks resulting from the Cr/Cr^{2+} couple can confidently be identified based on their proximity to the DRE's potential. The potentials at which they occur are far more repeatable than when measured against the Mo QRE. Figure 110 shows the anodic peak potentials, $E_{p,a}$, and the cathodic peak potentials, $E_{p,c}$, of the Cr/Cr^{2+} redox peaks with respect to the log of concentration at 500˚C and 700˚C. The redox peaks are observed between 0.8 V and 1.2 V vs. DRE. At 700˚C, the peak potentials have the anticipated logarithmic dependence on Cr^{2+}

concentration, however, the peak potentials at 500˚C deviate from this trend. The adherence to the cell model at lower concentrations and temperatures is further investigated in the following sections. Here, aspects of the data are compared to the approximate expected trend from equation 70.

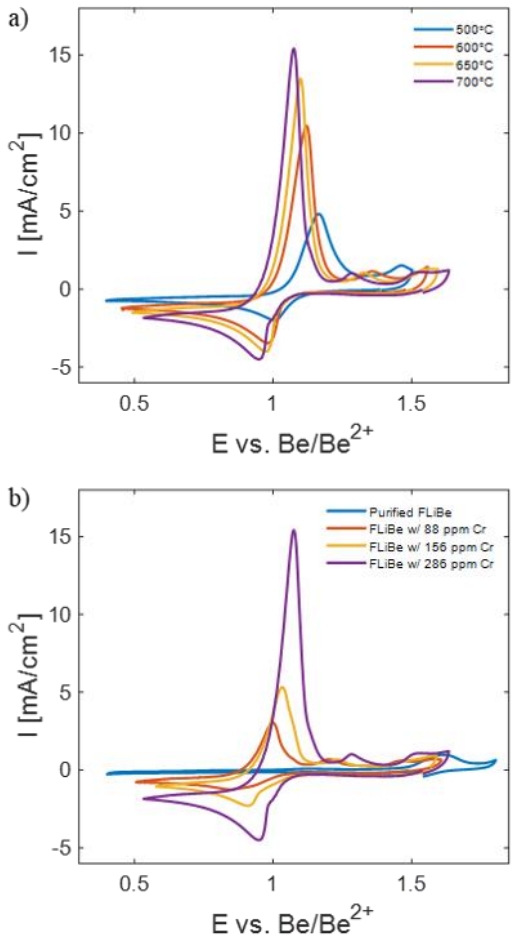

Figure 109. CVs of a) FLiBe containing 286 ppm Cr at various temperatures and b) FLiBe containing various Cr concentrations at 700˚C. Scan rate is 80 mV/sec.

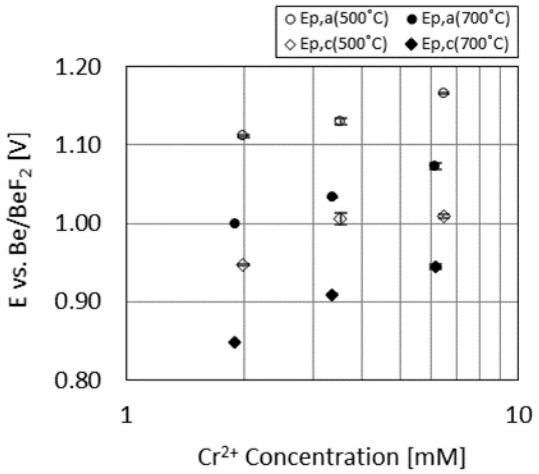

Figure 110. CV anodic and cathodic peak potentials of the Cr/Cr^{2+} couple with respect to the log of concentration at 500˚C and 700˚C. CVs are shown for salt samples 2, 4 and 6. Scan rate 80 mV/sec.

$E^{eq}_{Cr^{2+}/Cr}$ *temperature dependence* — Some factors which contribute to the temperature dependence of the equilibrium reduction potential of dissolved chromium fluoride can be approximated. When the temperature is increased from 500˚C to 700˚C at fixed Cr^{2+} concentration, the following changes are expected from equation 70.

- Standard reduction potentials – using experimental data in FLiBe from Baes [60] the difference between the standard reduction potentials, $E^{o}_{Cr^{2+}/Cr}$ and $E^{o}_{Be^{2+}/Be}$, can be approximated by the expression $1.562 - 0.186(\mathrm{T(K)}/10^3)$ V. Over the temperature range the contribution of the standard reduction potentials will be to decrease $E^{eq}_{Cr^{2+}/Cr}$ by 29 mV.
- Be^{2+} activity – using theoretical values from Hitch [66], the activity of Be^{2+} changes minimally from 0.063 to 0.067. The second term in equation 44 will increase $E^{eq}_{Cr^{2+}/Cr}$ by 21 mV.
- Logarithmic terms – at 286 ppm CrF_2, the third term in equation 71 is estimated to decrease $E^{eq}_{Cr^{2+}/Cr}$ by approximately 44 mV.

The model predicts an overall decrease in $E^{eq}_{Cr^{2+}/Cr}$ of 41 mV. In Figure 6, the same temperature increase leads to a decrease in the Cr/Cr^{2+} peak potentials by approximately 60 to 100 mV. At each concentration,

the effect of increasing temperature on $E^{eq}_{Cr^{2+}/Cr}$ follows a similar trend to the one predicted by equation 70. In equation 71, the term containing $\gamma_{Cr^{2+}}$ cannot be approximated and is not accounted for in this analysis. This term is also temperature dependent and likely to contribute a negative change in reduction potential that accounts for the discrepancy between the predicted and experimental results.

$E^{eq}_{Cr^{2+}/Cr}$ *concentration dependence* — The concentration dependence of the observed Cr/Cr^{2+} reduction potential was also studied at 700°C. Assuming the Cr detected by ICP-OES is completely dissolved in FLiBe, the value of the third term in equation 71 increases by approximately 21 mV when the concentration is increased from 88 ppm to 286 ppm Cr^{2+}. In Figure 110, the peak potentials increase by approximately 100mV over that concentration range. With the limited data, the behavior of the Cr^{2+} activity coefficient is not well understood. It remains unclear whether $\gamma_{Cr^{2+}}$ remains constant over the concentration range investigated and if the underlying assumption of equation 72 can be made.

Using this reference electrode, the Cr/Cr^{2+} redox couple behaves in accordance with electrochemistry theory, however not all factors which influence the peak potentials can be defined easily. While the Nernst equation is straightforward, the logarithmic dependence on species activity and uncertainties involved with measuring waveforms at low concentrations make approximating a species' concentration from its reduction potential challenging. For these reasons, other techniques must be unitized for corrosion product concentration measurement.

The utility of measuring the Cr/Cr^{2+} couple with respect to the DRE is the ability to reliably identify dissolved Cr^{2+} at most useful operating temperatures based on general knowledge of the redox peak potential range in which they occur. Figure 107 indicates that the DRE could distinguish between different corrosion products in FLiBe based on their redox peak potentials. Figure 109 and Figure 110 demonstrate that the DRE is sufficiently stable to enable qualitative observation of the Cr/Cr^{2+} redox couple.

3.4.1.2 Quantitative methods with CV Peak Current

Quantitative methods based on peak current density are attractive, in part, because they do not rely on a thermodynamic reference electrode. For a soluble-insoluble reaction, a relation between the

voltammogram cathodic peak current, $j_{p,soluble-insoluble}$, and the concentration of the electroactive species was solved by Berzins and Delahay [81], [82].

$$j_{p,soluble-insoluble} = 0.61A[Cr^{2+}]\sqrt{\frac{F^3 n^3 D_{Cr^{2+}} v}{RT}} \quad (73)$$

A is the area of the working electrode, *n* is the number of electrons transferred equal to 2, $D_{Cr^{2+}}$ is the diffusion coefficient of Cr^{2+}, and *v* is the potential scan rate. A linear diffusion approximation is adopted since the electrode has a diameter many orders of magnitude larger than the diffusion layer of Cr^{2+} established by electrolysis. The direct proportionality between current and species concentration, rather than a logarithmic dependence, avoids the problem of inaccuracy at low concentrations and deal more reliably with the appearance of peak 5c. If the cathodic peak current density due to reaction 66 can be reliably measured, the model could allow direct quantification of corrosion product concentration *in situ.*

To treat peak current quantitatively it is necessary to extract the faradaic peak current density from a voltammogram. The cathodic peak current density was analyzed using specialized batch waveform analysis. Figure 111 shows a graphical representation of waveform analysis. It is assumed that the faradaic and double layer charging processes are separable and that the double layer capacitance is independent of potential scan rate. The faradaic current, j_f, is therefore expressed as

$$j_f = j_{total} - C_{dl}(dE/dt) \quad (74)$$

where j_{total} is the total current measured and C_{dl} is the double layer capacitance. When normalized with respect to the electrode surface area, the two processes are separated by fitting a linear baseline to the waveform shown in Figure 111. Faradaic anodic current density, $j_{p,a}$, and cathodic current density, $j_{p,c}$, are the difference between the peak current density measurement and the charging current baseline at the peak potential.

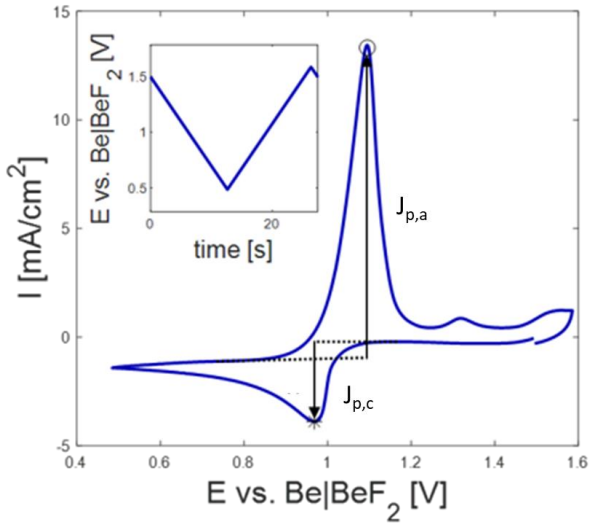

Figure 111. CV of FLiBe with 286 ppm Cr at 650°C. Analysis of current peaks is performed on the first scan cycle.

In this work, only the dominant redox couple peaks are analyzed quantitatively. Measurement of the second redox couple peaks would assume that the diffusion of the two species takes place independently and that the fluxes are additive. The I-E curve is the sum of the individual I-E curves meaning that the peak current of the second reaction must be obtained by fitting a baseline accounting for the decay current of the first reaction.

A typical characteristic of soluble-insoluble reactions, such as 66, is the sharp oxidation peak and ratio of $|j_{p,a}/ j_{p,c}| > 1$. To validate that equation 72 can be applied to this redox couple, the reversibility of the Cr/Cr^{2+} couple was investigated by varying the CV scan rate, v. In Figure 112, the potential corresponding to peak 2c does not shift with increasing scan rate. In Figure 113, the cathodic peak current density, $I_{p,c}$, is shown as a function of the square root of scan rate, $v^{1/2}$. The plots are linear up to scan rates of 300 mV/sec. A similar trend was observed in other samples at 700°C. There is a slight deviation from linearity at high temperatures and scan rates. In Figure 112, peak 5c appears more prominently at scan rates higher than 300 mV/sec. It is not clear whether the appearance of peak 5c directly causes the departure from linearity. It is also possible that the system is not reversible at scan rates higher than 300 mV/sec.

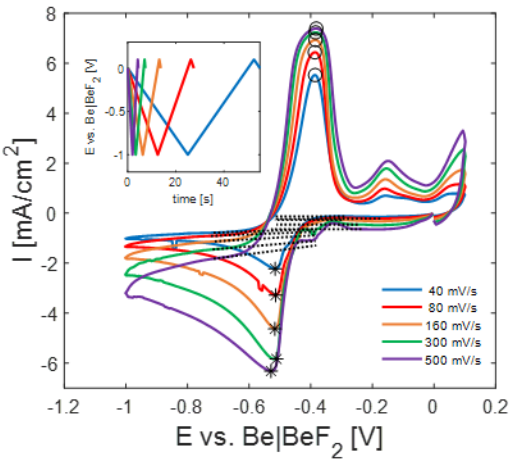

Figure 112. Cyclic voltammograms of FLiBe with 207 ppm Cr at 650°C at various potential scan rates.

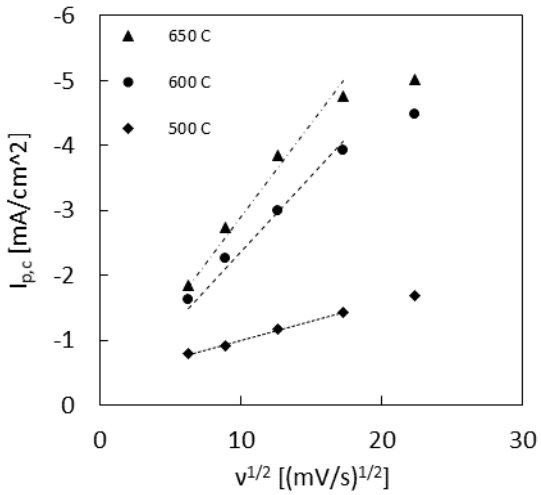

Figure 113. CV faradaic cathodic peak current density at various temperatures as a function of the square root of potential scan rate.

Linear regression of the peak current density at scan rates below 300 mV/sec revealed that at all temperatures, except for 500˚C, the peak current density goes to zero at zero scan rate (Intercept $p>0.05$). At the higher temperatures and lower scan rates the reduction of Cr^{2+} is considered controlled by diffusion and equation 72 can be applied to analysis of peak 2c. At 500˚C, it appears that the reduction of Cr^{2+} is not controlled by diffusion and that equation 72 does not apply. This may explain the poor fit of the data to the model. While temperature likely influences the kinetics of the electrochemical reaction, the exact cause of the deviation from reversibility at 500˚C is not known at this time.

3.4.1.3 Peak Current Correlation to Chromium Fluoride Concentration

Online electrochemical sensors will require working curves for each electroactive species in order to relate peak current density to concentration. The CV cathodic peak current density for the salt compositions were measured at temperatures between 500°C and 650°C, and at certain concentration at 700°C. The added Cr concentrations, which range between 88 and 352 ppm, are comparable to concentrations experienced during the MSRE [160]. Figure 114, shows the average cathodic peak current density of peak 2c between 500°C and 700°C. In general, the cathodic peak current density increases with Cr^{2+} concentration. At 500°C, 600°C and 650°C linear relationships between peak current density and concentration are obtained at low and high concetrations, however, there is a change in slope between sample sets 2-4 and 5-7 that is inconsistent with the Berzins-Delahay model. The measurement error of electrode surface area and ICP-OES are not large enough to account for the discrepancy. There was no conclusive relationship between the behavior of the cathodic peak current density and the presence of peak 5c. For this reason, further analysis was required to determine under what conditions the model is applicable.

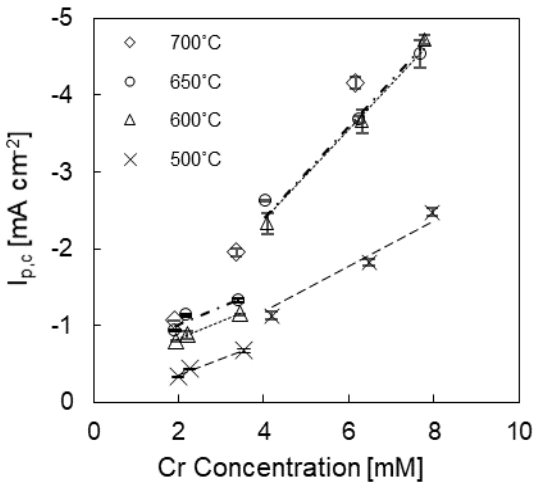

Figure 114. CV faradaic cathodic peak current density at various temperatures as a function Cr concentration.

The experimental data was analyzed to verify that a key assumption made in the derivation of the Berzins-Delahay model applies. To derive the solution it is assumed the activity of Cr^0 on the electrode

surface is unity [81], [82]. At least one complete monolayer of deposited metal is required to assume that it has unit activity [139]. Since the reaction occurs at more negative potentials than the initial WE potential, it is assumed that there is initially no Cr^0 on the electrode. In very dilute solutions, the amount of electric charge passed during electrolysis may be insufficient to produce complete surface coverage. The amount of electric charge needed to form a monolayer of Cr^0 is approximately 0.61 mC cm^{-2}. To ascertain whether the unit activity assumption is applicable to these very dilute solutions the amount of faradaic charge passed in each cathodic sweep was calculated. The electric charge used to form peak 2c is calculated by integrating the faradaic peak current vs. time in the mixed charge transfer region. Analysis of sample 2 through 7 at the four temperatures revealed that the electric charge passed is between 0.53 mC cm^{-2} and 2.4 mC cm^{-2}. The discrepancy in the current density trend occurs between samples 4 and 5. These samples show similar electric charge transfers, about 0.88 mC cm^{-2}. These values are comparable to the amount of electric charge required to produce a monolayer of Cr. In a real system, complete surface coverage likely demands more than one monolayer of Cr^0. Therefore, it is possible that at the lower concentrations this electrode system may deviate from the assumed case. A solution to this problem may be to use smaller electrodes; however, the appropriate diffusion model and derivation for a soluble-insoluble reaction must be maintained.

With the inference that the Berzins-Delahay model is applicable to this electrode geometry in only the most concentrated solutions studied, least squares regressions were performed at 600˚C and 650˚C to predict peak current density based on Cr^{2+} concentration. Unfortunately, analysis could not be preformed at 500°C due to insufficient reversibility and was not permitted at 700°C due to insufficient data. The relationships of cathodic peak current density at these concentrations are virtually identical at 600˚C and 650˚C. The slope is -590 ± 20 A cm mol^{-1} with small relative errors that do not exceed 4% with a 95% confidence interval (CI).

The diffusion rate of Cr^{2+} in FLiBe could be useful to the development of corrosion models in molten salt systems. There is little to no experimental data related to the diffusion of Cr^{2+} in FLiBe salt. The slope of the most concentrated solutions at 600˚C and 650˚C in Figure 114 was used to calculate a Cr^{2+} diffusion coefficient, $D_{Cr^{2+}}$, of 1.2 ± 0.2 x 10^{-5} cm^2 s^{-1}. The calculation considers the error of the surface

area measurement which is approximately 5%. Relative errors of $D_{Cr^{2+}}$ are below 8% with a 95% CI at 600˚C and 650˚C.

3.4.2 Electrochemical investigation of 316H Stainless Steel exposure to FLiBe containing CrF_2 and FeF_2

To evaluate the performance of the CV salt analysis method and also gain insights into the role of corrosion products in molten fluoride salt corrosion, the CV method was applied to a 1000 hours static corrosion experiment. ICP-OES salt analysis, CV, and detailedmaterials characterization were performed before and after the corrosion experiment. The ICP-OES was pivotal for benchmarking the salt compositions used in CV analysis. The CV waveform behavior before and after corrosion was then related to changes in salt composition. Finally, changes in 316H composition and microstructure were related to the changes in salt chemistry.

3.4.2.1 FLiBe salt analysis using ICP-OES

The cationic concentrations of the salt were measured using ICP-OES before and after the corrosion experiments as a measure of the magnitude of corrosion of 316H. Table 30 shows the concentration of the predominant metal impurities (Cr, Fe, Mn, Ni) in each capsule salt before and after exposure. Capsule 1 contained as-purified FLiBe salt that initially had less than 15 ppm of Cr, Mn, and Ni. The initial salt composition of capsule 2, where CrF_2 was added, contained 245 ± 3 ppm Cr. Capsules 3 and 4, where FeF_2 was added, contained 99 ppm and 392 ppm Fe, respectively. The limit of quantification (LOQ) for Fe is approximately 65 ppm.

After exposure, the Cr content in the salt increased for all capsules. The concentration of the predominant dilute metals after exposure are shown in Table 2. In addition to Cr, the depletion of manganese is an important corrosion phenomenon for some steels in molten salts [14]. Mn is a minor alloying element in stainless steel. Salts in all capsules experienced an increase in Mn concentration of approximately 40 to 50 ppm. The free energy of the formation of MnF_2 in molten FLiBe is even more negative than CrF_2, meaning that the formation of MnF_2 as a corrosion product is highly favorable energetically [15].

The changes in Fe concentration of capsules 3 and 4 result from impurity driven corrosion. The concentration of Fe in these salts dropped below the LOQ as a result of exposure to 316 stainless steel. The corresponding increase in Cr content after corrosion is believed to occur the reaction

$$FeF_2(d) + Cr(s) \rightarrow Fe(s) + CrF_2(d) \quad (75)$$

The largest net change in concentration of chromium occurred in capsule 4 with a higher initial concentration of FeF_2.

Table 30. ICP-OES metals analysis before and after corrosion tests. The limit of quantification (LOQ) for Fe is approximately 65 ppm. Values below the LOQ are not reported.

Capsule	Before-corrosion				After-corrosion			
	Cr	Fe	Mn	Ni	Cr	Fe	Mn	Ni
	(ppm)				(ppm)			
1	6 ± 1	-	4.2 ± 0.4	14 ± 3	263 ± 7	-	40 ± 1	8.5 ± 0.3
2	245 ± 3	-	3.8 ± 0.4	14 ± 3	452 ± 3	-	47.2 ± 0.2	8.7 ± 0.1
3	7 ± 1	99	3.4 ± 0.4	11 ± 3	219 ± 5	-	42.4 ± 0.8	9.6 ± 0.1
4	6 ± 1	392	3.5 ± 0.4	10 ± 3	450 ± 8	-	55.7 ± 0.2	9.3 ± 0.1

3.4.2.2 Cyclic Voltammetry of FLiBe salts before and after exposure to 316H

As mentioned above, cyclic voltammetry (CV) techniques are a useful supplement to ICP methods for understanding corrosion with potential for use for *in situ* analysis of molten salts. Figure 115 shows the CVs of salts in capsules 1 through 4 before and after exposure to 316H for 1000 hours at 700 °C. Anodic (positive) and cathodic (negative) current peaks correspond to oxidation and reduction of electroactive species, respectively. The magnitude and potential at which the peaks in current occur are dependent upon the identity of the species and its activity in the melt.

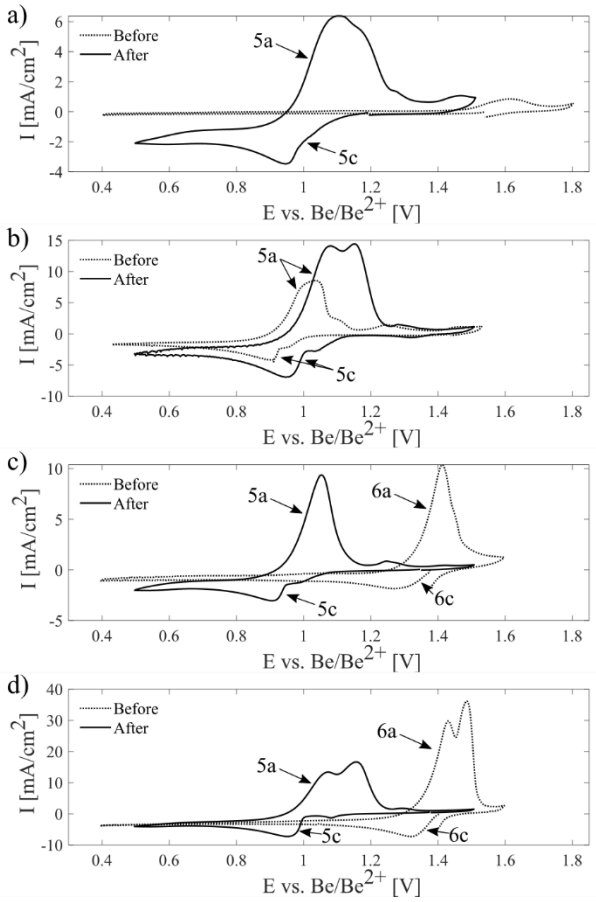

Figure 115. Cyclic voltammograms of corrosion FLiBe salts before and after 1000 hours exposure in a) capsule 1, b) capsule 2, c) capsule 3 and d) capsule 4. Scan Rate 80 mV/sec, Mo WE, Be/Be^{2+} dynamic reference electrode, Glassy Carbon CE.

In each CV, it is assumed that the pair of anodic and cathodic peaks with the lowest potential with respect to Be/Be^{2+} reference reaction corresponds to the general half-cell reaction,

$$M^{n+} + ne^{-} \leftrightarrow M \qquad (76)$$

where soluble M^{n+} is in equilibrium with insoluble M. If electrolysis fully covers the surface of the electrode with M, the activity of the deposit is unity and reaction 76 will have a half-cell reduction potential given by the Nernst's equation. In the author's work [4], it was shown that the Cr/Cr^{2+} redox couple is a reversible reaction at 700 °C with a half-cell reduction potential that obeys equation 58. A method that uses the variation in CV peak potentials as a metric for changes in reduction potential was developed in [4] and

is adopted here. Comparisons of the anodic and cathodic peak potentials, $E_{p,a}$ and $E_{p,c}$, are made to identify the species *M* participating in reaction 76.

The most obvious change occurred in capsule 1, which contained as-purified FLiBe salt. In Figure 115 (a), the CV of the as-purified FLiBe before corrosion (dotted line) has no significant redox peaks indicating that the concentrations of dissolved species, such as Cr^{2+} and Fe^{2+}, are low. ICP-OES reveals that after corrosion the Cr concentration of capsule 1 increased from 6 ± 1 ppm to 263 ± 7 ppm. In the CV after corrosion (solid line), the redox peaks 5a and 5c have peak potentials at 1.10 and 0.95 V vs. Be/Be^{2+}, respectively. Comparison of the peak potentials to previous work indicates that the reaction corresponds to the Cr/Cr^{2+} redox couple, which is generally observed between 0.8 V and 1.2 V vs. Be/Be^{2+} at 700 °C [4].

The CVs of the salt in capsule 2 show the sensitivity of the technique to changes in the analyte concentration that is approximately consistent with the results of ICP-OES metals analysis. As shown in Table 30, the Cr in capsule 2 increased from 245 ± 3 ppm to 452 ± 3 ppm after exposure to 316H. In Figure 115 (b), CVs before and after corrosion show an increase in the activity of a dissolved species. The cathodic peak potential of Cr/Cr^{2+} redox reaction increases by approximately 40 mV. This is only slightly higher than the 26 mV change in $E_{(Cr^{2+}/Cr)}$ calculated by using the concentration of Cr in capsule 2 before and after corrosion in equation 4 and taking the difference. While this method of determining concentration is not accurate, since $a_{M^{n+}}$ is unknown and its relation to potential is logarithmic, it is clear that corrosion has led to a measurable change in salt chemistry that is observed at least qualitatively by CV.

The exact cause of the apparent corrosion in capsules 1 and 2 remains somewhat speculative. There are two plausible causes. First, the purification of fluoride salts is an imperfect process. Trace impurities that may not be accounted for in the available data may contribute to corrosion. A comparison of purified vs. non-purified salt was not performed in this study. Second, while the atmosphere was maintained to a high standard compared to industrial and research standards, it is theoretically still possible for a small amount of impurities to get incorporated into the salt and produce HF enabling reaction 1 to proceed. A

method of sampling the FLiBe salt's HF concentration that would not potentially be detrimental to the corrosion experiment was not available.

A remarkable change in salt chemistry is observed with CVs in capsules 3 and 4. Initial salt mixtures containing 99 ppm Fe and 392 ppm Fe showed redox peaks 6a and 6c between 1.2 and 1.5 V vs. Be/Be^{2+} at 700 °C which corresponds to the reaction,

$$Fe^{2+} + 2e^{-} \leftrightarrow Fe^{0} \tag{77}$$

Following corrosion, new anodic and cathodic peaks lie between 0.8 V and 1.2 V vs. Be/Be^{2+} at 700 °C. The change in the reduction potentials of the dominant redox peaks is quite large. According to equation 58, a large decrease in Fe^{2+} concentration could lead to a change in $E_{(Fe^{2+}/Fe)}$ of several hundred mV, but the intensity of the current density peaks would become much smaller than peak 6c. It is therefore likely that peaks 5a and 5c correspond to a species with a lower standard reduction potential. The decrease in Fe and increase in Cr concentrations in capsules 3 and 4, shown in Table 30, after corrosion leads to the conclusion that peaks 5a and 5c correspond to the Cr/Cr^{2+} redox couple.

While the dominant set of redox peaks observed in each CV are consistent with the expected dissolved species, distortions of some of the redox peaks suggest that more complex electrochemical phenomena are present, as observed in several scans including for capsule 2 before corrosion and all capsules post-corrosion. Possible origins for these peaks have been previously discussed, including underpotential deposition, and other possible soluble-soluble reactions [4]. These immutable peaks are indicative of additional redox reactions whose redox behavior is convoluted with that of the redox reaction of interest.

The redox couple(s) which appear in addition to the Cr/Cr^{2+} redox reaction after corrosion are speculated to have several possible identities. For instance, dissolved chromium fluoride may likely take on II and III oxidation states in FLiBe [16]. Other salt contaminants may raise or lower the activity of Cr^{2+} and Cr^{3+}. Dissolved manganese is also electrochemically active and can produce current peaks of its own. The reduction potential of a soluble-insoluble redox reaction of Mn relative to that of Cr/Cr^{2+} will depend on their relative activities. The concentration of Mn measured by ICP-OES is significant enough that an

appreciable electrochemical reaction could conceivably be measured with CV. Neither the effect of dissolved FeF_2 on the ratio of the Cr^{2+}/Cr^{3+} activities nor the electrochemical behavior of the Mn redox couple have been extensively studied in FLiBe.

While the ability to reliably distinguish some corrosion products, such as Cr^{2+} and Fe^{2+}, from one another is beneficial to salt chemistry and corrosion research, the occurrence of more than one set of redox peaks in close proximity presents a challenge for quantitative CV analysis. A quantitative approach to analysis taken in previous work [4] and other experiments [17]-[21] assumes that the electrochemical system consists of a redox couple between a single soluble reactant and an insoluble product, such as reaction 76. The model does not explicitly deal with the case in which more than one electrochemically active, soluble species is present. Several studies [22]-[23] have discussed the implementation of more rigorous theoretical approaches to quantitative CV analysis.

3.4.2.3 Weight change of 316H exposed to different FLiBe salt chemistries

The weight change of 316H was measured after exposure to each salt chemistry to quantify the effect of the imposed conditions. In Figure 116, the average weight change of three 316H coupons placed in capsules 1 through 4 is shown. All samples experience mass loss. While significant changes in salt chemistry were observed in each capsule, it is difficult to interpret the effect of each salt chemistry based on weight change alone.

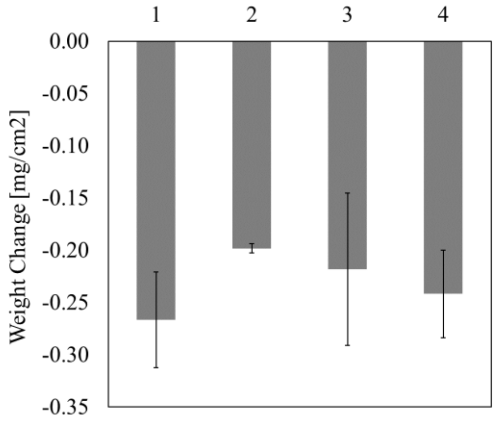

Figure 116. Weight change of 316H following exposure to salts in capsules 1 through 4 for 1000 hours at 700 °C.

The as-purified salt in capsule 1 provides a benchmark to compare other samples in this study. These samples experienced an average weight loss of 0.26 ± 0.05 mg/cm^2. This is comparable to results from experiments that exposed 316L stainless steel to similar salts and the same capsule material. Zheng et al. [24] found that 316L stainless steel experienced approximately 0.2 mg/cm^2 of weight loss when exposed to as-purified ^{7}Li enriched MSRE FLiBe salt for 1000 hours at 700 ˚C. Chrobak [25] reported that 316L stainless steel exposed to as-purified non-^{7}Li enriched FLiBe salt for 2000 hours at 700 ˚C showed 0.90 ± 0.05 mg/cm^2 of weight loss.

When compared to capsule 1, the weight change results of coupons in the other capsules are not statistically very different. As shown in Figure 116, the coupons in capsule 2 experienced the lowest average weight loss of 0.198 ± 0.004 mg/cm^2. Capsules 3 and 4 showed 0.22 ± 0.07 mg/cm^2 and 0.24 ± 0.04 mg/cm^2 of weight loss, respectively. Given the uncertainty, the weight change results suggest that all capsules experience the same net corrosion. To better assess materials degradation, microstructural characterization was performed using X-ray Diffraction (XRD), scanning electron microscopy (SEM), energy dispersive spectroscopy (EDS).

3.4.2.4 Post corrosion material characterization analysis

XRD performed on 316H following corrosion showed some microstructural modification of the surface. Figure 117 shows that varying amounts of austenite and ferrite are present on the surface of 316H exposed to the different salt chemistries. Austenite (111), (110), and (220) peaks are present in all samples. The ferrite (110) peak is observed in the as-received 316H while the additional ferrite (110), (200) and (211) peaks are observed in coupons exposed to as-purified FLiBe and FLiBe containing FeF_2. Zheng et al. [24] showed that 316L stainless steel exposed to as-purified ^{7}Li enriched FLiBe resulted in ferrite phase formation in the near-surface region of the sample. Investigation of the ferrite content as a function of depth revealed little ferrite in the bulk suggesting that the phenomenon is not thermally induced, but rather corrosion-induced. There is variation in the intensity of the austenite (111) and ferrite (110) peaks. A comparison of these two peaks shows the significant formation of ferrite in as-purified FLiBe and FLiBe with FeF_2. There is little correlation between impurity activity and ferrite formation. Interestingly, no ferrite formation is observed in (c), the samples from the capsule which contained FLiBe with CrF_2. The exact mechanism for ferrite formation when steel is exposed to FLiBe remains unclear, as the loss of Cr should stabilize austenite rather than ferrite.

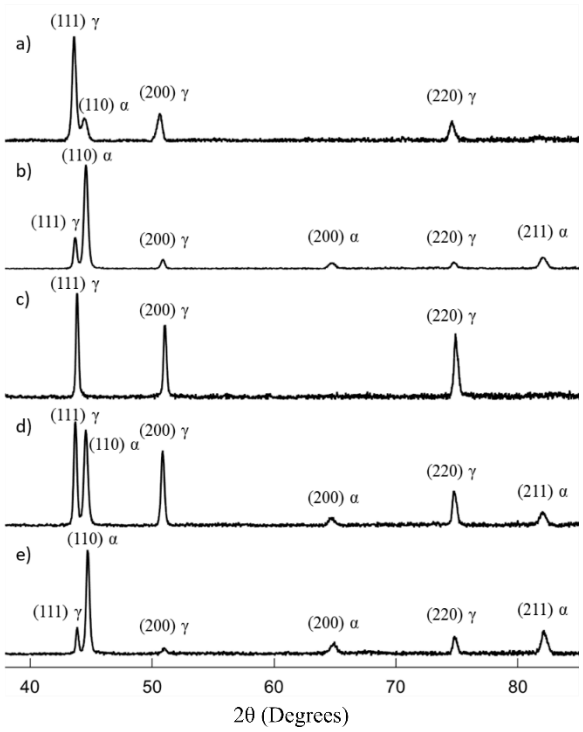

Figure 117. XRD patterns of 316H exposed to (a) as-received 316H, (b) as-purified FLiBe, FLiBe with (c) 245 ppm CrF_2, (d) 99 ppm FeF_2 and (e) 392 ppm FeF_2 after 1000 hours at 700 °C.

The near-surface regions of coupons in capsules 1 through 4 were examined using SEM for the influence of each salt chemistry. The exposed surface of each 316H coupon is shown in Figure 118. Again, when exposed in a 316L capsule, 316H showed faceting of the surface. Different salt mixtures resulted in different amounts of surface roughening. Small particles with diameters less than 1 micrometer were prevalent on samples exposed in capsule 1 and some were observed on samples in capsules 2 and 3. Like the 316 stainless steel results reported for FLiNaK earlier, EDS analysis confirmed that the particulates observed on the surface of steel after exposure to as-purified FLiBe to be molybdenum-rich. The exact origin of the particles is not exactly known. The depletion of Cr may promote the precipitation of Mo in the near-surface region. If this hypothesis is true, the higher density of Mo-rich precipitates in Figure 118 (a) than in Figure 118 (b) may indicate that the coupons in capsule 1 experienced more Cr depletion than in capsule 2. Further characterization was performed on samples in capsules 3 and 4 to better understand why no Mo precipitates appear on their surfaces.

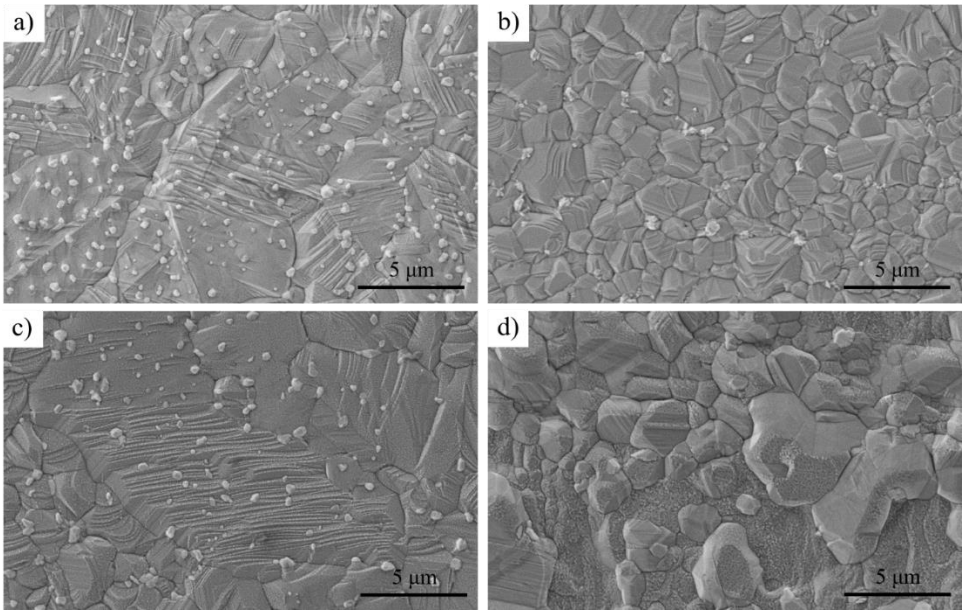

Figure 118. SEM image of corroded 316H surface exposed to (a) as-purified FLiBe, FLiBe with (b) 245 ppm CrF_2, (c) 99 ppm FeF_2 and (d) 392 ppm FeF_2 after 1000 hours at 700 °C.

A coupon from each capsule was cross-sectioned and analyzed using EDS to determine how each salt chemistry affects the distribution of alloying elements in the near-surface region. In Figure 119, EDS compositional line scans through a grain in the near-surface region of each coupon show the elemental depletion from the bulk of 316H grains. In capsules 1 and 2, the concentration of Cr in the bulk grain at the surface decreases only by a few weight percent. This implies that, at this temperature, corrosion at the exposed grain surface occurs very slowly and supports the hypothesis that the majority of Cr depletion occurs at the grain boundary where Cr can diffuse towards the surface at a higher rate.

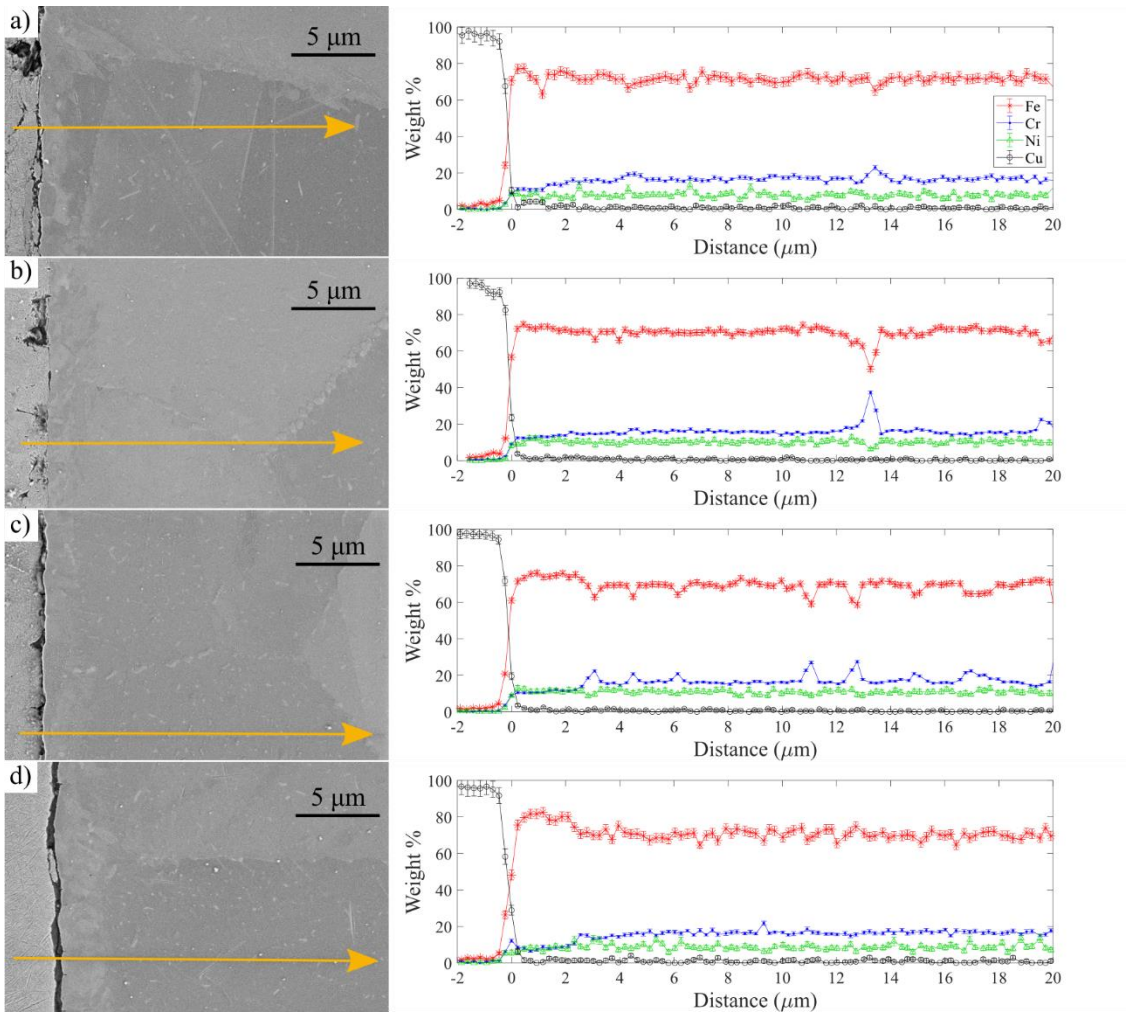

Figure 119. EDS line scan of near-surface region of 316H exposed to (a) as-purified FLiBe, FLiBe with (b) 245 ppm CrF_2, (c) 99 ppm FeF_2 and (d) 392 ppm FeF_2 after 1000 hours at 700 °C.

The morphology and compositional of the near surface region of coupons in each capsule were analyzed using SEM and EDS compositional maps. Figure 120 (a), (d), (g), (j) show SEM images of coupons in capsules 1-4. Figure 120 (b), (e), (h), (k) show EDS compositional maps of chromium in each coupon. Figure 120 (c), (i), (i), (l) show EDS compositional maps of iron in each coupon. In each SEM image a grain boundary that intersects the exposed surface is visible. In all capsules, EDS analysis shows that the grain boundaries in the bulk material, away from the exposed surface, are deficient in Fe and rich in Cr. The Cr rich precipitates are likely chromium carbides resulting from extensive thermal aging at these high corrosion test temperatures. In the near-surface region, there are, however, distinct differences in the distribution of Cr and Fe as a result of exposure to each salt chemistry. To account for the different surface

features the *depth of corrosion attack* was measured in terms of chromium depletion depth along grain boundaries rather than with respect to the apparent exposed surface. Figure 120 (b) shows that there is a depletion of Cr from the grain boundary to a length of 7.7 μm in capsule 1, while it is difficult to determine an appreciable depth of corrosion attack in capsule 2, as shown Figure 120 (e). Figure 120 (h) and Figure 120 (k) show coupons from capsules 3 and 4 which suffered corrosion attack to a depth of 3.1 μm and 8.8 μm. Additionally, these coupons also show an unusual Cr deficient and Fe rich layer parallel to the exposed surface.

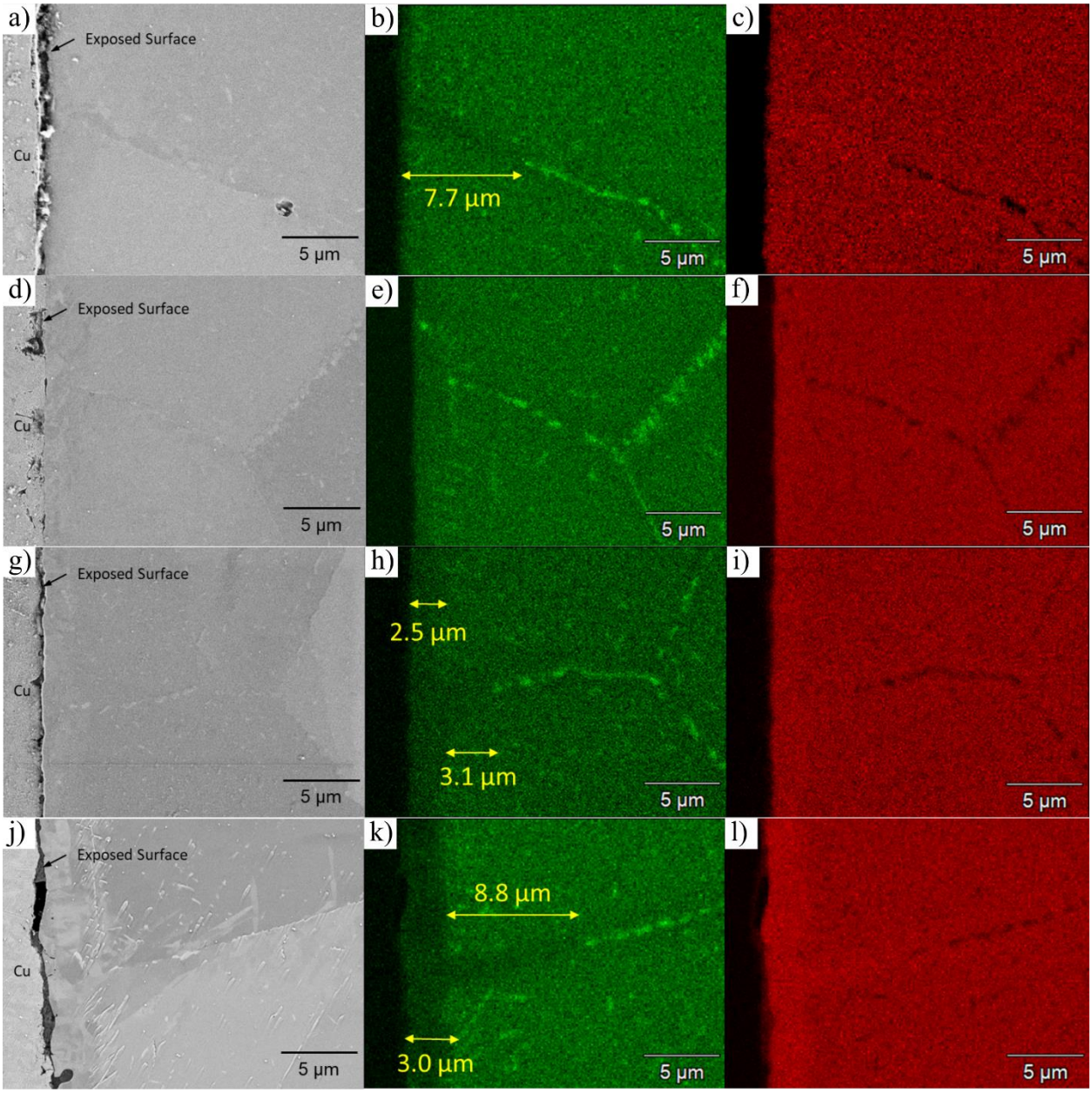

Figure 120. SEM & EDS line scan of near-surface region of 316H exposed to (a)-(c) as-purified FLiBe, FLiBe with (d)-(f) 245 ppm CrF_2, (g)-(i) 99 ppm FeF_2 and (j)-(l) 392 ppm FeF_2 after 1000 hours at 700 °C. (a), (d), (g), (j) SEM image, (b), (e), (h), (k) EDS chromium map, (c), (f), (i), (l) EDS iron map.

In Figure 120 (b), the 7.7 µm depth of corrosion attack in as-purified FLiBe is consistent with similar experiments in purified FLiBe which showed depths of corrosion attack on the order of 5 to 10 µm in 1000 hours at 700 °C [24]. Interestingly, the different material grain size and surface density of grain boundaries found in [24] do not dramatically change the depth of corrosion attack. This supports the

hypothesis that, at this temperature, transport of Cr to the material surface is largely governed by the rate of diffusion of Cr along grain boundaries.

The addition of CrF_2 decreased the apparent grain boundary attack depth, as shown in Figure 120. The near-surface region also experienced less Cr depletion, consistent with the weight loss data in Figure 116. The increase in Cr concentration in the salt in capsule 2 after corrosion, shown by both ICP-OES and electrochemistry, signifies that 316H is still susceptible to some corrosion of Cr even in the presence of relatively high activity chromium fluoride.

In capsules 3 and 4, unlike capsules 1 and 2, 316H exposed to salts with high levels of dissolved FeF_2 show a unique surface feature that is not typically present after exposure to purified FLiBe. In Figure 120 (i) and (l), there is an emergence of a Fe rich surface layer that could be linked to the low net weight change of the exposed material. Two possible explanations for the emergence of the Fe rich layer have been considered. The first is that corrosion enhanced by the high activity of Fe^{2+} may lead to more aggressive corrosion not only at the grain boundaries but also in the bulk material. This may partially explain the occurrence of the Cr deficient layer but does not adequately account for the disappearance of Fe originally dissolved in the salt. The second explanation is a reaction involving the simultaneous oxidation of Cr and reduction of Fe metal at the exposed surface. Comparing capsules 1 and 4, both ICP-OES and electrochemical methods indicated that FLiBe which initially contained 392 ppm FeF_2 contained almost twice the amount of Cr present in as-purified FLiBe post corrosion, yet the weight change of 316H stainless steel coupons in these capsules are comparable in Figure 116. The simultaneous dissolution of Cr and deposition of reduced iron decreases the net weight loss of the material. Reaction 75 explains both the microstructural features present in Figure 120 (i) and (l) and the small net change in the weight of the coupons.

EDS compositional line scans were used to further investigate the nature of the surface layer on coupons in capsules 3 and 4. Figure 119 (c) and (d) show an obvious deficiency in Cr at the material surface, but there is still appreciable Cr in the first 3 μm of material thickness. The Cr concentration profile

extended 5 μm into the material suggesting that Cr from the alloy bulk diffuses into the Fe rich surface layer.

ICP-OES, electrochemistry and materials characterization determined that the rate of corrosion in salt-containing 99 ppm FeF_2 is lower than as-purified FLiBe, a surprising conclusion given that raising the activity of FeF_2 was hypothesized to lead to increased corrosion. One plausible explanation, based on EDS analysis, is that the deposition of Fe on the sample surface forms a diffusion barrier. Cr from the bulk material would be required to diffuse through the developing iron-rich layer to sustain reaction 66 as the dominant corrosion mechanism in capsules 3 and 4. The non-zero concentration of Cr at the material surface shows that the rate of diffusion is sufficient to allow reaction 75 to proceed. It is, therefore, possible that most dissolved FeF_2 can participate in reaction 75. This is consistent with ICP-OES and electrochemistry results that show that the salt has decreased to levels of FeF_2 below the LOQ following exposure to 316H. The results of capsules 3 and 4 show a strong correlation between the concentration of Fe^{2+} and Cr^{2+} before and after corrosion that is consistent with the hypothesized impurity driven corrosion.

4 Conclusions

In support of MSR development, corrosion and related electrochemical studies of candidate structural alloys, pure metals, and a model binary alloy have been studied in the coolant salts FLiNaK and FLiBe at 700 ˚C. Specialized facilities, including environment-controlled gloveboxes, salt purification systems, and versatile large furnace wells were designed and fabricated for this research. The study involved long-term static corrosion testing followed by detailed microstructural characterization, compositional analysis of the salts before and after corrosion tests using ICP-OES and ICP-MS methods, and detailed electrochemical experiments to achieve a holistic assessment of corrosion phenomena.

Corrosion testing of 316L and 316H stainless steel in molten FLiNaK were conducted in capsules of pyrolytic boron nitride (PBN), 316L stainless steel, and glassy carbon capsules to investigate the role the effects of dissimilar materials on corrosion. The slightly higher carbon content in 316H stainless steel had a notable effect on the mechanisms of corrosion. The role of microstructure on corrosion of the stainless steels in molten fluoride salt was also investigated by performing an array of heat treatments. Sensitization of the stainless steel prior to and during the corrosion test influenced the corrosion mechanisms and was more pronounced in 316H stainless steel on account of its higher carbon content. Sensitization leads to a thicker network of Cr-rich carbide precipitates at the grain boundaries which beneficially affects molten fluoride salt corrosion, by minimizing outward diffusion of Cr along the grain boundaries. Along these lines, pre-sensitization of 316H stainless steel prior to corrosion testing had a marked effect on corrosion mechanisms, suggesting a competition between kinetics of sensitization and out-diffusion of Cr along the grain boundaries into the molten salt, in the initial phases of corrosion. Three quantifiable modes of corrosion were observed, namely, surface recession (uniform corrosion), preferential elemental dissolution within the bulk grains, and preferential elemental dissolution along grain boundaries. Although there were mechanistic differences in corrosion between the two stainless steels, their overall corrosion performance was comparable, a result that is of considerable significance to the MSR application, given that 316H is the only ASME BPVC qualified material that can currently be utilized for the manufacture of structural

components of MSRs. Grain boundary Cr dissolution was the most significant mode of corrosion attack in the stainless steels. Weld filler material 16-8-2 (also a type of stainless steel) used commonly for joining stainless steel was also investigated for molten salt corrosion given the importance of welds in the construction of MSR. The compositionally banded solidification microstructure of the weld filler resulted in preferential corrosion of Cr-rich bands in the microstructure.

The corrosion of several nickel-based alloys was investigated in molten FLiNaK in the aforementioned materials capsules. Hastelloy-N (Alloy N) was tested and used to bench-mark the performance of advanced higher creep strength Alloy 141, and Alloy 3 provided by ORNL. Corrosion stability of strengthening second-phase precipitate particles was a particular focus in these advanced alloys. The alloys showed preferential dissolution of alloying elements both along the grain boundaries and grain matrix. Selective corrosion of certain strengthening precipitate phases was also observed, but there was minimal surface recession. Here again, the capsule material influenced the mechanism and modes of corrosion. Nickel capsules promoted the corrosion of specific alloying elements (Fe in Alloy N, Ta in Alloy 141, and Hf, Nb, Ta, and Ti in Alloy3) as evidenced by their disproportionate presence on the salt and their plate-out on the salt facing surface of the capsule. The glassy carbon capsule accelerated the depletion of alloying elements, an affect that was shown to favor the formation of steep compositional gradients of corrosion prone elements (e.g., Cr) in the near-surface regions of the alloy which mitigates long-term corrosion by enriching the surface with corrosion-resistant elements and phases. PBN capsules had the least influence on the corrosion behavior of the alloys. The stability of second phase precipitates in molten salts was also investigated. In Alloy 3 for example, molybdenum-carbide was stable, but carbides containing Hf, Nb, Ta, Ti were not stable. XPS analysis revealed the formation of a carbon film on the alloy surface as a result of the reaction of certain carbide phases with the fluoride salt.

Precisely designed experimental systems for high-temperature molten salt electrochemistry allowed for a more fundamental understanding of the corrosion processes. Potentiodynamic polarization was applied to Cr, Fe, Ni, the binary alloy Ni-20Cr, and 316L stainless steel in FLiNaK at 700 ˚C to investigate corrosion mechanisms under an externally applied potential and to measure fundamental electrochemical parameters

that govern corrosion. A notable achievement here was the innovative application of the K/K^+ dynamic reference electrode (DRE) that allows for more reliable and reproducible evaluation the electrochemical parameters, such as apparent redox potential, that sheds light on the dominant redox reactions occurring under various conditions, as well as corrosion rate. The DRE forms *in situ* in the salt and obviates the need for the introduction of a physical electrodes in the molten salt, which can affect the reliability of results. Using this approach, the apparent redox potentials and kinetic parameters of pure metals Fe, Cr, Ni, and alloys 316L and Ni-20Cr were successfully measured. Post-polarization examination of the electrodes showed that the microstructural mechanisms of corrosion to be similar to those exposed in static salt environment, demonstrating the feasibility of polarization tests for accelerated screening of alloys for corrosion performance in molten fluoride salts. The pure metals experienced uniform corrosion and the corrosion reactions appear to be activation controlled. Based on open circuit potential measurements and characterization of the specimens after salt exposure, Ni and Fe appear to be relatively stable in FLiNaK, however, Cr dissolved rapidly. The relative hierarchy of the Ni, Fe, and Cr redox potentials was consistent with experimental observations and thermodynamic predictions based on standard Gibbs free energy of formation of metal-fluorides. The redox potential values for these three metals provided insights into the corrosion mechanisms observed in the alloys. The corrosion behavior of Ni-20Cr was dependent on the applied potential relative to the redox potential of Ni and Cr. Preferential dissolution of Cr was observed at potentials below the Ni^{2+}/Ni redox potential, however more uniform corrosion of the alloy surface was observed when the potential exceeded the Ni^{2+}/Ni redox potential due to dissolution of both elements. 316L, on the other hand, had the same redox potential as the Fe^{2+}/Fe reaction due to near-surface dissolution of Cr prior to application of the overpotential. Both Cr and Fe experienced comparable corrosion rates, which led to an overall surface recession at all anodic overpotentials, with no evidence of preferential dissolution of individual alloying elements. These experiments clearly demonstrated the feasibility of applying cathodic protection in molten salt systems and for creating an electrochemical series to predict galvanic corrosion between various metals. The polarization plots exhibited the Tafel behavior, and the thickness loss results calculated from electrochemical data and Faraday's law were consistent with the thickness loss

experienced by electrodes as measured after the polarization tests. Pure metals experience more rapid thickness loss in increasingly anodic environments and experience uniform surface corrosion. Alloys experience more delayed thickness loss because the selective dissolution of alloying elements takes precedence. At sufficiently high anodic potentials, dissolution of the alloy's matrix becomes energetically favorable, and the rate of thickness loss increases dramatically and occurs uniformly.

The use of electrochemical cyclic voltammetry methods for quantitative concentration measurements of corrosion products, such as Cr^{2+}, was investigated for the study of structural materials corrosion in molten FLiBe salt in temperatures between 500 ˚C and 700 ˚C. The electrochemical reversibility of the Cr/Cr^{2+} redox couple was demonstrated at temperatures between 600˚C and 700˚C. These methods were benchmarked using the ICP-OES technique to independently verify the concentrations of Cr and Fe in the FLiBe salt. The redox potential of the Cr/Cr^{2+} couple was reported with respect to the Be/Be^{2+} DRE also developed in this study analogous to the K/K^{+} DRE. The relationship between Cr^{2+} concentration and salt temperature on the apparent reduction potential of Cr^{2+} was observed to obey the Nernst equation. A method for measuring Cr^{2+} concentration using CV cathodic peak current was investigated. The peak current density was repeatable but deviated from the expected proportional trend at lower concentrations. Linear relationships between cathodic peak current density and Cr^{2+} concentration were obtained at 600˚C and 650˚C. From these relationships, the diffusion coefficient of Cr^{2+} in the FLiBe salt at these temperatures was determined.

ICP and CV methods were applied for the measurement of trace impurities, CrF_2 and FeF_2, (common corrosion products) and to confirm that chromium is the predominant corrosion product of 316H stainless steel. In all cases, 316H stainless steel experienced mass loss, however, the mass loss measurements alone did not yield a discernible difference despite the clear differences in salt chromium content after corrosion. Additional, SEM, EDS compositional analysis, and XRD showed the unique influence that each impurity had on the surface of 316H stainless steel and provide additional insight into the weight change results. Voltammetry techniques applied for the determination of dilute species concentration demonstrated the ability to distinguish between common corrosion products, such as

dissolved CrF_2 and FeF_2. Dissolved CrF_2 and FeF_2 have several effects on the microstructure and weight change of 316H. Residual impurities in FLiBe can lead to an appreciable depletion of Cr along grain boundaries and mass loss. Corrosion is somewhat decreased by the higher activity of CrF_2 in the salt. The depletion of Cr and the development of a Fe-rich surface layer in salts that initially contained FeF_2 demonstrate the importance of impurity driven corrosion, and validates the feasibility of the cyclic voltametry technique to monitor the salt chemistry during MSR operation to control and monitor the corrosion health of structural materials.

References

[1] "Generation IV Nuclear Reactors," *World Nucl. Assoc.*, Dec. 2017, [Online]. Available: http://www.world-nuclear.org/information-library/nuclear-fuel-cycle/nuclear-power-reactors/generation-iv-nuclear-reactors.aspx

[2] H. G. MacPherson, "The Molten Salt Reactor Adventure," *Nucl. Sci. Eng.*, vol. 90, no. 374–380, p. 6, 1985.

[3] "Molten Salt Reactors - World Nuclear Association." https://world-nuclear.org/information-library/current-and-future-generation/molten-salt-reactors.aspx (accessed Mar. 22, 2022).

[4] "Annual Energy Outlook 2018 with Projections to 2050," U.S. Energy Information Administration, AEO2018, Feb. 2018. Accessed: Mar. 17, 2018. [Online]. Available: https://www.eia.gov/outlooks/aeo/

[5] S. Ansolabehere *et al.*, "The Future of Nuclear Power: An Interdisciplinary MIT Study," Massachusetts Institute of Technology, 2003. [Online]. Available: http://energy.mit.edu/research/future-nuclear-power/

[6] "Energy, Electricity and Nuclear Power Estimates for the Period up to 2050," Sep. 16, 2020. https://www.iaea.org/publications/14786/energy-electricity-and-nuclear-power-estimates-for-the-period-up-to-2050 (accessed Jan. 25, 2022).

[7] "Annual Energy Outlook 2021." https://www.eia.gov/outlooks/aeo/ (accessed Jan. 25, 2022).

[8] "The Advanced Nuclear Industry," Jun. 15, 2015. https://www.thirdway.org/report/the-advanced-nuclear-industry (accessed Mar. 17, 2018).

[9] H. Bloom, *The chemistry of molten salts; an introduction to the physical and inorganic chemistry of molten salts and salt vapors*. New York: W. A. Benjamin, 1967. Accessed: Mar. 27, 2018. [Online]. Available: https://search.library.wisc.edu/catalog/9910312075902121

[10] J. R. Keiser, J. H. DeVan, and D. L. Manning, "Corrosion resistance of type 316 stainless steel to Li_2BeF_4. [66-34 Mole % LiF--BeF_2] - ORNL/TM-5782." Oak Ridge National Lab, TN USA, 1977. Accessed: Nov. 25, 2016. [Online]. Available: http://www.osti.gov/servlets/purl/7110792/

[11] Manohar S. Sohal, Matthias A. Ebner, Piyush Sabharwall, and Phil Sharpe, "Engineering Database of Liquid Salt Thermophysical and Thermochemical Properties," INL/EXT-10-18297, 980801, Mar. 2010. doi: 10.2172/980801.

[12] J. Pacio and Th. Wetzel, "Assessment of liquid metal technology status and research paths for their use as efficient heat transfer fluids in solar central receiver systems," *Sol. Energy*, vol. 93, pp. 11–22, Jul. 2013, doi: 10.1016/j.solener.2013.03.025.

[13] C. Forsberg, L. Hu, P. Peterson, and K. Sridharan, "Fluoride-Salt-Cooled High- Temperature Reactor (FHR) for Power and Process Heat - 11-3272." Battelle Energy Alliance, LLC, 2015. [Online]. Available: http://www.osti.gov/scitech/servlets/purl/1183687

[14] S. J. Zinkle and G. S. Was, "Materials challenges in nuclear energy," *Acta Mater.*, vol. 61, no. 3, pp. 735–758, Feb. 2013, doi: 10.1016/j.actamat.2012.11.004.

[15] W. R. Grimes, "Chemical Research and Development for Molten-Salt Breeder Reactors," Oak Ridge National Laboratory, ORNL-TM-1853, 1967. [Online]. Available: http://moltensalt.org/references/static/downloads/pdf/ORNL-TM-1853.pdf

[16] V. Ignatiev and A. Surenkov, "Corrosion phenomena induced by molten salts in Generation IV nuclear reactors." Elsevier Inc, 2016.

[17] J. J. Duderstadt, *Nuclear reactor analysis*. New York: Wiley, [1976], 1976. Accessed: Apr. 24, 2018. [Online]. Available: https://search.library.wisc.edu/catalog/999632425002121

[18] D. F. Williams, "Assessment of Candidate Molten Salt Coolants for the Advanced High-Temperatuer Reactor (AHTR)," Oak Ridge National Laboratory, ORNL/TM-2006/12, 2006. [Online]. Available: https://info.ornl.gov/sites/publications/Files/Pub57476.pdf

[19] H. F. Ebling and M. A. Scheil, "Time-Temperature-Sensitization (TTS) Diagrams for Types 347, 304L, and 316L Stainless Steels," in *Advances in the Technology of Stainless Steels and Related Alloys*, Committee A-10, Ed. 100 Barr Harbor Drive, PO Box C700, West Conshohocken, PA 19428-2959: ASTM International, 1965, pp. 275-275–10. doi: 10.1520/STP43752S.

[20] N. Ishiyama, M. Mayuzumi, Y. Mizutani, and J. Tani, "Stress Corrosion Cracking of Type 316 and 316L Stainless Steel in High Temperature Water," Jan. 2005.

[21] L. E. Murr, A. Advani, and D. G. Atteridge, "Effects of deformation (strain) and heat treatment on grain boundary sensitization and precipitation in austenitic stainless steels," *Mater. Charact.*, vol. 24, no. 2, pp. 135–158, Mar. 1990, doi: 10.1016/1044-5803(90)90032-F.

[22] P. C. S. Wu, "Sensitization, intergranular attack, stress corrosion cracking, and irradiation effects on the corrosion of iron--chromium--nickel alloys," Westinghouse Electric Corp., Madison, PA (USA). Advanced Reactors Div., ORNL/TM-6311, Apr. 1978. doi: 10.2172/6696127.

[23] R. E. Gehlbach and H. E. McCoy, Jr., "Phase Instability in Hastelloy N," in *International Symposium on Structural Stability in Superalloys (1968)*, 1968, pp. 346–366. doi: 10.7449/1968/Superalloys_1968_346_366.

[24] "Superalloys: A Primer and History." https://www.tms.org/Meetings/Specialty/Superalloys2000/SuperalloysHistory.html (accessed Apr. 25, 2020).

[25] H. E. McCoy, "The INOR-8 Story," *Oak Ridge Natl. Lab. Rev.*, no. Fall 1969, pp. 35–49, 1969.

[26] H. E. McCoy and B. McNabb, "Intergranular Cracking of INOR-8 in the MSRE," Oak Ridge National Laboratory, Oak Ridge, Tennessee, ORNL--4829, 4581899, Nov. 1972. doi: 10.2172/4581899.

[27] J. R. Keiser, "Status of Tellurium-Hastelloy N Studies in Molten Fluoride Salts," Oak Ridge National Laboratory, Oak Ridge, TN, Technical Report ORNL/TM-6002, Oct. 1977.

[28] H. E. McCoy, "Status of materials development for molten salt reactors," Oak Ridge National Laboratory, Oak Ridge, Tennessee, QRNL/TM-5920, Jan. 1978. [Online]. Available: http://moltensalt.org/references/static/downloads/pdf/ORNL-TM-5920.pdf

[29] R. N. Wright and T.-L. Sham, "Status of Metallic Structural Materials for Molten Salt Reactors," INL/EXT--18-45171-Rev000, 1467482, May 2018. doi: 10.2172/1467482.

[30] N. N. Burova and S. B. Maslenkov, "Structural characteristics of nickel alloys with tantalum," *Met. Sci. Heat Treat.*, vol. 21, no. 5, pp. 350–353, May 1979, doi: 10.1007/BF00780771.

[31] G. Muralidharan, D. F. Wilson, and D. E. Holcomb, "Intermediate Strength Alloys for High Temperature Service in Liquid-Salt Cooled Energy Systems," US20150197832A1, Jul. 16, 2015 Accessed: Apr. 24, 2020. [Online]. Available: https://patents.google.com/patent/US20150197832A1/en

[32] G. Muralidharan, D. F. Wilson, and D. E. Holcomb, "Intermediate strength alloys for high temperature service in liquid-salt cooled energy systems," US9683280B2, Jun. 20, 2017 Accessed: Oct. 26, 2020. [Online]. Available: https://patents.google.com/patent/US9683280B2/en

[33] "Provided curtesy of G. Muralidharan."

[34] J. Koger, “Chromium depletion and void formation in Fe-Ni-Cr alloys during molten salt corrosion and related processes,” *Chromium Deplet. Void Form. Fe-Ni-Cr Alloys Molten Salt Corros. Relat. Process.*, 1974.

[35] M. Elbakhshwan *et al.*, “Corrosion and Thermal Stability of CrMnFeNi High Entropy Alloy in Molten FLiBe Salt,” *Sci. Rep.*, vol. 9, no. 1, Dec. 2019, doi: 10.1038/s41598-019-55653-2.

[36] Y. Wang *et al.*, “Accelerated Discovery of Molten Salt Corrosion-resistant Alloy by High-throughput Experimental and Modeling Methods Coupled to Data Analytics,” *ArXiv210410235 Cond-Mat Physicsphysics*, Apr. 2021, Accessed: Feb. 02, 2022. [Online]. Available: http://arxiv.org/abs/2104.10235

[37] W. D. Manly *et al.*, “AIRCRAFT REACTOR EXPERIMENT--METALLURGICAL ASPECTS - ORNL-2349.” Oak Ridge National Lab, Tenn, 1958.

[38] G. Zheng, B. Kelleher, G. Cao, M. Anderson, T. Allen, and K. Sridharan, “Corrosion of 316 Stainless Steel in High Temperature Molten Li2BeF4 (FliBe) Salt,” *J. Nucl. Mater.*, vol. 461, pp. 143–150, Mar. 2015.

[39] D. Olander, “Redox condition in molten fluoride salts: Definition and control,” *J. Nucl. Mater.*, vol. 300, no. 2, pp. 270–272, 2002, doi: 10.1016/S0022-3115(01)00742-5.

[40] *HSC Chemistry Software*. Outotec.

[41] J. Zhang *et al.*, “Redox potential control in molten salt systems for corrosion mitigation,” *Corros. Sci.*, vol. 144, pp. 44–53, Nov. 2018, doi: 10.1016/j.corsci.2018.08.035.

[42] Y. Wang, K. Sridharan, and A. Couet, “Method for identification of redox control parameters for corrosion mitigation in molten fluoride salts,” *J. Nucl. Mater.*, vol. 543, p. 152624, Jan. 2021, doi: 10.1016/j.jnucmat.2020.152624.

[43] J. C. Ard *et al.*, “Development of the Molten Salt Thermal Properties Database − Thermochemical (MSTDB−TC), example applications, and LiCl−RbCl and UF3−UF4 system assessments,” *J. Nucl. Mater.*, vol. 563, p. 153631, May 2022, doi: 10.1016/j.jnucmat.2022.153631.

[44] J. Schorne-Pinto, J. A. Yingling, M. S. Christian, A. M. Mofrad, M. A. A. Aslani, and T. M. Besmann, “Correlational Approach to Predict the Enthalpy of Mixing for Chloride Melt Systems,” *ACS Omega*, vol. 7, no. 1, pp. 362–371, Jan. 2022, doi: 10.1021/acsomega.1c04755.

[45] C. F. Baes, “A polymer model for BeF 2 and SiO 2 melts,” *J. Solid State Chem.*, vol. 1, no. 2, pp. 159–169, 1970, doi: 10.1016/0022-4596(70)90008-3.

[46] D. Olander, “Equilibrium Pressures over BeF2/LiF(Flibe) Molten Mixtures,” *Fusion Sci. Technol.*, 2002, doi: 10.13182/FST02-6.

[47] B. L. Tremillon, “Acid-Base Effects in Molten Electrolytes,” in *Molten Salt Chemistry*, Springer, Dordrecht, 1987, pp. 279–303. doi: 10.1007/978-94-009-3863-2_14.

[48] D. F. Williams, L. M. Toth, and K. T. Clarno, “Assessment of Candidate Molten Salt Coolants for the Advanced High-Temperature Reactor,” Oak Ridge National Laboratory, Nuclear Science and Technology Division, ORNL/TM-2006/12, Mar. 2006.

[49] M. A. Bredig, *Mixtures of metals with molten salts /*. Oak Ridge, Tenn., 1963. [Online]. Available: http://hdl.handle.net/2027/mdp.39015077306762

[50] G. Zheng, B. Kelleher, G. Cao, M. Anderson, T. Allen, and K. Sridharan, “Corrosion of 316 stainless steel in high temperature molten Li2BeF4 (FLiBe) salt,” *J. Nucl. Mater.*, vol. 461, pp. 143–150, 2015, doi: 10.1016/j.jnucmat.2015.03.004.

[51] J. W. Koger, “Effect of FeF2 Addition on Mass Transfer in a Hastelloy N - LiF-BeF2-UF4 Thermal Convection Loop System,” Oak Ridge National Laboratory, Metals and Ceramics Division, ORNL-TM-4188, Dec. 1972.

[52] W. D. Manly, G. M. Adamson, J. H. Coobs, J. H. DeVan, and D. A. Douglas, “Aircraft Reactor Experiment-Metallurgical Aspects,” Oak Ridge National Laboratory, Oak Ridge National Laboratory, Oak Ridge, Tennessee, AEC Research and Development Report ORNL-2349, Dec. 1957.

[53] J. W. Koger, “Evaluation of Hastelloy N Alloys After Nine Years Exposure to Both a Molten Fluoride Salt and Air at Temperatures from 700 to 560˚C,” Oak Ridge National Laboratory, Oak Ridge, Tennessee, Dec. 1972. Accessed: Apr. 13, 2018. [Online]. Available: http://moltensalt.org/references/static/downloads/pdf/ORNL-TM-4189.pdf

[54] S. S. Raiman *et al.*, “Corrosion of 316H stainless steel in flowing FLiNaK salt,” *J. Nucl. Mater.*, vol. 561, p. 153551, Apr. 2022, doi: 10.1016/j.jnucmat.2022.153551.

[55] C. Falconer *et al.*, “Non-galvanic mass transport in molten fluoride salt isothermal corrosion cells,” *Corros. Sci.*, vol. 177, p. 108955, Dec. 2020, doi: 10.1016/j.corsci.2020.108955.

[56] C. Falconer, M. Elbakhshwan, W. Doniger, M. Weinstein, K. Sridharan, and A. Couet, “Activity gradient driven mass transport in molten fluoride salt medium,” *Npj Mater. Degrad.*, vol. 6, no. 1, Art. no. 1, Apr. 2022, doi: 10.1038/s41529-022-00239-z.

[57] X. Yang *et al.*, “Corrosion of SiC induced by Hastelloy N alloy and its corrosion products in LiF–NaF–KF molten salt,” *Corros. Sci.*, vol. 109, pp. 62–67, Aug. 2016, doi: 10.1016/j.corsci.2016.03.029.

[58] K. J. Chan, R. J. Ambrecht, J. M. Luong, W. T. Choi, and P. M. Singh, “Carburization effects on the corrosion of Cr, Fe, Ni, W, and Mo in fluoride-salt cooled high temperature reactor (FHR) coolant,” *Ann. Nucl. Energy*, vol. 120, pp. 279–285, Oct. 2018, doi: 10.1016/j.anucene.2018.05.013.

[59] K. J. Chan and P. M. Singh, “Corrosion Behavior of Pre-Carburized Hastelloy N, Haynes 244, Haynes 230, and Incoloy 800H in Molten FLiNaK,” 2020, doi: 10.1080/00295450.2020.1809311.

[60] C. F. J. Baes, “The chemistry and thermodynamics of molten salt reactor fuels,” *Nucl Met Met Soc AIME 15 617-44*, 1969.

[61] R. B. Evans, *Self-diffusion of chromium in nickel-base alloys*. Oak Ridge National Laboratory, 1961. [Online]. Available: http://hdl.handle.net/2027/mdp.39015077308032

[62] F. Scholz, *Electroanalytical Methods: Guide to Experiments and Applications*, 1st ed. Springer Berlin Heidelberg, 2002.

[63] P. H. Rieger, *Electrochemistry*. Dordrecht: Springer Netherlands, 1994. doi: 10.1007/978-94-011-0691-7.

[64] A. J. Bard, *Electrochemical methods : fundamentals and applications*. New York: Wiley, 1980.

[65] C. M. Blood, “Solubility and stability of structural metal difluorides in molten fluoride mixtures - ORNL-TM--760,” Oak Ridge National Lab, TennUSA, 1964.

[66] B. F. Hitch and C. F. Baes Jr., “An electromotive force study of molten lithium fluoride-beryllium fluoride solutions,” *Inorg. Chem.*, vol. 8, no. 2, pp. 201–207, 1969.

[67] D. A. Jones, *Principles and prevention of corrosion*. Second edition. Upper Saddle River, NJ: Prentice Hall, [1996] ©1996, 1996. Accessed: May 01, 2020. [Online]. Available: https://search.library.wisc.edu/catalog/9910280411002121

[68] D. Pletcher, *A First Course in Electrode Processes*. 2009. Accessed: May 02, 2020. [Online]. Available: http://pubs.rsc.org/en/content/ebook/978-1-84755-893-0

[69] D. Enos, “The Potentiodynamic Polarization Scan: Technical Report 33.” 1997. [Online]. Available: https://www.ameteksi.com/-/media/ameteksi/download_links/documentations/library/solartonanalytical/electrochemistry/technical%20report%2033%20enos%20potentiodynamic%20scan.pdf?la=en

[70] R. T. Loto and C. A. Loto, “Potentiodynamic Polarization Behavior and Pitting Corrosion Analysis of 2101 Duplex and 301 Austenitic Stainless Steel in Sulfuric Acid Concentrations,” *J. Fail. Anal. Prev.*, vol. 17, no. 4, pp. 672–679, Aug. 2017, doi: 10.1007/s11668-017-0291-6.

[71] X. Cheng, Z. Feng, C. Li, C. Dong, and X. Li, “Investigation of oxide film formation on 316L stainless steel in high-temperature aqueous environments,” *Electrochimica Acta*, vol. 56, no. 17, pp. 5860–5865, Jul. 2011, doi: 10.1016/j.electacta.2011.04.127.

[72] A. P. Wang, T. Zhang, and J. Q. Wang, “Ni-based fully amorphous metallic coating with high corrosion resistance,” *Philos. Mag. Lett.*, vol. 86, no. 1, pp. 5–11, Jan. 2006, doi: 10.1080/09500830500479718.

[73] G01 Committee, “Reference Test Method for Making Potentiodynamic Anodic Polarization Measurements,” ASTM International. doi: 10.1520/G0005-14E01.

[74] H. Ai *et al.*, “On the possibility of severe corrosion of a Ni-W-Cr alloy in fluoride molten salts at high temperature,” *Corros. Sci.*, vol. 149, pp. 218–225, Apr. 2019, doi: 10.1016/j.corsci.2019.01.012.

[75] Y. L. Wang, Q. Wang, H. J. Liu, and C. L. Zeng, “Effect of grain refinement on the corrosion of Ni-Cr alloys in molten (Li,Na,K)F,” *Corros. Sci.*, vol. 109, pp. 43–49, Aug. 2016, doi: 10.1016/j.corsci.2016.03.027.

[76] Y. Wang, H. Liu, G. Yu, J. Hou, and C. Zeng, “Electrochemical study of the corrosion of a Ni-based alloy GH3535 in molten (Li,Na,K)F at 700°C,” *J. Fluor. Chem.*, vol. 178, pp. 14–22, Oct. 2015, doi: 10.1016/j.jfluchem.2015.06.014.

[77] J. Qiu, A. Wu, Y. Li, Y. Xu, R. Scarlat, and D. D. Macdonald, “Galvanic corrosion of Type 316L stainless steel and Graphite in molten fluoride salt,” *Corros. Sci.*, p. 108677, Apr. 2020, doi: 10.1016/j.corsci.2020.108677.

[78] Y. Wang, Q. Yang, and J. Zhang, “Transport and kinetics properties of LaF3 in FLiNaK molten salt determined by electrochemical methods,” *J. Fluor. Chem.*, vol. 233, p. 109502, May 2020, doi: 10.1016/j.jfluchem.2020.109502.

[79] Y. Wang, C. Zeng, and W. Li, “The influence of temperature gradient on the corrosion of materials in molten fluorides,” *Corros. Sci.*, vol. 136, pp. 180–187, May 2018, doi: 10.1016/j.corsci.2018.03.003.

[80] N. S. Patel, V. Pavlík, B. Kubíková, M. Nosko, V. Danielik, and M. Boča, “Corrosion behaviour of Ni-based superalloys in molten FLiNaK salts,” *Corros. Eng. Sci. Technol.*, vol. 54, no. 1, pp. 46–53, Feb. 2019, doi: 10.1080/1478422X.2018.1525829.

[81] T. Berzins and P. Delahay, “Oscillographic Polarographic Waves for the Reversible Deposition of Metals on Solid Electrodes,” *J. Am. Chem. Soc.*, vol. 75, no. 3, pp. 555–559, Feb. 1953, doi: 10.1021/ja01099a013.

[82] P. Delahay, *New instrumental methods in electrochemistry; theory, instrumentation, and applications to analytical and physical chemistry. With a chapter on high-frequency methods*. New York: Interscience Publishers, 1954. Accessed: Jul. 29, 2018. [Online]. Available: https://search.library.wisc.edu/catalog/999539830302121

[83] H. Peng, M. Shen, Y. Zuo, X. Tang, R. Tang, and L. Xie, “Electrochemical technique for detecting the formation of uranium-containing precipitates in molten fluorides,” *Electrochimica Acta*, vol. 222, pp. 1528–1537, 2016, doi: 10.1016/j.electacta.2016.11.135.

[84] G. D. Del Cul, “Redox Potential of Novel Electrochemical Buffers Useful for Corrosion Prevention in Molten Fluorides,” *ECS Proc. Vol.*, vol. 2002–19, no. 1, pp. 431–436, Jan. 2002, doi: 10.1149/200219.0431PV.

[85] M. Gibilaro, L. Massot, and P. Chamelot, “A way to limit the corrosion in the Molten Salt Reactor concept: the salt redox potential control,” *Electrochimica Acta*, vol. 160, pp. 209–213, 2015, doi: 10.1016/j.electacta.2015.01.142.

[86] L. Massot, P. Chamelot, and P. Taxil, “Cathodic behaviour of samarium(III) in LiF–CaF2 media on molybdenum and nickel electrodes,” *Electrochimica Acta*, vol. 50, no. 28, pp. 5510–5517, Sep. 2005, doi: 10.1016/j.electacta.2005.03.046.

[87] M. Straka, M. Korenko, F. Lisý, and L. Szatmáry, “Electrochemistry of samarium in lithium-beryllium fluoride salt mixture,” *J. Rare Earths*, vol. 29, no. 8, pp. 798–803, Aug. 2011, doi: 10.1016/S1002-0721(10)60545-5.

[88] D. F. Williams and L. M. Toth, *ORNL/GEN4/LTR-05-011 Chemical Considerations for the Selection of the Coolant for the Advanced High-Temperature Reactor*. 2005.

[89] H. G. MacPherson, “Quarterly Progress Report for Period Ending October 31, 1957,” Oak Ridge National Laboratory, Quarterly Progress Report ORNL-2431, Feb. 1958.

[90] S. Guo, N. Shay, Y. Wang, W. Zhou, and J. Zhang, “Measurement of europium (III)/europium (II) couple in fluoride molten salt for redox control in a molten salt reactor concept,” *J. Nucl. Mater.*, vol. 496, pp. 197–206, Dec. 2017, doi: 10.1016/j.jnucmat.2017.09.027.

[91] H. W. Jenkins, G. Mamantov, and D. L. Manning, “Electrode Potentials of Several Redox Couples in Molten Fluorides,” *J. Electrochem. Soc.*, vol. 117, no. 2, p. 183, Feb. 1970, doi: 10.1149/1.2407461.

[92] M. Korenko, M. Straka, L. Szatmáry, M. Ambrová, and J. Uhlíř, “Electrochemical separation of uranium in the molten system LiF–NaF–KF–UF4,” *J. Nucl. Mater.*, vol. 440, pp. 332–337, Sep. 2013, doi: 10.1016/j.jnucmat.2013.04.078.

[93] D. Ludwig, L. Olson, K. Sridharan, M. Anderson, and T. Allen, “High temperature electrochemistry of molten fluoride salt for measurement of dissolved chromium,” *Corros. Eng. Sci. Technol.*, vol. 46, no. 4, pp. 360–364, Jun. 2011, doi: 10.1179/147842209X12579401586645.

[94] H. Peng, M. Shen, C. Wang, T. Su, Y. Zuo, and L. Xie, “Electrochemical investigation of the stable chromium species in molten FLINAK,” *RSC Adv.*, vol. 5, no. 94, pp. 76689–76695, Sep. 2015, doi: 10.1039/C5RA09919F.

[95] H. Peng and M. Shen, “Electrochemical Investigation on the Stable Iron Species in Molten FLINAK,” 2016. doi: 10.21767/2470-9867.1000011.

[96] D. Rappleye, D. Horvath, Z. Wang, C. Zhang, and M. F. Simpson, “Methods for determining the working electrode interfacial area for electroanalytical measurements of metal ions in molten LiCl-KCl,” *ECS Trans.*, vol. 75, no. 15, pp. 79–85, 2016, doi: 10.1149/07515.0079ecst.

[97] L. M. Toth, G. D. Del Cul, S. Dai, and D. H. Metcalf, “Molten fluoride fuel salt chemistry,” *AIP Conf. Proc.*, vol. 324, no. 1, pp. 1139–1142, 1995, doi: 10.1063/1.47211.

[98] M. M. Tylka, J. Willit, J. Prakash, and M. A. Williamson, “Application of Voltammetry for Quantitative Analysis of Actinides in Molten Salts,” *J. Electrochem. Soc.*, vol. 162, no. 12, pp. H852–H859, 2015, doi: 10.1149/2.0281512jes.

[99] M. M. Tylka, J. L. Willit, J. Prakash, and M. A. Williamson, “Method development for quantitative analysis of actinides in molten salts,” *J. Electrochem. Soc.*, vol. 162, no. 9, pp. H625–H633, 2015, doi: 10.1149/2.0401509jes.

[100] T. Yoko and R. A. Bailey, “Electrochemical Studies of Chromium in Molten LiF - NaF - KF (FLINAK),” *J. Electrochem. Soc.*, vol. 131, no. 11, pp. 2590–2595, Nov. 1984, doi: 10.1149/1.2115363.

[101] R. Zakirov, V. Ignatiev, V. Subbotin, and A. Toropov, “Electrochemical Properties of Zirconium, Plutonium and Lanthanides in Fluoride Melts,” RRC “Kurchatov Institute,” INIS-FR--3004, 2004. Accessed: May 06, 2020. [Online]. Available: http://inis.iaea.org/Search/search.aspx?orig_q=RN:36016088

[102] W. H. Doniger and K. Sridharan, “Application of voltammetry for quantitative analysis of chromium in molten 2LiF-BeF2 (FLiBe) salt,” *J. Electroanal. Chem.*, vol. 838, pp. 73–81, Apr. 2019, doi: 10.1016/j.jelechem.2019.02.048.

[103] F. Carotti, H. Wu, and R. O. Scarlat, “Characterization of a Thermodynamic Reference Electrode for Molten LiF-BeF2 (FLiBe),” *J. Electrochem. Soc.*, vol. 164, no. 12, pp. H854–H861, Jan. 2017, doi: 10.1149/2.1591712jes.

[104] B. Kelleher, K. Dolan, M. Anderson, and K. Sridharan, “Observed Redox Potential Range of Li 2 BeF 4 Using a Dynamic Reference Electrode,” *Nucl. Technol.*, vol. 195, no. 3, pp. 239–252, 2016, doi: 10.13182/NT15-140.

[105] K. Dolan, “Redox Potential Measurement and Control for the Fluoride-Salt-Cooled High-Temperature Reactor,” MS Thesis, Nuclear Engineering and Engineering Physics, University of Wisconsin - Madison, 2015.

[106] K. Ema, Y. Ito, T. Takenaka, and J. Oishi, “Relation between potentials of Li,K/Li+,K+ dynamic reference electrode and HF/H2 gas electrode in a molten LiF-KF system,” *Electrochimica Acta*, vol. 32, no. 10, pp. 1537–1540, Oct. 1987, doi: 10.1016/0013-4686(87)85099-5.

[107] V. K. Afonichkin *et al.*, “Dynamic reference electrode for investigation of fluoride melts containing beryllium difluoride,” *J. Fluor. Chem.*, vol. 130, no. 1, pp. 83–88, 2009, doi: 10.1016/j.jfluchem.2008.07.017.

[108] G. Durán-Klie, D. Rodrigues, and S. Delpech, “Dynamic Reference Electrode development for redox potential measurements in fluoride molten salt at high temperature,” *Electrochimica Acta*, vol. 195, pp. 19–26, Mar. 2016, doi: 10.1016/j.electacta.2016.02.042.

[109] H. Qiao, T. Nohira, and Y. Ito, “Electrochemical formation of Pd–La alloy films in a LiF–NaF–KF–LaF3 melt,” *J. Alloys Compd.*, vol. 359, no. 1, pp. 230–235, Sep. 2003, doi: 10.1016/S0925-8388(03)00203-2.

[110] W. H. Doniger, C. Falconer, M. Elbakhshwan, K. Britsch, A. Couet, and K. Sridharan, “Investigation of impurity driven corrosion behavior in molten 2LiF-BeF2 salt,” *Corros. Sci.*, p. 108823, Jun. 2020, doi: 10.1016/j.corsci.2020.108823.

[111] L. Massot, M. Gibilaro, D. Quaranta, and P. Chamelot, “Corrosion Products Electrochemical Behaviour into Molten LiF-NaF: Investigation of Cr(II) System,” *J. Electrochem. Soc.*, vol. 168, no. 2, p. 026510, Feb. 2021, doi: 10.1149/1945-7111/abe088.

[112] A. A. Frigo, “Heat-shield design for glovebox applications.,” Argonne National Lab., IL (US), ANL/CMT/CP-96761, Jul. 1998. Accessed: Mar. 21, 2022. [Online]. Available: https://www.osti.gov/biblio/10869-heat-shield-design-glovebox-applications

[113] “29 CFR Part 1910 Air Contaminants; Final Rule,” *Fed. Regist.*, vol. 54, no. 12, p. 653, 1989.

[114] "10 CFR Part 850 -- Chronic Beryllium Disease Prevention Program." https://www.ecfr.gov/current/title-10/chapter-III/part-850 (accessed Mar. 21, 2022).

[115] "Beryllium Lymphocyte Proliferation Test," *National Jewish Health*. https://nationaljewish.org/conditions/beryllium-disease/diagnosis/beryllium-lymphocyte-proliferation (accessed Mar. 21, 2022).

[116] B. C. Kelleher, "Purification and Chemical Control of Molten Li2-BeF4 for a Fluoride Salt Cooled Reactor," PhD, University of Wisconsin - Madison, 2015.

[117] B. C. Kelleher, K. P. Dolan, P. Brooks, M. H. Anderson, and K. Sridharan, "Batch-Scale Hydrofluorination of Li2BeF 4 to Support Molten Salt Reactor Development," *J. Nucl. Eng. Radiat. Sci.*, vol. 1, no. 4, p. 041010/1-041010/12, 2015, doi: 10.1115/1.4030963.

[118] J. H. Shaffer, "Preparation and Handling of Salt Mixtures for the Molten Salt Reactor Experiment - ORNL-4616." Oak Ridge National Lab, Tenn, 1971. Accessed: Feb. 04, 2017. [Online]. Available: http://www.osti.gov/servlets/purl/4074869/

[119] "The fundamentals of gas tungsten arc welding: Preparation, consumables, and equipment necessary for the process." https://www.thefabricator.com/thewelder/article/arcwelding/the-fundamentals-of-gas-tungsten-arc-welding--preparation-consumables-and-equipment-necessary-for-the-process (accessed May 01, 2022).

[120] O. US EPA, "EPA Method 3050B: Acid Digestion of Sediments, Sludges, and Soils," Jun. 12, 2019. https://www.epa.gov/esam/epa-method-3050b-acid-digestion-sediments-sludges-and-soils (accessed Mar. 21, 2022).

[121] S. S. Raiman and S. Lee, "Aggregation and data analysis of corrosion studies in molten chloride and fluoride salts," *J. Nucl. Mater.*, vol. 511, pp. 523–535, Dec. 2018, doi: 10.1016/j.jnucmat.2018.07.036.

[122] M. Maric *et al.*, "The effect of cold-rolling on the microstructure and corrosion behaviour of 316L alloy in FLiNaK molten salt," *Corros. Sci.*, vol. 142, pp. 133–144, Sep. 2018, doi: 10.1016/j.corsci.2018.07.006.

[123] K. T. Jacob, S. Raj, and L. Rannesh, "Vegard's law: a fundamental relation or an approximation?," *Int. J. Mater. Res.*, vol. 98, no. 9, pp. 776–779, Sep. 2007, doi: 10.3139/146.101545.

[124] Y. Jia *et al.*, "Effect of SO42- ion impurity on stress corrosion behavior of Ni-16Mo-7Cr alloy in FLiNaK salt," *J. Nucl. Mater.*, vol. 547, p. 152809, Apr. 2021, doi: 10.1016/j.jnucmat.2021.152809.

[125] A. Smigelskas, "Zinc diffusion in alpha brass," *undefined*, 1947, Accessed: Apr. 22, 2022. [Online]. Available: https://www.semanticscholar.org/paper/Zinc-diffusion-in-alpha-brass-Smigelskas/77658d16ca2fa4afeba22909128587e1d78581b8

[126] E04 Committee, "Test Methods for Determining Average Grain Size," ASTM International. doi: 10.1520/E0112-10.

[127] H. Zhu, B. Li, M. Chen, C. Qiu, and Z. Tang, "Improvement of Corrosion Resistance of Hastelloy-N Alloy in LiF-NaF-KF Molten Salt by Laser Cladding Pure Metallic Coatings," 2018. doi: 10.3390/coatings8090322.

[128] L. J. Swartzendruber, "The Fe-Ir (Iron-Iridium) system," *Bull. Alloy Phase Diagr.*, vol. 5, no. 1, pp. 48–52, Feb. 1984, doi: 10.1007/BF02868724.

[129] T. Tokunaga, S. Matsumoto, H. Ohtani, and M. Hasebe, "Thermodynamic Analysis of the Phase Equilibria in the Nb-Ni-Zr System," *Mater. Trans.*, vol. 48, no. 9, pp. 2263–2271, 2007, doi: 10.2320/matertrans.MB200713.

[130] H. Okamoto, "Ni-Ta (nickel-tantalum)," *J. Phase Equilibria*, vol. 21, no. 5, p. 497, Oct. 2000.

[131] K. S. Chan, P. Yi-Ming, and L. Yi-Der, "Computation of Ni-Cr Phase Diagram via a Combined First-Principles Quantum Mechanical and CALPHAD Approach," *Metall. Mater. Trans. Phys. Metall. Mater. Sci. A*, vol. 37A, no. 7, pp. 2039–2050, Jul. 2006.

[132] M. A. Turchanin, T. Ya. Velikanova, P. G. Agraval, A. R. Abdulov, and L. A. Dreval', "Thermodynamic assessment of the Cu-Ti-Zr system. III. Cu-Ti-Zr system," *Powder Metall. Met. Ceram.*, vol. 47, no. 9, pp. 586–606, Sep. 2008, doi: 10.1007/s11106-008-9062-y.

[133] "Experimental Study and Reassessment of the Ni–Hf Binary System." https://www-degruyter-com.ezproxy.library.wisc.edu/document/doi/10.3139/ijmr-2001-0088/html (accessed Apr. 14, 2022).

[134] J. F. Moulder and J. Chastain, *Handbook of x-ray photoelectron spectroscopy: a reference book of standard spectra for identification and interpretation of XPS data*. Eden Prairie Minnesota: Physical Electronics, 1995.

[135] H. W. Jenkins, G. Mamantov, and D. L. Manning, "E.M.F. measurements on the nickel-nickel(II) couple in molten fluorides," *J. Electroanal. Chem. Interfacial Electrochem.*, vol. 19, no. 4, pp. 385–389, Dec. 1968, doi: 10.1016/S0022-0728(68)80101-9.

[136] H. R. Bronstein and D. L. Manning, "Lanthanum Trifluoride as a Membrane in a Reference Electrode for Use in Certain Molten Fluorides," *J. Electrochem. Soc.*, vol. 119, no. 2, pp. 125–128, Feb. 1972, doi: 10.1149/1.2404146.

[137] C. G. Kontoyannis, "Pyrolytic boron nitride coated graphite as a container of reference electrodes for molten fluorides," *Electrochimica Acta*, vol. 40, no. 15, pp. 2547–2551, Oct. 1995, doi: 10.1016/0013-4686(94)00364-7.

[138] Y. L. Wang, Q. Wang, H. J. Liu, and C. L. Zeng, "Effects of the oxidants H2O and CrF3 on the corrosion of pure metals in molten (Li,Na,K)F," *Corros. Sci.*, vol. 103, pp. 268–282, Feb. 2016, doi: 10.1016/j.corsci.2015.11.032.

[139] A. J. Bard and L. R. Faulkner, *Electrochemical Methods: Fundamentals and Applications*, 2nd ed. Wiley Global Education, 2000.

[140] B. El-Dasher, J. Farmer, J. Ferreira, M. S. de Caro, A. Rubenchik, and A. Kimura, "Corrosion of oxide dispersion strengthened iron–chromium steels and tantalum in fluoride salt coolant: An in situ compatibility study for fusion and fusion–fission hybrid reactor concepts," *J. Nucl. Mater.*, vol. 419, no. 1–3, pp. 15–23, Dec. 2011, doi: 10.1016/j.jnucmat.2011.07.036.

[141] Y. Liu *et al.*, "Corrosion of Cr in molten salts with different fluoroacidity in the presence of CrF3," *Corros. Sci.*, vol. 169, p. 108636, Jun. 2020, doi: 10.1016/j.corsci.2020.108636.

[142] J. Qiu *et al.*, "Electrochemical study of the dissolution of oxide films grown on type 316L stainless steel in molten fluoride salt," *Corros. Sci.*, vol. 186, p. 109457, Jul. 2021, doi: 10.1016/j.corsci.2021.109457.

[143] J. W. Koger, "Alloy Compatibility with LiF-BeF2 Salts Containing ThF4 and UF4," Oak Ridge National Laboratory, Oak Ridge National Laboratory, Oak Ridge, Tennessee, 1972.

[144] A. I. Surenkov, V. V. Ignat'ev, S. S. Abalin, S. A. Konakov, and V. S. Uglov, "Corrosion Resistance and Mechanical Stability of Nickel Alloys in Molten-Salt Nuclear Reactors," *At. Energy*, vol. 124, no. 1, pp. 43–49, May 2018, doi: 10.1007/s10512-018-0372-y.

[145] V. Ignatiev and A. Surenkov, "Voltammetric measurements on the [U(IV)]/[U(III)] couple and embrittlement of high nickel alloys in fuel LiF-BeF2-UF4 salt with tellurium addition in application to molten salt reactor," *Corros. Sci.*, vol. 160, p. 108164, Nov. 2019, doi: 10.1016/j.corsci.2019.108164.

[146] K. M. Sankar and P. M. Singh, “Effect of Li metal addition on corrosion control of Hastelloy N and stainless steel 316H in molten LiF-NaF-KF,” *J. Nucl. Mater.*, vol. 555, p. 153098, Nov. 2021, doi: 10.1016/j.jnucmat.2021.153098.

[147] W. Zhou *et al.*, “Proton irradiation-decelerated intergranular corrosion of Ni-Cr alloys in molten salt,” *Nat. Commun.*, vol. 11, no. 1, p. 3430, Dec. 2020, doi: 10.1038/s41467-020-17244-y.

[148] J. Keiser and J. Devan, “Corrosion Resistance of Type 316 Stainless Steel to Li2BeF4,” *Am Nucl Soc Trans 1975 22 160*, 1975.

[149] M. Kondo *et al.*, “Corrosion characteristics of reduced activation ferritic steel, JLF-1 (8.92Cr–2W) in molten salts Flibe and Flinak,” *Fusion Eng. Des.*, vol. 84, no. 7–11, pp. 1081–1085, Jun. 2009, doi: 10.1016/j.fusengdes.2009.02.046.

[150] J. Qiu *et al.*, “Effect of SO42− on the corrosion of 316L stainless steel in molten FLiNaK salt,” *Corros. Sci.*, vol. 144, pp. 224–229, Nov. 2018, doi: 10.1016/j.corsci.2018.08.057.

[151] H. Yin *et al.*, “Effect of CrF 3 on the corrosion behaviour of Hastelloy-N and 316L stainless steel alloys in FLiNaK molten salt,” *Corros. Sci.*, vol. 131, pp. 355–364, Feb. 2018, doi: 10.1016/j.corsci.2017.12.008.

[152] H. Xu *et al.*, “Non-uniform corrosion of UNS N10003 alloy induced by trace SO42- in molten FLiNaK salt,” *Corros. Sci.*, vol. 192, p. 109802, Nov. 2021, doi: 10.1016/j.corsci.2021.109802.

[153] P. Masset *et al.*, “Electrochemistry of Uranium in Molten LiCl-KCl Eutectic,” *J. Electrochem. Soc.*, vol. 152, no. 6, pp. A1109–A1115, Jun. 2005, doi: 10.1149/1.1901083.

[154] P. Masset, R. J. M. Konings, R. Malmbeck, J. Serp, and J.-P. Glatz, “Thermochemical properties of lanthanides (Ln=La,Nd) and actinides (An=U,Np,Pu,Am) in the molten LiCl–KCl eutectic,” *J. Nucl. Mater.*, vol. 344, no. 1, pp. 173–179, Sep. 2005, doi: 10.1016/j.jnucmat.2005.04.038.

[155] A. V. Novoselova and V. V. Smolenskii, “Electrochemical and thermodynamic properties of lanthanides (Nd, Sm, Eu, Tm, Yb) in Alkali metal chloride melts,” *Radiochemistry*, vol. 55, no. 3, pp. 243–256, May 2013, doi: 10.1134/S1066362213030016.

[156] J. Serp, R. J. M. Konings, R. Malmbeck, J. Rebizant, C. Scheppler, and J.-P. Glatz, “Electrochemical behaviour of plutonium ion in LiCl–KCl eutectic melts,” *J. Electroanal. Chem.*, vol. 561, pp. 143–148, Jan. 2004, doi: 10.1016/j.jelechem.2003.07.027.

[157] O. Shirai, T. Iwai, Y. Suzuki, Y. Sakamura, and H. Tanaka, “Electrochemical behavior of actinide ions in LiCl–KCl eutectic melts,” *J. Alloys Compd.*, vol. 271–273, pp. 685–688, Jun. 1998, doi: 10.1016/S0925-8388(98)00187-X.

[158] O. Shirai, M. Iizuka, T. Iwai, and Y. Arai, “Electrode reaction of the Np3+/Np couple in LiCl–KCl eutectic melts,” *J. Appl. Electrochem.*, vol. 31, no. 9, pp. 1055–1060, Sep. 2001, doi: 10.1023/A:1017987110008.

[159] H. G. MacPherson, “Molten-Salt Reactor Program Quarterly Progress Report: October 1958,” ORNL 2626. Accessed: Feb. 18, 2018. [Online]. Available: https://digital.library.unt.edu/ark:/67531/metadc100265/citation/

[160] R. E. Thoma, “Chemical Aspects of MSRE Operations - ORNL - 4658.” Oak Ridge National Lab, Tenn, 1971. Accessed: Feb. 04, 2017. [Online]. Available: http://www.osti.gov/servlets/purl/4675946/